# CRACK IDENTIFICATION IN ROTORS WITH FULL-SPECTRUM

*A Thesis Submitted in Partial Fulfilment of the Requirements for the Degree of*

**DOCTOR OF PHILOSOPHY**

*by*

**SHRAVANKUMAR C**

**DEPARTMENT OF MECHANICAL ENGINEERING**

**INDIAN INSTITUTE OF TECHNOLOGY GUWAHATI**

**GUWAHATI 781 039 INDIA**

**MAY 2014**

# CRACK IDENTIFICATION IN ROTORS WITH FULL-SPECTRUM

*A Thesis Submitted in Partial Fulfilment of the Requirements*

*for the Degree of*

**DOCTOR OF PHILOSOPHY**

*by*

**SHRAVANKUMAR C**

**(Roll No. 09610304)**

**DEPARTMENT OF MECHANICAL ENGINEERING**

**INDIAN INSTITUTE OF TECHNOLOGY GUWAHATI**

**GUWAHATI 781 039 INDIA**

**MAY 2014**

**Department of Mechanical Engineering,**

Indian Institute of Technology Guwahati,

Guwahati- 781 039, INDIA.

# CERTIFICATE

It is hereby certified that the work contained in this thesis titled **Crack Identification in Rotors with Full-Spectrum**, submitted by **Mr. Shravankumar C** (Roll No. 09610304) to the Indian Institute of Technology Guwahati for the award of the degree of Doctor of Philosophy, has been carried out under my supervision in the Department of Mechanical Engineering, Indian Institute of Technology Guwahati. This work has not been submitted elsewhere for the award of any other degree or diploma.

May 2014

**Dr. Rajiv Tiwari**

Professor

Department of Mechanical Engineering

Indian Institute of Technology Guwahati

Guwahati – 781 039, INDIA

## Acknowledgements

I hereby thank my supervisor, Prof. Rajiv Tiwari, for his persistent guidance and suggestions during my Ph.D. studentship. I express my gratitude to him for enabling me to understand, explore, and perform in coursework, lab works as well as for my thesis, during the last five years. I thank him both for his encouragement and criticism, for the benefit of my thesis work. I wish to further correspond and learn from him in the coming days too. I also extend my thanks to my doctoral committee members, namely, Dr. S K Dwivedy, Dr. S Panda, and Dr. A Chakraborty for the review and comments provided during my progress seminars. I thank the IIT Guwahati administration for whatever amenities I have utilised during my stay at the campus. I thank the past and present heads of Mechanical Engineering Department, Dr. D Chakraborty and Dr. P Mahanta for availing various departmental facilities. I also thank my seniors, colleagues, and teachers for providing their help as useful discussions or other means.

I would particularly like to mention the names of senior Ph.D. students Sachin kumar Singh (ME); D Govind (EEE) for helping me to understand certain concepts on cracks and signal processing respectively. I have carried out a part of the experimental work, of generating a fatigue crack, at National Aerospace Laboratories, Bangalore. For this, I extend my thanks to Dr. VR Ranganath, Mr. N. Jagannathan (NAL, Bangalore) and Mr. A. Mahibalan (CVRDE, Chennai), without whose help the experimental study would not have been feasible. I also thank D J Bordoloi , Upen Gohain (IITG) and Sandeep Singh (NERIST) for helping me with the experimental work at IIT Guwahati.

I pay my foremost respect to my parents and grandparents, banking on whose advice and well-wishes I have been able to successfully carry out my Ph.D. I will cherish the memories I have spent with all of my friends here at Guwahati and elsewhere. I remember my brother for providing his possible support. I remember all others who were helpful to me during my stay at Guwahati.

May 2014
Guwahati

Shravankumar C

## Abstract

Condition-based maintenance is now-a-days recognized as the most efficient strategy for carrying out maintenance in industrial machineries. Fatigue cracks in the shaft are a very common but catastrophic fault, as accidents in turbine rotors have been reported since 1950s. Also, the shaft failure due to fatigue crack causes increase in downtime and maintenance costs. Condition monitoring employs methodologies broadly ranging from the signal-based and model-based methods to the model testing and non-traditional non-parametric methods.

In this work, model based identification algorithms have been developed to identify a crack in a shaft. A switching crack rotor model from the literature is studied. The crack is identified using a single parameter, i.e. the additive stiffness it introduces in the shaft section. Unbalance eccentricity and viscous damping of the rotor are also identified simultaneously. Displacement responses in time domain are used as input to developed identification algorithms. The algorithms are then extended to identify crack forces, the estimates which can aid in understanding the actual breathing mechanism of a crack.

The crack force and displacement time histories are transformed to frequency domain by means of full spectrum. This is done to directly use frequency responses as input to the identification algorithm, rather than using time responses. Compared to a normal spectrum, a full spectrum is helpful in obtaining the coefficients of reverse whirling frequency components, which constitute the crack force excitation and displacement responses.

The cracked rotor model is extended to consider both translational and rotational displacements. During development of identification algorithms using the extended model, dynamic condensation method eliminates the practical difficulty of measuring rotational coordinates and obtains the reduced system equations of motion.

The developed identification algorithms are numerically illustrated and tested for different measurement speed ranges and with different levels of measurement noise. The assumed and estimated parameters are compared for the efficiency of the developed algorithms. Based on the algorithms and numerical results, a flowchart showing general guidelines for crack identification has been provided.

An experimental study was conducted on a test rotor set up with a fatigue crack artificially initiated on its shaft. Data acquisition methods and processing of acquired signals have been elaborated. Phase compensation and removal of shaft bow have been performed. Repeatability of the experimentally obtained estimates is checked for different sets of measurements. The experimental inferences indicate the presence of rotor crack and estimate the crack forces.

## Contents

## List of Figures

## List of Tables

## Nomenclature

| | |
|---|---|
| $a$ | Major axis of forward circular orbit, a variable |
| $\bar{a}$ | Initiated crack length |
| $\mathbf{A}$ | Regression matrix |
| $b$ | Minor axis of reverse circular orbit, a variable |
| $\mathbf{b}$ | Regressand or known vector |
| $B$ | Specimen thickness (Shaft diameter) |
| $c$ | Viscous damping |
| $\mathbf{C}$ | Damping matrix |
| $d$ | Integer for frequency indexing |
| $\mathbf{D}_{1,2}$ | Sub-matrices |
| $e$ | Disc eccentricity due to unbalance |
| $E$ | Young's modulus of elasticity |
| $f$ | Crack force |
| $f_{\max}$ | Maximum or bandwidth frequency |
| $f_s$ | Sampling rate |
| $\mathbf{f}$ | Force vector |
| $\mathbf{G}$ | Gyroscopic matrix |
| $h_{ij}$ | Intact shaft flexibilities |
| $\Delta h_{ij}$ | Additional flexibility in the $i^{\text{th}}$ direction due to forcing in the $j^{\text{th}}$ direction |
| $\Delta\mathbf{H}$ | Local flexibility matrix at crack section |
| $i = -n,..,0,1,..+n$ | Integer showing number of the harmonic component |
| $I$ | Area moment of inertia |
| $\mathbf{I}$ | Identity matrix |

| | |
|---|---|
| Im | Imaginary part of |
| $j = \sqrt{-1}$ | Imaginary number |
| $k_{ij}$ | Direct and coupled shaft stiffness terms |
| $l$ | Real number, time domain index |
| $m$ | Disc mass |
| $M$ | Moment |
| **M** | Mass matrix |
| $n$ | Real number |
| $N_p$ | Percentage of Noise |
| $N$ | Sample length of time or frequency response |
| $p$ | Complex force |
| $q$ | Index for number of measurement speeds |
| **q** | Displacement vector |
| **Q** | Complex displacement |
| $r$ | Complex displacement |
| $R$ | Random real number between 0 and 1, Orbit Radius |
| **R** | Overall rotational transformation matrix |
| $s$ | Periodic, time-varying crack switching function |
| $t$ | Time |
| $\Delta t$ | Sampling time |
| $T$ | Acquisition time for time response |
| **u** | Displacement vector |
| $U$ | Complex translational displacement |
| $t$ | Time |
| $\Delta t$ | Sample time |

| | |
|---|---|
| $\bar{w}$ | Crack width |
| $w_x$ | Static deflection |
| $x$ | Response direction perpendicular to crack front |
| $\mathbf{x}$ | Intercept or unknown vector |
| $X$ | $x$ displacement coefficient from real DFT |
| $y$ | Response direction along crack front |
| $Y$ | $y$ displacement coefficient from real DFT |
| $\mathbf{Z}$ | A matrix |
| $\mathbf{z}$ | Column vector |
| o$xyz$ | Inertial frame of reference for system |
| $Cxyz$ | Inertial frame at disc position |
| $\dot{}$ | First order time derivative |
| $\ddot{}$ | Second order time derivative |
| $\times$ | Order of frequency |
| $\infty$ | Infinity |

**Subscripts**

| | |
|---|---|
| *central* | Central frequency of the spin-speed range |
| *d* | Diametric |
| *diag* | A diagonal matrix |
| *g* | Final time instance |
| *i* | $i^{th}$ Co-efficient of force or displacement |
| *m* | Master DOF |
| max | Maximum fatigue load |
| mean | Mean fatigue load |

| | |
|---|---|
| min | Minimum fatigue load |
| $n$ | Corresponding to $n^{th}$ frequency component in half-spectrum |
| $nf$ | Natural frequency |
| $noise$ | With noise |
| $p$ | Polar |
| $rot$ | Rotating frame |
| $s$ | Slave DOF |
| $st$ | due to static deflection |
| $unb$ | due to unbalance |
| $x$ | along $x$ co-ordinate axis |
| $y$ | along $y$ co-ordinate axis |
| $z$ | along $z$ co-ordinate axis |
| $\xi$ | along $\xi$ co-ordinate axis |
| $\eta$ | along $\eta$ co-ordinate axis |
| $\xi z$ | Plane of moment |
| $\eta z$ | Plane of moment |

**Superscripts**

| | |
|---|---|
| $c$ | With crack |
| $d$ | Dynamically reduced system matrices |
| int | intact shaft |
| $T$ | Transpose |
| $x$ | along $x$ co-ordinate axis |
| $y$ | along $y$ co-ordinate axis |
| $'$ | System matrices and vectors of 4-DOF cracked rotor model |

**Greek Symbols**

| | |
|---|---|
| $\alpha$ | Angle of tilt |
| $\beta$ | Phase angle between crack front direction and unbalance |
| $\varphi$ | Transverse rotational displacement |
| $\Phi$ | Complex rotational displacement |
| $\nu$ | State-space co-ordinate for velocity |
| $\bar{\nu}$ | Positional amplitude of shaft specimen |
| $\omega$ | Spin-speed |

**Abbreviations**

| | |
|---|---|
| DFT | Discrete Fourier Transform |
| FFT | Fast Fourier Transform |
| Im | Imaginary part of |
| Re | Real part of |
| SIF | Stress Intensity Factor |

# CHAPTER 1

# Introduction and Literature Survey

## 1.1 Importance of Study

Rotating machinery such as turbines, generators, electric motors and rotary engines have revolutionised the industrial world. This has necessitated the study of rotor dynamics as well as its maintenance during operation. Condition-based maintenance is fast becoming recognised as the most efficient strategy for carrying out maintenance in industrial machineries. The rotor shaft is a critical part as it transmits power. A rotor shaft system can be subjected to multiple faults such as unbalance, cracks, misalignment, looseness, rub or bow during its operation. The machine failure because of these faults would result in the failure of safety, increase of downtime and maintenance costs. Hence, it becomes important to assess the health of the shaft continuously for its safe operation.

One of the most common losses of the structural integrity of rotor shafts occurs in the form of fatigue crack. Fatigue cracks may be generated in rotors due to asymmetry in geometry, stress concentration such as keys, threads, notches etc., mechanical faults and thermal stresses as in steam and gas turbines. Different types of cracks such as the transverse, slant, and helical cracks have been reported. Undetected cracks in a shaft can lead to catastrophic damages. Hence, online condition monitoring of a rotor shaft for the crack propagation is a necessity.

Different condition monitoring techniques are applied in industries including:

- Vibration condition monitoring and diagnostics
- Lubricant analysis

- Acoustic emission
- Infrared thermography
- Ultrasound emission
- Motor current signature analysis
- Other techniques including visual inspection, scanning electron microscopy, oil analysis and wear debris analysis

According to the review by Sabnavis et al. (2004), methods for the crack identification is broadly divided into three groups as: Model-based and signal-based methods; Modal testing; and Non-traditional methods.

In signal-based methods, the vibration signature of the machine is compared with that of a reference signature, taken when there was no crack in the shaft. On the other hand, model-based methods are based on the analytical or numerical models. They simulate the behavior of cracked shafts during operation and attempt to correlate the observed vibration signature with the presence of a crack at discrete locations on the shaft. In model-testing, changes in system modal characteristics such as changes in mode shapes and system natural frequencies are used for the crack detection. Genetic algorithm, neural network, fuzzy logic, along with signal-processing techniques such as wavelet, Hilbert transform outlines non-traditional methods for the crack identification.

In the following sections, literature reviews are presented and organized in five parts as: reviews on condition monitoring, crack modelling, crack identification, crack identification using full-spectrum signal processing, and experimental studies on crack identification.

## 1.2 Condition Monitoring of Rotating Machinery

Condition monitoring is the study of measuring various machine parameters related to the mechanical condition of machinery. It helps to judge whether the machine is in good or bad mechanical condition, which could prevent from otherwise unforeseen damages. Condition monitoring is strongly associated with *Condition-Based Maintenance* (CBM strategy) where the machine breakdown is continuously predicted through regular condition monitoring and an optimum maintenance is carried out (Randall, 2011). Long back Woodley (1978) predicted that maintenance costs in British industry could be reduced by approximately 65%, by appropriate implementation of CBM. Friswell (2007) gave a review of inverse methods used in the damage identification. Most of the methods are based on *model updating* techniques which are broadly classified as *sensitivity methods* and *direct methods*. Sensitivity methods allow a wide choice of physically meaningful fault parameters and rely on minimising a penalty function, which consists of error between measurements and model predictions. On the other hand, direct methods reproduce the measured data by updating the whole mass or stiffness matrices.

According to Rytter (1993) the four stages of damage estimation are:

Level 1: Detecting the presence of damage in the structure/machine

Level 2: Level 1 and localisation of the damaged location

Level 3: Level 2 and severity of the damage

Level 4: Level 3 and prognosis for remaining useful life of the structure/machine

Among these, the localisation and the prognosis are advantages of model-based inverse methods. Sensitivity-based methods minimise an error function between the measured and computed modal

data (which is a function of unknown parameters). A frequent problem is that changes in measurements between the damaged and healthy structures/machines are much smaller than those observed between the modelled and healthy structures/machines. Then, model updating with the measured data could be done.

One common problem in the damage identification is modelling error, which requires suitable parameters to be included for undamaged model errors. Modelling errors can be reduced using finite element model updating or by using the difference of responses between the damaged and undamaged models. Other problems include environmental and non-stationary effects, nonlinearity, and frequency range. The problem with frequency range is that the high-frequency range vibration measurements locate localised damages accurately, but require sensor and actuator locations to be close. Since inverse approaches rely on a model of the damage, the success of the estimation is dependent on the quality of the model used to capture physical phenomena realistically.

Edwards et al. (1998) reviewed methods on fault diagnostics in rotating machinery. They concluded from several past works that model-based methods were the heart of fault diagnosis. Among model-based methods, the observer based fault detection methods have been widely used.

Isermann (1994) suggested that more than one method of fault diagnostics and identification (FDI) should be used to best reach an accurate diagnosis. Condition monitoring is considered a crucial aspect of the subject, because of the cost of production and maintenance of rotating machinery. Common rotordynamic faults include the self-excited vibration due to system instability, vibration due to some externally applied loads, such as the cracked and bent shafts, and mass unbalances.

Initial studies on the vibration-based condition monitoring in rotating systems have been carried out by Stewart (1976), Smith (1980), and Taylor (1995). Smith discussed how to recognise general kinds of faults from their vibration characteristics. Stewart and Taylor also studied processing of measured data for fault diagnosis.

Different researchers have studied different faults and fault identification methods. Downham (1976) compiled case-studies for faults such as the turbine blade failure, and the gear and bearing wear. Thomas (1984) outlined a vibration monitoring strategy for large turbo generators. Hill and Baines (1988) discussed the design of an *expert system* for the analysis of measured data, which consists of computer algorithms simulating a human expert. It was concluded that an expert system approach to vibration monitoring may be advantageous provided detailed design of the system is taken care. *Bearing defects* was studied by McFidden and Smith (1984) by giving insight into vibration spectra. Iwatsubo (1976) considered possible errors occurring in vibration analysis and how they affect the calculation of *critical speeds*, *instability*, and *unbalance*. It was found that errors in bearing dynamic coefficients have a much larger effect on the variance of system instability than do errors in mass and stiffness terms. He et al. (1990) presented a method for identifying *rub failure*. Principal components and autoregressive spectra technique (PCAT) was used for identifying the coloured noise due to rub failure in large machinery. Childs and Jordan (1997) concluded that a clearance at the rub location improves the system stability. Lee and Joh (1994) developed directional frequency response functions (dFRFs) to identify the *support anisotropy and the shaft asymmetry*.

Isermann and Balle (1997) presented a short overview of the historical development of model-based fault detection, as well as suggestions for standardising fault-detection terminology. Basic

terminology was provided in the RAM (Reliability, Availability and Maintainability) dictionary (1988), in contributions to International Federation for Information Processing (1983), and in German standards such as DIN standards and VDI/VDE-Richtlinien. Based on process parameters, model-based methods are classified as: (i) the state and output observers (or estimators), (ii) parity equations, and (iii) the parameter estimation. Based on the measurement of output response signals, the classification is as: (i) bandpass filters, (ii) spectral analysis, and (iii) maximum-entropy estimation. If features from fault detection show stochastic behaviour, the classification is as: (i) mean and variance estimation, (ii) likelihood-ratio test, and (iii) run-sum test or two-probe *t*-test. Classification methods are used when several symptoms change differently for certain faults. Classification methods are: (i) geometrical distance and probabilistic methods, (ii) artificial neural networks, and fuzzy clustering. If more information about relation between symptoms and faults is available, reasoning methods are used such as: (i) probabilistic reasoning, (ii) probabilistic reasoning with fuzzy logic, and (iii) reasoning with artificial neural networks. It is concluded that parameter estimation and observer based methods are the most frequently applied methods for fault detection. In most applications, fault detection is supported by simple hypothesis testing and fault isolation is carried out using neural networks.

Doebling et al. (1996) provided a wide literature review of categorisation of condition monitoring methods and their application to a wide range of multi-disciplinary structural applications. As of 1996, all the damage identification methods available were largely visual or localised methods, which required knowledge and accessibility of the damage location *a priori*. The need for global damage methods that could be applied to complex structures led to the development of methods that examined the vibration characteristics of the structure. Levels of damage identification were defined in line with Rytter (1993). Frequency shifts were the earliest and widely studied methods

for damage detection. It could be further classified as a forward problem, where the damage is modelled mathematically and comparison of measured and predicted frequencies is done; and an inverse problem, which calculates damage parameters from the frequency shifts. Mode shape changes and changes in mode shape curvatures are also used. Other methods include methods based on the measurement of dynamic flexibility, where the flexibility changes were measured directly or through error matrices; matrix update methods based on minimisation of objective functions and constraints; nonlinear methods; and classifier based methods such as neural networks.

Patton (1997) discussed the robustness issues in the model-based fault detection and isolation. The goal of robustness is defined as providing a rapid and reliable detection and isolation of system faults when the plant (or process) under control is disturbed, and when the mathematical model upon which the diagnosis is based cannot fully reproduce the dynamics. Quantitative model-based fault detection uses a dynamic model of the system to generate estimates of the measured and unmeasured variables of the system. The estimates are compared with actual measurements thereby generating error signals known as residuals. Quantitative models used for fault detection are generally linear, using either time or frequency domains. However, known non-linear equations of a physical system are also used. The most common model-based methods use state-space observers or Kalman filters. Residual generation and decision making are its main steps.

Different approaches used in the vibration based condition monitoring have been summarised. Quantitative model-based methods are preferred in comparison to sensitivity based methods, which minimise the error function between computed and measured modal data; or classifier methods such as probabilistic, neural network or fuzzy logic. Estimating damage parameters using

model-based identification has advantages of using the model further for quantification as well as for prognosis. For a good expert system, a detailed design of the system is to be taken care. Now, a review on crack modelling is presented.

## 1.3 Crack Modelling

Mathematical modelling of a crack is primarily important for the crack identification in rotor systems. The modeling of a crack involves three main factors: the stiffness, damping and nonlinearity. The stiffness and non-linearity have been concentrated more in literature. Few researchers have considered other factors such as: thermal effects (Bachschmid, 2004); the damping in the crack modeling was considered by Wauer (1990). All models involve reduction in the stiffness at the crack section. A review paper on the modelling of crack, based on the strain energy release rate (SERR) approach was presented by Papadopoulos (2008).

Thomson (1943) and Kirmsher (1944) modelled a notch as a reduction of the shaft cross-section. They simulated the effect of notch on the structural flexibility by using the reduced section of the structure, and discussed the effect of location and size of notch on the change in natural frequencies of the damaged beam. With the evolution of fracture mechanics in 1950's, Irwin (1957) and others later on (Rice, 1968; Wells, 1973; Dimarogonas, 1983) related the local flexibility of a fatigue crack to the crack stress intensity factor (SIF). Based on this, methods were developed to obtain SIF from the local bending stiffness and vice versa. Formulae for the SIF as a function of the crack depth were provided in handbooks of several authors including Tada (1985). Adams et al. (1978) modelled the crack as a linear spring.

Mayes and Davies (1976) studied the effect of transverse cracks on a rotor-dynamic system. The crack was modeled using the virtual work principle, applying the conservation of energy to describe the crack behaviour. The stress distribution, given by stress intensity factors, and knowledge of bending moments around the crack are pre-requisites. The theory showed that the response due to crack may either be zero (unbalance in phase with crack) or may have two distinct synchronous responses (unbalance $180^0$ out of phase with crack). Experimental results proved that when the phase of unbalance is between $-45^0$ and $135^0$ with respect to the crack, the crack is most significant. Outside these limits, the shaft tends to behave as if it were intact. The 2× response is dependent on the unbalance force vector and takes a maximum value when the unbalance and the crack are in phase.

Adams et al. (1978) modelled the crack as a linear spring of an infinitesimal length separating two sections of a bar. The elastic stiffness was determined from the changes in lowest two natural frequencies. Grabowski (1980) studied the vibration behaviour of a turbine rotor containing a transverse crack. The breathing crack was modeled using a spring-mounted hinge, whose opening/closing characteristic depends on the self-weight deflection as well as on the bending vibration. But the range of spin-speed for this model was restricted below the first critical speed.

Dimarogonas and Papadopoulos (1983) studied the vibration of cracked shafts in bending. An open crack and a closing crack (under the assumption of weight dominance) were studied. A transverse crack was modelled by considering only bending deformation. Shear stresses were not considered and the shaft was subject only to pure bending moment. The solution for SIF of a crack section was not available. Hence, the solution for an infinitesimal strip was used and integrated along the crack length. Based on Paris equations and strain energy density functions, flexibility integral

expressions were obtained along the two principal crack directions. Flexibilities were found to be a function of the ratio of crack depth to radius. First, an open crack was studied. Equations of motion in the rotor fixed co-ordinates and instabilities were discussed. Forced vibration responses and effect of unbalance was observed. An analytical study of the closing crack was also done, based on a bilinear spring model, as well as the flexibility function as truncated Fourier series.

Christidies and Barr (1984) developed the continuous cracked beam model based on the variational principle. They developed beam theory with associated boundary conditions for a uniform Euler-Bernoulli beam containing one or more pair of symmetric cracks. They proposed a local empirical function decaying exponentially with the distance from crack, to model the stress field induced due to the crack. They used the extended Hu-Washizu principle for the cracked Euler-Bernoulli beam.

Nelson and Nataraj (1986) proposed a method in which the shaft was modelled using finite element methods. The crack element assumes a breathing crack model, which produced an effective second moment of area around the crack while it is open. A switching function was incorporated to represent the actual opening and closing of the crack, which was periodic and represented by a Fourier series. The function had a value of one for the crack being open and zero for the crack being closed. Only the first few terms of series were included in the analysis, and results compared with the earlier published analytical and experimental work. They noted that the sign of minor axis for each harmonic was dependent on the shaft speed. This means that as the shaft speed varies, the harmonics experience reversals in the direction of whirl.

Jun et al. (1992) developed a cracked model based on the traditional fracture mechanics theory. Using only direct stiffness terms, the crack may only be fully open or fully closed. In reality,

however, there must exist a period of time when the crack is only partially open. The cross-coupled stiffness matrix therefore more adequately represents a breathing crack.

Gasch (1993) studied the dynamic behaviour of a simple rotating shaft with a transverse crack. In particular, forced vibrations and the stability behaviour were studied. He assumed linearity due to the weight dominance approach, which was valid even in the unstable ranges of rotation. A hinge model was used, which introduced only one fault parameter, namely, the additive stiffness due to crack. The system equations of motion were derived and linearised using the assumption of weight dominance. Accordingly, only the static deflection of the rotor system determined the crack opening/closing and not the vibration displacement. The ratio of cross crack flexibility to main crack flexibility as a function of the crack depth was observed, on the basis of which the cross flexibility was neglected. The main flexibility was in the direction perpendicular to the crack front. It was observed that hinge model was good for small cracks whose opening/closing was abrupt; while Mayes' modified function was good for deeper cracks where opening/closing was more gradual. The square wave was used as a switching function and the crack stiffness matrix was obtained as a transformation of the crack flexibility matrix defined in a rotating co-ordinate system. The stability using Floquet analysis was studied. Forced vibration responses due to the crack and unbalance forces were studied. The complex responses in time and frequency domains were discussed. The author suggested the spectral analysis (or trend analysis) over long periods where regular increase in amplitudes of 1× (Once per revolution harmonic of spin), 2×, and 3× frequency components could be monitored as possibilities for the crack identification.

Friswell and Penny (2002) studied crack modelling for the structural health monitoring. Common crack models were noted as the local stiffness reduction, discrete spring models, complex FEM

models, and the bilinear breathing crack model. Mathematical models are particularly required for the crack depth and the location identification using inverse methods. More accurate crack models are observed from the approaches of Christidies and Barr (1984), Sinha et al. (2002), and Lee and Chung (2001). Friswell and Penny considered finite element models based on these approaches for an open crack and a breathing crack. For the open crack, two FEM models, one with beam elements and other with plate elements were compared. Also, the crack element was modelled both as a reduction in stiffness elements and as a rotational spring at which a node was placed. The reduced stiffness was obtained using the Christidies and Barr's continuous system approach for a cracked beam. Also, the flexibility matrix based on fracture mechanics approach suggested by Lee and Chung (2001) was also used. The percentage change in natural frequencies for a damaged beam was observed using all different methods. Experimental natural frequencies were also compared based on Rizos et al. (1990). It was concluded that simple models were suitable for health monitoring. Similarly, a bilinear stiffness model for a breathing crack was studied and the method was observed to estimate the crack location.

Dharmaraju et al. (2004) studied the crack identification in a beam based on force-response measurements. The crack was modeled as an open crack and its flexibility matrix was defined based on the fracture mechanics approach. The rotary and shear deformations were not considered. System equations of motion were obtained using the finite element method. A transformation matrix was used to obtain the crack stiffness matrix which was coupled in two orthogonal directions. Numerical responses were simulated using an external force vector.

Sekhar (2004) studied the crack identification in rotor systems using a model-based approach. Faults were taken into account by equivalent loads which were virtual forces and moments. Effects of bearings, foundations and gyroscopic effects were included in system matrices. Residual

vibrations represented the difference between measurements of the undamaged and damaged systems. Signal processing methods such as adjusting time scale and interpolating sample frequencies were required while generating residual vibration signals. For calculating equivalent loads, residual vibrations were required at all DOFs. For this, the modal expansion was used and modal co-ordinates were estimated. Crack was modeled based on the flexibility matrix approach. The stiffness due to the crack multiplied with displacement vector yielded the equivalent force for faults. The fault parameter vector was estimated using least-squares approach. The crack depth and its position were identified.

Darpe et al. (2004) studied the coupled bending, longitudinal, and torsion vibrations of a cracked rotor. The stiffness matrix of a Timoshenko beam was modified to account for a crack with all six degrees of freedom (DOFs). The coupling of longitudinal and torsional vibrations was studied in this work. The model included the coupling between all three modes of vibration. The finite element model of Timoshenko beam was used in which the cracked beam element with modified stiffness matrix fitted during the assembly. The additional stiffness matrix due to crack was derived based on the strain energy due to crack. To study the crack flexibility variation with the crack opening/closing, a concept of Crack Closure Line (CCL) was introduced. They showed deviation of the CCL position and the variation of the crack flexibility coefficients was obtained as a function of CCL.

Darpe (2007) presented a finite element model of a rotor with a slant crack. He derived a flexibility matrix by taking into account the orientation of crack. The influence of orientation of the slant crack on stiffness values was investigated. It was shown that, in comparison with transverse cracks, slant crack stiffness matrices had additional cross-coupled stiffness terms. Also, cross-

coupled stiffness values were larger for the slant crack, which led to a stronger cross-coupling in bending-torsional-longitudinal vibration, compared to the transverse crack.

Al-Shudeifat and Butcher (2011) proposed breathing functions for the transverse breathing crack of the cracked rotor system. A linear stress/strain relation was assumed in the crack location to formulate the actual crack breathing. As the shaft rotates, location of the centroid and neutral axis of the cracked element change with rotation. The breathing was formulated for using the constant area moment of inertia of the cracked element and the time varying area moment of inertia of the crack. For each time step, after the crack starts to close, new values for the area and area moment of inertia are calculated based on which the centroid location is updated. Based on this, a finite element stiffness matrix was derived. The finite element system equations of motion were solved using the harmonic balance method. There was shift in the critical and subcritical speeds. The exact critical and subcritical speeds, and their shift due to increase in the crack depth were obtained from the waterfall plots. There was also appearance of orbits with two and three outer loops, during passage through the first subcritical forward and backward whirls, respectively. These orbits were observed within the static deflection range for relatively high unbalance force. The theoretical results were observed to be similar to experimental results performed on a rotor kit.

Singh and Tiwari (2010) studied the multi-crack identification in the shaft system using transverse response functions. The beam with multiple cracks was modelled using finite element methods with the Timoshenko beam theory. Two cracks were modelled as flexibility matrices, based on the fracture mechanics approach. Rayleigh damping factors were considered. External force excitation was considered in the vertical direction. Assembled system equations of motion were obtained in frequency domain. An algorithm was formulated for identifying crack location based on change in

the elastic shaft curvature. The difficulty of this method was the effect of noise on curvature measurement, which was reduced by measurements at several frequencies. A number of axial measurement locations were chosen. Deflections at three consecutive axial positions were selected to find out coefficients of the quadratic polynomial between them, which was proportional to the curvature of the shaft. Polynomial coefficients from the cracked shaft were normalised with coefficients from that of the intact shaft. Coefficients were further compressed to range between 0 and 1. A Crack Probability Function (CPF) was defined as absolute distance of these coefficients from their mean. Numerical simulations were conducted to identify the initial number and location of cracks, by plotting the variation of coefficients against measurement locations. Cracks were located by high values of the CPF. In order to identify the actual location and size, an optimisation algorithm was designed. It was concluded that the algorithm using the normalized polynomial coefficients had advantages over other algorithms in cancelling the effect of stepped shafts.

Ebrahimi et al. (2014) developed a continuous model for flexural vibration analysis of a rotor with an open edged crack. Models developed by Behzad (2008) were modified for obtaining displacement and stress fields in two directions. Hamilton principle was used to obtain the system equations of motion as a partial differential equation. The solutions for an open edged crack were obtained using Galerkin methods and then compared with finite element model results.

In this section, different crack models were presented. The most common model of crack used is the crack flexibility matrix based on the fracture mechanics approach. Based on this, not only the form of flexibility matrix is defined but its coefficients are also theoretically evaluated from the SIF. Various models are used, such as, local stiffness reduction, spring models, FEM models, bilinear switching functions, continuous cracked beam models, equivalent loads, and reduction of second moment of area. The crack models are mostly based on the increase in the flexibility at the cross-section due to occurrence of crack. Coupling effects due to crack have also been studied. Now, a review on crack identification methods is presented.

## 1.4 Crack Identification

The characteristic of a crack in a rotor system is that it introduces local flexibility, which causes a change in the system dynamics. Thus, an inverse problem can be studied based on changes in modal parameters and the free and forced vibration responses of cracked structures. But, more accurate models are needed which consider: the coupling between different motion such as the bending, longitudinal, and torsional vibrations; the splitting of natural frequencies due to the presence of a crack; the nonlinearity in stiffness due to breathing; and the friction between cracked surfaces. These features have been explored by several researchers for crack identification. Also, a rotor crack opens and closes with the shaft spin. When the crack is fully closed, its local stiffness is maximum, and when the crack is fully open, it is minimum. At other positions, the crack is partially open and partially closed. This open/closing mechanism generally distinguishes a rotor crack from other structural cracks. Now, various literatures on identification of cracks in rotor systems is elaborately discussed.

Dimentberg (1961) showed that the total motion of an asymmetric shaft centre was the sum of a vector that turned with the angular velocity and a vector that turned with twice the angular velocity. Result was a spiral like orbit that was determined by relative length of two vectors. This was because the shaft crossed two limiting stiffnesses twice during one revolution. The weight of the shaft was balanced by this varying stiffness. The shaft would rest at a higher position when the stiffness was more and vice a versa. This oscillation caused the 2× component in the frequency spectrum. Hence, 2× component in the frequency spectrum was a strong indication of the presence of a crack in the shaft. However, the bearing misalignment could also result in the 2× and 3× components in the spectrum. The bow in a rotor introduced 1× component in the spectra and the mass unbalance also introduced 1× component.

Dimarogonas and Papodopoulos (1983) identified an open crack. For an open crack, with small crack depths, it was observed that the natural frequency of the cracked rotor equals half the intact rotor natural frequency. This information was used for crack identification as only mechanisms with dissimilar moments of inertia in two perpendicular directions can introduce such a frequency. For a closing crack, it was suggested that because of more nonlinearity one had to resort to the numerical integration.

Gounaris and Dimarogonas (1988) derived a finite element of a cracked prismatic beam for structural analysis. It was noted that the crack was modelled using a crack flexibility matrix based on the principles of fracture mechanics. In such a case, the crack stiffness matrix is obtained as an inverse of the flexibility matrix. However, for small cracks, the crack flexibilities are very small and consequently the stiffness matrices are larger. This might lead to numerical problems during the solution, such as singular matrices. To overcome this, authors developed the stiffness matrix

for a cracked beam element, based on transfer matrices and shape functions. Numerical results observed the discontinuity at the crack in plots of the vibration slope.

Pandey et al. (1991) obtained relationship between the changes in eigen-parameters, the damage location, and the damage size. A parameter, namely the curvature mode shape was investigated as a possible candidate for identifying and locating damage in a structure. It was shown that the absolute changes in curvature mode shapes were localised in the region of the damage and hence could be used to detect damage in a structure. The change in the parameter increased with the increase in the size of the damage. The finite element analysis was used.

Gasch (1993) introduced a perturbation method into his analysis of a linearised crack model with direct stiffness terms. He provided suggestions for the detection of cracks, such as the long-term monitoring of the mean additional static deflection and the trend analysis over long periods. 1×, 2×, and 3× response amplitudes will all increase in the direct proportion to crack size.

Dharmaraju et al. (2004) used an inverse engineering problem based on the model updating for identifying a crack in a beam. The system frequency equation of motion was reduced to a regression form, containing unknown crack flexibility coefficients in a vector. Care was taken to avoid nonlinear estimators due to the inversion of crack flexibility matrix. The static (Guyan) reduction scheme was used to overcome the problem of excessive number of measurements required. An error function was defined in terms of the theoretical and estimated flexibility coefficients and it was used for determining the crack depth with the help of least-squares technique in conjunction with the bisection root searching method. The identification algorithm was found robust against moderate level of measurement noise.

Sekhar (2004) used a crack model based on equivalent loads to identify its depth and location on the shaft. The nature and symptoms of the fault were ascertained using the Fast Fourier transform (FFT). It was found that the estimation of crack depth, to a good extent, was dependent on the number of measurement locations. Sekhar (2004) used the model-based continuous wavelet transform (CWT) approach to extract sub-harmonics from the coast-down time domain vibration signal from journal locations of cracked rotors on fluid film bearings. The coast-down phenomenon was analysed by considering the dissipation through the journal film and by evaluating the deceleration for each speed. The CWT of a time-varying function was defined as the sum over all time of the signal multiplied by scaled shifted versions of the wavelet function. Characteristic sub-harmonic peaks, which could not be detected by the normal FFT due to the non-stationary nature of the signals, could be detected by the CWT.

Darpe *et al.* (2004) identified the crack from the coupling effect it introduces in the crack flexibility matrix. Rotor responses due to the crack and unbalance forces were obtained. The intact rotor showed absence of higher harmonic frequencies. Even when additional torsional excitation was provided to the intact shaft, no coupling effect was seen in the response of other modes. The response due to the cracked rotor contained 1× 2× and 3× frequency components in its lateral vibration spectrum; the longitudinal and torsional spectrum showed 1× and 2×, while the torsional spectrum showed additional 4× component. This indicated a prominent coupling mechanism due to the crack. Next, with the crack, an additional harmonic torsional excitation was given, at a frequency closer to the bending natural frequency. An interaction of the torsional and bending frequencies showed the appearance of sum and difference frequencies around the bending natural frequency. Similar results established the coupling between the torsion and bending vibrations as well as the bending and longitudinal vibrations.

El Arem and Maitournam (2008) developed a cracked beam finite element for studying cracked rotor dynamics and stability analyses. According to them, the bilinear stiffness model of crack was a simplistic approach that led to some reserves about the quality of quantitative results stemming from its exploitation. On the other hand, three dimensional crack models were free from the simplifying hypothesis and approximations. The crack stiffness variation was deduced from finite element computations accounting for the unilateral contact between crack lips. They preferred using 3-D (3-Dimensional) FEM models, also as there were hardly any SIF formulas for cracks on cylindrical shafts till that time. The shaft was only considered as an assembly of elemental rectangular strips, which was similar to the FEM software approach. Crack models based on FEM models and beam models were obtained and compared.

Liu and Jiang (2013) studied the signal-based crack identification of rotor subjected to the torsional excitation. The coupling of the lateral and torsional vibrations is observed in the case of transverse cracks along with change in 1× frequency component, whereas the slant crack has large changes in 2× frequency component.

In this section, various crack identification methods have been discussed. The presence of 2× frequency component of the spin speed in the frequency spectrum of cracked rotor is considered as a strong indicator of crack. This also causes a sub-harmonic critical speed at half of the system natural frequency. Cracks are also identified from changes in modal parameters such as natural frequencies and mode shapes. Because of the complexity in crack identification, trend analysis for increase in 1×, 2×, and 3× vibration response amplitudes is suggested. Model-based methods are also used which identify crack parameters such as the crack stiffness, location, and its depth based on an inverse problem approach. 3-D finite element models have also been used for identification.

Since the crack force contains frequency components, both in the same and reverse directions of rotor spin, a suitable frequency tool known as the full-spectrum has been used for its analysis. A review on the full-spectrum is presented in the following section.

## 1.5 Full-Spectrum

Southwick (1993) discussed about full-spectrum plots in two parts. He noted that the full-spectrum and orbit plots required signals from two orthogonal sources. Generating an ellipse with rotating vectors was explained. A single frequency elliptical orbit could be constituted from a particular positive (forward) and negative (reverse) vibration frequency components of a full spectrum. The ellipticity and precession of the orbit depends on the amplitude relationship of two vectors. The orientation of the major axis of the ellipse depends on the phase relationship between the vectors. The most definitive signal characteristics of an unstable vibration are a circular or nearly circular orbit with large amplitude and a forward precession at a frequency of approximately $\lambda\Omega$ where $\lambda$ is the fluid circumferential average velocity ratio and $\Omega$ is the rotative speed. The second part discussed about identifying complex faults such as rubs, preloads, misalignments, and shaft cracks using full-spectrum plots. High friction rubs generating reverse frequency components could be identified using the full-spectrum. A shaft crack is commonly identified from 2× component. Also, there is a phase change in both 1× and 2× vectors. From machinery diagnostic point of view the first and second rule of cracks is defined. According to the first rule, if a shaft is cracked it is almost certainly bowed. According to the second rule, a rotor with an asymmetric stiffness and a radial side load, rotating at a speed near half of any resonance frequency may experience high 2× vibration amplitude and 2× phase shift.

In order to study the non-stationary vibration in large machines Lee and Han (1998) integrated the techniques of Wigner Distributions (WD) and Short Period Fourier Transforms (SPFT) with the full-spectrum. The technique was termed as Directional Wigner Distribution (dWD). It was used to study instantaneous whirl orbits during the rotor run up. The Shape and Directivity Index (SDI) was proposed and used to quantify the shape and directivity information of whirling motion.

Goldman and Muszynska (1999) briefed applications of the full spectrum to rotating machinery diagnostics, which were available in commercial Bently Nevada packages such as ADRE (Automated Diagnostics for Rotating Equipment) and WDM (Windows Data Manager). The information hidden in the half-spectrum is the correlation between vibration patterns from different transducers. This is displayed by the full-spectrum. At a glance, the full-spectrum plot shows whether the rotor orbit or machine casing motion frequency components are forward or reverse in relation to the direction of shaft rotation. This information is characteristic of specific machinery faults. The advantage of full-spectrum is that they contain information of relative phase correlation between spectral components of orthogonal signals. This enables reconstruction of filtered orbits from full-spectrum frequency components, which is not possible in traditional half-spectrums. A full-spectrum works on the process that an elliptical orbit can be presented as a sum of two circular orbits: one rotating in the direction of rotation (forward) and other in its opposite (backward) direction. The angle between the horizontal probe and the ellipse major axis determines the relative phase of forward and reverse components. For certain cases, the ellipse can degenerate into a straight line or a circle. The article included a tabulation of various rotating machinery faults that could be identified using full-spectrum plots. Tuma and Bilos (2004) studied the fluid induced instability of rotor systems with journal bearings during the run up and coast down operations using the full multi-spectra. The whirl frequency component and fluid induced instability components were identified.

Bachschmid et al. (2004) made use of SDI to analyse the ellipticity of filtered orbit as well as the amplitude and inclination angle of the rotor orbit major axis in the case of a large turbo-generator unit that was subjected to rotor-to-stator rubs. Results were used to update the model and identify the location and severity of the fault.

Patel and Darpe (2011) used the full-spectrum generated by orbit decomposition for the detection of rotor crack and misalignment. Non-stationary oscillations of a rotating shaft with nonlinear spring characteristics during acceleration through a critical speed were studied by Ishida et al. (1997). Approximate solutions for non-stationary oscillations were obtained by means of the asymptotic method and the amplitude variation curves of each oscillation component were obtained by the complex-FFT method. It was concluded that the complex-FFT was the most suitable method for the analysis of non-stationary oscillations.

The full-spectrum and its applications were presented in this section. A review on experimental studies of the rotor crack is presented in the next section.

## 1.6 Experimental Studies on Rotor Cracks

Fatigue cracks in a rotor system make it susceptible to catastrophic failures. The vibration based detection of fatigue cracks has been a current challenge in the condition-based maintenance. Literature on rotor cracks widely involves numerical studies with the model-based identification of fatigue cracks, but very few experimental studies have been attempted. Most of the experimental studies involved the study of hacksaw or wire cut EDM (Electric discharge machining) crack or welded shaft crack. However, induced cracks in such test rigs do not resemble the characteristic breathing behavior of a fatigue crack.

Gudmundson (1983) studied cross-sectional cracks in beams. Two different modelling methods were considered: the flexibility matrix based on SIF's and finite element equations. Experiments were conducted with a saw-cut edge-cracked cantilever beam, for varying crack lengths and a width of 0.4 mm. A signal generator gave a continuous sine-sweep in a narrow frequency band around the eigen frequency, which was to be measured. The lowest bending eigen frequencies in two orthogonal directions were obtained. Eigen frequencies were presented as a function of the crack length. In order to investigate the effect of crack closure on vibrations of a cracked beam, a fatigue crack was introduced in the beam. During the crack growth, observations were that the frequencies were constant up to a crack length to width ratio of 0.5 and then they slowly decreased. Measured frequencies deviated from frequencies obtained for an open crack. These observations were attributed to the crack closure effect, where the crack remains closed for small vibration amplitudes due to residual stresses. Theoretical results were observed to be in agreement with experimental results.

Mayes and Davies (1984) studied the vibration behaviour of a multi-shaft, multi-bearing system in the presence of a propagating transverse crack; which are more applicable to real machines. The crack was modeled as a reduced second moment of inertia of the shaft section. Theoretically, a small crack behaved as a slotted shaft with additional forces from opening/closing. Thereby, the variation of 2× component with the out-of-balance was negligible. The expression for dynamic bending moment causing the crack opening was considered along with damping forces. The test rig consisted of two solidly coupled rotors mounted on four journal bearings, each mounted on a flexible support. A section of the rotor shaft is machined to have a step with a reduced diameter of 25 mm and notch in its centre. A crack propagated from the notch at a running speed of 2000 rpm. A crack of 6.5 mm was studied. The rig was initially balanced and crack initiated from a 5-mm slot

spark eroded transversely into the centre of the reduced section. The crack depth was monitored using the potential-drop method. Run down measurements were considered with bearing pedestal and shaft-to-bearing vibrations. In order to obtain dynamic stresses at the crack, the shaft was strain gauged on the opposite side of the crack. From the frequency analysis, the crack opening/closing was observed to follow a profile of $(1 + \cos\phi)$ with 1× stiffness variation. It was concluded that dynamics must be taken into account for fracture mechanics calculations of crack growth rates when the crack was large.

Darpe et al. (2003) experimentally investigated coupled vibration responses of a cracked rotor to the periodic axial excitation. A fatigue crack was induced on the shaft transversely using a three-point bending machine. Once the crack propagated to a desired depth, the specimen was machined to remove the notch. The machining removed the initial slit and slight bow that occurred during the loading on the fatigue bending machine. From experimental observations, the coupling of longitudinal and bending vibrations was established by the presence of axial excitation frequencies in the spectrum of lateral vibrations. It was also observed that the bending natural frequency could be excited by matching any one of harmonics of the axial excitation frequency, or by matching any of the sum and difference combination frequencies. Findings were suggested for the rotor crack detection utilising the response of rotor to the axial excitation, particularly during slow-roll conditions.

Pennacchi et al. (2006) performed a model-based identification of transverse fatigue cracks in rotors, with methods suitable to applying for industrial machines. A linear cracked rotor model was considered, and the crack breathing was modelled using Fourier series of harmonic components. Finite element method was considered and bending moments on nodes of the crack element were

calculated. A test rig EUROPE of EDF (Electricite de France) was used, which consisted of three parts of shafts resting on oil-film bearings. Proximity probes were located very close to bearings. Three different cases of cracks were studied: a slot made by electro-erosion which was representative of an open crack, a fatigue crack initiated from the notch having depth of 14% of the shaft diameter, and a fatigue crack with a depth of 34% of the shaft diameter. The 1×, 2×, and 3× revolution components were primarily observed. The 1× component had additional effects of the shaft bow and the unbalance. For the case of slot, breathing was absent and only 2× component due to asymmetry in the stiffness was observed. It was used in identifying the moments and crack parameters. For the case of fatigue cracks, the position of crack and relative depth was identified, from 2× revolution component. 1× and 3× components were considered for the identification, only in the case of 47% of the crack depth. Additional deflections due to the crack were observed to be 2μm and less than 5μm at bearings, based on which the crack identification was considered.

Zhou et al. (2005) studied experimentally the nonlinear dynamic behavior of a cracked rotor. The online crack detection was considered. The artificial transverse crack was made in the shaft by means of three-point bending fatigue method. For the crack propagation, a right angled notch was used. Four shaft specimens were tested, one with no crack, two with fatigue cracks, and one with an open slot. From results, the orbit of the cracked rotor had a clear two-circle topological shape. The speed range in which this characteristic existed depended on the crack depth. This phenomenon was absent for an intact shaft. Among frequency components, the two-order was the leading component. When the depth of crack increased, amplitudes of 2× and 3× critical speed components increased. For the case of disc eccentricity, it was observed that vibration amplitudes may increase or decrease depending on directions of the crack and unbalance vectors. These inherent features of the crack were observed even in presence of disturbances such as the oil film,

rub impact and noise. Generally, the energy of higher order components was low; however in the case of deep cracks, these were predominant and the one-order frequency component was dominant only near the critical speed.

Sinha (2007) introduced higher order spectra (HOS) tools, namely the bi-spectrum and the tri-spectrum, for the identification of crack and misalignment faults in a rotor system. HOS tools classified the crack and misalignment faults, which were important as the characteristic response of both faults, had 2× frequency component of the shaft rotation. Conventionally, HOS tools were used to detect the non-linear behaviour in responses such as for the coupling of harmonic components. The bi-spectrum is the double Fourier transformation of the third-order moment of a time signal. Similarly, the tri-spectrum is the triple Fourier transformation of the fourth order moment of a time signal. The crack was developed by welding two pieces, which could create breathing effect. The crack depth was half of the shaft diameter. A change in the orbit behavior, which is obtained at a speed near half of the critical speed of a cracked rotor, indicated the change in phase and amplitude of 2× component. Then, the misalignment of around 0.5 mm was introduced between two bearing pedestals. From results, a total of four peaks appeared in the bi-spectrum for the crack fault; where as a total of five peaks appeared in the case of misalignment fault. Similar results were obtained using the tri-spectrum, which could classify the crack and misalignment faults.

Karthikeyan and Tiwari (2010) conducted an experimental investigation on the detection, location, and sizing of a structural flaw in a beam, using forced response measurements. A circular beam supported on ball bearings was used for the set up. Initially, system modelling was done for the beam using Timoshenko beam theory. An open flaw was considered and modelled as a 4×4

flexibility matrix. A harmonic forcing of known amplitude and sine-sweep frequency was considered. The flexibility matrix for the element with flaw was considered as the sum of flexibility matrices for the intact shaft and the crack. Flexibility matrices and Rayleigh damping matrices were different for the intact and cracked elements. Since transverse rotational Degrees of freedom (DOF's) could not be measured accurately, the standard dynamic condensation was used. Assembled equations of motion and least-squares solutions were obtained. In order to condition regression matrices, Tikhnov regularisation schemes were used. Two algorithms were designed: a crack location algorithm, and a flaw sizing algorithm. For the crack location, the fundamental natural frequency was calculated as a function of flaw locations, for an initial guess of the flaw depth ratio. Their variation was plotted against assumed flaw locations, and intersections were obtained as flaw locations. In a flaw sizing algorithm, one of the obtained flaw locations was selected to find out flaw flexibility coefficients and the flaw depth ratio. The flaw depth ratio was updated in the location algorithm iteratively, for the convergence of crack location and crack depth ratio. In the experimental set up, the forces and displacement responses were measured. Experimental measurements were correlated with numerically simulated measurements and used to update the theoretical model accordingly. Estimated flaw parameters were found to be in good agreement with the measured data in different frequencies.

Cai (2011) studied vibration based crack detection in shafts. Three different types of transverse cracks were studied, namely, the fatigue crack, the welded crack and the wire-cut crack. It was concluded that the fatigue induced crack by three-point bending was the most accurate method to evaluate the vibration characteristics of cracked shafts. It was also indicated that existing switching models and harmonic models cannot accurately describe the periodic stiffness of a transverse crack.

Singh and Tiwari (2012) performed experimentation on cracked shafts and identified the presence of multiple cracks. Two shafts were taken for experiments. Shaft deflections were measured with the Eddy current displacement sensors. However, due to measurement errors the detection was not effective. The quality of measurements was improved using a laser vibrometer for measuring shaft deflection. Based on experimental results, a scheme was proposed for the better estimation of the double derivative of shaft deflections. The scheme consisted of increasing the distance between two measurement locations to reduce the effect of measurement noise while estimating the double derivative. Experimental results were improved further by implementation of the scheme.

Chasalevris and Papadopoulos (2013) used coupled bending vibrations introduced due to crack for its early detection. The external excitation is provided by means of an Active Magnetic Bearing. The signals of the vertical response of intact system are subtracted with the responses from the shaft with crack. The CWT's of the resulting signals are obtained. For the chosen scale corresponding to the excitation the envelope of the coefficients is obtained using Hilbert transform. Further, the fast Fourier transform is obtained, which shows a coupled response with high sensitivity in the 2× frequency component. Singh and Tiwari (2014) experimentally identified crack based on algorithms detecting the slope discontinuity. Transverse deflections are measured at regular axial locations of the shaft. For this purpose, a laser vibrometer along with reflective tapes is used. External sine-sweep excitation is provided between 1 Hz to 60 Hz. Frequency response functions (FRF's) measurements are obtained, which are used as input for the developed algorithms. Crack probability functions provide the probability of crack presence between two

locations. Thus, multiple cracks on the shaft are detected. A scheme is proposed for better estimates, by reducing the number of measurements for a given length.

This section discussed different experimental methods used for study of fatigue cracks. Now, scopes and objectives of the present work are discussed.

**1.7 Scopes of Work on the Crack Identification**

The literature review focuses on the condition monitoring of a transverse crack in rotor systems. A review on the classification of condition monitoring methods and their application to various rotor faults has been discussed. Crack models such as a spring, reduced stiffness, flexibility matrix based on SIF's, finite element models, and continuous beam models have been reviewed. A review also discusses the use of new signal processing methods such as the full-spectrum for rotor applications. Finally, a review on the state-of-art of experimental study of cracks in rotor systems and their identification has been presented. From the review of literature on crack identification, following scopes are summarised.

- Among condition monitoring methods, quantitative model-based methods have been widely preferred. They have the main advantage of quantifying the fault, along with possible location and prognosis. Some of its limitations are: quality of fault model; modeling errors; changes in measured data due to environmental effects; estimation at high frequency ranges; robustness of nonlinear models and state space observers.
- Also, there is requirement for reduction of dependence on input measurements such as the force excitation. Need also exists for early fault detection as well as for the robustness of monitoring methods.

- Online condition-monitoring and simultaneous monitoring of multiple faults is still a challenge. Identification of faults like crack, rub, and misalignment still require a comprehensive research.
- Variety of crack models is discussed in the literature. Modelling based on fracture mechanics is widely used, though approximations are used for obtaining the SIF. Similarly, modelling cracks using the theory of shafts with dissimilar moments of inertia has disadvantage that multiple rotor faults exhibit similar behaviour.
- 2D and 3D FEA models of cracks are observed to contain modelling errors and are also complicated and computationally intensive to model simple beam like structures with cracks.
- There are further scopes for study on effects of coupled vibrations and nonlinearity in crack models. The study on the stability behavior of crack models is also required.
- Cracks modelled for rotor systems accommodate the switching mechanism of crack. The switching crack breathing behaviour has been modelled in literature by using a hinge model. It has also been modelled by defining a crack closure line. It is also represented as a harmonic series of a trigonometric function. A lot of scope exists for more accurate modelling of crack breathing functions.
- Estimation of crack parameters such as stiffness, size, and location has been performed. Attempts for estimating the characteristic switching/breathing forces from cracked rotor responses can be carried out for estimating crack forces and for better understanding of the crack behaviour.
- Identification algorithms are better adapted while using frequency responses. Traditional frequency spectrums as well as novel signal-processing methods such as full-spectrum are discussed. Full-spectrum has been chiefly discussed for signal-based identification of crack

and other faults. Since, the full-spectrum signal processing is highly suitable for crack problems; it can be exploited for the model-based crack identification.

- Various crack identification algorithms have been proposed in the literature. All the developed condition monitoring methods primarily depend on the analytical model of the crack. So, this provides the necessity for thorough validation of the developed identification algorithms using experimental methods.
- The literature on experimental study of cracks mainly involves saw-cut or EDM or welded shafts, for studying a rotor crack. But, they do not simulate the breathing behaviour of a transverse fatigue crack. Very few works on fatigue cracks have been found. Hence, more investigation on the artificial generation and study of a fatigue crack becomes necessary.
- From the above discussions and observations, the motivation of the present work has been formed. The objectives of the present work are now discussed.

## 1.8 Objectives of the Present Study

The objectives of the present work include:

- To study the mathematical model of a cracked rotor. A switching crack model with transverse vibration in two orthogonal directions will be considered. The model will contain the crack and other system parameters and also the forces due to crack switching. The model will be used to develop identification algorithms for parameter estimation. Simultaneous estimation of crack, unbalance, and viscous damping parameters will be carried out. Identification algorithms will also be developed to estimate unknown crack forces caused due to switching behavior.
- To obtain the system responses of the cracked rotor model. The displacement responses in time domain and magnitude and phase plots in frequency domain will be obtained. The

critical speed of spin frequency and its harmonics will be obtained. For these, the crack and other unknown parameters will be assumed. This constitutes the direct problem.

- To carry out crack identification using time and frequency responses. The displacement time responses will be used to estimate the crack and other unknown parameters. As the crack force and its response contains forward as well as reverse whirling frequency components (i.e., frequency components opposite to the spin direction), a full-spectrum signal processing method will be used in the frequency domain. This will obtain complex Fourier coefficients of force and response of the cracked rotor.
- To numerically illustrate the developed identification algorithms. Different ranges of measurement spin speeds will be chosen. Also, the error in the estimates for different levels of measurement noise in the responses will be studied.
- To perform the above studies for a more general cracked rotor model. This cracked rotor model will consider both translational and rotational motion along two transverse directions. The model will be used for crack identification as described in the above steps. Prior to identification the immeasurable angular displacements will be removed by means of dynamic reduction.
- To fabricate a cracked rotor test set up. A shaft with a V-Notch will be used to generate a fatigue crack from the notch tip. Three point bending test with fatigue cyclic loading will be used for the purpose. A fatigue crack is necessary as a notch or any other flaw cannot mimic the opening/closing profile of a switching crack. The test set up will be assembled along with data acquisition and signal processing instruments.
- To test the developed identification algorithms using experimentally acquired displacement responses. Phase compensation and removal of shaft bend effect will be carried out.

## 1.9 Organisation of the Thesis

The thesis is organized into seven chapters. The introduction and literature review are presented in Chapter 1. The mathematical modelling along with its numerical simulations is presented in Chapter 2. In Chapter 3, identification algorithms are developed for estimation of fault parameters, namely additive crack stiffness and disc eccentricity due to unbalance. Additionally, the system viscous damping is also identified. Algorithms are then extended to identify the switching crack forces. Comparison of the numerically obtained parameter estimates with their assumed values will check the correctness of the proposed algorithms. Chapter 4 discusses the development and application of full-spectrum signal-processing method for the cracked problem. Full-spectrum displacement coefficients and force coefficients are obtained as inputs to the proposed identification algorithms. The algorithms are also numerically illustrated. In Chapter 5, a mathematical model of a cracked rotor with the gyroscopic effect is developed. This chapter illustrates a crack model which can be applied for finite element methods along with the application of dynamic condensation for eliminating rotational measurement co-ordinates. Finally, Chapter 6 discusses the development of an experimental setup with a fatigue crack in the rotor shaft. The data acquisition and post-processing of vibration signals are presented, along with the testing of identification algorithms with experimental responses. Conclusions, limitations and applicability, and future scopes from the present work are presented in Chapter 7.

# CHAPTER 2

## Modelling and Analysis of a Cracked Rotor with Switching Behaviour

### 2.1 Introduction

This chapter presents mathematical models of a Laval rotor with a transverse fatigue crack. The model of the rotor studied in this chapter has *translational displacements* (2-Degrees of freedom (DOF) system) only. The modelling of fatigue crack is based on a *crack flexibility matrix*, which is well developed in the literature on cracked rotors. A *transformation matrix* converts the crack model in the rotational co-ordinate system into the inertial co-ordinate system. Following sections also discuss *linearization* of the crack model and the overall system equations of motion (EOMs). These are given by second-order ordinary differential equations. Forces acting on the system consist of force vectors due to the crack and the unbalance. It is well known that an unbalance force produces response; at a frequency same as the rotor spin-speed. On the other hand, the crack force produces responses containing multiple frequency components, which are harmonics of the shaft rotation frequency (or the spin-speed). Thus, the unbalance and the crack together provide *excitations of multiple harmonics* to the rotor system. The crack force contains harmonics which excite the rotor either in the same direction of spin (forward whirl) or in the reverse direction of spin (backward or reverse whirl). The steady-state response of the system to these excitations can be studied essentially by means of *time-histories* and *frequency responses*. The present chapter discusses the solution procedures for the time and frequency response analyses. Numerical illustrations are also provided with a simple rotor configuration data.

## 2.2 System Modelling of a 2-DOF Cracked Rotor

The mathematical model for dynamics of a cracked rotor is presented. A Laval rotor, which is a simply supported elastic shaft with a centrally located disc, is considered. It is a lumped model with the shaft assumed as massless. This section considers a 2-DOF model with the transverse translational motion in two orthogonal directions. However, it ignores gyroscopic couple and elastic coupling due to the disc. Figure 2.1 shows such a rotor with a fatigue crack near the disc.

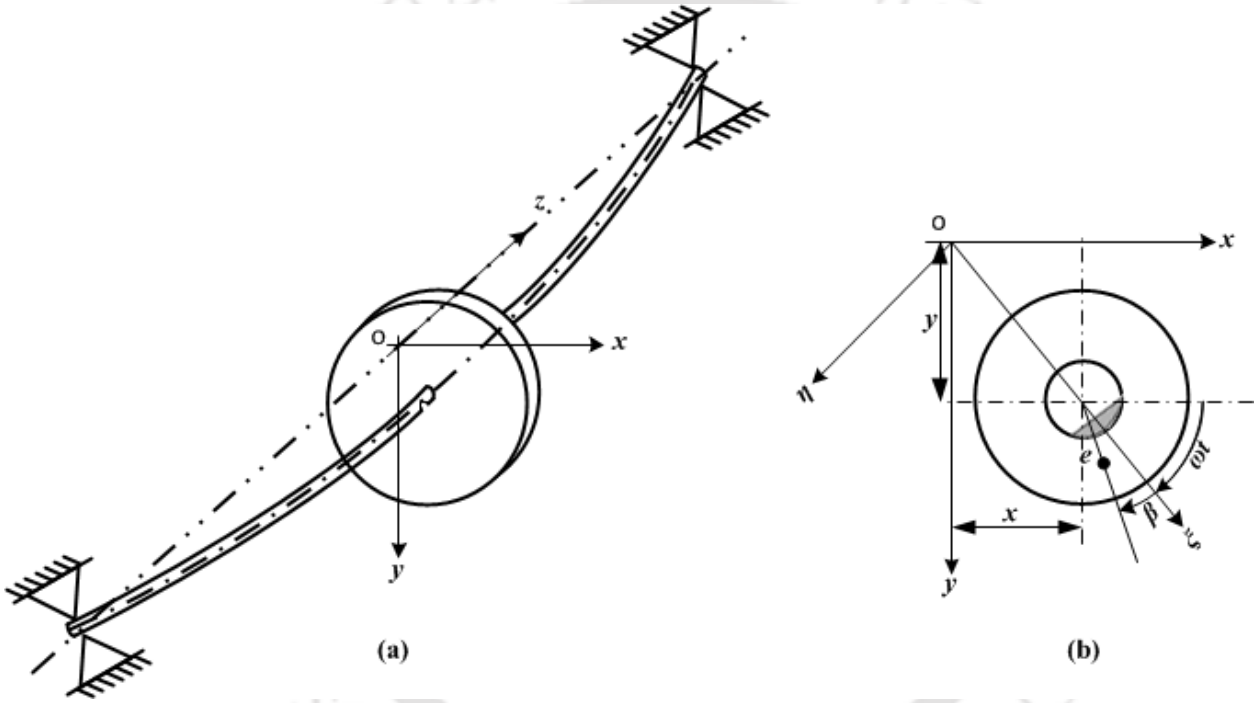


Figure 2.1 (a) A Laval rotor with a cracked shaft (b) The unbalance disc and cracked shaft in inertial co-ordinate system $x$-o-$y$ and rotating co-ordinate system $\xi$-o-$\eta$

### 2.2.1 General System Equations of Motion

In general, EOMs are written as follows for a rotor system with an intact shaft.

$$\mathbf{M}\ddot{\mathbf{u}} + \mathbf{C}\dot{\mathbf{u}} + \mathbf{K}\mathbf{u} = \mathbf{f}_{st} + \mathbf{f}_{unb} \tag{2.1}$$

For a 2-DOF model, the following system matrices and force vectors are defined in an inertial co-ordinate system.

$$\mathbf{M}=\begin{bmatrix} m & 0 \\ 0 & m \end{bmatrix}; \quad \mathbf{C}=\begin{bmatrix} c & 0 \\ 0 & c \end{bmatrix}; \quad \mathbf{K}=\begin{bmatrix} k & 0 \\ 0 & k \end{bmatrix}; \quad \mathbf{u}=\begin{Bmatrix} u_x \\ u_y \end{Bmatrix}$$

$$\mathbf{f}_{st}=\begin{Bmatrix} mg \\ 0 \end{Bmatrix}; \qquad \mathbf{f}_{unb}=me\omega^2\begin{Bmatrix} \cos(\omega t+\beta) \\ \sin(\omega t+\beta) \end{Bmatrix} \tag{2.2}$$

In Eqn. (2.2), $\mathbf{M}$ , $\mathbf{C}$ and $\mathbf{K}$ are the mass, damping and stiffness matrices of the rotor system, $\mathbf{f}_{st}$ is the weight vector , $\mathbf{f}_{unb}$ is the force vector due to the disc unbalance, $\mathbf{u}$ is the displacement vector in the inertial co-ordinate system, $m$ is the disc mass, $c$ is the viscous damping in the rotor system, $k$ is the stiffness of the shaft, $u_x$ and $u_y$ are displacements at the centre of shaft in the plane of the disc, $\omega$ is the rotor spin speed, $e$ is the eccentricity of the disc (i.e., the distance between the centre of gravity and the shaft centre of the disc), and $\beta$ is the unbalance phase angle measured from $\xi$ in the rotating co-ordinate system (see Figure 2.1).Bold capital letters are used for matrices and bold small letters are used for vectors. Refer nomenclature for details.

The crack section introduces a local flexibility matrix into EOMs (Eqn.(2.1)), say $\Delta\mathbf{K}$ . It is known from the literature (Grabowski, 1980) that a rotor crack opens/closes due to variation of stresses with the shaft rotation. This *crack flexibility* parameter can vary due to the periodical shaft rotation ($\theta = \omega t$) and as well it varies due to rotor vibration displacement, $\mathbf{u}$ . Thus, the local flexibility matrix shows a *non-linear* behaviour (i.e., $\Delta\mathbf{K}(u,t)$). The non-linear EOM of the cracked Laval rotor is, hence, written as follows,

$$\mathbf{M}\ddot{\mathbf{u}}(t)+\mathbf{C}\dot{\mathbf{u}}(t)+\left(\mathbf{K}+\Delta\mathbf{K}\left(u,t\right)\right)\mathbf{u}(t)=\mathbf{f}_{st}+\mathbf{f}_{unb} \tag{2.3}$$

It is seen from literatures (Grabowski, 1980; Gasch, 1993) that the mean static deflection in heavy rotor systems is an order more(around 20 times) than unbalance responses even around critical speed of the order of 4 times. Hence, it is justified not to consider nonlinear models of the cracked rotor below or near the critical speed range. The linearization of the cracked rotor EOMs is elaborated in the following section.

### 2.2.2 Linearisation of System Equations of Motion

The present work studies linear rotor models. Hence, the crack flexibility matrix in EOMs (Eqn. (2.3)) requires linearization. It is linearised by the assumption of *weight-dominance* for elastic deflections (Gasch, 1993). Under the weight-dominance, the rotor displacement ($\mathbf{u}(t)$) is very small compared to its static deflection ($\mathbf{u}_0$). This means, while $\mathbf{u}_0 \gg \mathbf{u}\left(t\right)$, the crack opening/closing depends only on the shaft rotation under the effect of gravity of the rotor system (i.e., $\Delta\mathbf{K}\left(u,t\right)\rightarrow\Delta\mathbf{K}\left(t\right)$). This assumption of linearization has practical validity in the case of heavy rotors such as generators, turbines, etc. The vibration response of the rotor includes the static deflection, $\mathbf{u}_0$, and the displacement vector, $\mathbf{u}\left(t\right)$. Thus, the EOM (Eqn. (2.3)) can be re-written as,

$$\mathbf{M}\ddot{\mathbf{u}}(t)+\mathbf{C}\dot{\mathbf{u}}(t)+\left(\mathbf{K}+\Delta\mathbf{K}\left(u,t\right)\right)\left(\mathbf{u}_0+\mathbf{u}(t)\right)=\mathbf{f}_{st}+\mathbf{f}_{unb} \tag{2.4}$$

Assuming the weight-dominance, and subsequently neglecting term of $\Delta\mathbf{K}\left(t\right)\mathbf{u}\left(t\right)$, and also as $\mathbf{K}\mathbf{u}_0=\mathbf{f}_{st}$, the linearised system EOM is obtained as follows

$$\mathbf{M\ddot{u}} + \mathbf{C\dot{u}} + \mathbf{Ku} = -\mathbf{\Delta K u}_0 + \mathbf{f}_{unb} \tag{2.5}$$

The above equation is now linear, but periodically time-variant. Force vectors on the RHS of EOMs are due to the crack and the unbalance, respectively.

### 2.2.3 Modelling of the Crack

It is known from literature review (Dimarogonas, 1996) that the form of *crack flexibility matrix* based on the fracture mechanics approach is widely used as crack model. Elements of the flexibility matrix, in general, includes coupling of lateral, longitudinal, and axial vibration effects. The crack flexibility matrix is defined as follows (Papadopoulos and Dimarogonas, 1988; Darpe, 2007).The related DOFs are also shown in vector **u.**

$$\mathbf{\Delta H u} = \begin{bmatrix} \Delta h_{11} & 0 & 0 & \Delta h_{14} & \Delta h_{15} & 0 \\ 0 & \Delta h_{22} & 0 & 0 & 0 & \Delta h_{26} \\ 0 & 0 & \Delta h_{33} & 0 & 0 & \Delta h_{36} \\ \Delta h_{41} & 0 & 0 & \Delta h_{44} & \Delta h_{45} & 0 \\ \Delta h_{51} & 0 & 0 & \Delta h_{54} & \Delta h_{55} & 0 \\ 0 & \Delta h_{62} & \Delta h_{63} & 0 & 0 & \Delta h_{66} \end{bmatrix} \begin{Bmatrix} z \\ x \\ y \\ \theta_x \\ \theta_y \\ \theta_z \end{Bmatrix} \tag{2.6}$$

In this equation, $\Delta h_{ij}$ denotes the compliance or the flexibility. It is defined as the deflection in $i^{th}$ direction due to the force in $j^{th}$ direction. Subscript 1 corresponds to the axial force, subscripts 2 and 3 correspond to shearing forces, subscripts 4 and 5 correspond to the bending moment about two lateral directions, and subscript 6 corresponds to the torque. A combination of subscripts corresponds to cross-coupled terms. Figure 2.2 shows various forces and moments acting on a cracked shaft cross-section in an inertial frame of reference.

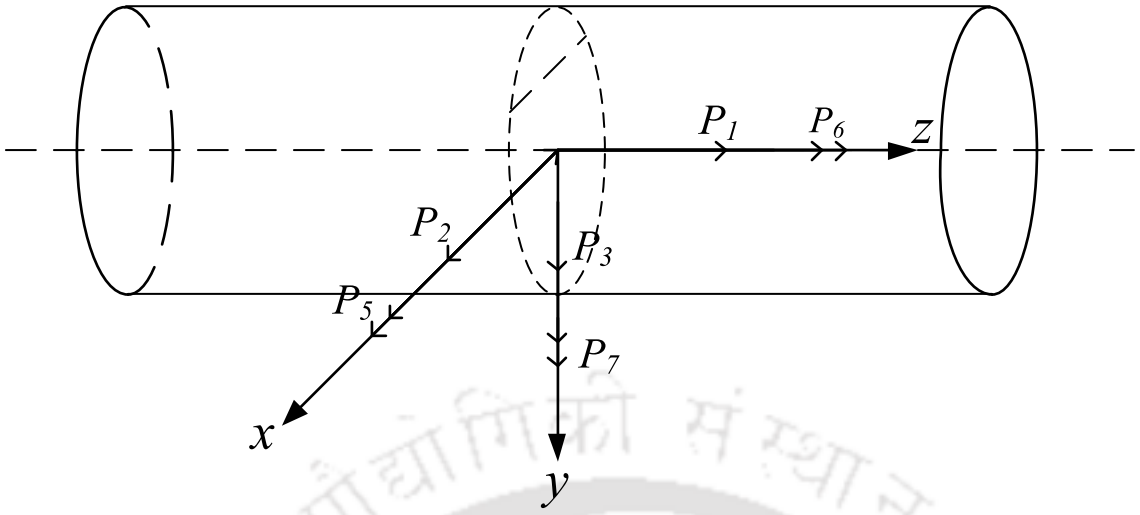


Figure 2.2 A shaft element showing various loads at the crack section

The crack flexibility matrix in Eqn. (2.6) corresponds to a 6-DOF rotor system. In the case of a 2-DOF model, crack flexibilities in two orthogonal directions alone are significant, namely, the direction perpendicular to the crack front (i.e., $\xi$) and the direction along the crack front (i.e., $\eta$) (Refer Figure 2.1). For deep cracks (whose depth is greater than the shaft radius), the flexibility along $\eta$ direction $(\Delta h_{33})$ is negligible compared to the flexibility along $\xi$ direction $(\Delta h_{22})$ (Gasch, 1993). Thus, the following relationship holds in the rotational frame of reference $\xi$-o-$\eta$.

$$\begin{Bmatrix} u_\xi \\ u_\eta \end{Bmatrix} = \begin{bmatrix} h_{22} + \Delta h_{22} & 0 \\ 0 & h_{22} + \Delta h_{33} \end{bmatrix} \begin{Bmatrix} f_\xi \\ f_\eta \end{Bmatrix} \tag{2.7}$$

In Eqn. (2.7), $u_\xi$ and $u_\eta$ are transverse translational displacements in the rotating frame of reference, $h_{22}$ is the flexibility of the intact shaft $\Delta h_{22}$ and $\Delta h_{33}$ are additional flexibilities of the shaft due to the crack, measured along $\xi$ and $\eta$ directions, respectively. $f_\xi$ and $f_\eta$ are excitation forces along the $\xi$ and $\eta$ directions.

*Common rotor crack types*: Rotor cracks that are in early stages of propagation have an abrupt opening/closing (as in Figure 2.3 closes abruptly at about $90^0$ and opens just as suddenly at $270^0$). Such cracks are termed as *switching cracks* (Mayes and Davies, 1984; Gasch, 1993). Breathing and switching both represent functions for crack opening/closing. While breathing refers to gradual opening/closing mechanism, switching refers to instantaneous or more abrupt opening/closing. Hence, switching can also be considered as a special case of breathing.

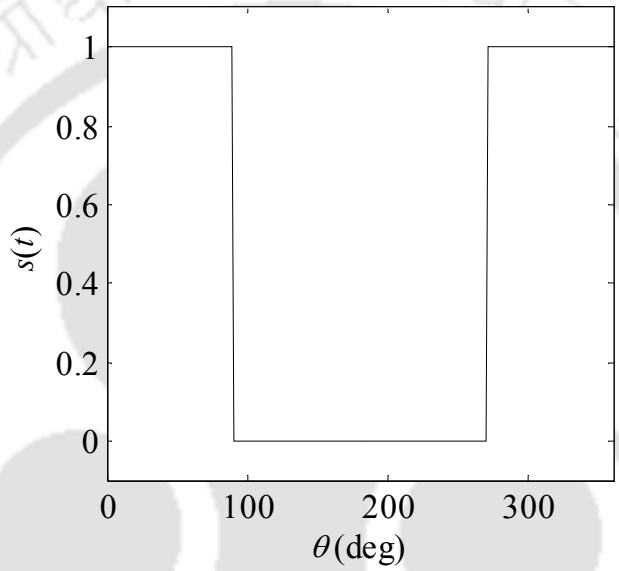


Figure 2.3 A switching crack

A *hinge model* simulates the opening/closing profile, given by a bi-linear square-wave function as follows (Gasch, 1993).

*Bi-linear Hinge model for switching crack*:

$$s(t) = 1, \text{ when the crack is open and}$$

$$s(t) = 0, \text{ when the crack is closed} \qquad (2.8)$$

Fourier series approximation of the bi-linear square wave is given as

$$s(t) = \left(1/2\right) + \left(2/\pi\right)\cos\omega t - \left(2/3\pi\right)\cos 3\omega t + \left(2/5\pi\right)\cos 5\omega t - \ldots \tag{2.9}$$

On the other hand, a *breathing crack* has a more gradual opening/closing profile. Any suitable non-linear function such as *Mayes' modified function* (Gasch, 1993) simulates its opening/closing profile. Mayes' function for the breathing crack is given as

$$s\left(t\right) = \tfrac{1}{2}\left(1 + \cos\omega t\right) \tag{2.10}$$

In the present work, switching crack function represented by Eqn. (2.9) is used for numerical simulations. Thus, a crack switching/breathing function $s(t)$ introduces a time variation into the crack flexibility matrix and it is defined as,

$$\begin{Bmatrix} u_\xi \\ u_\eta \end{Bmatrix} = \left( \begin{bmatrix} h_{22} & 0 \\ 0 & h_{22} \end{bmatrix} + s(t) \begin{bmatrix} \Delta h_{22} & 0 \\ 0 & 0 \end{bmatrix} \right) \begin{Bmatrix} f_\xi \\ f_\eta \end{Bmatrix} \tag{2.11}$$

The matrix inversion of Eqn. (2.11) provides the additional stiffness matrix at the rotor crack section. The inverted matrix is split into the intact shaft stiffness matrix, $\mathbf{K}_{rot}$, and the additive stiffness matrix due to crack, $\mathbf{\Delta K}_{rot}$, in the rotating co-ordinate system as

$$\begin{Bmatrix} f_\xi \\ f_\eta \end{Bmatrix} = \left( \mathbf{K}_{rot} + s(t)\mathbf{\Delta K}_{rot} \right) \begin{Bmatrix} u_\xi \\ u_\eta \end{Bmatrix} \tag{2.12}$$

with,

$$\mathbf{K}_{rot} = \begin{bmatrix} k_{22} & 0 \\ 0 & k_{22} \end{bmatrix} \quad \text{and} \quad \mathbf{\Delta K}_{rot} = -\begin{bmatrix} \Delta k_{22} & 0 \\ 0 & 0 \end{bmatrix}$$

The subscript *rot* denotes matrices defined in rotating frame of reference. Thus, Eqn. (2.12) provides the crack model for a 2-DOF rotor. In this equation, $k_{22}$ is the stiffness of the intact shaft; $\Delta k_{22}$ is the additional stiffness due to the crack along direction of $\xi$. The negative sign implies reduction in the shaft stiffness due to the crack.

### 2.2.4 Transformation Matrix and Final System Equations of Motion

It can be noted from Eqn. (2.12) that the intact shaft and crack stiffness matrices are defined in the rotating frame of reference. But, for applying the crack model (Eqn. (2.12)) into EOMs (i.e., Eqn. (2.5)) these matrices need to be first transformed into the inertial frame of reference. The transformation of co-ordinates from the rotating to inertial co-ordinate systems is defined by the following transformation matrix.

$$\begin{Bmatrix} u_\xi \\ u_\eta \end{Bmatrix} = \begin{bmatrix} \cos\omega t & \sin\omega t \\ -\sin\omega t & \cos\omega t \end{bmatrix} \begin{Bmatrix} u_x \\ u_y \end{Bmatrix} \tag{2.13}$$

Denoting the transformation matrix in Eqn. (2.13) as $\mathbf{T}(t)$ , the transformation of crack stiffness matrix to *x*-o-*y* co-ordinate system is as follows,

$$\begin{Bmatrix} f_x \\ f_y \end{Bmatrix} = \mathbf{T}^T \left( \mathbf{K}_{rot} - s(t)\Delta\mathbf{K}_{rot} \right) \mathbf{T} \begin{Bmatrix} u_x \\ u_y \end{Bmatrix} \tag{2.14}$$

with,

$$\mathbf{T} = \begin{bmatrix} \cos\omega t & \sin\omega t \\ -\sin\omega t & \cos\omega t \end{bmatrix}$$

The transformation results in the following equations

$$\begin{Bmatrix} f_x \\ f_y \end{Bmatrix} = \left(\mathbf{K} + \mathbf{\Delta K}(t)\right) \begin{Bmatrix} u_x \\ u_y \end{Bmatrix} \tag{2.15}$$

with,

$$\mathbf{K} = \begin{bmatrix} k_{22} & 0 \\ 0 & k_{22} \end{bmatrix} \quad \text{and} \quad \mathbf{\Delta K}(t) = -\tfrac{1}{2} s(t) \Delta k_{22} \begin{bmatrix} 1+\cos 2\omega t & \sin 2\omega t \\ \sin 2\omega t & 1-\cos 2\omega t \end{bmatrix}$$

Substituting these for the intact shaft and crack stiffness matrices into Eqn. (2.5), the final system EOMs of a cracked rotor in the inertial co-ordinate system is given as follows,

$$\begin{bmatrix} m & 0 \\ 0 & m \end{bmatrix} \begin{Bmatrix} \ddot{u}_x \\ \ddot{u}_y \end{Bmatrix} + \begin{bmatrix} c & 0 \\ 0 & c \end{bmatrix} \begin{Bmatrix} \dot{u}_x \\ \dot{u}_y \end{Bmatrix} + \begin{bmatrix} k_{22} & 0 \\ 0 & k_{22} \end{bmatrix} \begin{Bmatrix} u_x \\ u_y \end{Bmatrix} = \tfrac{1}{2} s(t) \Delta k_{22} \begin{bmatrix} 1+\cos 2\omega t & \sin 2\omega t \\ \sin 2\omega t & 1-\cos 2\omega t \end{bmatrix} \begin{Bmatrix} w_x \\ 0 \end{Bmatrix} + me\omega^2 \begin{Bmatrix} \cos(\omega t + \beta) \\ \sin(\omega t + \beta) \end{Bmatrix} \tag{2.16}$$

where $w_x$ is the static deflection of shaft in the $x$ direction. Force vectors on the RHS of Eqn.(2.16) are forces due to the crack and the unbalance, respectively.

In this section, mathematical model for a 2-DOF cracked rotor system has been discussed. The crack is modeled based on its flexibility matrix. The system EOMs is *linear*, *second order*, and *time invariant*. Now, responses in time and frequency domains are discussed.

### 2.3 Responses in Time Domain

A time-history defines the system response with respect to the time, when the rotor system is subject to forced vibration. The system response can be vibration displacements, velocities, or

on responses and finally in the system identification, especially in the presence of noise in the response. For more complex system a closed-form solution would not be feasible and in those cases only numerical integration would be practicable. The following subsections discusses the closed-form and numerical solutions for a 2-DOF cracked rotor system.

### 2.3.1 Closed-form Solutions

System EOMs of a 2-DOF cracked rotor system describing the transverse translational motion along *x* and *y* directions is given in Eqn. (2.16). The System EOMs can be combined in a complex form. These equations are linear, uncoupled and can be independently solved for the present model, however, subsequently EOMs are coupled for 4-DOF system in rotational displacements while considering gyroscopic effects. Displacements *x* and *y* are combined as a complex vector with *y* axis as an imaginary axis. Rewriting the EOM in the complex form has the advantages of reducing the number of equations and the complex displacement responses obtained can be directly used as an input to obtain full-spectrum frequency responses. Multiplying the equation in the second row of system EOMs (Eqn. (2.16)) by j and adding it to the equation in the first row, we get,

$$m\ddot{r} + c\dot{r} + kr = \tfrac{1}{2} w_x s(t) \Delta k_{22} \left(1 + e^{2\,\mathrm{j}\omega t}\right) + me\omega^2 e^{\mathrm{j}(\omega t + \beta)} \tag{2.17}$$

with $r = u_x + \mathrm{j}\, u_y$, with $\mathrm{j} = \sqrt{-1}$. Here, s($t$) models a switching crack as discussed in Eqn. (2.8) and Eqn. (2.9). Using Euler's identity on $s(t)$ as given in Eqn. (2.9) and substituting it in Eqn. (2.17) the above equation, the first term on RHS of the EOM (Eqn. (2.17)) can be simplified and written as a series of various harmonics as,

$$\tfrac{1}{2} w_x s(t)\Delta k_{22}\left(1+e^{2\mathrm{j}\omega t}\right) = w_x \Delta k_{22}\left[0.25+0.319e^{\mathrm{j}\omega t}+0.106e^{-\mathrm{j}\omega t}+0.25e^{\mathrm{j}2\omega t}+0.106e^{\mathrm{j}3\omega t}\right.$$
$$\left.-0.021e^{-\mathrm{j}3\omega t}-0.021e^{\mathrm{j}5\omega t}+0.032e^{-\mathrm{j}5\omega t}+0.032e^{\mathrm{j}7\omega t}\right] \quad (2.18)$$

In general, it can be expressed as, $w_x \Delta k_{22} \sum_{i=-\infty}^{+\infty} p_i e^{\mathrm{j}i\omega t}$ . In Eqn. 2.18, $s(t)$ is substituted with Eqn. 2.9 which is the truncated Fourier series of the square wave function. For multiplying with the factor $\left(1+e^{2\mathrm{j}\omega t}\right)$ the cosine terms of $s(t)$ are rewritten using Euler's identity as $\cos(\omega t) = \frac{e^{\mathrm{j}\omega t}+e^{-\mathrm{j}\omega t}}{2}$. Then on multiplying and simplification, the right hand side of Eqn. 2.18 is obtained. Here, $p_i$'s are coefficients of different frequency components (i.e., positive and negative) of the crack force as can be seen in Eqn. (2.18). Using time domain responses, these $p_i$'s can be estimated; whereas in frequency domain, these pi's are obtained as Fourier coefficients of the frequency response spectrum. This will be elaborately discussed in subsequent sections on the frequency response.

Now from Eqn. (2.18), it can be seen that for the fourth and higher harmonics, $p_i$'s are very small or nearly zero. Also, $p_i$ are independent of the crack depth for the entire range of $t/R < 0.5$ for which the hinge model is valid, where $t$ is the crack depth, and $R$ is the shaft radius (Gasch, 1993). Particular integrals of Eqn. (2.17) can be used to obtain the closed-form solution as,

$$r(t) = \sum_{i=-\infty}^{+\infty} \frac{p_i \Delta k_{22} w_x}{-m(i\omega)^2 + c(\mathrm{j}i\omega) + k_{11}} e^{\mathrm{j}i\omega t} + \frac{me\omega^2 e^{\mathrm{j}\beta}}{-m\omega^2 + c(\mathrm{j}\omega) + k_{11}} e^{\mathrm{j}\omega t} \quad (2.19)$$

For the present case, $i$ takes the values of 1, 2, 3, 5, 7, 0, -1, -3, -5. However, in general it can have any finite number of terms. The displacement response with time can be obtained from the above equation.

*Interpretation of $p_i$*: According to Goldman and Muszynska (1999), a filtered orbit of any particular frequency component has, in general, an elliptical shape. An elliptical orbit can be presented as a sum of two circular orbits: one is the locus of the vector rotating in the direction of rotation (forward whirl) and other is the locus of the vector rotating in the opposite direction (reverse whirl). Both rotate at the same frequency. Accordingly, the contribution of once per revolution frequency component $i = +1$ with $p_1 = 0.319$ in the crack force of Eqn. (2.18) is a forward circular orbit; whereas the contribution of frequency component $i = -1$ with $p_1 = 0.106$ is a reverse circular orbit. They both superimpose to give an elliptical orbit (Refer Figure 2.4 (a)) whirling in the same direction spin. The critical speed due to $i = \pm 1$ frequency component of crack force occurs at $\omega = \omega_{nf}$. Here, $\omega$ is the spin-speed and $\omega_{nf}$ is the first critical speed of the rotor system. The contribution of $i = +2$ with $p_1 = 0.25$ describes a circular orbit passed twice per revolution (Refer Figure 2.4 (b)) in the forward sense with its critical speed occurring at $\omega = \frac{1}{2}\omega_{nf}$.

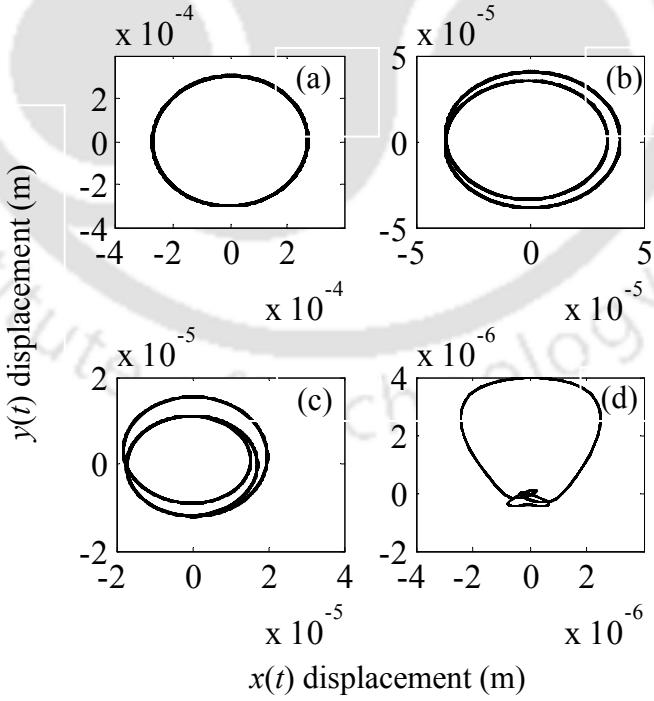


Figure 2.4 Orbits of the cracked rotor shaft with the disc unbalance at resonances of (a) once per revolution (b) twice per revolution (c) thrice per revolution and (d) four times per revolution

The contribution of $i = \pm 3$, $p_3 = 0.106$ and $p_{-3} = -0.021$describes an elliptical orbit in a forward sense, passed three times per revolution of the rotor (Figure 2.4 (c)). The critical speed is at $\omega = \frac{1}{3}\omega_{nf}$. Similarly, $i = \pm 5$ with $p_5 = -0.021$ and $p_{-5} = 0.009$ describes an elliptical orbit in a forward sense with the critical speed at $\omega = \frac{1}{5}\omega_{nf}$, where as $i = +7$ with $p_7 = 0.009$ describes a circular orbit in the forward sense with the critical speed at $\omega = \frac{1}{7}\omega_{nf}$. The contribution of all $i = \pm 1, +2, \pm 3, \pm 5$ and $+7$ superimpose to give total orbit of the rotor model. Orbit plots in Figure 2.4 (a)-(d) describe the path of the shaft centre of the cracked rotor.

The closed-form solution (Eqn. (2.19)) developed in the present section are suitable only for simple linear models with a few parameters. But, in practice the rotor system requires complex modelling with more number of parameters and its closed-form solution may not be available. Then, numerical methods of solution are required. For example, in the present work the switching crack model is bi-linear (Eqn. (2.8)). In a closed-form solution, linear solutions are obtained for individual frequency components of the switching function (Eqn. (2.18)) and the overall solution obtained using the superposition principle. Also, there is limitation to number of Fourier coefficients of the switching function that can be analytically obtained (Eqn. (2.18)). But, in case of time integrated solutions these limitations can be eliminated, where the switching crack function can be solved directly as a function of time.

### 2.3.2 Time Integrated Responses

EOMs are initially written in the state space form, which converts a second-order differential equation into two single-order equations. The state space form of system EOMs (Eqn. (2.17)) is written as,

$$\dot{r} = v$$

and

$$r = -\frac{m}{k_{11}}\dot{v} - \frac{c}{k_{11}}v + \frac{1}{k_{11}}\left( w_x \Delta k_{22} \sum_{i=-\infty}^{+\infty} p_i e^{\mathrm{j}i\omega t} + me\omega^2 e^{\mathrm{j}(\omega t+\beta)} \right) \tag{2.20}$$

These state space equations are solved using the Runge-Kutta method (fourth order) and the time-integrated vibration responses are obtained. Both the closed-form and time-integrated responses have been used subsequently for the identification.

## 2.4 Frequency Response Analysis

In frequency response analyses, the system response is computed at discrete excitation frequencies. The forcing is thus a function of frequency. It gives a measure of magnitude and phase of the vibration response (say, displacement) as a function of frequency, in comparison to the force. In subsequent chapter, frequency response analyses will be done with the full-spectrum analysis, which is much more practical approach and directly can be obtained from time integrated responses or measured time domain data from a rotor test set up with the fatigue crack. However, the present section analysis would give a reference for correctness and accuracy of the full spectrum analysis. In the following subsection, system EOMs in *frequency domain* is obtained for a 2-DOF cracked rotor model.

### 2.4.1 Frequency Responses

The assumed solution for system EOMs (Eqn.(2.17)) is given by $r(t)$. For a particular harmonic $i$ of the forcing function, the assumed solution is $r_i(\omega)e^{\mathrm{j}i\omega t}$. Since, system EOMs are linear, using the principle of superposition, the assumed solution of each harmonic $i$ are summed up as follows

$$r(t) = \sum_{i=-n}^{n} r_i(\omega) e^{\mathrm{j}i\omega t} \tag{2.21}$$

Substituting the assumed solution into EOMs (Eqn.(2.17)), response equations in frequency domain are obtained as follows.

$$\left[\left\{-(i\omega)^2 m\right\} + \left\{(\mathrm{j}i\omega c) + k_{11}\right\}\right] r_i = \Delta k_{22} w_x p_i + f_{unb} \tag{2.22}$$

where $i$ denote the harmonic integer of various frequency components corresponding to the crack and unbalance forces. These frequency components are harmonics of the rotational frequency or spin speed, $\omega$. Index $i$ can be positive or negative according to the direction of frequency component being same or reverse relative to the direction of shaft rotation (i.e., forward or backward whirls). The contribution of each harmonic component to the forcing function is denoted by $p_i$, which are termed as *force coefficients*. The interpretation of $p_i$ is explained in the previous section. The response corresponding to each harmonic is given by $r_i$, which are termed as *displacement coefficients*. While in time domain, $p_i$'s are obtained from the magnitudes of the closed-form expression of the crack forcing function, as given in Eqn. (2.18).However, in frequency domain, the $p_i$'s can be directly obtained from frequency spectrum of the force function. Since, $p_i$'s are both *forward* or *reverse* because of the sense of rotation, a contemporary frequency spectrum tool, namely the full-spectrum is initially used to obtain $p_i$'s as well as $r_i$'s. The

conventional tools such as Fast Fourier Transforms (FFT) do not describe the sense of rotation of frequency components. A more practical approach of full-spectrum equations and corresponding identification, based on it, has been discussed in a subsequent chapter. The present chapter analysis will help in ensuring the correctness and the effectiveness of the proposed full spectrum based methodology. Now, numerical illustrations for generation of vibration responses in time domain are presented.

## 2.5 Numerical Simulations of a 2-DOFCracked Rotor

A Laval rotor, consisting of a simply supported elastic shaft with a disc at the mid span, is considered for numerical illustration (Refer Figure 2.1).A crack modelled as a switching crack is considered near the disc. The rotor system data considered for the problem are summarised in Table 2-1.

Table 2-1 Two-DOF rotor system data used for numerical simulation

| Parameters | Value |
|---|---|
| Disc mass, $m$ | 2 kg |
| Intact shaft stiffness, $k$ | $3.2135\times10^{5}$ N/m |
| Additive (negative) crack stiffness, $\Delta k_{22}$ | $1.61\times10^{4}$ N/m |
| Viscous damping in rotor system, $c$ | 16.03 N-s/m |
| Phase of unbalance, $\beta$ | $10(\pi/180)$ rad |
| Shaft deflection due to disc weight, $w_x$ | $w_x = mg / k = 6.105\times10^{-5}$ m |
| Disc eccentricity, $e$ | $0.1\times10^{-6}$ m |

### 2.5.1 Time Domain Responses

Forced vibration responses of the cracked rotor, due to the disc unbalance and crack forces are obtained from the closed-form (Eqn. (2.19)) as well as by time-integrated solutions (Eqn. (2.20)). Displacements along $x$ and $y$ directions obtained from the closed-form solution are plotted in Figure 2.5.

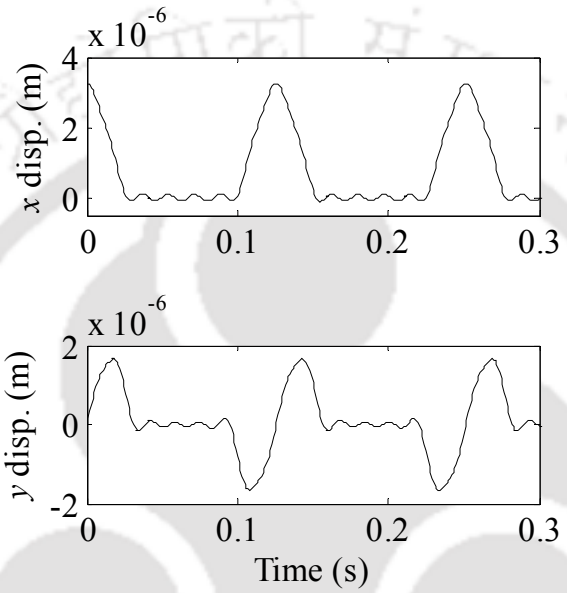


Figure 2.5 Displacement variation with time of the cracked rotor along the $x$ and $y$ directions obtained from closed-form solution

The same responses are also obtained using the time-integration solution. Because of the zero initial displacement and velocity conditions considered for the time integration, there is an initial transient observed in responses, as shown in Figure 2.6. This transient part in the response should be discarded. The very purpose of generating time-integration responses is that it generalises the method for even more complex systems and the closed form solutions are used to bench mark numerically generated responses and especially in identification algorithms of subsequent chapters.

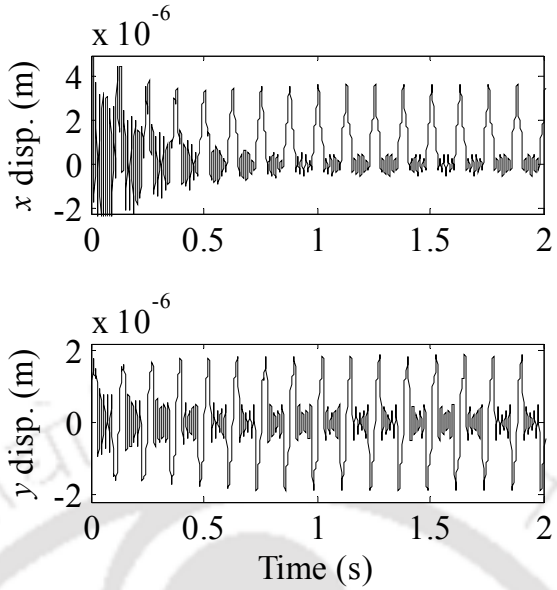


Figure 2.6 Displacement variation with time of the cracked rotor along the *x* and *y* directions obtained from the time-integrated solution

Displacements obtained above using the closed-form and time-integrated solutions do not contain any noise. But measured responses from a practical rotor are embedded with noise. In order to mimic a practical rotor response, random noise is generated and added to the numerically generated responses. Here, the Gaussian white noise is used for the simulation. It is defined as a statistical noise that has its probability density function equal to that of the normal distribution. It is a random signal with a flat power spectral density, uncorrelated and normally distributed with a mean zero and unit variance. The noising response signal could be obtained as

$$r_{noise}(t) = r(t) + \left\{ r(t) \frac{(R-0.5) N_p}{100} \right\} \tag{2.23}$$

Here, $R$ is a random scalar value with mean 0 and standard deviation 1.

Numerical responses are added with 1, 2 and 5 percentages ($N_p$/100) of its values as the noise. The effect of 5% noise on response signals is shown in Figure 2.7. The waviness in the plot shows the signal with the noise.

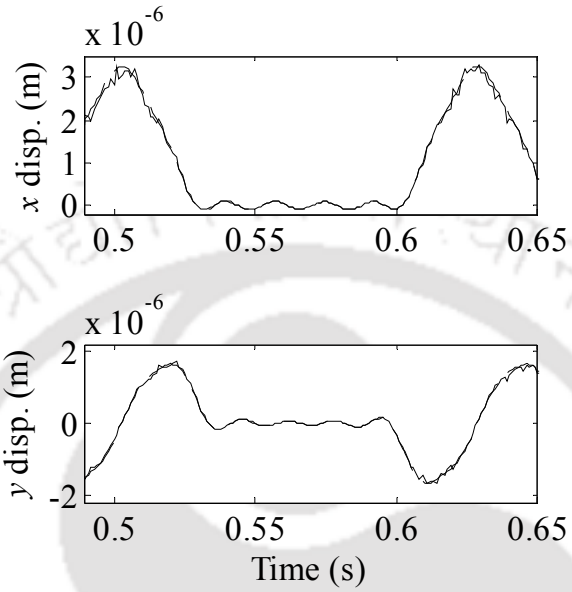


Figure 2.7 Comparison of displacement responses with noise (——) and without noise (- - -)

### 2.5.2 Frequency Domain Responses

Frequency response equations (Eqn. 2.22) are used to obtain magnitude and phase angle plots as a function of the spin frequency. The first critical speed and critical speeds corresponding to twice per revolution and thrice per revolution frequency components of the crack force are shown in Fig. 2.11.The first critical speed is observed at 400.8 rad/s, whereas the critical speed of twice per revolution frequency component of crack force occurs at 200.4 rad/s and the critical speed of thrice per revolution frequency component of crack force occurs at 133.6 rad/s.

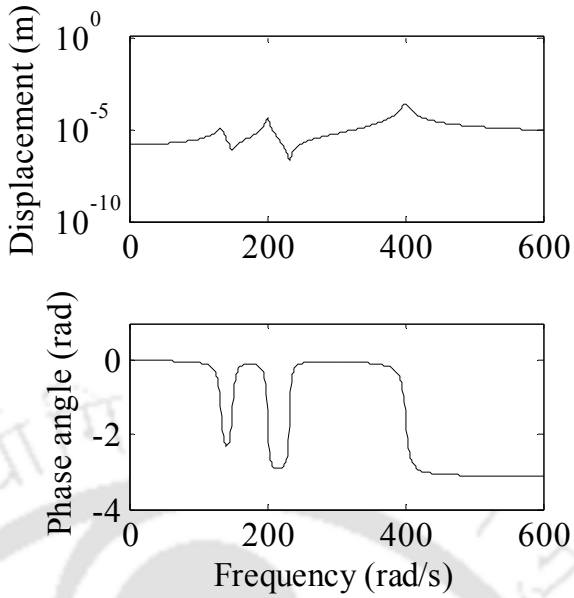


Figure 2.8 Magnitude and Phase angle plot of frequency response

### 2.5.3 Orbit Plots

The displacement in the *x* and *y* directions are combined to obtain orbit plots. Orbit plots are important in analyzing the actual motion of the disc centre and it also indicates certain rotor faults. The contribution of various harmonic components of the crack force to orbit plots has been discussed in Section 2.3.1. At rotor spin speed of 400 rad/s, a single loop is observed in the orbit plot as shown in Figure 2.9(a), which is due to the near critical speed of once per revolution frequency component of the crack force (Refer Figure 2.8). Similarly, at a rotor speed of 200 rad/s there are two loops observed in Figure 2.9 (b), which is due to the near critical speed of twice per revolution component of the crack force (i.e., 200.4 rad/s). This orbit profile is widely used as a crack indicator, and referred to as the characteristic double-loop. Similarly, the three and four looped orbits are obtained near critical speeds of three times and four times per revolution frequency components of the crack force. The viscous damping in rotor system (*c*) used for numerical simulation is 16.03 N-s/m and the disc mass is 2 kg. As the first critical of the rotor response is observed at 400 rad/s, the corresponding damping ratio of the system is $\zeta = 0.01$.

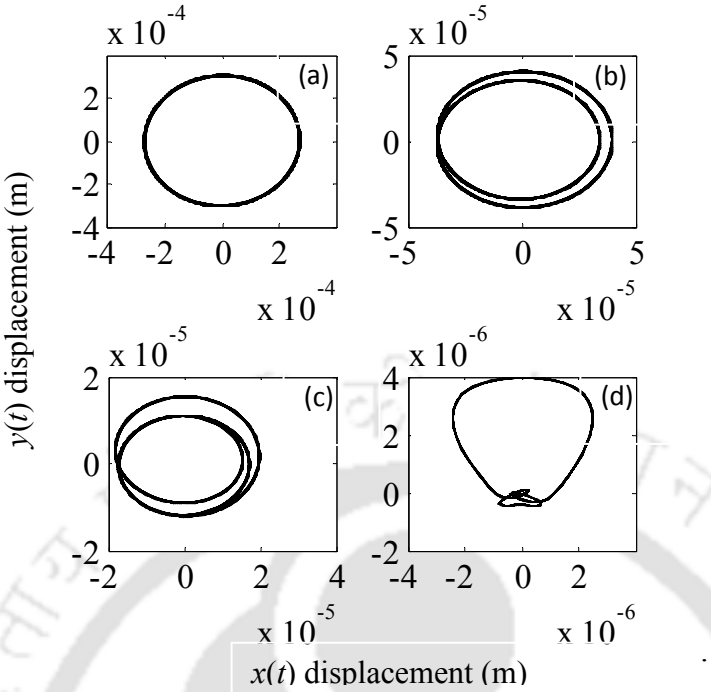


Figure 2.9 Orbit plots of cracked rotor near critical speeds of (a) once per revolution (b) twice per revolution (c) thrice per revolution and (d) four times per revolution components of crack force

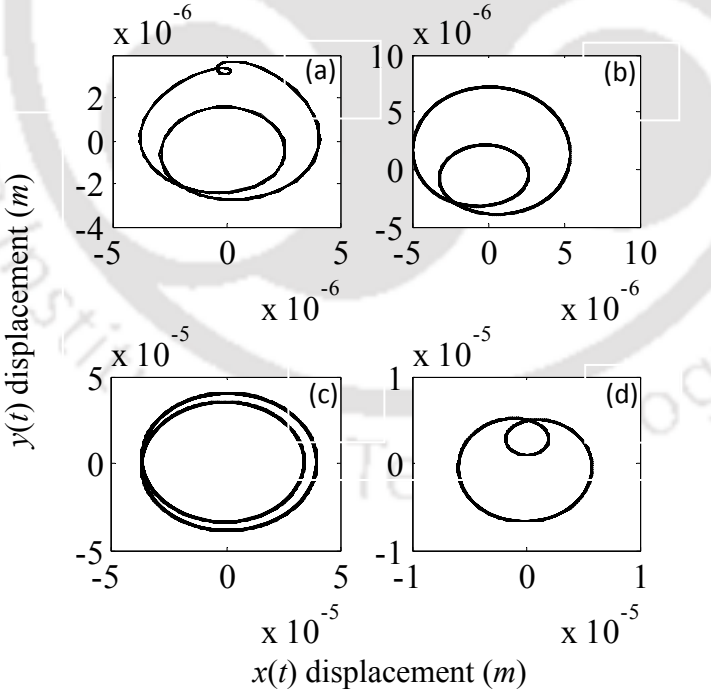


Figure 2.10 Orbit plots of cracked rotor shaft at various measurement speeds: (a) 180 rad/s (b) 190 rad/s (c) 200 rad/s and (d) 210 rad/s during passage through critical speed due to twice per revolution frequency component

Orbit plots simulated in the neighborhood of critical speeds of twice per revolution (i.e., 180, 190, 200, and 210 rad/s) and thrice per revolution (i.e., 100,120,130, and 140 rad/s) components of the crack force are shown in Figure 2.10 and Figure 2.11.

It is observed that during passage through the critical speed of twice per revolution frequency component (i.e., 200.4 rad/s); the orbit changes its direction by nearly π rad. Similarly, the orbit with two inner loops in the neighborhood of thrice per revolution frequency component (i.e., 133.6 rad/s) changes its direction by nearly π/2 rad (Figure 2.10 (a)-(d)). Similar results were also discussed in literatures on the rotor crack (Al-Shudeifat, 2011).

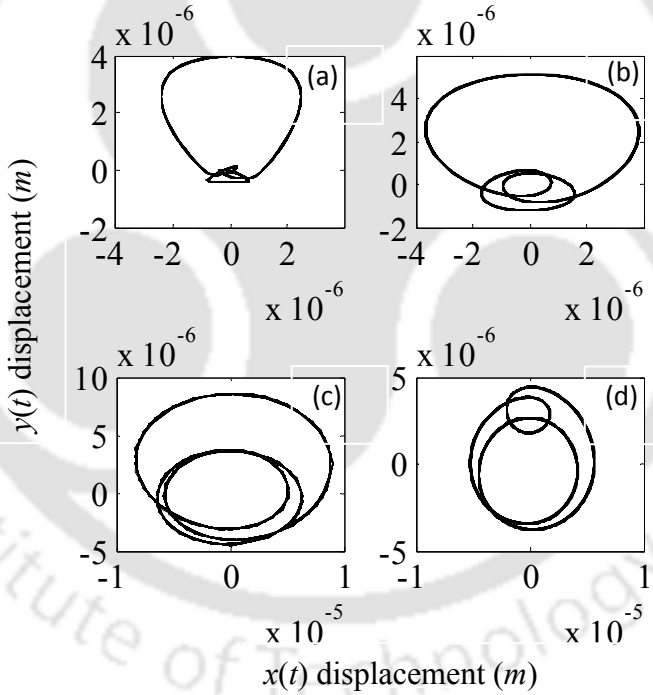


Figure 2.11 Orbit plots of cracked rotor shaft at various measurement speeds: (a) 100 rad/s (b) 120 rad/s (c) 130 rad/s and (d) 140 rad/s during passage through critical speed due to thrice per revolution frequency component

This section presents the numerical simulation of a simple cracked rotor system with translational displacements in two orthogonal directions. The displacement responses, frequency responses, and orbit plots were discussed.

### 2.5.4 Concluding Remarks

- In this chapter, system EOMs for a 2 DOF model for the cracked rotor has been obtained. EOMs are solved in time and frequency domains.
- Numerical illustrations are performed on a sample rotor data, and the time and frequency responses are studied. Cracked rotor displacement responses with a switching crack model are obtained using both the closed-form and time-integrated solutions. The closed-form responses can be directly used as input for further identification.
- The time-integrated displacement responses have an initial transient response, which needs to be discarded while using as an input for the crack identification.
- Critical speeds are obtained by means of frequency responses. The first critical speed is observed at 400 rad/s, whereas critical speeds due to twice per revolution and thrice per revolution frequency components are observed at 200 rad/s and 133 rad/s, respectively. These critical speeds will be used in subsequent chapters to decide the range of measurement speeds during the crack identification.
- Now, an identification algorithm using time responses is discussed in the subsequent chapter.

# CHAPTER 3

# Identification of Crack Parameters using Time Domain Responses

## 3.1 Introduction

The present chapter develops identification algorithms for the rotor crack and unbalance parameters. Two Identification algorithms have been developed, one for the estimation of fault parameters (crack and unbalance) along with the viscous damping, and another for the estimation of crack breathing forces. These identification algorithms contribute to the crack identification in rotor systems. Vast literature is available for modelling crack breathing functions based on fracture mechanics approach or as a function of harmonic series. However, the experimental estimates of the crack breathing forces can prove important for an understanding of the actual behaviour of a fatigue crack in a rotor system. This has been attempted in the present work. Identification algorithms are developed based on an inverse problem approach, and the estimates are obtained using the least-squares estimation method.

## 3.2 Model-Based Identification Algorithms using Time Responses

The *inverse problem approach* is employed to identify the crack parameter, i.e., the additive crack stiffness, together with other rotor system parameters, namely, the damping and the eccentricity. This is *partial system parameter identification*, since some of system parameters that are used in the estimation algorithm, like the mass and the intact shaft stiffness are already known since their modelling is relatively easy and accurate. Hence, this is also referred to as the *grey system*. Advances in the sensor technology, the increase of computing power in terms of amount of data that can be collected and the speed at which this huge amount of data can be

system EOMs. Now, an algorithm is presented that simultaneously estimates the unbalance, damping and crack parameters from rotor system vibration responses.

### 3.2.1 Identification of the Crack, Unbalance, and Viscous Damping Parameters

From the system EOM, Eqn. (2.17) and its closed-form solution Eqn. (2.19), it is seen that the equations of motion of the rotor system with the transverse crack have components of multiple harmonics. The assumed solution $r_i(t)$ for a particular harmonic of the crack force excitation is $r_i(\omega)e^{\mathrm{j}i\omega t}$. Since equations of motion are linear, using the principle of superposition, the assumed solution is written as a summation of solutions for individual harmonics, as follows,

$$r(t) = r_{-5}e^{-5\mathrm{j}\omega t} + r_{-3}e^{-3\mathrm{j}\omega t} + r_{-1}e^{-\mathrm{j}\omega t} + r_0 e^{0\times\mathrm{j}\omega t} + r_1 e^{\mathrm{j}\omega t} + r_2 e^{2\mathrm{j}\omega t} + r_3 e^{3\mathrm{j}\omega t} + r_5 e^{5\mathrm{j}\omega t} + r_7 e^{7\mathrm{j}\omega t} \qquad (3.1)$$

Substituting the assumed solution into system EOMs (Eqn. (2.17)), we obtain response equations in frequency domain as given in Eqn. (2.22). Here, harmonics $i$ = -5, -3, -1, 0, 1, 2, 3, 5, and 7 are only chosen. The present chapter attempts to identify unknown parameters, only using time responses of the system $r(t)$ as an input. Initially, *displacement coefficients* $r_i$ need to be estimated, which are used as an input for subsequent identification algorithm. It is to be noted that $r_i$ can be alternatively obtained from frequency responses, which is discussed in a subsequent chapter.

Eqn. (3.1) can be rearranged in a matrix form, for a particular time instant $t$, as

$$\begin{bmatrix} 1 & e^{\mathrm{j}\omega t} & e^{2\mathrm{j}\omega t} & e^{3\mathrm{j}\omega t} & e^{5\mathrm{j}\omega t} & e^{7\mathrm{j}\omega t} & e^{-\mathrm{j}\omega t} & e^{-3\mathrm{j}\omega t} & e^{-5\mathrm{j}\omega t} \end{bmatrix}_{(1\times 9)} \begin{Bmatrix} r_0 \\ r_1 \\ r_2 \\ r_3 \\ r_5 \\ r_7 \\ r_{-1} \\ r_{-3} \\ r_{-5} \end{Bmatrix}_{(9\times 1)} = \{r(t)\}_{(1\times 1)} \quad (3.2)$$

From Eqn. (3.2) it can be seen that the number of equation is one whereas the number of unknown coefficients are nine. Hence, it is a heavily underdetermined system of equations. It can be converted to an overdetermined system of equations, if the number of equations in Eqn. (3.2) is increased. Accordingly, similar equations can be written for $g$ different instances of time ($g$> 9 where $t_g$ is the final time instance), which can convert it to an overdetermined system of equations. That would manifest the estimation problem in the form as, $\mathbf{A}_1\mathbf{x}_1 = \mathbf{b}_1$. Here, matrix $\mathbf{A}_1$ is a known matrix containing exponential terms of harmonic components, $\mathbf{x}_1$ is an unknown vector of coefficients, and $\mathbf{b}_1$ is the known column vector of responses. The input to $\mathbf{b}_1$ consists of time responses $r(t)$. The over-determined system of matrix equations is written as follows: $\mathbf{A}_1\mathbf{x}_1 = \mathbf{b}_1$ (3.3)

Here,

$$\mathbf{A}_{\mathbf{1}(g\times 9)} = \begin{bmatrix} 1 & e^{\mathrm{j}\omega t_1} & e^{\mathrm{j}(2\omega)t_1} & e^{\mathrm{j}(3\omega)t_1} & e^{\mathrm{j}(5\omega)t_1} & e^{\mathrm{j}(7\omega)t_1} & e^{\mathrm{j}(-\omega)t_1} & e^{\mathrm{j}(-3\omega)t_1} & e^{\mathrm{j}(-5\omega)t_1} \\ 1 & e^{\mathrm{j}\omega t_2} & e^{\mathrm{j}(2\omega)t_2} & e^{\mathrm{j}(3\omega)t_1} & e^{\mathrm{j}(5\omega)t_2} & e^{\mathrm{j}(7\omega)t_2} & e^{\mathrm{j}(-\omega)t_2} & e^{\mathrm{j}(-3\omega)t_2} & e^{\mathrm{j}(-5\omega)t_2} \\ \vdots & \vdots & \vdots & \vdots & \vdots & \vdots & \vdots & \vdots & \vdots \\ \vdots & \vdots & \vdots & \vdots & \vdots & \vdots & \vdots & \vdots & \vdots \\ \vdots & \vdots & \vdots & \vdots & \vdots & \vdots & \vdots & \vdots & \vdots \\ 1 & e^{\mathrm{j}\omega t_g} & e^{\mathrm{j}(2\omega)t_g} & e^{\mathrm{j}(3\omega)t_g} & e^{\mathrm{j}(5\omega)t_g} & e^{\mathrm{j}(7\omega)t_g} & e^{\mathrm{j}(-\omega)t_g} & e^{\mathrm{j}(-3\omega)t_g} & e^{\mathrm{j}(-5\omega)t_g} \end{bmatrix}$$

$$\mathbf{x}_{\mathbf{1}(9\times1)} = \begin{Bmatrix} r_0(\omega) \\ r_1(\omega) \\ r_2(\omega) \\ r_3(\omega) \\ r_5(\omega) \\ r_7(\omega) \\ r_{-1}(\omega) \\ r_{-3}(\omega) \\ r_{-5}(\omega) \end{Bmatrix}; \qquad \mathbf{b}_{1(g\times1)} = \begin{Bmatrix} r(t_1) \\ r(t_2) \\ \vdots \\ r(t_g) \end{Bmatrix} \quad (3.4)$$

Thus, the equation is written for *g* different response data corresponding to time instances $t_1$ to $t_g$. $t_1$ and $t_g$ must be chosen for a length of at least one time period of the time response, so that it tracks the complete information of the response for one shaft rotation from 00 to 3600. Having a sufficiently longer signal for choosing the input data $(r(t_1), r(t_2), ..., r(t_g))$ provides well-conditioned matrices and good approximation for least square estimates. It uses the displacement data obtained from either the closed-form or time-integration method as the input for the identification. Unique solution of $\mathbf{x}_1$ can be obtained if the matrix $\mathbf{A}_1$ is square and satisfies the conditions for matrix inversion. In the general case, $\mathbf{A}_1$ may be any rectangular matrix and cannot be inverted with sufficient conditions. Hence, an approximate solution of $\mathbf{x}_1$ (or estimates) is found using the *least-squares solution*, which is a common form of the *linear regression*. The equation is considered in a linear regression form, where $\mathbf{A}_1$ is the regression matrix or the *regressor*, $\mathbf{b}_1$ is the vector of known quantities (or *regressand*), and $\mathbf{x}_1$ is the *intercept or the unknown vector* to be determined. The least-squares solution then gives the unknown vector containing the displacement coefficients.

$$\mathbf{x}_1 = \left(\mathbf{A}_1{}^T \mathbf{A}_1\right)^{-1} \mathbf{A}_1{}^T \mathbf{b}_1 \tag{3.5}$$

Once displacement coefficients are identified, the estimates $\mathbf{x}_1$ are fed to another identification that estimates unknown system parameters, namely, the additive stiffness due to crack, the disc eccentricity, and the viscous damping. The EOM in complex form, i.e., Eqn. (2.22), can be rearranged such that all quantities containing unknown parameters are on one side and known quantities with known parameters are on the other side. Then, Eqn. (2.22) can be rearranged as,

$$\left(\mathrm{j}i\omega c\right) r_i - me\omega^2 e^{\mathrm{j}\beta} - \Delta k_{22} w_x p_i = \left(\left(i\omega\right)^2 m - k_{22}\right) r_i \tag{3.6}$$

The unknown parameters can be written in a vector, for a particular harmonic component *i*, as follows,

$$\left[\left(\mathrm{j}i\omega\right) r_i \quad -m\omega^2 \quad -w_x p_i\right]_{(1\times 3)} \begin{Bmatrix} c \\ e \\ \Delta k_{22} \end{Bmatrix}_{(3\times 1)} = \left\{\left(\left(i\omega\right)^2 m - k_{22}\right) r_i\right\}_{(1\times 1)} \tag{3.7}$$

As can be seen, the system has 1 equation and 3 unknowns. This is an underdetermined system of a linear equation. It can be converted into an over-determined system of equations by increasing the number of equations. In Eqn. (2.22), *i* chooses values of -5, -3, -1, 0, 1, 2, 3, 5, and 7. Hence, nine linear equations corresponding to individual harmonic component can be written in a matrix form. This converts the system into an overdetermined one. This equation is written in regression form as $\mathbf{A}_2\mathbf{x}_2 = \mathbf{b}_2$, where matrix $\mathbf{A_2}$ is a known matrix, $\mathbf{x_2}$ is the vector of unknown parameters, and $\mathbf{b_2}$ is a known column vector. The input to $\mathbf{A_2}$ consists of frequency responses (i.e., displacement

coefficients, $r_i$) estimated in earlier step and Fourier coefficients of the crack force (i.e., force coefficients, $p_i$). This regression equation is written as,

$$\mathbf{A}_2\mathbf{x}_2 = \mathbf{b}_2 \qquad (3.8)$$

with,

$$\left(\mathbf{A}_2\right)_{9\times3} = \begin{bmatrix} 0 & 0 & -w_x p_0 \\ \mathrm{j}(\omega) r_1 & -m\omega^2 e^{j\beta} & -w_x p_1 \\ \mathrm{j}(2\omega) r_2 & 0 & -w_x p_2 \\ \mathrm{j}(3\omega) r_3 & 0 & -w_x p_3 \\ \mathrm{j}(5\omega) r_5 & 0 & -w_x p_5 \\ \mathrm{j}(7\omega) r_7 & 0 & -w_x p_7 \\ \mathrm{j}(-\omega) r_{-1} & 0 & -w_x p_{-1} \\ \mathrm{j}(-3\omega) r_{-3} & 0 & -w_x p_{-3} \\ \mathrm{j}(-5\omega) r_{-5} & 0 & -w_x p_{-5} \end{bmatrix}; \left(\mathbf{b}_2\right)_{9\times1} = \begin{Bmatrix} (-k_{22}) r_0 \\ (\omega^2 m - k_{22}) r_1 \\ (4\omega^2 m - k_{22}) r_2 \\ (9\omega^2 m - k_{22}) r_3 \\ (25\omega^2 m - k_{22}) r_5 \\ (49\omega^2 m - k_{22}) r_7 \\ (\omega^2 m - k_{22}) r_{-1} \\ (9\omega^2 m - k_{22}) r_{-3} \\ (25\omega^2 m - k_{22}) r_{-5} \end{Bmatrix}; \left(\mathbf{X}_2\right)_{3\times1} = \begin{Bmatrix} c \\ e \\ \Delta k_{22} \end{Bmatrix} \qquad (3.9)$$

Combining equations Eqn. (3.4) and Eqn. (3.9), $\mathbf{b}_2$ can be written as,

$$\mathbf{b}_2 = \mathbf{z}_{diag}\mathbf{x}_1 = \mathbf{z}_{diag}\left(\mathbf{A}_1{}^T\mathbf{A}_1\right)^{-1}\mathbf{A}_1{}^T\mathbf{b}_1 \qquad (3.10)$$

The diagonal matrix is defined as,

$$\mathbf{z}_{diag}\left(i,i\right) = \mathbf{z}\left(i,1\right) \qquad \text{where } i = 1,2,...,9 \qquad (3.11)$$

with,

$$\mathbf{z} = m\omega^2 \begin{Bmatrix} -\bar{\omega}_{nf}^2 \\ 1-\bar{\omega}_{nf}^2 \\ 4-\bar{\omega}_{nf}^2 \\ 9-\bar{\omega}_{nf}^2 \\ 25-\bar{\omega}_{nf}^2 \\ 49-\bar{\omega}_{nf}^2 \\ 1-\bar{\omega}_{nf}^2 \\ 9-\bar{\omega}_{nf}^2 \\ 25-\bar{\omega}_{nf}^2 \end{Bmatrix}; \qquad \omega_{nf} = \sqrt{\frac{k_{11}}{m}}; \qquad \bar{\omega}_{nf} = \frac{\omega_{nf}}{\omega}$$

Using Eqn. (3.10), the solution of Eqn. (3.9) is given as,

$$\mathbf{x}_2 = \left(\mathbf{A}_2{}^T\mathbf{A}_2\right)^{-1}\mathbf{A}_2{}^T\mathbf{z}_{diag}\left(\mathbf{A}_1{}^T\mathbf{A}_1\right)^{-1}\mathbf{A}_1{}^T\mathbf{b}_1 \tag{3.12}$$

This equation combines the solution for two steps of regression equations, i.e., Eqn. (3.4) and Eqn. (3.9), into one. Thus, an identification algorithm has been presented, that uses displacements in time domain as its input, and obtains the unknown vector containing parameters of the crack, the unbalance, and the damping. Solution as a least squares problem is used to obtain the required estimates. A numerical illustration of the proposed identification algorithm is discussed in section 3.3. In subsequent chapter, the identification algorithm discussed here would be extended to frequency domain data and with the help of more advantageous full spectrum algorithm.

Now, another identification algorithm is described that estimates various terms of the crack force, thus providing an idea of the periodically varying switching crack forces.

### 3.2.2 Identification of Crack Forces of the Switching Crack

The switching crack is represented using a square wave function (refer Figure 2.3). It is mathematically expressed using a Fourier series expansion as in Eqn. (2.9). The crack excitation

was obtained as $\frac{1}{2}w_x s(t)\Delta k_{22}\left(1+e^{2\mathrm{j}\omega t}\right)$ and further generalised as, $w_x \Delta k_{22}\sum_{i=-\infty}^{+\infty} p_i e^{\mathrm{j}i\omega t}$ .It can be observed that the crack force is a multiplication of the static deflection, additive crack stiffness, force coefficient $p_i$ and exponential terms of harmonics of the crack force excitation. This implies that by estimating $\Delta k_{22}\sum_{i=-\infty}^{+\infty} p_i$ , the profile of the periodically varying crack force can be obtained at any defined spin-speed and time interval.

Hence, Eqn. (2.22) is rearranged and written in a matrix equation, for a particular harmonic *i* as,

$$\left[\left(\mathrm{j}i\omega\right)r_i \quad -m\omega^2 \quad -w_x\right]_{(1\times 3)}\begin{Bmatrix} c \\ e \\ \Delta k_{22}p_i \end{Bmatrix}_{(3\times 1)} = \left\{\left(\left(i\omega\right)^2 m - k_0\right)r_i\right\}_{(1\times 1)} \tag{3.13}$$

This is a modification on Eqn. (3.7). Thus, the estimation of damping, unbalance eccentricity and additive stiffness due to the crack, i.e., Eqn. (3.9) is modified into the following estimation equations containing the terms $\Delta k_{22}p_i$ in the unknown vector as illustrated below. Noting that the regression equation Eqn. (3.9) contains terms to be estimated for the crack force, i.e., $p_i$ and the additive crack stiffness, $\Delta k_{22}$. Here $p_i$ terms are treated as unknowns, and the equation is rearranged into a new regression equation where $p_i$ terms of $\mathbf{A}_2$ are included in the unknown vector $\mathbf{x}_2$ together with $\Delta k_{22}$. It is given in the following regression form,

$$\mathbf{A}_3\mathbf{x}_3 = \mathbf{b}_2 \tag{3.14}$$

with

$$\mathbf{A}_{3(9\times11)} = \begin{bmatrix} 0 & -m\omega^2 e^{j\beta} & 0 & -w_x & 0 & 0 & 0 & 0 & 0 & 0 & 0 \\ j(\omega)r_0 & 0 & -w_x & 0 & 0 & 0 & 0 & 0 & 0 & 0 & 0 \\ j(2\omega)r_2 & 0 & 0 & 0 & -w_x & 0 & 0 & 0 & 0 & 0 & 0 \\ j(3\omega)r_3 & 0 & 0 & 0 & 0 & -w_x & 0 & 0 & 0 & 0 & 0 \\ j(5\omega)r_5 & 0 & 0 & 0 & 0 & 0 & -w_x & 0 & 0 & 0 & 0 \\ j(7\omega)r_7 & 0 & 0 & 0 & 0 & 0 & 0 & -w_x & 0 & 0 & 0 \\ j(-\omega)r_{-1} & 0 & 0 & 0 & 0 & 0 & 0 & 0 & -w_x & 0 & 0 \\ j(-3\omega)r_{-3} & 0 & 0 & 0 & 0 & 0 & 0 & 0 & 0 & -w_x & 0 \\ j(-5\omega)r_{-5} & 0 & 0 & 0 & 0 & 0 & 0 & 0 & 0 & 0 & -w_x \end{bmatrix}$$

$$\mathbf{x}_{3(11\times1)} = \begin{Bmatrix} c \\ e \\ \Delta k_{22} p_1 \\ \Delta k_{22} p_0 \\ \Delta k_{22} p_2 \\ \Delta k_{22} p_3 \\ \Delta k_{22} p_5 \\ \Delta k_{22} p_7 \\ \Delta k_{22} p_{-1} \\ \Delta k_{22} p_{-3} \\ \Delta k_{22} p_{-5} \end{Bmatrix}; \qquad \mathbf{b}_{2(9\times1)} = \begin{Bmatrix} (\omega^2 m - k_{22}) r_1 \\ (-k_{22}) r_0 \\ (4\omega^2 m - k_{22}) r_2 \\ (9\omega^2 m - k_{22}) r_3 \\ (25\omega^2 m - k_{22}) r_5 \\ (49\omega^2 m - k_{22}) r_7 \\ (\omega^2 m - k_{22}) r_{-1} \\ (9\omega^2 m - k_{22}) r_{-3} \\ (25\omega^2 m - k_{22}) r_{-5} \end{Bmatrix} \tag{3.15}$$

Using displacement versus time responses, the solution for estimates of the crack force, $\mathbf{x}_3$, are obtained in two steps of the regression equation. As in the previous case, it can also be provided as a combined solution of two regression steps, as follows,

$$\mathbf{x}_3 = \left(\mathbf{A}_3{}^T \mathbf{A}_3\right)^{-1} \mathbf{A}_3{}^T \mathbf{z}_{diag} \left(\mathbf{A}_1{}^T \mathbf{A}_1\right)^{-1} \mathbf{A}_1{}^T \mathbf{b}_1 \tag{3.16}$$

These estimates will be further used to obtain the actual opening/closing profile of the shaft crack. Thus, an identification algorithm for the simultaneous estimation of damping, eccentricity and

additive crack stiffness; as well as an identification algorithm for the estimation of crack excitation force parameters has been presented. These identification algorithms can be used only with time domain responses. The numerical illustrations for these identification algorithms are now presented and discussed.

### 3.3 Numerical Simulations of Identification Algorithms in Time Domain

The simulation of numerical responses in the time and frequency domains was discussed in the previous chapter. The data of rotor system and fault parameters used for the simulation were initially assumed. Obtaining the time and frequency responses from assumed data constitutes the *direct problem*. Different levels of white-noise were also added to the simulated signal to mimic an experimental condition during the measurement of responses. Now, some of the system parameters and fault parameters can be assumed to be unknown parameters, and their new estimates are obtained from developed identification algorithms using numerically generated responses. This procedure is the *inverse problem approach*. Identification algorithms have been already developed in the previous sections **3.2.1** and **3.2.2**, to be used with the time domain responses. Displacement coefficients, $r_i$, can be estimated from time responses using Eqn. (3.4) and the unknown crack and system parameters can be estimated using Eqn. (3.9). Similarly, switching crack forces can be estimated using Eqn. (3.15). The testing of these identification algorithms is carried out in the present section. A flow chart showing steps for identification is provided in Figure 3.1.

### 3.3.1 Simultaneous Estimation of Damping, Eccentricity, and Additive Crack Stiffness

Displacement responses that are generated in time domain from Eqn. (2.19), and are shown in Figure 2.5andFigure 2.6, are used as an input to identify rotor parameters in Eqn. (3.4) and Eqn. (3.9). Different ranges of measurement spin speeds are chosen and the estimation of parameters is performed. These measurement *spin speed ranges* are chosen based on *displacement versus frequency plots* as discussed in the following paragraph.

Figure 3.2 shows the displacement plot corresponding to the once per revolution frequency component of crack force and a critical speed is observed at 400.8 rad/s. The displacements corresponding to the twice per revolution component of the crack force gives a critical speed at 200.4 rad/s, while the displacements corresponding to thrice and five times per revolution components of the crack force excitation give critical speeds at133.6 rad/s and 80.16 rad/s, respectively. Similar plot with both magnitude and phase has been presented in previous chapter in Figure 2.8. It was also noted in Eqn. (2.18) that $p_i$ corresponding to once per revolution, twice per revolution and thrice per revolution components only have considerable magnitude, while the $p_i$ corresponding to other higher harmonic components of the crack force are negligible. This holds same for $r_i$'s also. So, spin-speed ranges are selected such that it encompasses critical speeds due to once, twice and thrice per revolution frequency components of the crack force.

To avoid measurement error near critical speeds, measurements outside the half-power frequency band is advisable. *Half-power points* are two frequencies on either side of the magnitude of critical speed. They are often referred to as *side bands* and their corresponding magnitudes will be $X = 0.707\ X_{res}$, where $X_{res}$ is the magnitude at the critical speed and $X$ is the magnitude at half-power points.

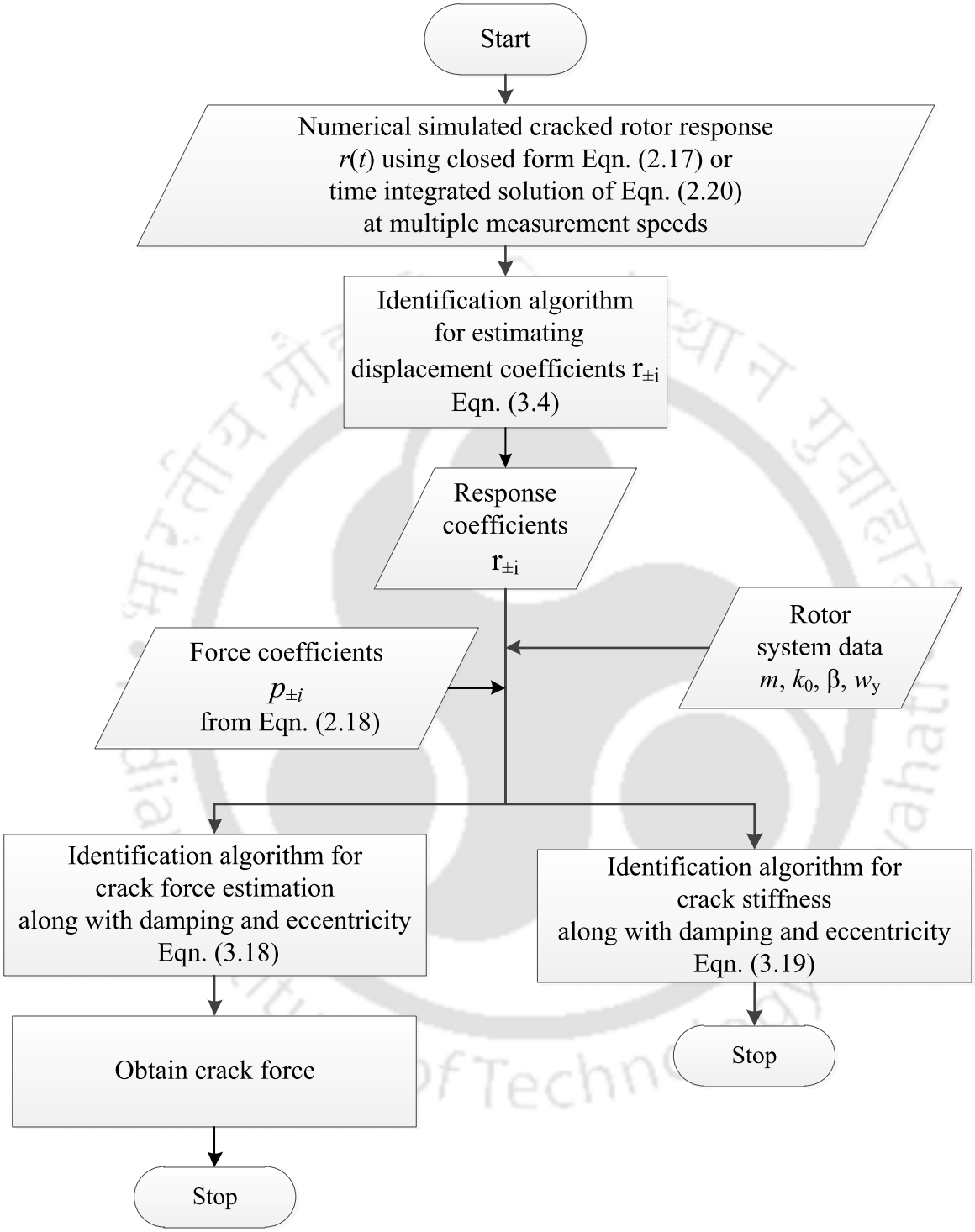


Figure 3.1 Flow Chart showing steps for identification of crack and unknown system parameters in time domain

It is noted from Figure 3.2 that half-power point frequencies corresponding to critical speeds of displacement at thrice per revolution component are 132.3 rad/s and 133.6 rad/s. Similarly, half-power points corresponding to twice per revolution component are 198.4 rad/s and 202.4 rad/s, and that corresponding to once per revolution component are 396.9 rad/s and 405 rad/s. It is also noted from that response magnitudes corresponding to the twice and thrice per revolution components of the crack force are dominant in the range 30 rad/s to 133 rad/s and 135 rad/s to 198 rad/s, while response magnitudes corresponding to once per revolution component is dominant in the range from 400 rad/s and above. Different displacement harmonics and their corresponding range of frequencies are summarised in Table 3-1.

Table 3-1 Different cases of rotor speed ranges

| Cases | Range of frequencies(rad/s) |
|---|---|
| Case A | 30 to 132.3 |
| Case B | 133.6 to 198.4 |
| Case C | 202.4 to 396.9 |
| Case D | 405 to 600 |
| Case E | 1 to 600 |

From these considerations, the range of response frequencies are selected from 1 rad/s to 132.3 rad/s (i.e., up to the lower limit of the half-power point of thrice per revolution excitation and is referred as Case A), from the upper limit of half-power point of thrice per revolution component to that of the lower limit of the twice per revolution component (i.e., from 133.6 rad/s to 198.4 rad/s is referred as Case B), from the upper limit of half-power point of twice per revolution component to that of lower limit of the once per revolution component (i.e., from 202.4 rad/s to 396.9 rad/s is

referred as Case C)and above the upper limit of half-power point of once per revolution component (i.e., above 405 rad/s is referred as Case D). Various frequency ranges of above cases are considered together as a single range and are referred as Case E.

The estimation is performed at multiple rotor speeds. A set of frequencies at intervals of 1 rad/s in a given case of frequency range is taken as a displacement data set, and further used for the parameter estimation. For accommodating the estimation with a set of multiple rotor speeds, the regression equations are modified as explained follows.

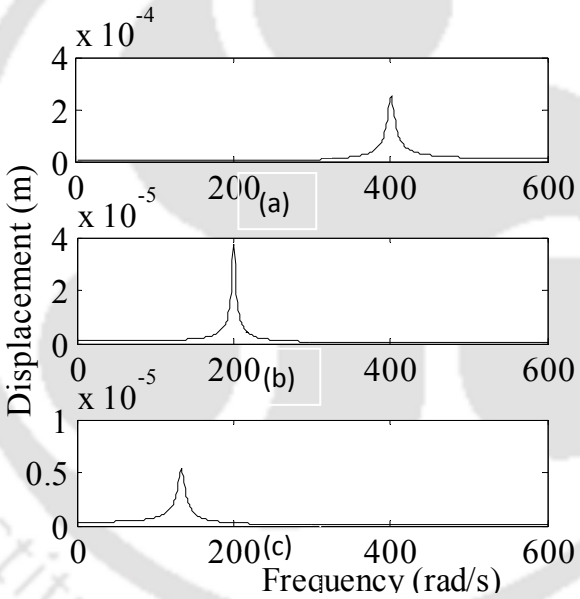


Figure 3.2 Displacements of rotor corresponding to (a) once per revolution (b) twice per revolution and (c) thrice per revolution components of the crack displacement

*Identification at multiple measurement speeds*: Identification algorithms presented Eqn. (3.4), Eqn. (3.9), and Eqn. (3.15) correspond to a single measurement speed. For accommodating estimation with a set of multiple measurement speeds say $\omega_1$ to $\omega_q$, the regression equation (Eqn. (3.4)) is modified as,

$$\begin{bmatrix} \mathbf{A}_1(\omega_1) \\ \mathbf{A}_1(\omega_2) \\ \vdots \\ \mathbf{A}_1(\omega_q) \end{bmatrix}_{(nq\times 9)} \quad \mathbf{x}_{1(9\times 1)} = \begin{Bmatrix} \mathbf{b}_1(\omega_1) \\ \mathbf{b}_1(\omega_2) \\ \vdots \\ \mathbf{b}_1(\omega_q) \end{Bmatrix}_{(nq\times 1)} \tag{3.17}$$

Similarly, the regression equation (Eqn. (3.9)) is modified as,

$$\begin{bmatrix} \mathbf{A}_2(\omega_1) \\ \mathbf{A}_2(\omega_2) \\ \vdots \\ \mathbf{A}_2(\omega_q) \end{bmatrix}_{(9q\times 3)} \quad \mathbf{x}_{2(3\times 1)} = \begin{Bmatrix} \mathbf{b}_2(\omega_1) \\ \mathbf{b}_2(\omega_2) \\ \vdots \\ \mathbf{b}_2(\omega_q) \end{Bmatrix}_{(9q\times 1)} \tag{3.18}$$

Finally, the regression equation Eqn. (3.15) is modified as,

$$\begin{bmatrix} \mathbf{A}_3(\omega_1) \\ \mathbf{A}_3(\omega_2) \\ \vdots \\ \mathbf{A}_3(\omega_q) \end{bmatrix}_{(9q\times 11)} \quad \mathbf{x}_{3(11\times 1)} = \begin{Bmatrix} \mathbf{b}_2(\omega_1) \\ \mathbf{b}_2(\omega_2) \\ \vdots \\ \mathbf{b}_2(\omega_q) \end{Bmatrix}_{(9q\times 1)} \tag{3.19}$$

In these regression equations, the number of estimation equations is increased to accommodate for displacements at multiple independent spin-speeds. When the number of regression equations are increased the estimation is better averaged and the effect of noise is reduced drastically (Tiwari, 2005). Now, the estimates obtained using different sets of spin-speeds are discussed. For Case A (Table 3-1), responses are used in the identification algorithm and estimates are obtained. Estimates are also obtained for a variety of noise levels of 1, 2 and 5 percentages and are summarised as in Table 3-2. The estimates are found to conform well to assumed parameters,

with a maximum percentage error of 2.7% for estimated eccentricity at 5% noise level, as can be seen in Figure 3.3 (a).

For Cases B, C, D and E also the estimates are obtained for noise levels of 1, 2 and 5 percentages. The estimates for 5% noise are summarised in

Table **3-3**. Plots of the percentage error of estimates in Figure 3.3 (b-e) show that the estimates confirm well to assumed parameters. The maximum percentage error for Case B is 2.5% for the estimated eccentricity, for Case C it is 3.2% for the estimated crack stiffness, for Case D it is 2.7% for the estimated eccentricity and for Case E it is 2.5% for the estimated crack stiffness. Among all cases the maximum percentage error of 3.2% is observed for 5% noise level. Now, numerical simulation results for the estimation of crack force together with damping and disc eccentricity is presented in the next section.

### 3.3.2 Simultaneous Estimation of Damping, Eccentricity, and Crack Forces

As mentioned earlier the estimation of crack force terms, i.e., the additive crack stiffness multiplied by coefficients of different harmonics of crack force provides valuable information for understanding the practical *switching profile* of the transverse crack. The identification algorithm for the estimation of force terms of a switching crack is presented in the regression equation (i.e., Eqn. (3.15)). The regression matrix is ill-conditioned because of sparse non-zero elements.

In order to improve the accuracy of the estimates, the regression equation is modified to include responses at multiple measurement speeds as discussed in Eqn. (4.21). Now, the estimates obtained using different sets of rotor speeds are discussed.

The sets of rotor speeds are chosen from range of frequencies described by Cases A to E in the previous section. For Case A (refer Table 3-1), displacement responses are used as input for the identification algorithm. From the regression equation, using Eqn. (3.12), amplitude parts of the assumed solution are obtained for $q$ different rotor speeds. This data is used further in the regression equation Eqn. (3.16) to estimate the damping, eccentricity and crack force terms.

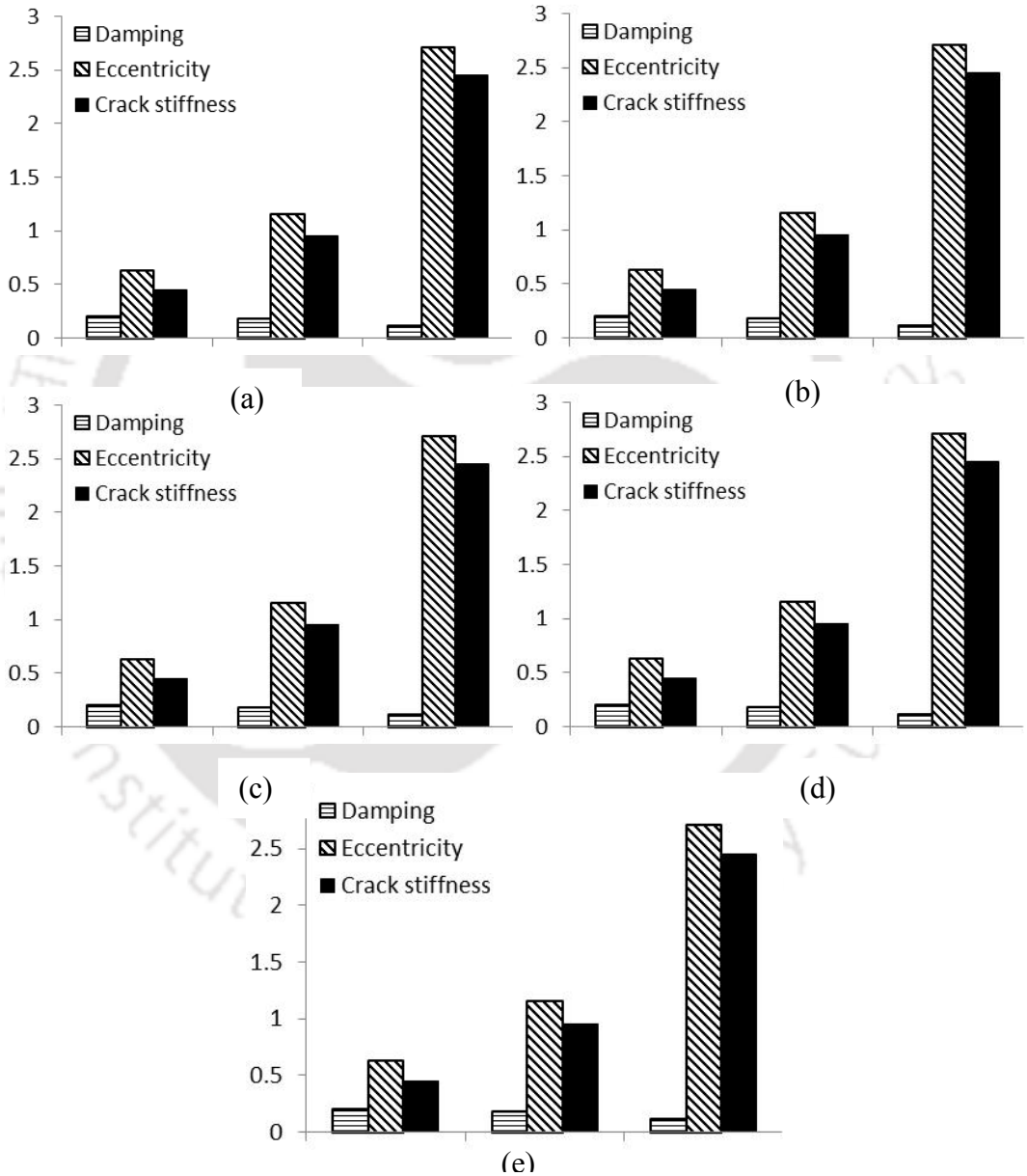


Figure 3.3 Percentage error of estimates for various noise levels and in the measurement speed range of (a) 5- 130 rad/s (b) 135- 190 rad/s (c) 210- 390 rad/s (d) 410- 600 rad/s and (e) 5- 600 rad/s

Table 3-2 Estimation of parameters in the speed range of 0 to 130 rad/s at the interval of 1 rad/s

| Parameters | $c$ (N-s/m) | | | | $e$ ($\times 10^6$ m) | | | | $\Delta k_{22}$($\times 10^{-4}$ N/m) | | | |
|---|---|---|---|---|---|---|---|---|---|---|---|---|
| Assumed values | 16.03 | | | | 5.00 | | | | 1.61 | | | |
| Noise | 0 | 1 | 2 | 5 | 0 | 1 | 2 | 5 | 0 | 1 | 2 | 5 |
| Estimates from CF response | 16.03 | 16.06 | 16.09 | 16.15 | 5.00 | 4.94 | 4.88 | 4.72 | 1.61 | 1.60 | 1.60 | 1.58 |
| Estimates from TI response | 16.07 | 16.07 | 16.06 | 16.05 | 4.99 | 4.97 | 4.94 | 4.86 | 1.61 | 1.60 | 1.59 | 1.57 |

Table 3-3 Estimates of parameters for measurement speed ranges Cases B, C, D and E with 5% response noise

| Measurement speed range | | 135 to 190 rad/s at 1 rad/s interval | 210 to 390 rad/s at 1 rad/s interval | 410 to 600 rad/s at 1 rad/s interval | 1 to 600 rad/s at 2 rad/s interval |
|---|---|---|---|---|---|
| $c$ (N-s/m) | CF* | 16.04 | 16.05 | 16.08 | 16.03 |
| | TI | 16.05 | 16.14 | 16.09 | 16.10 |
| $e$ ($\times 10^6$ m) | CF | 4.87 | 4.92 | 4.87 | 4.88 |
| | TI | 4.87 | 4.91 | 4.87 | 4.87 |
| $\Delta k_{22}$($\times 10^{-4}$ N/m) | CF | 1.57 | 1.55 | 1.56 | 1.55 |
| | TI | 1.57 | 1.55 | 1.57 | 1.56 |

*(CF – Estimates from *closed-form* responses; TI- Estimates from *time-integrated* responses)

Estimates are also obtained for different noise levels of 1, 2, and 5 percentages. They are presented in Table 3-4.In order to check for the accuracy of the estimates, the crack force is plotted with assumed and estimated crack force terms at a particular spin-speed and compared. Figure 3.5shows the comparison of assumed and estimated crack forces at a spin speed of 50 rad/s. The comparison is shown for the 2% and 5% noise levels for responses in both horizontal and vertical directions. It is seen that the estimated crack forces conform very well to the assumed crack force. For Cases B, C, D, and E the estimates are similarly obtained for 1, 2, and 5% noise levels. The estimates at 5% noise are presented in Table 3-5. Figure 3.6 shows the comparison of assumed and estimated crack forces at 170 rad/s for the 2% and 5% noise levels. Similar comparisons are made for Cases C and D at spin speeds of 300 rad/s and 500 rad/s for the 2% and 5% noise levels as shown in Figure 3.7 and Figure 3.8, respectively.

From these plots, it is seen that the estimated crack forces conform very well with to the assumed ones. The estimated parameters also match well with their assumed counterparts. Thus; the developed algorithms are tested for their robustness. This concludes the numerical illustrations of the identification algorithms for crack and unknown system parameters.

The generalised crack force is given as $w_x \Delta k_{22} \sum_{i=-\infty}^{+\infty} p_i e^{i i\omega t}$. Here, the crack force is a product of static deflection ($w_x$), additive crack stiffness ($\Delta k_{22}$) and the summation over various harmonics ($i\omega$) of crack force coefficients ($p_i$), and their exponential terms. The assumed values of the above mentioned parameters are provided in Table 2.1 and Eq. 2.18. Using these values, the curves of the assumed crack forces have been plotted for a known time span. Similarly, the estimated crack force is plotted using the crack force estimates given in Tables 3.4-3.5.

The order of difference between assumed and estimated crack force parameters is $10^{-2}$ N. For example, for measurement speed of 50 rad/s, the maximum value of assumed force is 1.0330 N, whereas the maximum value of estimated force is 1.0038 N. The comparison of percentage error of estimates is shown in Figure 3.4. Here, the number in the abscissa represents the estimated parameter corresponding to the same row number in vector $\{X\}$ shown in Eqn. (3.20).

$$X = \{c \quad e \quad \Delta k_{22} \quad \Delta k_{22}p_0 \quad \Delta k_{22}p_1 \quad \Delta k_{22}p_2 \quad \Delta k_{22}p_3 \quad \Delta k_{22}p_5 \quad \Delta k_{22}p_7 \quad \Delta k_{22}p_{-1} \quad \Delta k_{22}p_{-3} \quad \Delta k_{22}p_{-5}\}^T \tag{3.20}$$

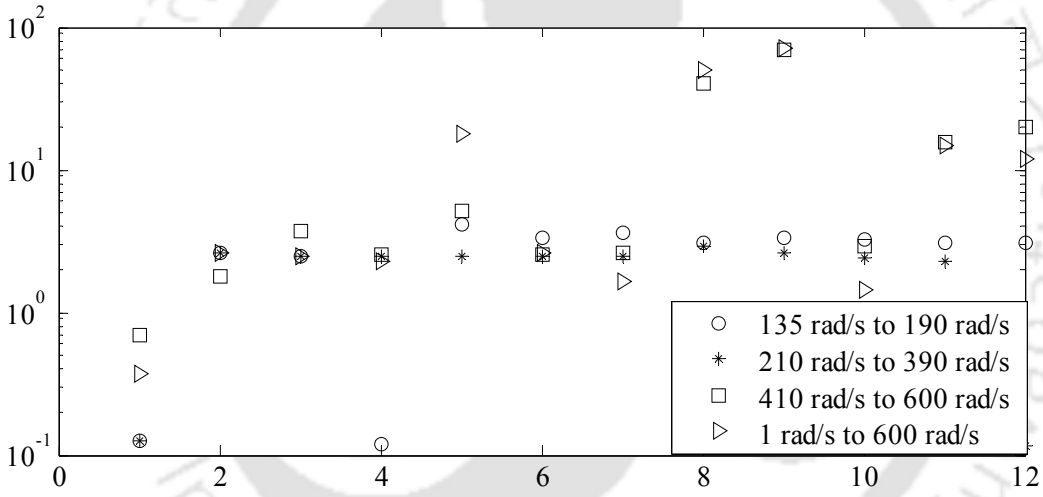


Figure 3.4 Comparison of percentage error of estimates for different cases of measurement speed ranges

Table 3-4 Simultaneous estimation of damping, eccentricity and crack force parameters using displacement measurements in the spin-speed range of 1 to 130 rad/s

| Parameters | | $c$ (N-s/m) | $e$ ($\times 10^6$ m) | $\Delta k_{22}p_0$ (N/m) | $\Delta k_{22}p_1$ (N/m) | $\Delta k_{22}p_2$ (N/m) | $\Delta k_{22}p_3$ (N/m) | $\Delta k_{22}p_5$ (N/m) | $\Delta k_{22}p_7$ (N/m) | $\Delta k_{22}p_{-1}$ (N/m) | $\Delta k_{22}p_{-3}$ (N/m) | $\Delta k_{22}p_{-5}$ (N/m) |
|---|---|---|---|---|---|---|---|---|---|---|---|---|
| Assumed values | | 16.03 | 5.00 | 4017.0 | 5125.7 | 4017.0 | 1703.2 | -337.4 | 514.2 | 1703.2 | -337.4 | 514.2 |
| 0% noise | CF* | 15.97 | 5.25 | 4115.5 | 5037.6 | 3983.2 | 1685.3 | -334.9 | 510.4 | 1690.7 | -335.8 | 510.0 |
| | TI | 15.98 | 5.25 | 4115.5 | 5037.8 | 3983.4 | 1684.9 | -335.3 | 511.5 | 1690.7 | -335.5 | 510.7 |
| 1% noise | CF | 15.95 | 5.22 | 4094.8 | 5012.5 | 3963.3 | 1676.8 | -333.2 | 508.0 | 1682.2 | -334.1 | 507.7 |
| | TI | 15.98 | 5.22 | 4094.9 | 5012.9 | 3963.5 | 1676.3 | -333.7 | 508.6 | 1682.2 | -333.8 | 508.2 |
| 2% noise | CF | 15.94 | 5.20 | 4074.2 | 4987.4 | 3943.3 | 1668.4 | -331.5 | 505.6 | 1673.6 | -332.3 | 505.3 |
| | TI | 15.97 | 5.19 | 4074.2 | 4988.0 | 3943.5 | 1667.6 | -332.0 | 505.7 | 1673.8 | -332.1 | 505.8 |
| 5% noise | CF | 15.94 | 5.11 | 4012.2 | 4912.1 | 3883.6 | 1642.9 | -326.4 | 498.3 | 1647.9 | -327.2 | 498.2 |
| | TI | 15.96 | 5.11 | 4012.2 | 4913.4 | 3883.8 | 1642.0 | -327.1 | 497.1 | 1648.3 | -327.0 | 498.3 |

*(CF – Estimates from *closed-form* responses; TI- Estimates from *time-integrated* responses)

Table 3-5 Simultaneous estimates of damping, eccentricity and crack force for spin-speed ranges (Cases B, C, D and E) with 5% response noise

| Parameters | | | $c$ (N-s/m) | $e$ ($\times 10^{-6}$ m) | $\Delta k_{22}p_0$ (N/m) | $\Delta k_{22}p_1$ (N/m) | $\Delta k_{22}p_2$ (N/m) | $\Delta k_{22}p_3$ (N/m) | $\Delta k_{22}p_5$ (N/m) | $\Delta k_{22}p_7$ (N/m) | $\Delta k_{22}p_{-1}$ (N/m) | $\Delta k_{22}p_{-3}$ (N/m) | $\Delta k_{22}p_{-5}$ (N/m) |
|---|---|---|---|---|---|---|---|---|---|---|---|---|---|
| Assumed values | | | 16.03 | 5.00 | 4017.0 | 5125.7 | 4017.0 | 1703.2 | -337.4 | 514.2 | 1703.2 | -337.4 | 514.2 |
| Measurement Speed range | 135 to 190 rad/s | CF* | 16.02 | 4.88 | 3916.7 | 4996.4 | 3918.2 | 1659.7 | -329.6 | 538.0 | 1661.8 | -328.7 | 513.9 |
| | | TI | 16.09 | 4.88 | 3918.1 | 4997.1 | 3918.7 | 1661.0 | -327.6 | 527.8 | 1662.2 | -329.6 | 514.8 |
| | 210 to 390 rad/s | CF | 16.04 | 4.93 | 3914.2 | 4885.7 | 3913.4 | 1676.6 | -245.3 | 255.2 | 1656.2 | -281.2 | 439.1 |
| | | TI | 16.12 | 4.94 | 3915.7 | 4861.8 | 3915.9 | 1658.7 | -202.0 | 157.7 | 1654.1 | -284.6 | 412.0 |
| | 410 to 600 rad/s | CF | 16.05 | 4.92 | 3927.0 | 4503.9 | 3893.5 | 1674.6 | -478.6 | 396.5 | 1668.7 | -343.4 | 424.1 |
| | | TI | 16.16 | 4.94 | 3926.2 | 4214.4 | 3912.6 | 1731.1 | -505.5 | 150.6 | 1678.7 | -387.0 | 575.2 |
| | 1 to 600 rad/s | CF | 16.03 | 4.88 | 3958.4 | 4965.3 | 3906.3 | 1759.0 | -250.3 | 975.9 | 1654.8 | -308.9 | 464.6 |
| | | TI | 16.09 | 4.88 | 3949.2 | 4971.4 | 3989.9 | 1721.8 | -103.9 | 343.2 | 1655.3 | -293.2 | 534.7 |

*(CF – Estimates from *closed-form* responses; TI- Estimates from *time-integrated* responses)

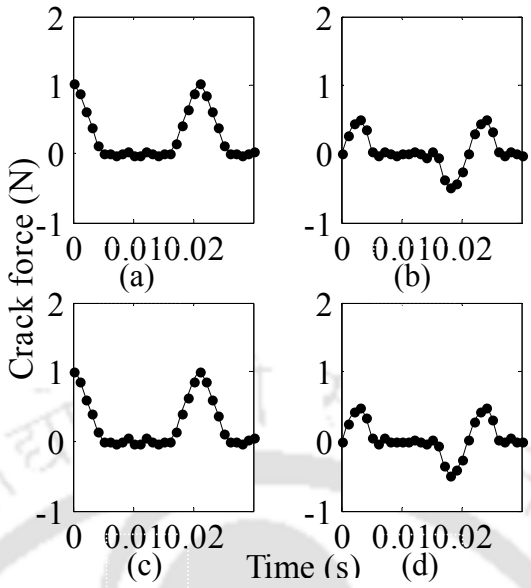


Figure 3.5 Comparison of crack forces between the assumed and estimated data at 50 rad/s (a) With 2% noise in *x* response (b) With 2% noise in *y* response (c) With 5% noise in *x* response (d) With 5% noise in *y* response; —— Assumed and ●●●●●● Estimated

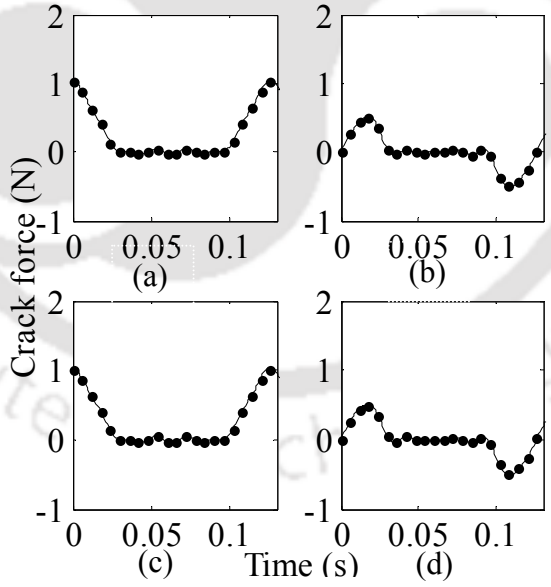


Figure 3.6 Comparison of crack forces between the assumed and estimated data at 170 rad/s (a) With 2% noise in *x* response (b) With 2% noise in *y* response (c) With 5% noise in *x* response (d) With 5% noise in *y* response; —— Assumed and ●●●●●● Estimated

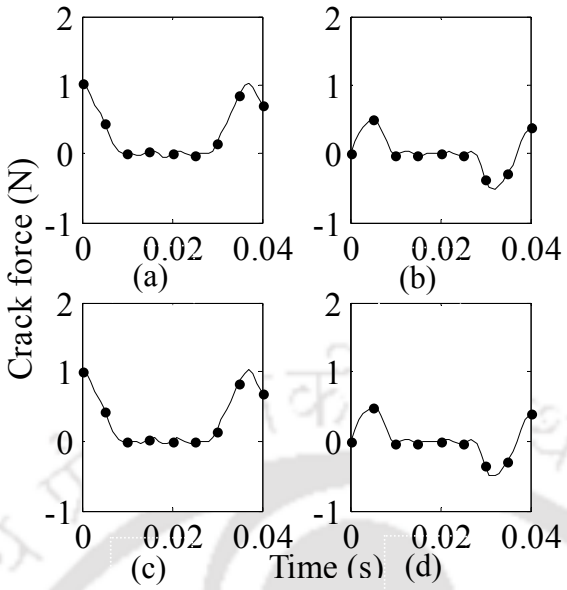


Figure 3.7 Comparison of crack forces between the assumed and estimated data at 300 rad/s (a) With 2% noise in *x* response (b) With 2% noise in *y* response (c) With 5% noise in *x* response (d) With 5% noise in *y* response; —— Assumed and ●●●●●● Estimated

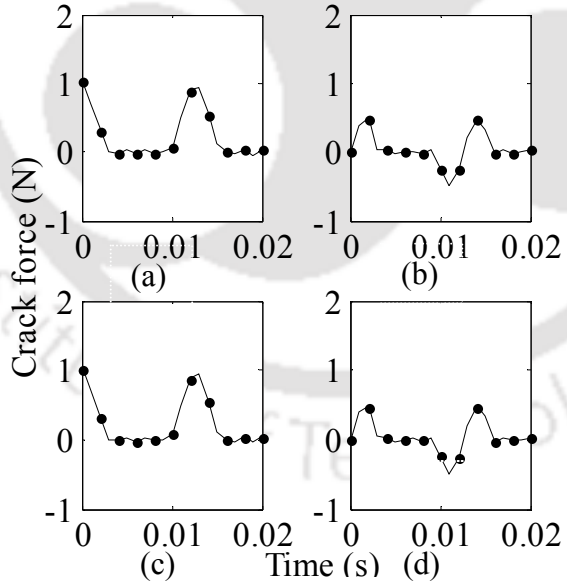


Figure 3.8 Comparison of the crack forces between the assumed and estimated data at 500 rad/s (a) With 2% noise in *x* response (b) With 2% noise in *y* response (c) With 5% noise in *x* response (d) With 5% noise in *y* response; —— Assumed and ●●●●●● Estimated

### 3.3.3 Concluding Remarks

The following conclusions could be drawn from the present chapter

- In this chapter, identification algorithms are developed for simultaneous estimation of crack parameter, i.e., additive crack stiffness together with unknown system parameters, i.e., unbalance eccentricity, and viscous damping.
- Inverse problem approach is used for identification. The system EOMs are written in a regression form and the parameters are obtained using least square estimates.
- For well conditioned algorithms, the identification is carried at multiple measurement speeds. The identification algorithms are tested in a defined range of spin-speeds.
- The maximum percentage error between assumed parameters and estimates, as observed for eccentricity or crack stiffness are around 3%. The percentage error of the estimates show that the robustness of developed identification algorithms even with noise.
- The algorithms are also extended to identify the crack force, which give information about the actual switching profile of a fatigue crack. The comparison of the assumed and estimated switching crack forces shows very good agreement.
- The developed identification algorithms are applicable and have been tested for Switching Crack. As the switching crack behavior is characteristic of a rotor fatigue crack which is in its initial or early stages of propagation, the model represents small or medium cracks. In this aspect, they can be effectively used for early crack detection.
- However, the developed algorithms use time responses for estimating response coefficients. On the other hand, these coefficients can be directly obtained using the frequency spectrum, which is based on FFT. This would also greatly reduce data handling of identification algorithms. The identification algorithm using the full-spectrum response data is elaborately discussed in the next chapter.

- Crack is a catastrophic fault, which after initiation can propagate very fast. This requires that the crack identification algorithm could identify the presence of crack before it reaches 5% to 10% depth. Switching function based on the hinge model represents such cracks that are in the early stages of propagation; thereby having abrupt opening/closing mechanism called as switching. Also, the identification algorithms use crack models based on the literature (Gasch, 1993) which have the advantage of identifying crack by a single parameter (i.e., additive stiffness it introduces in the shaft). Hence, this parameter has been identified. However, analytical expressions are available in literature (Dimaroganas, 1983) which relates crack flexibilities to the ratio of crack depth to shaft radius. These relations are based on beam theory and stress intensity factors that are estimated for a circular crack section. These relations can be further utilised to obtain crack size parameter.
- Though many switching and breathing functions exist in the literature, hardly any attempt on the estimation of the breathing function has been reported. Hence, the estimation of crack force is performed to obtain insight into the actual behavior of crack force during breathing.
- Apart from crack, eccentricity due to unbalance and shaft viscous damping are common unknown rotor parameters. Estimation of unbalance and damping parameters also illustrate the simultaneous estimation of multiple fault parameters using identification algorithm. The crack force depends on unbalance present in the rotor, which (residual unbalance) is otherwise unknown. Similarly, damping would change for different level of opening and closing of crack; hence, to have knowledge of all these parameters in cumulative sense, these have been estimated simultaneously.

# CHAPTER 4

# Model-Based Identification using Full-Spectrum Responses

## 4.1 Introduction

Two identification algorithms were developed in the previous chapter. One was for estimation of rotor crack parameter (i.e., crack stiffness) along with rotor system parameters (the disc eccentricity and the viscous damping); the other algorithm was for the estimation of crack forces which contribute to the switching phenomenon. Both the algorithms used displacement responses in time domain as their input (only estimates of time responses were used in Chapter 3 as in Eqn. (3.9)). Instead, using frequency responses as an input for identification has more advantage, as will be seen from the present chapter. Further, this chapter introduces the full-spectrum, a novel signal-processing tool for obtaining peculiar frequency responses in rotors, where both the forward and backward whirls may be present, simultaneously. Also, a numerical illustration of the identification algorithms is performed in frequency domain. A general guideline for the crack identification in rotors is given as a flowchart. Now, the full-spectrum is presented in detail in following sections.

## 4.2 Need for the Full-Spectrum

The conventional FFT gives the magnitude spectrum as well as the phase spectrum, and they together determine the actual rotor orbit. That means a considerable part of the rotor behavior is lost as both magnitude and phase information together determine the actual shape of the rotor orbit. Traditionally, a full-spectrum plot decomposes the rotor orbit into the forward whirl (positive) and backward whirl (negative) frequency components. At a glance, the full-spectrum plot shows whether the orbit of a particular frequency component is in forward (or same) or

backward (or reverse) direction with respect to the rotor spin direction. This is because the full-spectrum uses the relative phase correlation of vibration signals in two orthogonal directions, which constitute the orbit.

In the present work, the crack force consists of multiple harmonics of the spin-speed (Eqn. (2.18)). But, in the practical case, the crack force function would be unknown. Some of its harmonics would excite the rotor in the same sense of rotation or spin, whereas the other harmonics would excite the rotor in the reverse sense of spin. Harmonics, which excite the rotor in the same direction of spin, are denoted positive and their magnitude is given by $|p_{+i}|$ (i.e., *forward force coefficients*). Harmonics in the reverse direction as spin are considered negative and their magnitude is given by $|p_{-i}|$ (i.e., *reverse force coefficients*). Similarly, response coefficient magnitudes $|r_{+i}|$ and $|r_{-i}|$ are the forward and reverse displacement coefficients, respectively. It is not straightforward to obtain $p_{-i}$ or $r_{-i}$ reverse coefficients without using the full-spectrum.

It can be seen from Eqn. (2.22) that there is the need to know the reverse *force coefficients* ($p_{-i}$), which constitute the crack force as well as the closed-form and time-integrated responses. Identification algorithms for the estimation of crack stiffness, unknown system parameters, and crack forces, presented in Section 3.2 also use these coefficients. The *full-spectrum* of the time dependent part of crack force provides these coefficients. As the full-spectrum requires a complex time responses as an input, the system of equations of motion in the $x$ and $y$ directions are combined in the complex form as mentioned in Eqn. (2.17), and the *full-spectrum* of the complex response is obtained. The resultant full-spectrum will contain magnitude and phase information of both the forward and reverse displacement coefficients. Calculation procedures of obtaining the full-spectrum plots are now presented.

The need for any advanced signal processing tools such as the full-spectrum, Wigner distribution, and wavelets arises from the constraints associated with traditional signal processing techniques. Conventional signal handling methods such as time-histories, Fourier transforms and orbit plots analyse vibration signals either as a function of time or as a function of frequency but never as a function of both. Fluid excitation, rotor run-up or rundown, rotor cracks and others phenomena could lead to non-stationary vibration. However, the conventional FFT would only provide an average spectrum over a definite time period and the non-stationary characteristics of the vibration signal is completely lost. Thus, the *trinity* of amplitude, frequency and phase information is required to reveal all the characteristics of vibration signal completely in the frequency domain (Shi *et al*., 1999) of a rotor system.

In general, for the vibration measurement of a rotor, two transducers are used; one in horizontal direction ($x$) and another in the vertical direction ($y$). The plot of $x$ versus $y$ gives the *orbit plot*. Spectra obtained individually from each transducer are called as *half-spectra*. Because of their independent nature, the information on phase correlation between $x$ and $y$ spectra is not contained in these spectra. Hence, filtered orbits cannot be fully reconstructed using corresponding frequency components from the $x$ and $y$ half-spectra (Goldman and Muszynska, 1999). Also, half-spectra do not display the direction of frequency components, whether they are in the same direction as the rotor spin or in the reverse direction. These disadvantages are handled by the full-spectrum tool. The full-spectrum considers the phase correlation between the $x$ and $y$ spectra. At a glance, it shows whether the rotor orbit is in the forward or reverse direction with respect to the spin direction of the rotor (Goldman and Muszynska, 1999).If the magnitude of a forward frequency component is more than its backward component, it implies that their corresponding orbit has a

forward sense and vice versa. This information makes the full-spectrum a powerful tool for handling vibration signals of rotating machinery.

Let $p_{\pm i}$ correspond to full-spectrum coefficients of the time dependent part of crack force (i.e., $0.5s(t)(1 + e^{j2\omega t})$) in Eqn. (2.17). The function $s(t)$ and hence the time dependent part will be periodic. Full-spectrum force coefficients $p(d)$ (which are complex Fourier coefficients) are obtained as,

$$p(d) = \frac{1}{N}\sum_{l=0}^{N-1}\left\{s(l\Delta t)\left(1+e^{2\,\mathrm{j}\omega l\Delta t}\right)\right\}e^{-2\,\mathrm{j}\pi kl/N} \tag{4.1}$$

The f*ull-spectrum* converts a time domain complex signal of length $N$ (*sample length*) into a frequency domain signal of same length $N$. Its coefficients are complex. In Eqn. (4.1), the frequency index $d$ (length of the full spectrum signal) varies from 0 to $N$-1. The index $d$ from 0 to $N/2$ correspond to $p(+d)$ and $N/2$ to $N$-1 correspond to $p(-d)$; i.e., $p(N/2 + d) = p(-d)$ (Smith, 1997).Let $p_i$ correspond to $p(d)$ where $2\pi d/n = i\omega$, and $i = 1, 2,\ldots, l$ is the number of discrete data in the time history of $s(t)(1 + e^{j2\omega t})$ with $\Delta t$ as the *time interval* (sampling time). Here, $i$ correspond to various positive and negative harmonic components of the crack force. The *acquisition time* ($T$) of the time domain signal is $N\,\Delta t$. Samples are acquired at a *sampling rate* ($f_s$) which is $\frac{1}{\Delta t}$. The sampling rate also satisfies the *Nyquist-Shannon sampling theorem* (i.e., $f_s \geq 2f_{\max}$) where $f_{\max}$ is the maximum (*bandwidth*) frequency. In a similar manner, response coefficients $r_i$'s can be obtained as,

$$r(d) = \frac{1}{N}\sum_{l=0}^{N-1}\left\{r(l\Delta t)\right\}e^{-2\,\mathrm{j}dl/N} \tag{4.2}$$

A full-spectrum can be effectively plotted by placing zero frequency components (corresponding to DC) at the centre; positive frequencies to the right and negative frequencies to the left. The frequency at $N/2$ corresponds to the Nyquist frequency.

The following steps explain the computation of full spectrum:

- A numerical cracked rotor response in $x$ and $y$ lateral direction is simulated in time domain, for some measurement speed, say 50 rad/s.
- If the number of excitation harmonics considered for crack model in the given measurement range are chosen. For example, in the measurement spin speed range of 1 rad/s to 132 rad/s the following harmonics are chosen: -7×,-5×,-3×, 1×, 2×, 3×, 5× and 7×. Thus, the maximum frequency to be measured in this range is ± 924 rad/s. The sampling frequency $f_s = 1/\Delta t$, where $\Delta t$ is the response time step, is chosen such that $f_s \geq 2 f_{max}$ (Nyquist criterion), i.e., $f_s \geq 1848$ rad/s. Hence, the corresponding sampling time is $\Delta t \leq 0.0005$ s.
- The magnitude and phase of the full-spectrum frequency components depend on the sample length $N$ (Eqn. 4.1), which is the number of data in the time response. Hence, a sufficiently long signal is considered during the simulation
- Then, the time domain signal is transformed using full-spectrum equations (Eqn. 4.1 and Eqn. 4.2). The full-spectrum algorithm converts a complex time domain signal of length $N$ into a frequency domain signal of same length. The frequency index $d$ (length of the full spectrum signal) varies from 0 to $N$-1. The index $d$ from 0 to $N/2$ correspond to $p(+d)$ and N/2 to $N$-1 correspond to $p(-d)$; i.e. $p(N/2 + d) = p(-d)$.

Previous paragraphs explained the need for the full-spectrum in obtaining *force coefficients* and *displacement coefficients*. Now, a detailed pertinent discussion on methods of obtaining the full-spectrum is presented.

### 4.2.1 Full-Spectrum from Complex DFT

In this section, it is illustrated how the full-spectrum can be obtained using the Complex DFT of the time domain signal. First, an interpretation of a complex time signal (also called as *quadrature signal*) is given.

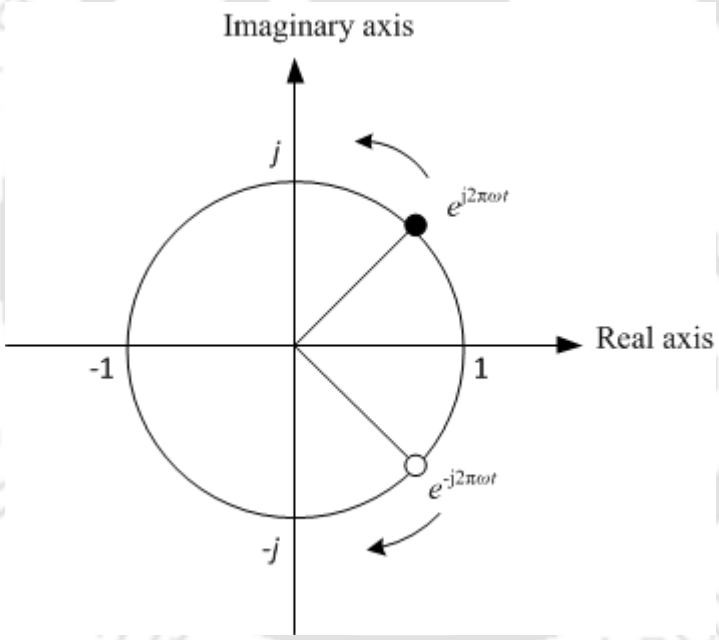


Figure 4.1 Rotation of two complex numbers with their phase angles changing with time

A *real signal* is a time domain signal obtained only from a single transducer. On the other hand, a *quadrature signal* is a signal with the real and imaginary parts. Karl Gauss (Gauss, 1799) first introduced that a single complex number can be represented as a point on the two-dimensional complex plane. The complex number $e^{j\omega t}$ has its phase angle increasing with time and orbits the

origin of the complex plane in a counter clockwise direction (Figure 4.1). The complex number $e^{j\omega t}$ is not just a mathematical quantity; it can be physically generated with two equal-magnitude signal generators, set to the same frequency but with the relative phase shift of $90^0$. The connector cables correspond to the cosine and sine signals, and when connected to horizontal and vertical channels of an oscilloscope, a bright spot rotating in counter clockwise direction is displayed (Lyons, 2008) . Similarly, the complex number $e^{-j\omega t}$ will orbit in a clockwise direction. Equations between complex numbers and ordinary sinusoids can be written using the Euler's identity. The complex DFT is written in the polar form, as (Smith, 1997).

$$\overline{X}[d] = \frac{1}{N}\sum_{l=0}^{N-1}\left(x[l] + j\, y[l]\right)e^{-j2\pi dl/N} \tag{4.3}$$

Here, the input time domain data, $\left(x[l] + j\, y[l]\right)$, and the output frequency domain data, $\overline{X}[d]$, both are arrays of complex numbers, with $d$ and $l$ running from 0 to $N$-1. As described above, frequencies between 0 and $N/2$ are positive, while frequencies between $N/2$ and $N$-1 are negative. Since the frequency spectrum of a discrete signal is periodic, negative frequencies between $N/2$ and $N$-1 are the same as between $-N/2$ and 0. Samples at 0 and $N/2$ which correspond to zero frequency (DC) and the Nyquist frequency which corresponds to one-half of the sample rate. The zero frequency and Nyquist frequency overlap on the line between positive and negative frequencies. Thus the complex DFT can be effectively used to represent the full-spectrum. Figure 4.4shows a sample illustration of a full-spectrum plot obtained from a complex response of a cracked rotor using the numerical simulation. A measurement spin speed of 50 Hz was used for the simulation. The displacement responses in $x$ and $y$ directions and corresponding orbit plots are given in Figure 4.2 and Figure 4.3 respectively.

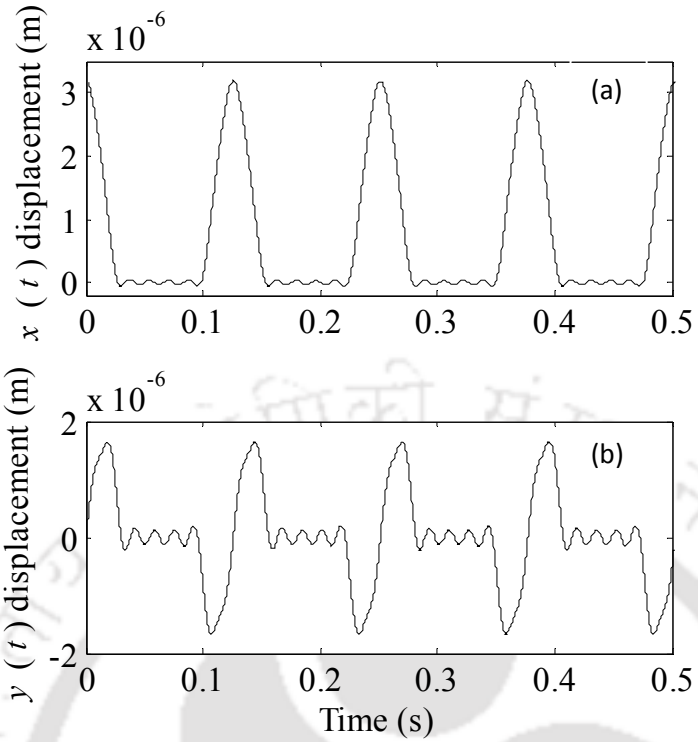


Figure 4.2 Displacement responses along (a) *x* direction (b) *y* direction

The magnitude and phase of frequency components obtained from the complex DFT plot are tabulated in Table 4-1.In the present section, it is illustrated how the full-spectrum can be obtained using the complex DFT of the time domain signal. Next, means of obtaining the full-spectrum using Real DFT equations; when only the conventional half-spectrum data are available; and when only orbit plots are available is illustrated. The full spectrum magnitude and phase values of frequency components obtained by means of different methods would be compared for the purpose of validating the results in Table 4-1.

The phase plot in Figure 4.4 is plotted between phase angle versus frequencies (rad/s) versus phase angles (rad). The range of phase angle is between $-\pi$ to $+\pi$. For a particular spin speed, the forward and reverse whirling time signal differs in phase by π rad. This can be seen in Figure 4.4 from horizontal lines corresponding to phase angles at $-\pi/2$ and $\pi/2$. At the frequencies which correspond to crack excitation in the magnitude plot (Figure 4.4 (a)); there is a phase change which is indicated by the peak at those corresponding frequencies in the phase plot (Figure 4.4 (a)).

However, the phase angles in the neighborhood of these peaks as well as at those corresponding to $-\pi/2$ and $\pi/2$ are fluctuating and appear noisy. This is because of the circulative nature of defining the phase angle between $-\pi$ to $\pi$, which assigns a phase angle of say 3.15 rad as -3.13 rad.

The definition of phase in Table 4.1 is as follows. The elliptical orbit corresponding to 2× super-synchronous frequency is represented subsequently in Figure 4.8. Here, the phase is obtained as $(\beta_2 - \alpha_2)/2$, where $\alpha_2$ is the phase corresponding to the forward circular orbit (+2×) and $\beta_2$ is the phase corresponding to reverse circular orbit (-2×). In Table 4.1, these phase values have been obtained from complex full-spectrum coefficients, which contain both the magnitude and phase information. One sided spectrum in two orthogonal directions, say, *x* and *y* lateral vibrations, together with phase information is equivalent to two sided (full) spectrum in terms of information content regarding magnitude and phase. The means to obtain full-spectrum from one sided magnitude and phase spectra is explained in Sections 4.2.2 and 4.2.3.

However, the information (magnitude and phase) regarding the reverse frequency components are not available explicitly from one sided spectra.

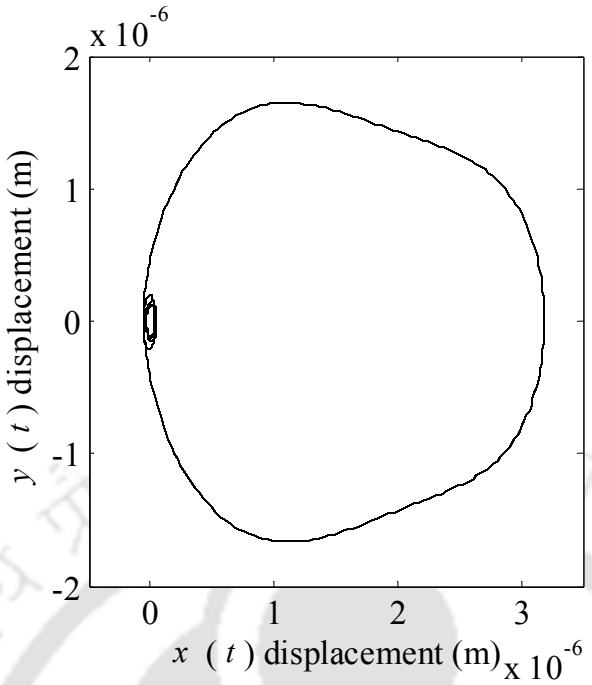


Figure 4.3 Orbit plot of $x$ versus $y$ displacement response

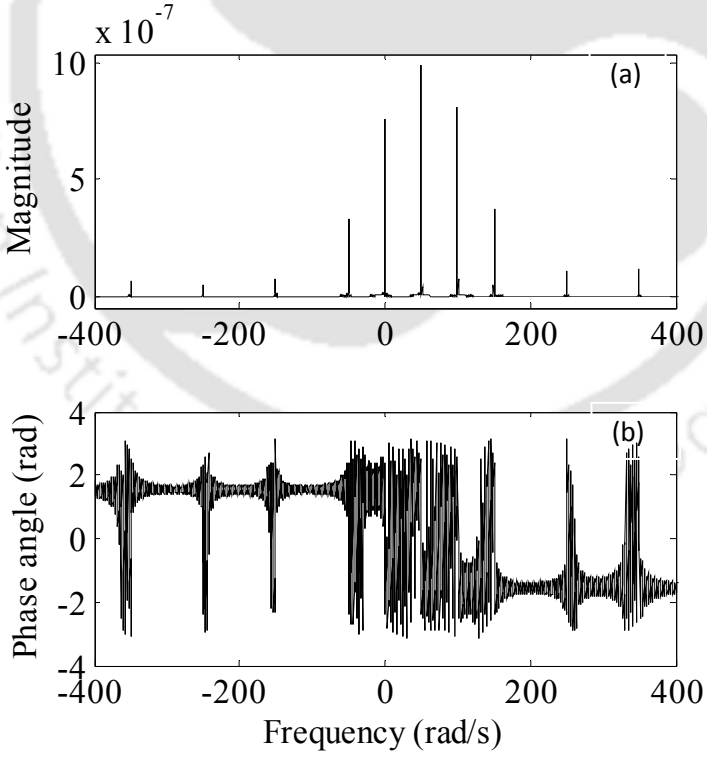


Figure 4.4 Full-spectrum plot of the complex cracked rotor response ($x$ + j $y$)
(a) magnitude and (b) phase plots

Table 4-1 Magnitude and phase of full-spectrum frequency components

| Frequency component (Forward or reverse) | | Real part ($\times 10^{-7}$) | Imaginary part ($\times 10^{-9}$) | Full-spectrum magnitude ($\times 10^{-6}$) | Phase angle (rad) |
|---|---|---|---|---|---|
| Forward frequency components | 1× | 9.887 | -2.231 | 0.989 | -0.002 |
| | 2× | 8.138 | 4.330 | 0.814 | -0.005 |
| | 3× | 3.767 | -3.278 | 0.377 | -0.009 |
| | 5× | -1.060 | 2.164 | 0.106 | 3.121 |
| | 7× | 1.163 | -8.547 | 0.117 | -0.073 |
| Reverse frequency components | -1× | 3.290 | 0.834 | 0.329 | 0.003 |
| | -3× | -0.753 | -0.656 | 0.075 | -3.133 |
| | -5× | 0.454 | 0.928 | 0.045 | 0.02 |
| | -7× | -0.646 | -4.750 | 0.065 | -3.068 |

### 4.2.2 Full-Spectrum from Real DFT

The conventional frequency spectrum plots that are used for vibration measurements are only half-spectrums. They can be obtained by using the real DFT of time responses in the vertical and horizontal directions, independently (Eqn. (4.4)). This is illustrated in the following section. Half-spectrums of real orthogonal signals $x$ or $y$ could be obtained using real DFT that is given as,

$$\mathrm{Re}\left(X\left[d\right]\right) = \frac{2}{N}\sum_{l=0}^{N-1} x\left[l\right]\cos\left(2\pi dl / N\right)$$

and (4.4)

$$\mathrm{Im}\left(X\left[d\right]\right) = \frac{-2}{N}\sum_{n=0}^{N-1} x\left[l\right]\sin\left(2\pi dl / N\right)$$

Here the frequency index *d* varies from 0 to *N*/2 only. (This is in contrast to Eqn. (4.3) where it varies from 0 to *N*-1). In other words, the *N* sample time domain signal *x*[*l*] is decomposed into a set of (*N*/2 +1) cosine waves, and (*N*/2 +1) sine waves (Eqn.(4.4)), with frequencies given by index *d*. Though the real DFT uses only real numbers, a *complex substitution* allows the frequency domain to be represented in the complex form,

$$X[d] = \mathrm{Re}(X[d]) + \mathrm{j}\,\mathrm{Im}(X[d]) \tag{4.5}$$

Similarly, for the time signal *y*, we have $Y[d] = \mathrm{Re}(Y[d]) + \mathrm{j}\,\mathrm{Im}(Y[d])$. Half-spectrum plots of a cracked rotor in the *x* and *y* directions are shown in Figure 4.5 and Figure 4.6. The magnitude and phase of the frequency components for these two plots are tabulated in Table 4-2 and Table **4-3**.

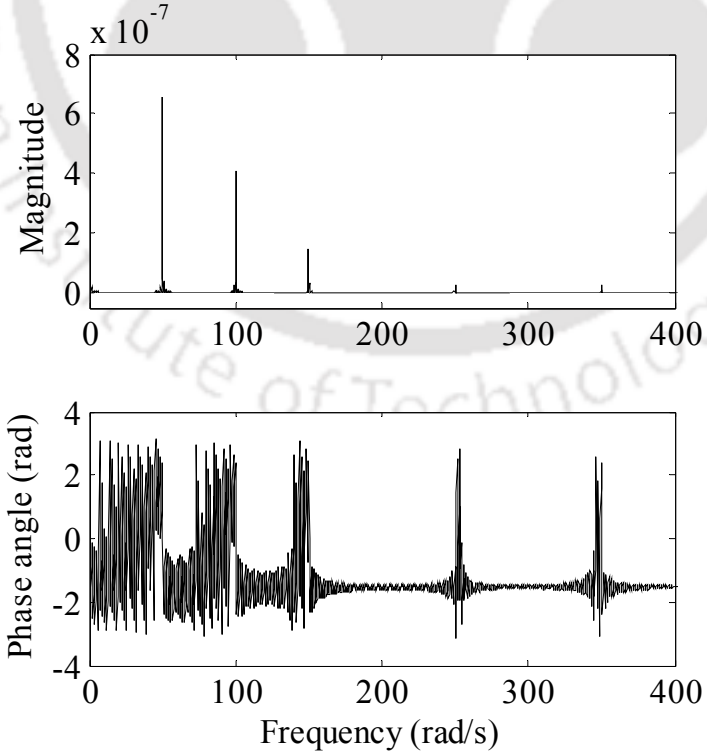


Figure 4.5 Half-spectrum of *x* response (a) magnitude (b) phase

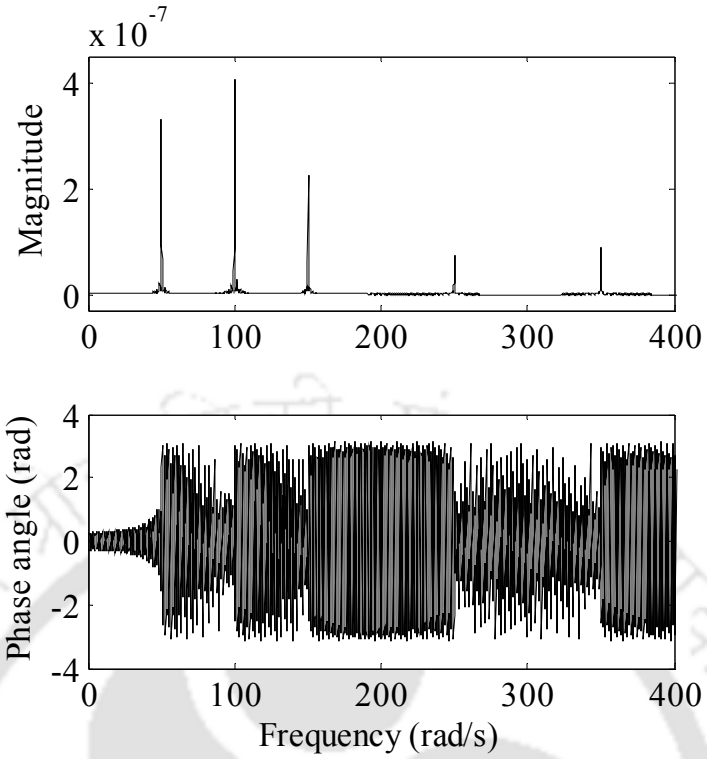


Figure 4.6 Half-spectrum of *y* response (a) magnitude (b) phase

Table 4-2 Magnitudes and phase of frequency components of half-spectrum of *x* response

| Frequency component | Magnitude($\times 10^{-6}$) | Phase angle(rad) |
|---|---|---|
| 1× | 0.659 | -0.002 |
| 2× | 0.407 | -0.005 |
| 3× | 0.151 | -0.009 |
| 5× | 0.030 | 3.121 |
| 7× | 0.026 | -0.073 |

The full-spectrum of quadrature signal ($x$ + j $y$) can be obtained using the complex DFT as shown in Eqn. (4.3). It can be noted that the real DFT has a scaling factor of 2 (Eqn. (4.4)), while the complex DFT does not have (Eqn. (4.3)) (Smith, 1997).

Table 4-3 Magnitudes and phase of frequency components of half-spectrum of *y* response

| Frequency component | Magnitude($\times 10^{-6}$) | Phase angle (rad) |
|---|---|---|
| 1× | 0.330 | -1.573 |
| 2× | 0.407 | -1.576 |
| 3× | 0.226 | -1.579 |
| 5× | 0.076 | 1.550 |
| 7× | 0.091 | -1.644 |

For example, the real DFT of a cosine wave with unit magnitude will give a spectral value of one corresponding to the cosine wave frequency. However, complex DFT of the same cosine wave gives two spectral values, a positive frequency with magnitude of 0.5 and a negative frequency with magnitude of 0.5 producing a cosine wave of magnitude 1. This can be understood from the fact that a cosine wave or sine wave in the time domain splits between a positive and negative frequency in the complex DFT spectrum in accordance with Euler's identities,

$$\cos \omega t = \tfrac{1}{2} e^{\mathrm{j}\omega t} + \tfrac{1}{2} e^{-\mathrm{j}\omega t}$$

and (4.6)

$$\sin \omega t = -\tfrac{1}{2}\,\mathrm{j}\, e^{\mathrm{j}\omega t} + \tfrac{1}{2}\,\mathrm{j}\, e^{-\mathrm{j}\omega t}$$

The FFT is an algorithm to calculate the complex DFT, which requires a complex time signal in its input. Cooley and Turkey (1965) introduced the FFT. Though algorithm similar to FFT had been discovered many years ago, for instance by Karl Gauss (Gauss, 1799), it lacked the digital technology to make it a practical tool. The real DFT or half-spectrum, which requires only a real time signal as its input, can also be calculated using the FFT algorithm. For this, the *N* point real time domain signal is moved into the real part of the complex DFTs' time domain, and all the set

of samples in imaginary part is set to zero (Smith, 1997). Calculation results in a real and imaginary signal in frequency domain, each of $N$ points. As described earlier, the frequency index corresponding to samples 0 through $N/2$ make the real DFT spectrum. Thus the *real DFT* or the *half-spectrum* from the FFT algorithm can be expressed as, for signal $x$, (note that imaginary part in input is set to zero).

$$X[d] = \frac{1}{N}\sum_{l=0}^{N-1}\left(x[l] + \mathrm{j}\times 0\right)e^{-\mathrm{j}2\pi dl/N} \tag{4.7}$$

On expanding using the Euler's identity,

$$X[d] = \left[\frac{1}{N}\sum_{l=0}^{N-1} x[l]\cos\frac{2\pi ld}{N}\right] + \mathrm{j}\left[\frac{1}{N}\sum_{l=0}^{N-1} -x[l]\sin\frac{2\pi ld}{N}\right] \tag{4.8}$$

For convenience, let $X[d] = a + \mathrm{j}\, b$, so that

$$a = \left[\frac{1}{N}\sum_{l=0}^{N-1} x[l]\cos\frac{2\pi ld}{N}\right]$$

and

$$b = \left[\frac{1}{N}\sum_{l=0}^{N-1} -x[l]\sin\frac{2\pi ld}{N}\right] \tag{4.9}$$

Similarly, for signal $y$, we have

$$Y[d] = \left[\frac{1}{N}\sum_{l=0}^{N-1} y[l]\cos\frac{2\pi ld}{N}\right] + \mathrm{j}\left[\frac{1}{N}\sum_{l=0}^{N-1} -y[l]\sin\frac{2\pi ld}{N}\right] \tag{4.10}$$

For convenience, let $Y[d] = c + \mathrm{j}\, d$, so that

$$c = \left[ \frac{1}{N} \sum_{l=0}^{N-1} y[l] \cos \frac{2\pi l d}{N} \right]$$

and (4.11)

$$d = \left[ \frac{1}{N} \sum_{l=0}^{N-1} -y[l] \sin \frac{2\pi l d}{N} \right]$$

Now, if two orthogonal signals $x$ and $y$ are combined as a quadrature signal ($x + \mathrm{j}\, y$), the complex DFT obtained through the FFT will be as follows,

$$\overline{X}[d] = \left( \left[ \frac{1}{N} \sum_{n=0}^{N-1} x[l] \cos \frac{2\pi l d}{N} \right] + \left[ \frac{1}{N} \sum_{n=0}^{N-1} y[l] \sin \frac{2\pi l d}{N} \right] \right) + \mathrm{j} \left( \left[ \frac{1}{N} \sum_{n=0}^{N-1} y[l] \cos \frac{2\pi l d}{N} \right] + \left[ \frac{1}{N} \sum_{n=0}^{N-1} -x[l] \sin \frac{2\pi l d}{N} \right] \right) \quad (4.12)$$

Thus,

$$\overline{X}[d] = (a - d) + \mathrm{j}\ (c + b) \quad (4.13)$$

This shows a *means of obtaining full-spectrum* of a quadrature signal, if only the independent half-spectrums of two real signals are available. Now, this is illustrated for the sample half-spectrum responses of a cracked rotor. The magnitude and phase of frequency components of the full-spectrum, which are obtained from the magnitude and phase information of $x$ and $y$ half-spectrums. Half spectrums are presented in (Table 4-2 and Table 4-3). Eqn. (4.13) is used for this purpose.

Table 4-4 Magnitude and phase of the full-spectrum frequency components obtained from the magnitude and phase information of half-spectrum components

| Frequency component | | Full-spectrum magnitude ($\times 10^{-6}$)( Eqn. (4.13)) | Phase angle (rad) |
|---|---|---|---|
| Forward Frequency components | 1× | 0.989 | -0.002 |
| | 2× | 0.814 | -0.005 |
| | 3× | 0.377 | -0.009 |
| | 5× | 0.106 | 3.121 |
| | 7× | 0.117 | -0.073 |
| Reverse Frequency components | -1× | 0.329 | -0.003 |
| | -3× | 0.075 | -3.133 |
| | -5× | 0.045 | 0.020 |
| | -7× | 0.065 | -3.068 |

The magnitude and phase of frequency components compare very well (Table 4-4 and Table 4-1) with that obtained directly from the full-spectrum of complex response/quadrature signal. Now, another method of obtaining full-spectrum magnitudes using half-spectrum plots, developed by Goldman and Muszynska (1999) is briefed with a sample illustration.

### 4.2.3 Full-Spectrum from Half-Spectrum

Goldman and Muszynska (1999) illustrated obtaining the full-spectrum responses from their corresponding half-spectrum magnitude and phase plots. If the rotor spins in a counter-clockwise direction and the rotor orbit frequency components are in the same sense $+\omega_n$, this is called the forward response or forward whirl.

Let, the magnitude and phase corresponding to the half-spectrum of the *x* signal be $X_n$ and $\alpha_n$. Let the magnitude and phase corresponding to the half-spectrums of the *y* signal be $Y_n$ and $\beta_n$. Thus, the complex representation of the *X* spectrum will be $X_n e^{j\alpha_n}$ and that of the *Y* spectrum will be $Y_n e^{j\beta_n}$; i.e., $(X_n \cos\alpha_n + j\, X_n \sin\alpha_n)$ for the *X* spectrum and $(Y_n \cos\beta_n + j\, Y_n \sin\beta_n)$ for the *Y* spectrum. As described earlier in Eqn. (4.13), the full-spectrum of the quadrature signal will be given as $(X_n \cos\alpha_n - Y_n \sin\beta_n)$ in the real part and $(X_n \sin\alpha_n + Y_n \cos\beta_n)$ in the imaginary part. This is schematically shown in Figure 4.7.

Similarly, when the rotor rotates in the counter-clockwise direction but the rotor orbit frequency components are in the opposite sense $-\omega_n$, this is called as *reverse response*. Magnitudes of the half-spectrum of *x* and *y* signals will be same as $X_n$ and $Y_n$. But the phase will be now in the clockwise direction from the keyphasor and will be $-\alpha_n$ and $-\beta_n$. Thus, the complex representation of *X* spectrum will be $X_n e^{-j\alpha_n}$, where as that of *Y* spectrum will be $Y_n e^{-j\beta_n}$; i.e., $(X_n \cos\alpha_n - j\, X_n \sin\alpha_n)$ for the *X* spectrum and $(Y_n \cos\beta_n - j\, Y_n \sin\beta_n)$ for the *Y* spectrum. As described in Eqn. (4.13), the full-spectrum of the quadrature signal will be $(X_n \cos\alpha_n + Y_n \sin\beta_n)$ as the real part and $(-X_n \sin\alpha_n + Y_n \cos\beta_n)$ as the imaginary part. The magnitude of the forward and reverse response is $\sqrt{\mathrm{Re}^2 + \mathrm{Im}^2}$. Thus the forward response magnitude is,

$$R_{\omega_n +} = \sqrt{(X_n \cos\alpha_n - Y_n \sin\beta_n)^2 + (X_n \sin\alpha_n + Y_n \cos\beta_n)^2} \tag{4.14}$$

and the magnitude of the reverse response is,

$$R_{\omega_n -} = \sqrt{(X_n \cos\alpha_n + Y_n \sin\beta_n)^2 + (-X_n \sin\alpha_n + Y_n \cos\beta_n)^2} \tag{4.15}$$

All magnitudes of frequency components (the forward and the reverse) that are obtained using the half-spectrum, conform very well to the magnitude of frequency components obtained directly from the full-spectrum. By comparing results obtained in Table 4-1 with results based on Goldman and Muszynska method (Table 4-5), the full-spectrum used in the present work is also validated. The comparison of magnitudes of the response coefficients corresponding to various frequency components of crack force, obtained from full-spectrum plots are given in Table 4-6. Similarly, the phase values are also compared for the full-spectrums plots obtained using complex DFT and real DFT methods. This is shown in Table 4-7.

Table 4-5 Magnitudes of frequency components of the full-spectrum obtained from the magnitude and phase information of individual half-spectrums

| Frequency component | *x* response | | *y* response | | Full-spectrum magnitude ($\times 10^{-6}$) (Eqn. (4.14); Eqn. (4.15)) |
|---|---|---|---|---|---|
| | Magnitude | Phase | Magnitude | Phase | |
| 1× | 0.659 | -0.002 | 0.330 | -1.573 | $R_{1+} = 0.989$ |
| | | | | | $R_{1-} = 0.329$ |
| 2× | 0.407 | -0.005 | 0.407 | -1.576 | $R_{2+} = 0.814$ |
| 3× | 0.151 | -0.009 | 0.226 | -1.579 | $R_{3+} = 0.377$ |
| | | | | | $R_{3-} = 0.075$ |
| 5× | 0.030 | 3.121 | 0.076 | 1.550 | $R_{5+} = 0.106$ |
| | | | | | $R_{5-} = 0.046$ |
| 7× | 0.026 | -0.073 | 0.091 | -1.644 | $R_{5+} = 0.117$ |
| | | | | | $R_{5-} = 0.065$ |

Table 4-6 Comparison of full-spectrum response coefficients obtained from different methods

| | | Magnitude of full-spectrum response coefficients | | |
|---|---|---|---|---|
| | Frequency component | From Complex DFT | From Real DFT | From Half-Spectrums |
| Forward frequency components | 1× | 0.989 | 0.989 | 0.989 |
| | 2× | 0.814 | 0.814 | 0.814 |
| | 3× | 0.377 | 0.377 | 0.377 |
| | 5× | 0.106 | 0.106 | 0.106 |
| | 7× | 0.117 | 0.117 | 0.117 |
| Reverse frequency components | -1× | 0.329 | 0.329 | 0.329 |
| | -3× | 0.075 | 0.075 | 0.075 |
| | -5× | 0.045 | 0.045 | 0.046 |
| | -7× | 0.065 | 0.065 | 0.065 |

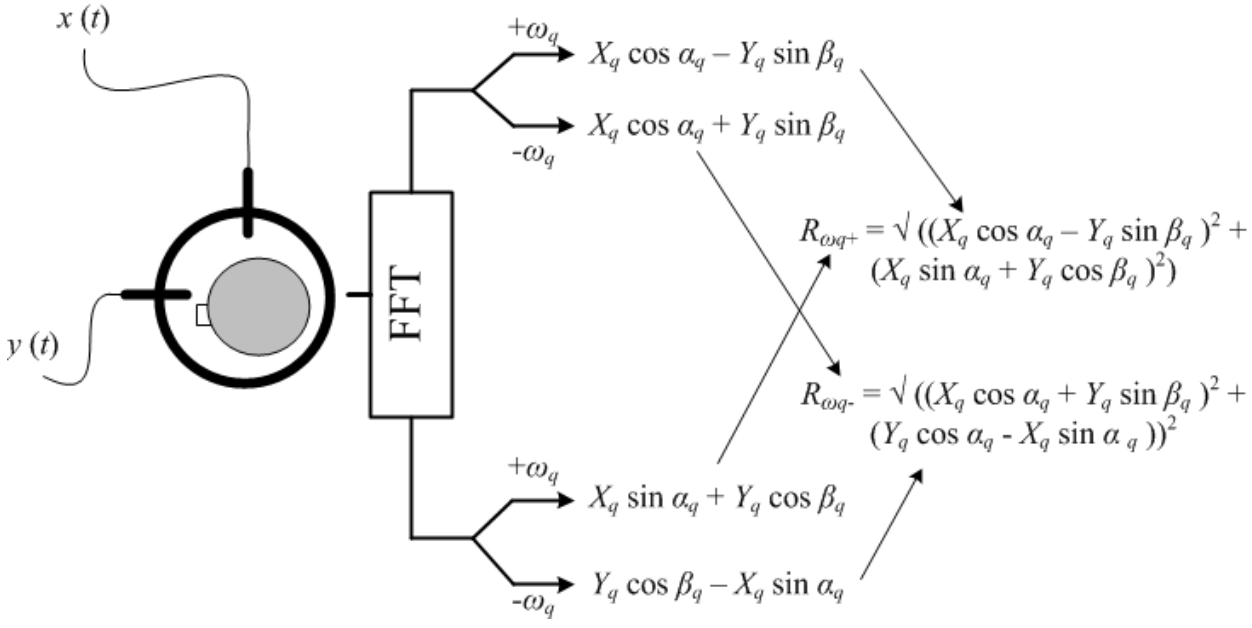


Figure 4.7 Obtaining full-spectrum from half-spectrum magnitude and phase (source: Goldman and Muszynska, 1999)

Table 4-7 Comparison of phase of full-spectrum response coefficients obtained by different methods

| | Phase of full-spectrum response coefficients | | |
|---|---|---|---|
| | Frequency component | From Complex DFT | From Real DFT |
| Forward frequency components | 1× | -0.002 | -0.002 |
| | 2× | -0.005 | -0.005 |
| | 3× | -0.009 | -0.009 |
| | 5× | 3.121 | 3.121 |
| | 7× | -0.073 | -0.073 |
| Reverse frequency components | -1× | 0.003 | -0.003 |
| | -3× | -3.133 | -3.133 |
| | -5× | 0.020 | 0.020 |
| | -7× | -3.068 | -3.068 |

Now, a method of obtaining full-spectrum components from orbit plots is briefed.

### 4.2.4 Full-Spectrum from Orbit Plots

An elliptical locus can be presented as a sum of two circular loci: one is the locus of the vector rotating in the direction of rotation (i.e., the forward response) and the other is the locus of the vector rotating in the opposite direction (i.e., the reverse response).Both vectors rotate at a same frequency which is the frequency of the filtered orbit.

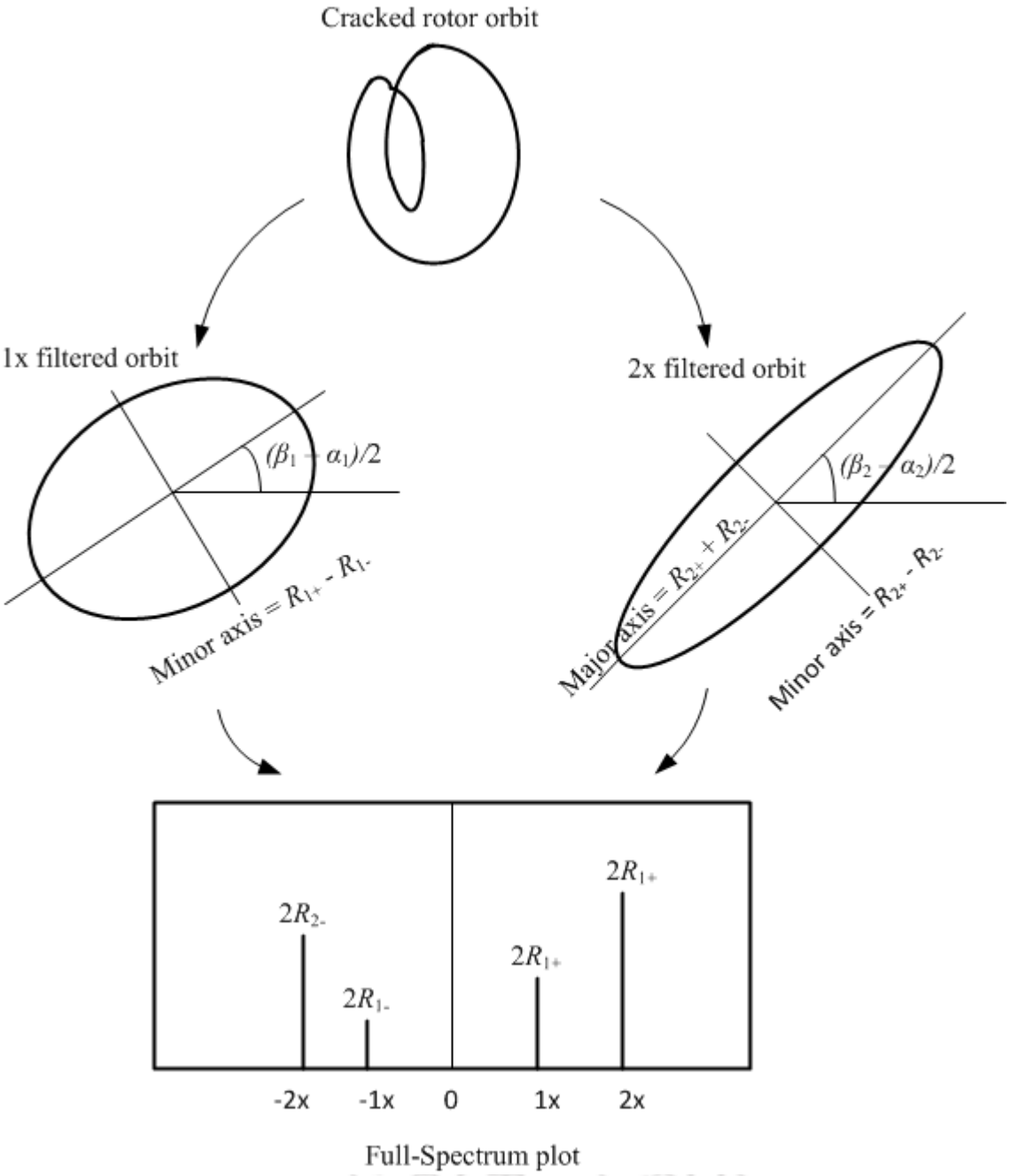


Figure 4.8 Obtaining full-spectrum from orbit plots (source: Goldman and Muszynska, (1999))

The instantaneous position of the rotor on the filtered orbit is presented as the sum of vectors of instantaneous positions of forward and reverse orbits; for example, an ellipse in canonical form, $x(t) = a\cos(\omega t)$ and $y(t) = b\sin(\omega t)$ where $a$ and $b$ are the major and minor axes. Then,

$$x(t) + \mathrm{j}\, y(t) = a\left[\frac{e^{\mathrm{j}\omega t} + e^{-\mathrm{j}\omega t}}{2}\right] + \mathrm{j}\ \mathrm{b}\left[\frac{e^{\mathrm{j}\omega t} - e^{-\mathrm{j}\omega t}}{2j}\right]$$
$$= \left(\frac{a+b}{2}\right)e^{\mathrm{j}\omega t} + \left(\frac{a-b}{2}\right)e^{-\mathrm{j}\omega t} \tag{4.16}$$

In special cases, the filtered orbit can be circular shape or straight line. If it is circular only either the forward or reverse component exist depending on magnitude of $R_{\omega+}$ and $R_{\omega-}$. If it is a straight line then the amplitude of forward component will be equal to the amplitude of reverse component. This method is directly based on the physics of the problem, i.e., the forward or reverse whirling orbits of the forcing due to crack. However, numerical illustrations for obtaining its full-spectrum coefficients has not been presented because of more cumbersome processing including band pass filtering.

The full-spectrum and various methods of obtaining full-spectrum of a complex time response were discussed in above sections. Sample illustrations were given for a complex cracked rotor response and results from different methods were compared to get unanimity in Table 4-6 and Table 4-7. From these tables it is observed that the compared magnitude and phase values of full-spectrum coefficients obtained using different methods are the same. In this work, it is considered best to obtain the full-spectrum coefficients more directly by using the complex DFT for complex time responses. Now, the frequency domain based identification algorithms are detailed.

## 4.3 Identification in Frequency Domain

Identification algorithms presented in previous chapter uses displacement versus time responses as their input. Advantages of using frequency responses are discussed in the previous section on the full-spectrum. In view of the same, identification algorithms developed in the previous chapter are now formulated and illustrated using full-spectrum responses.

*Identification of Crack, unbalance, and viscous damping*: For identifying the crack, the unbalance, and the viscous damping from time domain data, the identification algorithm given in previous section, i.e., Eqn. (3.15) has been used. The algorithm contains response coefficients $r_{\pm i}$, which were estimated using various time responses. This is not practical, as there will be large amount of experimental time domain data to handle and also there will be no prior knowledge on the contribution of various harmonics *i* of the crack force. Hence, it is preferable to directly obtain these response coefficients, by means of the full-spectrum, as given in Eqn. (4.2). In time domain, the number of harmonic components, *i*, that are chosen for the expression is limited to terms of corresponding closed-form expression (Eqn. (2.18)). Whereas, in frequency domain, a number of frequency coefficients can be directly obtained from the full-spectrum. Also, instead of a switching function any other time varying function can also be easily implemented. This also facilitates the contribution of more number of harmonic components as an input to the identification algorithm. The generalised form of Eqn. (3.8), for *n* harmonic components is as follows.

$$\mathbf{A}_{1((2n+1)\times 3)}=\begin{bmatrix} \mathrm{j}(-n\omega)r_{-n} & 0 & -w_x p_{-n} \\ . & . & . \\ . & . & . \\ . & . & . \\ \mathrm{j}(-\omega)r_{-1} & 0 & -w_x p_{-1} \\ 0 & 0 & -w_x p_0 \\ \mathrm{j}(\omega)r_1 & -m\omega^2 e^{\mathrm{j}\beta} & -w_x p_1 \\ \mathrm{j}(2\omega)r_2 & 0 & -w_x p_2 \\ . & . & . \\ . & . & . \\ . & . & . \\ \mathrm{j}(n\omega)r_n & 0 & -w_x p_n \end{bmatrix}; \quad \mathbf{b}_{1((2n+1)\times 1)}=\begin{Bmatrix} \left(n^2\omega^2 m-k_0\right)r_{-n} \\ . \\ . \\ . \\ \left(\omega^2 m-k_0\right)r_{-1} \\ -k_0 r_0 \\ \left(\omega^2 m-k_0\right)r_1 \\ \left(4\omega^2 m-k_0\right)r_2 \\ . \\ . \\ . \\ \left(n^2\omega^2 m-k_0\right)r_n \end{Bmatrix} \mathbf{x}_{1(3\times 1)}=\begin{Bmatrix} c \\ e \\ \Delta k_{22} \end{Bmatrix} \tag{4.17}$$

Here, the number of harmonic components considered in the algorithm is generalised and varies from 1 to *n* for forward components and -1 to *-n* for reverse components in steps of 1. Thus, all harmonic components can be considered, in contrast to algorithm in time-domain (Eqn.(3.9)), where the number of harmonics was limited to the closed-form expression (Eqn.(2.18)). This as noted is an advantage of using full-spectrum responses.

*Identification of Crack Force*: The identification of crack force terms is carried out using Eqn. (3.15), it uses only force coefficients $p_{\pm i}$, which are now directly obtained using full-spectrum. The full-spectrum equation Eqn. (4.1) is used for obtaining these coefficients for the input to the identification algorithm. The generalised form of Eqn. (3.14) is as follows. Refer section 3.2.2 for details.

$$\mathbf{A}_{2((2n+1)\times(2n+3))}=\begin{bmatrix}\mathbf{D}_1 & \mathbf{D}_2\end{bmatrix} \tag{4.18}$$

with,

$$\mathbf{D}_1 = \begin{bmatrix} \mathrm{j}(-n\omega)r_{-n} & 0 & -w_x & 0 & 0 & 0 & 0 \\ . & . & . & . & . & . & . \\ . & . & . & . & . & . & . \\ . & . & . & . & . & . & . \\ \mathrm{j}(-\omega)r_{-1} & 0 & 0 & 0 & 0 & 0 & -w_x \\ 0 & 0 & 0 & 0 & 0 & 0 & 0 \\ \mathrm{j}(\omega)r_1 & -m\omega^2 e^{\mathrm{j}\beta} & 0 & 0 & 0 & 0 & 0 \\ \mathrm{j}(2\omega)r_2 & 0 & 0 & 0 & 0 & 0 & 0 \\ . & . & . & . & . & . & . \\ . & . & . & . & . & . & . \\ . & . & . & . & . & . & . \\ \mathrm{j}(n\omega)r_n & 0 & 0 & 0 & 0 & 0 & 0 \end{bmatrix}$$

$$\mathbf{D}_2 = \begin{bmatrix} 0 & 0 & 0 & 0 & 0 & 0 & 0 \\ . & . & . & . & . & . & . \\ . & . & . & . & . & . & . \\ . & . & . & . & . & . & . \\ 0 & 0 & 0 & 0 & 0 & 0 & 0 \\ -w_x & 0 & 0 & 0 & 0 & 0 & 0 \\ 0 & -w_x & 0 & 0 & 0 & 0 & 0 \\ 0 & 0 & -w_x & 0 & 0 & 0 & 0 \\ . & . & . & . & . & . & . \\ . & . & . & . & . & . & . \\ . & . & . & . & . & . & . \\ 0 & 0 & 0 & 0 & 0 & 0 & -w_x \end{bmatrix}$$

$$\mathbf{x}_{2((2n+3)\times 1)} = \begin{Bmatrix} c \\ e \\ \Delta k_{22} p_{-n} \\ . \\ . \\ . \\ \Delta k_{22} p_{-1} \\ \Delta k_{22} p_0 \\ \Delta k_{22} p_1 \\ \Delta k_{22} p_2 \\ . \\ . \\ . \\ \Delta k_{22} p_n \end{Bmatrix}; \qquad \mathbf{b}_{1((2n+1)\times 1)} = \begin{Bmatrix} \left(n^2\omega^2 m - k_0\right) r_{-n} \\ . \\ . \\ . \\ \left(\omega^2 m - k_0\right) r_{-1} \\ -k_0 r_0 \\ \left(\omega^2 m - k_0\right) r_1 \\ \left(4\omega^2 m - k_0\right) r_2 \\ . \\ . \\ . \\ \left(n^2\omega^2 m - k_0\right) r_n \end{Bmatrix} \tag{4.19}$$

Here, the number of harmonic components considered in the algorithm is general and varies from 1 to *n* for forward components and -1 to -*n* for reverse components in steps of 1.

*Identification at multiple measurement speeds*: Identification algorithms presented above correspond to a single measurement speed. For accommodating estimation with a set of multiple measurement speeds, the regression equation (Eqn. (4.17)) is modified as,

$$\begin{bmatrix} \mathbf{A}_1(\omega_1) \\ \mathbf{A}_1(\omega_2) \\ \vdots \\ \mathbf{A}_1(\omega_q) \end{bmatrix}_{(2n+1)q\times 3} \qquad \mathbf{x}_{1(3\times 1)} = \begin{Bmatrix} \mathbf{b}_1(\omega_1) \\ \mathbf{b}_1(\omega_2) \\ \vdots \\ \mathbf{b}_1(\omega_q) \end{Bmatrix}_{(2n+1)q\times 1} \tag{4.20}$$

Similarly, the regression equation (Eqn. (4.19)) is modified as,

$$\begin{bmatrix} \mathbf{A}_2(\omega_1) \\ \mathbf{A}_2(\omega_2) \\ \vdots \\ \mathbf{A}_2(\omega_q) \end{bmatrix}_{(2n+1)q\times 3} \mathbf{x}_{2(3\times 1)} = \begin{Bmatrix} \mathbf{b}_1(\omega_1) \\ \mathbf{b}_1(\omega_2) \\ \vdots \\ \mathbf{b}_1(\omega_q) \end{Bmatrix}_{(2n+1)q\times 1} \tag{4.21}$$

The identification algorithms are presented for identification of crack, unbalance, and damping using data from full-spectrum responses. The force and response coefficients can be chosen directly from the full-spectrum plots, which also generalize identification algorithms. Now, the illustrations for the frequency domain based identification are presented.

## 4.4 Numerical Illustrations for Identification Algorithms using Full-Spectrum

In the present section, identification algorithms (Eqns. (4.17) and (4.19)) are used to estimate fault parameters. The estimation is performed completely in frequency domain. The force coefficients $p_i$ and response coefficients $r_i$ , which are obtained using the full-spectrum, are used as an input to identification algorithms. The estimation of parameters is discussed in following subsection.

### 4.4.1 Simultaneous Estimation of Damping, Eccentricity, and Additive Crack Stiffness in Frequency Domain

Different ranges of frequencies are chosen from which responses are taken for the identification algorithm. Figure 4.9 shows response plots in which the resonance in the response of once per revolution component of the crack force is at 400.6 rad/s. These plots are obtained using Eqn. (2.22) by plotting $r_i$ as a function of spin frequency $\omega$. The resonance in responses of the twice per revolution component occurs at 199.8 rad/s, while resonances in responses of thrice and four times per revolution components of the crack force are observed at 133.1 rad/s and 100 rad/s,

respectively. Similarly, resonances in responses of five per revolution, seven per revolution and nine per revolution are at 80 rad/s, 57 rad/s and 45 rad/s, respectively. These are shown in Figure 4.10.

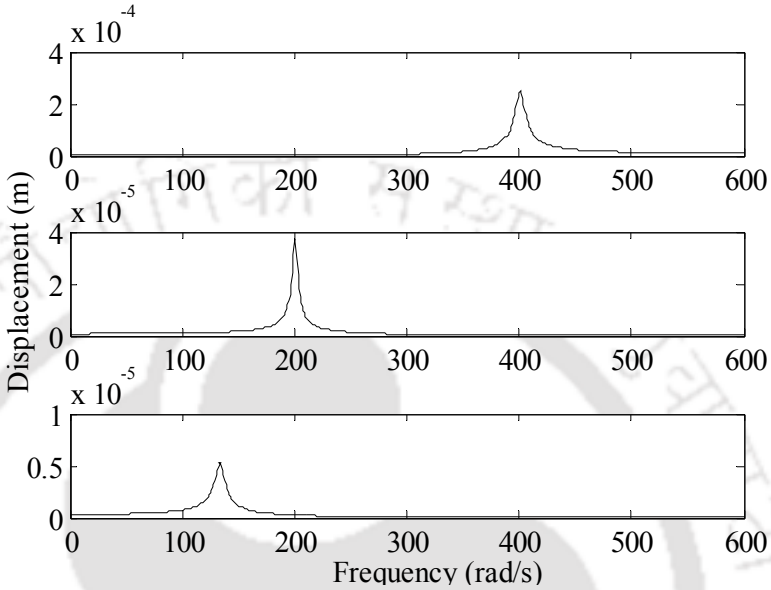


Figure 4.9 Plot to show resonance in the response of (a) once per revolution (b) twice per revolution and (c) thrice per revolution crack force harmonics for a Laval rotor with the unbalance

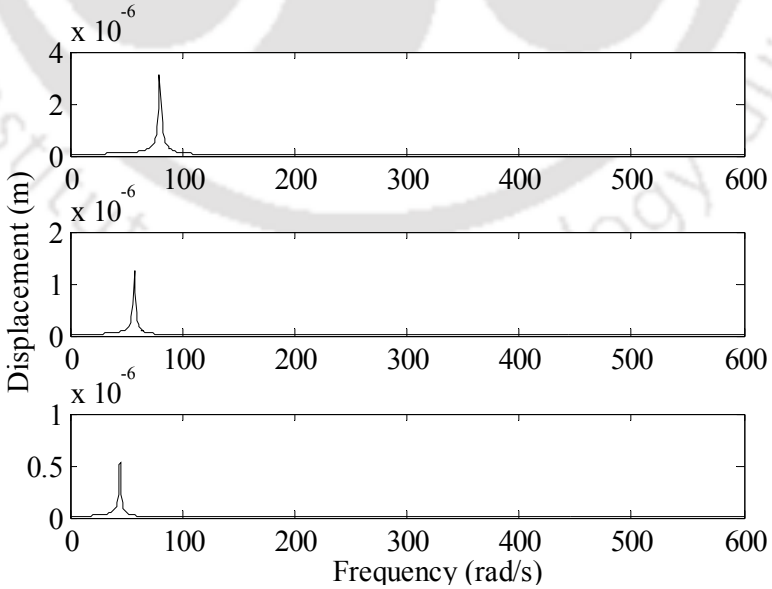


Figure 4.10 Plot to show the resonance in response of (a) five per revolution (b) seven per revolution and (c) nine per revolution crack force harmonics for a Laval rotor with unbalance

It was earlier noted that $p_i$'s corresponding to the fifth and higher harmonics are negligible. So, frequency ranges are selected such that it encompasses resonances of once, twice and thrice per revolution excitation components. To avoid measurement error near critical speeds often measurement outside the half-power frequency band is advisable as discussed in Section 3.3.1.

From these considerations, the range of frequencies is selected from 30 rad/s to 132.3 rad/s (i.e., up to the lower limit of the half-power point of thrice per revolution component as Case A. This also includes resonances of five, seven and nine per revolution components); from the upper limit of half-power point of thrice per revolution excitation to that of lower limit of the twice per revolution excitation (i.e., from 133.6 rad/s to 198.4 rad/s as Case B); from the upper limit of half-power point of twice per revolution excitation to that of lower limit of the once per revolution excitation (i.e., from 202.4 rad/s to 396.9 rad/s as Case C) and above the upper limit of half-power point of once per revolution excitation (i.e., above 405 rad/s as Case D).The general identification algorithm (Eqn.(4.17)) contains harmonics varying from -$n$ to $n$. Now, a particular number of harmonics can be chosen for each response range by making use of response plots with resonances. In a given speed range, harmonic components until the magnitude of $10^{-8}$ m (Refer Figure 4.9 and Figure 4.10) are chosen and lower magnitudes are neglected.

The estimates particularly crack forces were poor for higher harmonics. Higher harmonics magnitude is very low of the order of $10^{-9}$ m. The estimates could be poor because of noise effect on higher harmonics. But, in the case of estimates from time responses, the noise effect could be less because of more averaging. Also, the sampling time can determine the maximum frequency and harmonic in a full-spectrum plot. For example, a sampling time of 0.001s gives a sampling rate of 1000 Hz and a maximum full-spectrum frequency of 500 Hz. So, the harmonics were chosen

such that very low magnitudes of the order of $10^{-9}$ are not chosen and also the frequency value of harmonic, say, 7× will be less than that of the bandwidth frequency. Different measurement cases, their corresponding range of frequencies, and the number of harmonics considered in each case are summarised in Table 4-8.

The estimation is done at multiple rotor speeds as mentioned in Eqn. (4.20). A set of frequencies at intervals of 1 rad/s in a given frequency range is taken as a response set, and further used for the estimation of rotor system parameters. For accommodating estimation with a set of multiple rotor speeds (say *q* rotor speeds), the regression Eqn. (4.20) is used.

Table 4-8 Different speed range and harmonics considered for estimation

| Cases | Range of frequencies(rad/s) | Harmonics (*i*)considered for algorithm |
|---|---|---|
| Case A | 30 to 132.3 | -7, -5, -3, -1, 0,1, 2, 3, 5, 7 |
| Case B | 133.6 to 198.4 | -5, -3, -1, 0, 1, 2, 3, 5 |
| Case C | 202.4 to 396.9 | -3, -1, 0, 1, 2, 3 |
| Case D | 405 to 600 | -3, -1, 0, 1, 2, 3 |

*Obtaining force coefficients and displacement coefficients*: Full-spectrum responses (Eqn.(4.1) and Eqn.(4.2)) give Fourier coefficients of the crack force and the system response, which are further used as an input to *identification algorithm* in frequency domain (Eqn. (4.17) and Eqn. (4.19)). The variation of crack force (*i.e.*, $\frac{1}{2}s(t)\left(1+e^{2j\omega t}\right)$) along the *x* and *y* directions is shown in Figure 4.11.

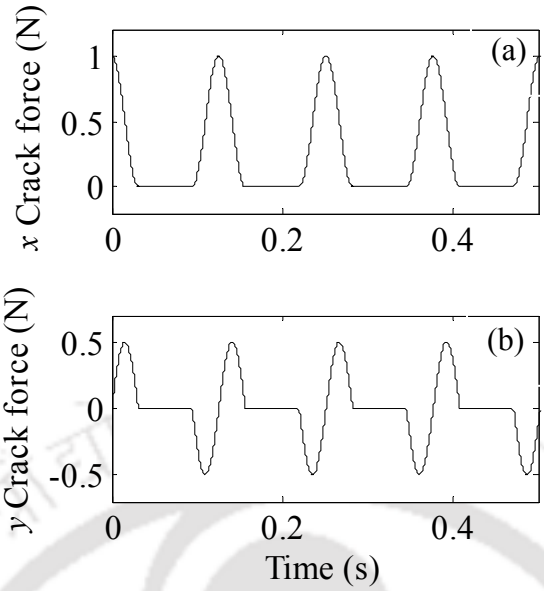


Figure 4.11 Variation of the crack force along (a) $x$ direction and (b) $y$ direction

The *full-spectrum plot* of crack force coefficients $p_i$ along ordinate is shown in Figure 4.12 for a spin speed of 50 rad/s. The coefficients are obtained using the full-spectrum equations which are described in Eqn. (4.17) and Eqn. (4.19). For any general forcing function of crack and its response, their $p_i$ and $r_i$ are complex. A switching function, being bi-linear its $p_i$'s are real.

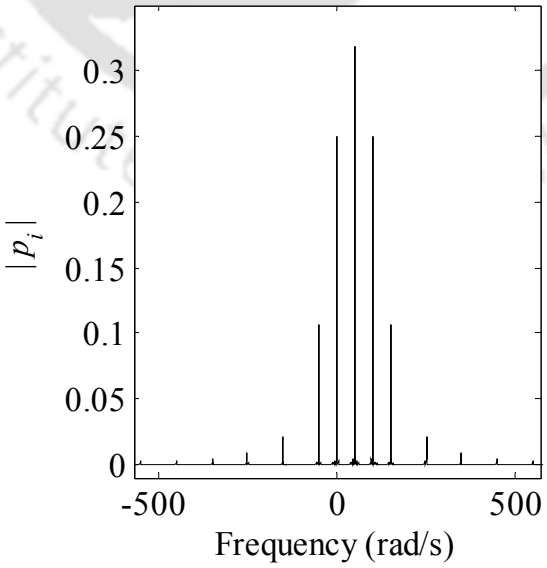


Figure 4.12 A full-spectrum plot showing force coefficients $p_i$'s

Table 4-9 Values of $p_i$ corresponding to full-spectrum coefficients of crack force

| $i$ | $p_i$ | $i$ | $p_i$ | $i$ | $p_i$ | $i$ | $p_i$ |
|---|---|---|---|---|---|---|---|
| 1 | 0.3183 | 0 | 0.2500 | 15 | 0.0016 | -15 | -0.0012 |
| 2 | 0.2500 | -1 | 0.1061 | 17 | -0.0013 | -17 | 0.0009 |
| 3 | 0.1061 | -3 | -0.0212 | 19 | 0.0009 | -19 | -0.0008 |
| 5 | -0.0212 | -5 | 0.0091 | 21 | -0.0008 | -21 | 0.0007 |
| 7 | 0.0091 | -7 | -0.0051 | 23 | 0.0007 | -23 | -0.0006 |
| 9 | -0.0051 | -9 | 0.0032 | 25 | -0.0006 | -25 | 0.0005 |
| 11 | 0.0032 | -11 | -0.0022 | 27 | 0.0005 | -27 | -0.0004 |
| 13 | -0.0022 | -13 | 0.0016 | 29 | -0.0004 | -29 | 0.0003 |

The various harmonics of a square wave, representing the switching crack and their corresponding coefficients are obtained from the full-spectrum (Figure 4.15) and are provided in Table 4-9. In a similar way, the full-spectrum of displacements of the cracked rotor is also obtained. It provides *displacement coefficients* $r_i$'s. The full-spectrum plot is shown in Figure 4.13. The magnitude of $p_i$'s corresponding to full-spectrum coefficients of crack force is shown in Table 4.9. The magnitudes corresponding to higher harmonics are very less of the order of $10^{-3}$. Hence, the range of harmonics chosen for testing algorithm correspond to +7× with a magnitude of 0.0091 and -7× with a magnitude of -0.0051.

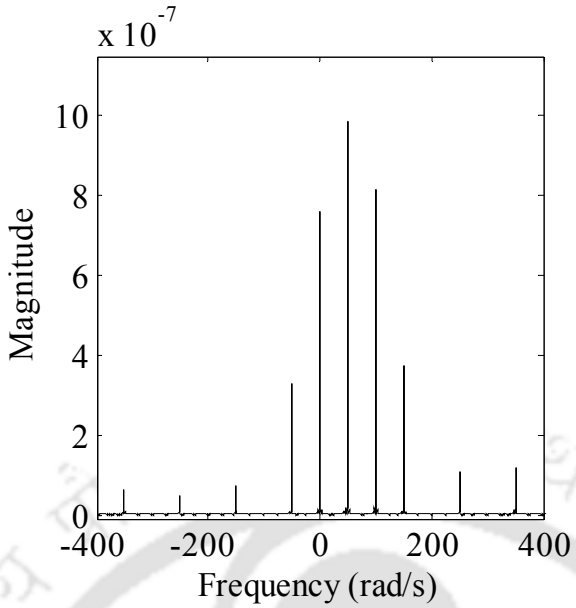


Figure 4.13 A full-spectrum plot showing displacement coefficients $r_i$'s

Full-spectrum coefficients $p_i$'s and $r_i$'s are obtained at multiple measurement speeds and used as an input for the crack identification. The estimates obtained using different set of rotor speeds are discussed. For response of Case A, displacements are used in the identification algorithm and estimates are obtained. These are obtained for a variety of noise levels of 1, 2, and 5 percentages in responses as summarized in Table 4-10. The estimates are observed to conform well to the assumed parameters. The maximum percentage error in estimates of damping is 1.4% for 5% noise level; for additive crack stiffness it is 2.6% at 5% noise level, and there is hardly any error in the estimates of disc eccentricity up to chosen accuracy even at 5% noise level.

Table 4-10 Estimates of parameters in the measurement speed range of 0 to 130 rad/s

| Parameter | $c$ (N-s/m) | | | | $e$ ($\times 10^6$ m) | | | | $\Delta k_{22}$($\times 10^{-4}$ N/m) | | | |
|---|---|---|---|---|---|---|---|---|---|---|---|---|
| Assumed values | 16.03 | | | | 0.1 | | | | 1.61 | | | |
| Noise Level % | 0 | 1 | 2 | 5 | 0 | 1 | 2 | 5 | 0 | 1 | 2 | 5 |
| Estimates from CF response | 16.03 | 16.07 | 16.12 | 16.25 | 0.099 | 0.099 | 0.099 | 0.097 | 1.61 | 1.60 | 1.59 | 1.57 |
| Estimates from TI response | 16.17 | 16.18 | 16.18 | 16.18 | 0.100 | 0.100 | 0.099 | 0.098 | 1.61 | 1.60 | 1.59 | 1.57 |

*(CF – Estimates from *closed-form* responses; TI- Estimates from *time-integrated* responses)

For cases B, C, and D also the estimates are obtained for noise levels of 1, 2, and 5 percentages. The estimates of 2% and 5% noise are summarized in Table 4-11. The maximum percentage error in the damping estimates is 0.9% for case B, 5.3% for case C, and 2.2% for case D. The maximum percentage error in the damping eccentricity is around 10% for cases B, C, and D for 5% noise level. The maximum percentage error in the additive crack stiffness is 3.2% for case B, 3.1% for case C, and 4.3% for case D.

### 4.4.2 Simultaneous Estimation of Damping, Eccentricity, and Crack Forces in Frequency Domain

The identification algorithm for the estimation of force terms of a switching crack is presented in the regression equation Eqn. (4.19). The regression matrix is ill-conditioned because of sparse non-zero elements. In order to improve the accuracy of the estimates, the regression equation (Eqn. (4.21)) is used.

For Case A, estimates are also obtained for different noise levels of 1, 2 and 5 percentages. The estimates from time integrated responses are also presented in Table 4-12. In order to check the accuracy of crack forces, the open/closing profile of switching crack is plotted with the assumed and estimated crack force terms at a particular spin speed and compared in Figure 4.14. The comparison is shown for the 2% and 5% noise levels for responses in both the horizontal and vertical directions. It is seen that the estimated crack force conforms very well to assumed forces.

Table 4-11 Estimates of parameters for measurement cases B, C, and D with 2% and 5% noise in response

| Measurement speed range | | | 135 to 190 rad/s at 1 rad/s interval | | 210 to 390 rad/s at 1 rad/s interval | | 410 to 600 rad/s at 1 rad/s interval | |
|---|---|---|---|---|---|---|---|---|
| Parameters | Assumed value | Noise level in % | 2% | 5% | 2% | 5% | 2% | 5% |
| $c$ (N-s/m) | 16.03 | CF* | 16.00 | 15.99 | 15.70 | 15.18 | 15.95 | 15.78 |
| | | TI | 16.18 | 16.17 | 16.41 | 16.42 | 16.37 | 16.38 |
| $e$ ($\times 10^6$ m) | 0.10 | CF | 0.093 | 0.091 | 0.097 | 0.095 | 0.101 | 0.112 |
| | | TI | 0.099 | 0.097 | 0.099 | 0.099 | 0.099 | 0.097 |
| $\Delta k_{22}$ ($\times 10^{-4}$ N/m) | 1.61 | CF | 1.59 | 1.56 | 1.59 | 1.56 | 1.58 | 1.54 |
| | | TI | 1.59 | 1.57 | 1.59 | 1.57 | 1.59 | 1.57 |

*(CF – Estimates from *closed-form* responses; TI- Estimates from *time-integrated* responses)

Table 4-12 Simultaneous estimation of damping, eccentricity, and crack force parameters in the measurement speed range 0 to 130 rad/s with different noise levels in responses

| Parameters | Assumed values | Noise level in % | | | | | | | |
|---|---|---|---|---|---|---|---|---|---|
| | | 0% | | 1% | | 2% | | 5% | |
| | | CF* | TI | CF | TI | CF | TI | CF | TI |
| $c$ (N-s/m) | 16.03 | 16.03 | 16.18 | 16.07 | 16.18 | 16.12 | 16.18 | 16.24 | 16.18 |
| $e$ ($\times 10^6$ m) | 0.100 | 0.100 | 0.099 | 0.100 | 0.099 | 0.099 | 0.099 | 0.097 | 0.097 |
| $\Delta k_{22}p_1$ (N/m) | 5114.4 | 5114.6 | 5115.0 | 5083.8 | 5089.6 | 5052.9 | 5064.1 | 4960.3 | 4987.7 |
| $\Delta k_{22}p_2$ (N/m) | 4017.0 | 4017.0 | 4017.2 | 3993.0 | 3997.2 | 3969.0 | 3977.2 | 3896.9 | 3917.3 |
| $\Delta k_{22}p_3$ (N/m) | 1704.8 | 1704.9 | 1704.7 | 1695.4 | 1696.2 | 1685.7 | 1687.8 | 1656.5 | 1662.3 |
| $\Delta k_{22}p_5$ (N/m) | -341.0 | -341.0 | -342.1 | -337.9 | -340.4 | -334.6 | -338.7 | -324.9 | -333.6 |
| $\Delta k_{22}p_7$ (N/m) | 146.1 | 146.2 | 146.2 | 144.0 | 145.3 | 141.7 | 144.5 | 135.0 | 142.0 |
| $\Delta k_{22}p_0$ (N/m) | 4017.0 | 4017.0 | 4016.9 | 3995.4 | 3996.9 | 3973.7 | 3976.9 | 3908.8 | 3917.0 |
| $\Delta k_{22}p_{-7}$ (N/m) | -81.1 | -81.2 | -81.4 | -80.5 | -81.09 | -81.7 | -80.8 | -95.00 | -80.0 |
| $\Delta k_{22}p_{-5}$ (N/m) | 146.1 | 146.2 | 146.7 | 138.8 | 145.9 | 139.1 | 145.2 | 104.5 | 142.9 |
| $\Delta k_{22}p_{-3}$ (N/m) | -341.0 | -341.0 | -340.6 | -337.93 | -338.9 | -334.8 | -337.2 | -325.5 | -332.2 |
| $\Delta k_{22}p_{-1}$ (N/m) | 1704.8 | 1704.9 | 1704.8 | 1696.5 | 1696.4 | 1688.1 | 1688.0 | 1662.9 | 1662.7 |

*(CF – Estimates from *closed-form* responses; TI- Estimates from *time-integrated* responses)

Table 4-13 Simultaneous estimation of damping, eccentricity and crack force parameters in the measurement speed range 135 to 190 rad/s (Case B) with different noise levels in response

| Parameters | Assumed values | Noise level in % | | | | | | | |
|---|---|---|---|---|---|---|---|---|---|
| | | 0% | | 1% | | 2% | | 5% | |
| | | CF* | TI | CF | TI | CF | TI | CF | TI |
| $c$ (N-s/m) | 16.03 | 16.03 | 16.18 | 16.02 | 16.40 | 16.00 | 16.18 | 15.94 | 16.17 |
| $e$ ($\times 10^6$ m) | 0.100 | 0.100 | 0.100 | 0.097 | 0.100 | 0.093 | 0.099 | 0.091 | 0.097 |
| $\Delta k_{22}p_1$ (N/m) | 5114.4 | 5114.6 | 5115.3 | 5094.1 | 5090.7 | 5073.6 | 5064.1 | 5012.1 | 4987.2 |
| $\Delta k_{22}p_2$ (N/m) | 4017.0 | 4017.0 | 4017.9 | 3994.8 | 3999.8 | 3972.5 | 3977.9 | 3906.3 | 3917.8 |
| $\Delta k_{22}p_3$ (N/m) | 1704.8 | 1704.9 | 1706.0 | 1696.4 | 1693.9 | 1687.8 | 1688.9 | 1661.9 | 1663.1 |
| $\Delta k_{22}p_5$ (N/m) | -341.0 | -341.0 | -342.9 | -343.0 | -342.9 | -344.9 | -338.9 | -350.7 | -332.9 |
| $\Delta k_{22}p_0$ (N/m) | 146.1 | 4017.0 | 4017.0 | 3993.7 | 3996.3 | 3970.4 | 3977.0 | 3900.5 | 3917.3 |
| $\Delta k_{22}p_{-5}$ (N/m) | 4017.0 | 146.2 | 146.6 | 124.4 | 146.4 | 110.0 | 146.2 | 117.4 | 145.5 |
| $\Delta k_{22}p_{-3}$ (N/m) | -81.1 | -341.0 | -342.3 | -344.5 | -340.4 | -348.0 | -338.5 | -358.5 | -332.9 |
| $\Delta k_{22}p_{-1}$ (N/m) | 146.1 | 1704.9 | 1704.6 | 1697.4 | 1696.0 | 1689.9 | 1687.4 | 1667.9 | 1661.6 |

*(CF – Estimates from *closed-form* responses; TI- Estimates from *time-integrated* responses)

Table 4-14 Simultaneous estimation of damping, eccentricity, and crack force parameters for measurement cases C and D with 2% and 5% noise levels in response

| Measurement speed range | | 210 to 390 rad/s | | | | 410 to 600 rad/s | | | |
|---|---|---|---|---|---|---|---|---|---|
| Parameters | Assumed values | Noise level in % | | | | | | | |
| | | 2% | | 5% | | 2% | | 5% | |
| | | CF | TI | CF | TI | CF | TI | CF | TI |
| $c$ (N-s/m) | 16.03 | 15.70 | 16.41 | 15.18 | 16.42 | 15.95 | 16.37 | 15.78 | 16.38 |
| $e$ ($\times 10^6$ m) | 0.100 | 0.097 | 0.099 | 0.095 | 0.099 | 0.103 | 0.099 | 0.112 | 0.097 |
| $\Delta k_{22}p_1$(N/m) | 5114.4 | 5059.3 | 5064.9 | 4977.5 | 4988.0 | 5080.7 | 5089.2 | 5081.7 | 5012.3 |
| $\Delta k_{22}p_2$(N/m) | 4017.0 | 3971.2 | 3979.6 | 3902.9 | 3918.9 | 3945.6 | 3978.9 | 3839.0 | 3918.9 |
| $\Delta k_{22}p_3$(N/m) | 1704.8 | 1699.7 | 1684.4 | 1691.7 | 1656.9 | 1664.7 | 1697.9 | 1604.3 | 1681.3 |
| $\Delta k_{22}p_0$(N/m) | -341.0 | 3966.7 | 3976.3 | 3895.4 | 3916.3 | 3976.8 | 3975.3 | 3916.6 | 3914.7 |
| $\Delta k_{22}p_{-3}$ (N/m) | 146.1 | -351.8 | -343.2 | -366.9 | -344.3 | -271.9 | -321.2 | -311.2 | -302.4 |
| $\Delta k_{22}p_{-1}$ (N/m) | 4017.0 | 1685.1 | 1685.4 | 1655.5 | 1660.0 | 1683.3 | 1694.2 | 1648.0 | 1668.6 |

*(CF – Estimates from *closed-form* responses; TI- Estimates from *time-integrated* responses)

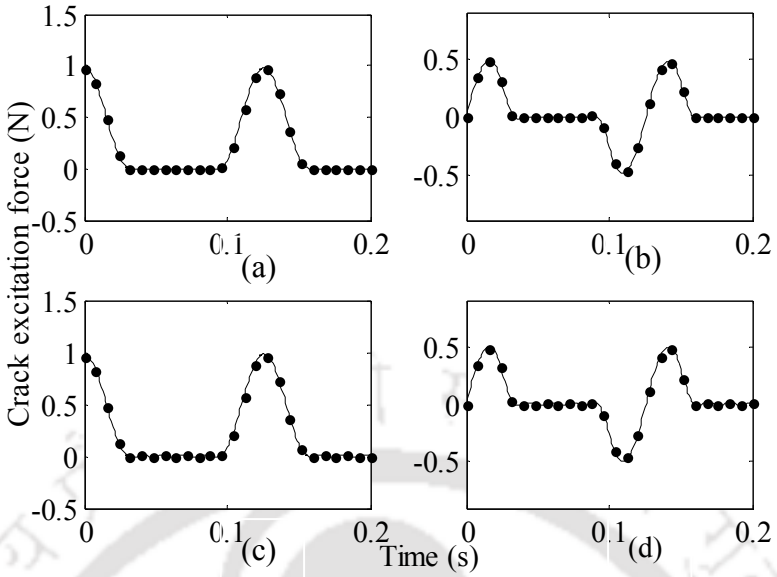


Figure 4.14 Comparison of the periodic crack force obtained using assumed and estimated data at 50 rad/s (a) With 2% noise in *x* response (b) With 2% noise in *y* response (c) With 5% noise in *x* response (d) With 5% noise in *y* response; —— Assumed and ●●●●●● Estimated

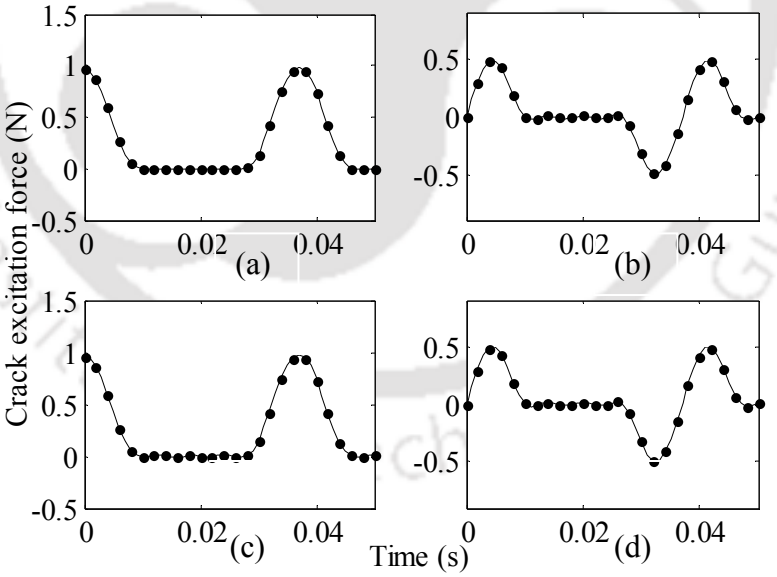


Figure 4.15 Comparison of the periodic crack force obtained using assumed and estimated data at 170 rad/s (a) With 2% noise in *x* response (b) With 2% noise in *y* response (c) With 5% noise in *x* response (d) With 5% noise in *y* response; —— Assumed and ●●●●●● Estimated

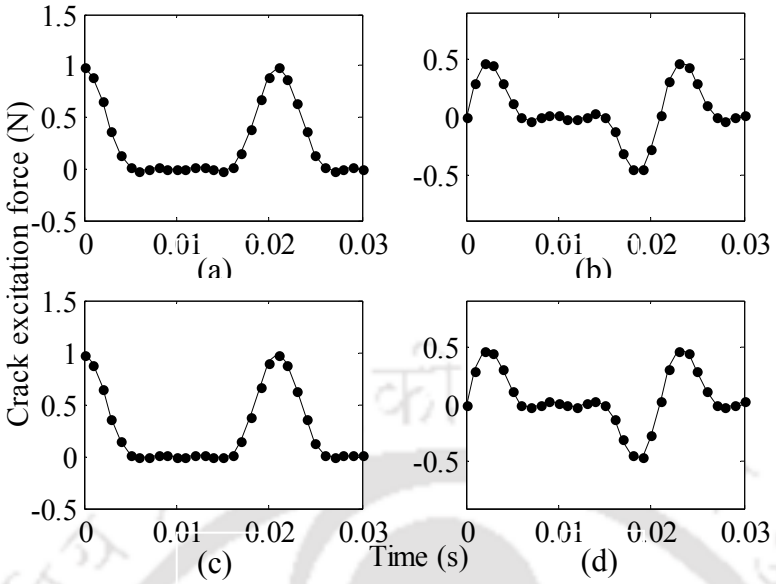


Figure 4.16 Comparison of the periodic crack force obtained using assumed and estimated data at 300 rad/s (a) With 2% noise in *x* response (b) With 2% noise in *y* response (c) With 5% noise in *x* response (d) With 5% noise in *y* response; —— Assumed and ●●●●● Estimated

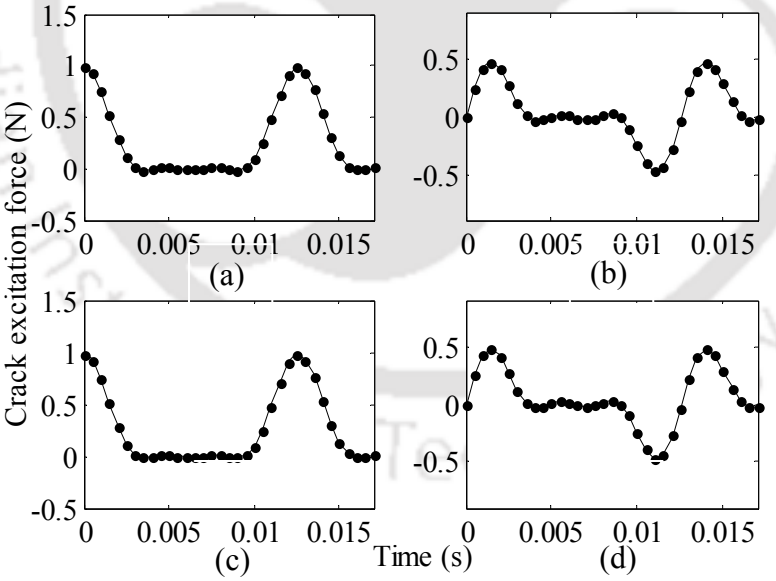


Figure 4.17 Comparison of the periodic crack force obtained using assumed and estimated data at 50 rad/s (a) With 2% noise in *x* response (b) With 2% noise in *y* response (c) With 5% noise in *x* response (d) With 5% noise in *y* response; —— Assumed and ●●●●● Estimated

For Cases B, C, and D, the estimates are similarly obtained for the 1, 2 and 5 percentage noise levels. The estimates at 5% noise for Case B, and Cases C and D are presented in Table 4-13 and Table 4-14, respectively. Figure 4.15 shows the comparison of assumed and estimated crack forces at 170 rad/s for the 2% and 5% noise levels. Similar comparisons are made for Cases C and D at spin speeds of 300 rad/s and 500 rad/s for 2% and 5% noise levels as shown in Figure 4.16 and Figure 4.17, respectively. From these figures, it is seen that the estimated crack forces conform well to the assumed ones.

In previous sections, identification algorithms have been developed using regression techniques and estimates of least-square method are obtained. The comparison of estimates with assumed parameters shows robustness of developed algorithms. The algorithms are general for any crack open/closing function, and have flexibility to handle required number of harmonics of crack force and responses. The use of full-spectrum data directly as input to the algorithms, has the advantage that the algorithms can be used for rotor responses with *reverse whirl* conditions as well. As already observed, the identification in frequency domain greatly reduces amount of data stored and handled for the identification.

Now, a comparison of the time domain and frequency domain estimates is observed.

**4.5 Comparison of Estimates from Time Domain and Frequency Domain Identification**

The estimates obtained from identification using frequency responses are presented in the previous section (Table 4-12 to Table 4-14). Similar estimates were obtained using identification algorithms based on time responses (Table 3-2 to Table 3-5)

Table 4-15 Comparison of damping, eccentricity, and crack stiffness identified using time-domain and frequency domain responses

| Spin-speed range | | Assumed values | 135 to 190 rad/s Frequency domain identification | Percentage error with assumed values | Assumed values | 135 to 190 rad/s Time domain identification | Percentage error with assumed values |
|---|---|---|---|---|---|---|---|
| $c$ (N-s/m) | CF* | 16.03 | 15.99 | 0.25 | 16.03 | 16.05 | 0.12 |
| | TI | | 16.17 | 0.87 | | 16.14 | 0.69 |
| $e$ ($\times 10^{6}$ m) | CF | 0.10 | 0.091 | 9.00 | 5.00 | 4.92 | 1.60 |
| | TI | | 0.097 | 3.00 | | 4.91 | 1.80 |
| $\Delta k_{22}$ ($\times 10^{-4}$ N/m) | CF | 1.61 | 1.56 | 3.10 | 1.61 | 1.55 | 3.73 |
| | TI | | 1.57 | 2.48 | | 1.55 | 3.73 |

*(CF – Estimates from *closed-form* responses; TI- Estimates from *time-integrated* responses)

Table 4-16 Comparison of crack force terms identified using time-domain and frequency domain responses

| Parameters | Assumed values (Frequency domain identification) | Parameter estimates 5% | | % error with assumed values | | Assumed values (Time domain identification) | Parameter estimates 5% | | % error with assumed values | |
|---|---|---|---|---|---|---|---|---|---|---|
| | | CF | TI | CF | TI | | CF | TI | CF | TI |
| $c$ (N-s/m) | 16.03 | 16.24 | 16.18 | 1.31 | 0.94 | 16.03 | 15.94 | 15.96 | 0.56 | 0.44 |
| $e$ ($\times 10^6$m) | 0.100 | 0.097 | 0.097 | 3.00 | 3.00 | 5.00 | 5.11 | 5.11 | 2.20 | 2.2 |
| $\Delta k_{22}p_1$(N/m) | 5114.4 | 4960.3 | 4987.7 | 3.01 | 2.47 | 5125.7 | 4912.1 | 4913.4 | 4.17 | 4.14 |
| $\Delta k_{22}p_2$(N/m) | 4017.0 | 3896.9 | 3917.3 | 2.99 | 2.48 | 4017.0 | 3883.6 | 3883.8 | 3.32 | 3.32 |
| $\Delta k_{22}p_3$(N/m) | 1704.8 | 1656.5 | 1662.3 | 2.83 | 2.49 | 1703.2 | 1642.9 | 1642.0 | 3.54 | 3.59 |
| $\Delta k_{22}p_5$(N/m) | -341.0 | -324.9 | -333.6 | 4.72 | 2.17 | -337.4 | -326.4 | -327.1 | 3.26 | 3.05 |
| $\Delta k_{22}p_0$ (N/m) | 4017 | 3908.8 | 3917.0 | 2.69 | 2.49 | 4017 | 4012.2 | 4012.2 | 0.12 | 0.12 |
| $\Delta k_{22}p_{-5}$(N/m) | 146.1 | 104.5 | 142.9 | 28.47 | 2.19 | 514.2 | 498.2 | 498.3 | 3.11 | 3.09 |
| $\Delta k_{22}p_{-3}$(N/m) | -341 | -325.5 | -332.2 | 4.54 | 2.58 | -337.4 | -327.2 | -327.0 | 3.02 | 3.08 |
| $\Delta k_{22}p_{-1}$(N/m) | 1704.8 | 1662.9 | 1662.7 | 2.46 | 2.47 | 1703.2 | 1647.9 | 1648.3 | 3.24 | 3.22 |

*(CF – Estimates from *closed-form* responses; TI- Estimates from *time-integrated* responses)

For comparison, the estimates from time domain identification and those from frequency domain identification are used and their percentage errors with assumed parameters are observed. The estimates are compared in the measurement speed range of 135 rad/s to 190 rad/s, which is near the critical speed due to twice per revolution frequency component of crack force. The case of 5% response noise is chosen for comparison. It can be noted from the above comparisons that the estimates of crack stiffness and crack force terms have less percentage error, for the case of full-spectrum based identification, using time integrated responses. Also, the number of steps for identification is reduced in identification algorithms using full-spectrum responses. The Figure 4.18 shows percentage error for estimates obtained for different cases of measurement speed ranges. Here, the number in the abscissa represents the estimated parameter corresponding to the same row number in vector $\{X\}$ in Eqn. (4.22).

$$X = \{c \quad e \quad \Delta k_{22} \quad \Delta k_{22}p_1 \quad \Delta k_{22}p_2 \quad \Delta k_{22}p_3 \quad \Delta k_{22}p_5 \quad \Delta k_{22}p_7 \quad \Delta k_{22}p_0 \quad \Delta k_{22}p_{-7} \quad \Delta k_{22}p_{-5} \quad \Delta k_{22}p_{-3} \; \Delta k_{22}p_{-1}\}^T \tag{4.22}$$

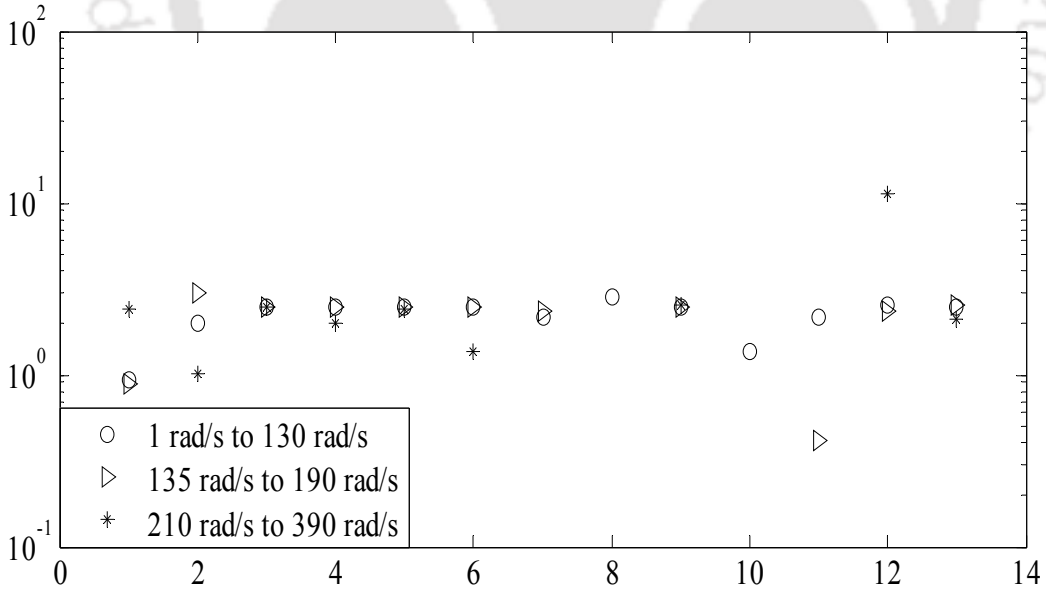


Figure 4.18 Comparison of percentage error of estimates for different cases of measurement speed ranges

## 4.6 Guidelines for Model-Based Crack Identification

The general guidelines for model-identification of crack and other unknown parameters are presented in this section. The steps for identification are as follows:

The ***cracked rotor responses***, namely, displacement versus time responses, and full-spectrum responses are obtained. These responses can be simulated for a chosen data of system and fault parameters. In such a case, it constitutes the direct problem. The responses can also be obtained directly by means of an experimental set up.

The second step is the ***Full-Spectrum analysis***. Here, displacement responses in two orthogonal directions are combined in a complex form and fed as input to the full-spectrum. The *displacement coefficients* $r_{\pm i}$ are obtained from the full-spectrum.

The third step is the ***Identification of switching crack forces***. The input to the identification algorithm consists of displacement coefficients of the previous step discussed above, and known system parameters, such as the mass, intact shaft stiffness, and static deflection of the rotor system. The estimated parameters are the terms of the switching force ($\Delta k_{\zeta} p_{\pm i}$), which constitute the crack forces, together with unbalance eccentricity, and viscous damping. The plot of the switching crack forces, can give the details of opening/closing profile of the fatigue crack in the actual case.

The fourth step is ***Full-Spectrum analysis of crack forces***. From the full-spectrum, the *force coefficients* $p_{\pm i}$ are obtained.

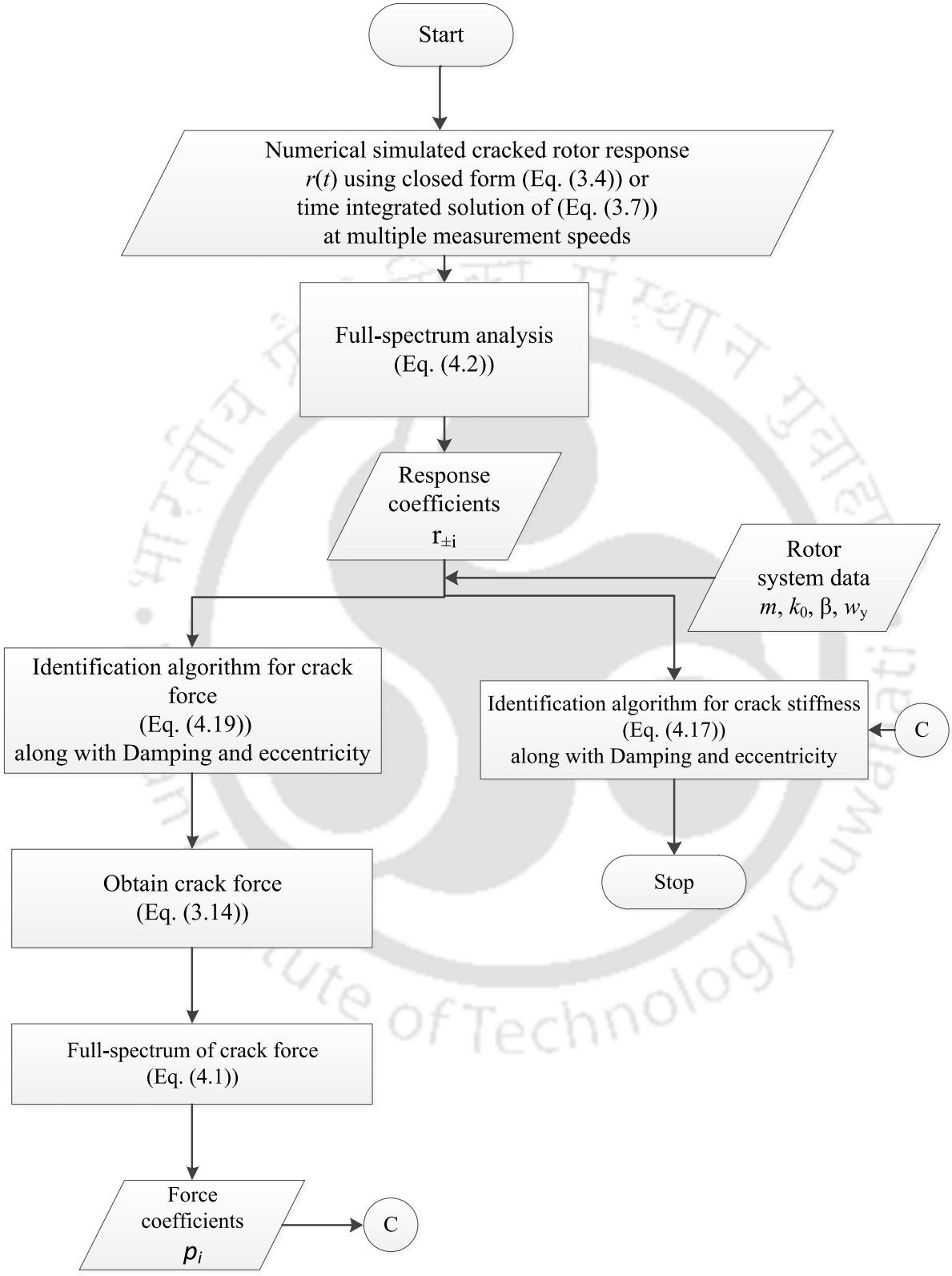


Figure 4.19 A flow-chart showing the steps for fault identification in cracked rotor system

The fifth step is ***Identification of crack stiffness***. Inputs to the identification algorithms include the displacement and force coefficients (from the step two and the step four), along with known system parameters. The unknown fault parameter, *i.e.* additive stiffness due to crack, is estimated for the condition monitoring of crack. In addition, the disc eccentricity and the viscous damping are also estimated.

The details are shown as flow-chart in Figure 4.19.

## 4.7 Concluding Remarks

- This chapter discusses the need of using the full-spectrum signal processing tool in the rotor crack problem. The full-spectrum requires complex displacement responses in time domain as an input. From full-spectrum both the forward and reverse frequency coefficients of crack forcing and responses can be obtained.
- Different methods of obtaining full-spectrum coefficients: i.e., *displacement coefficients* and *force coefficients* are illustrated for a sample data set. The methods include obtaining full-spectrum from complex DFT, FFT, half spectrum of orthogonal signals, and orbit plots. The magnitude and phase angles of coefficients from different methods (except from orbit plots) are obtained and compared to be same.
- Full-spectrum plots have been widely used to identify rotor faults such as rub, preload, misalignment and shaft crack. While a normal spectrum requires only a single input (a time response), a full-spectrum requires inputs from two orthogonal sources (i.e., an orbit response). Thus, full spectrum additionally contains direct information on the ellipticity of orbit and the direction of vibration. The main

advantage of full spectrum is that it also gives information about reverse whirling frequency components.

- The crack force consists of multiple harmonics of the spin-speed. Some of the harmonics excite the rotor in the same sense of rotation; whereas the other harmonics excite the rotor in the reverse sense of rotation. The magnitude and phase information of the reverse frequency components are directly obtained from the full-spectrum. In this aspect, full-spectrum is advantageous over normal spectrum. Also, a number of frequency components can be considered for identification.

- Since, there is no prior knowledge on the crack opening/closing function in a real case of the crack switching, it is preferable to use full-spectrum based identification algorithms, as they can include any required number of harmonics.
- The values of force coefficients of the switching crack function, obtained from full-spectrum have been presented for 30 forward and reverse harmonic components of the crack force.
- Identification algorithms are developed to estimate the fault and unknown system parameters, using full-spectrum coefficients as the input. Identification algorithms are generalised to include multiple harmonic components of the crack force.
- The algorithms are well-conditioned by including measurements at multiple spin speeds. Numerical illustrations are presented. The estimates compare well with the assumed values. Maximum percentage of 5% is observed in the damping andthe crack stiffness whereas the maximum percentage in eccentricity is less than 10%. These estimates show robustness of algorithms even in the presence of measurement noise.

- The estimates from time domain based identification are compared with the estimates from frequency domain based identification. The estimates of crack stiffness and crack force terms have less error in case of full-spectrum based identification with time-integrated responses.
- Identification algorithms are extended to identify switching crack forces. The estimates and the assumed crack forces are compared, and the algorithm is found robust even for the case of measurement noise.
- General guidelines for crack identification in rotor systems is presented based on developed identification algorithms.

# CHAPTER 5

# Identification of Crack in an Offset Laval Rotor

## 5.1 Introduction

In this chapter, the rotor model is extended to a 4-DOF model, which includes both translational and rotational displacement co-ordinates. It consists of a flexible mass less shaft with an offset unbalance disc and a transverse fatigue crack on the shaft. The effect of gyroscopic couple due to the offset disc is considered. As in earlier chapter, the switching crack model along with periodic crack forces is also considered. The EOMs are derived and combined in a complex form, which facilitates the use of full-spectrum tool. The time and frequency response plots with resonances are studied. During development of identification algorithms, *dynamic condensation* method is used to eliminate the rotational degrees of freedom from the system EOMs, which is otherwise difficult to measure in practice. The reduced EOMs are then used to develop identification algorithms to estimate the crack and unknown system parameters. Similarly, the switching crack forces are also estimated. The primary aim of the present chapter is to provide a more general model of the cracked rotor, which can be further extended for finite element models and to illustrate the application of dynamic condensation in conjunction with the crack identification algorithm for reducing the number of measurement.

## 5.2 System Modelling of a 4-DOF Cracked Rotor

This section presents a more general model for a cracked rotor. It is known that a rigid body has 6-DOFs. The torsion and axial motions are not considered in the present model. Thus, 4-DOFs model is sufficient for studying such a rotor motion. The crack is modelled as a flexibility matrix considering its parameters in the direction normal to crack front for the

translational and rotational motions. The crack switching function is included into the model by means of a time varying function. A Laval rotor system with an offset disc and a transverse crack on the shaft is shown inFigure 5.1 (a).

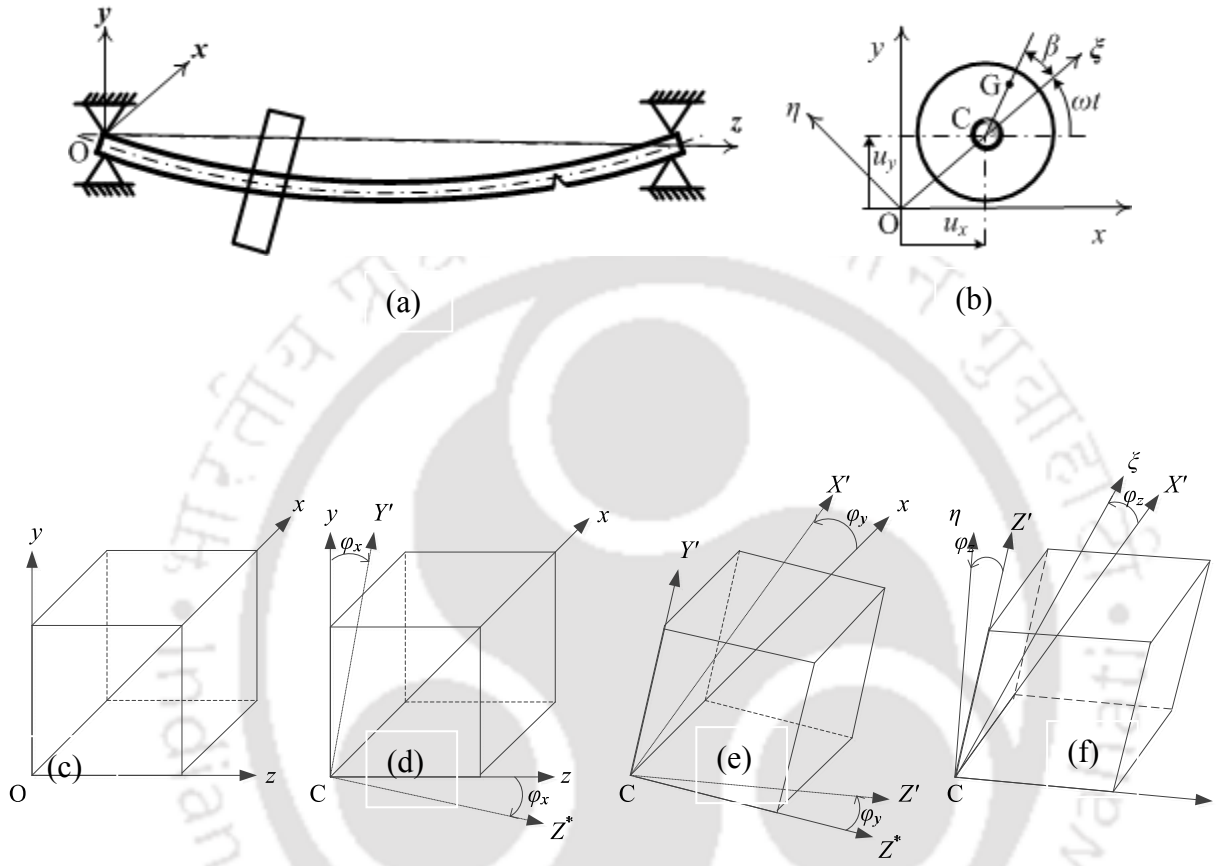


Figure 5.1 (a) A cracked Laval rotor with an offset disc (b) Disc unbalance and shaft crack in the inertial and rotating coordinates (c) Inertial frame of reference at bearing end (d) Transformation from inertial frame $Oxyz$ to rotating frame $CxY'Z^*$, due to rotation $\varphi_x$, (d)Transformation from inertial frame $CxY'Z^*$ to rotational frame $CX'Y'Z'$ due to rotation $\varphi_y$ and (e) Transformation from inertial frame $CX'Y'Z'$ to inertial frame $C\xi\eta Z'$ due to rotation $\varphi_z$

### 5.2.1 General System Equations of Motion

A Laval rotor, with an offset thin disc mounted on a massless elastic shaft, is considered as shown in Figure 5.1(a). O is the origin of co-ordinate system O*xyz* and is defined on the bearing axis, C is the centre of rotation of the disc, and G is the centre of disc unbalance. CG = *e* is the disc

eccentricity of static unbalance. The disc initial tilt which causes a couple unbalance is not considered in the present model.

The disc location being offset, transverse translational displacements ($u_x$ and $u_y$) and transverse rotational displacements ($\varphi_y$ and $\varphi_x$) are considered. A transverse crack is considered on the shaft. The crack axial location parameter is not considered in the model. Transverse rotational displacements are coupled because of gyroscopic effects. Also, shaft elastic couplings are considered between the translational and rotational displacements in the same plane on motion.

The general system EOM of the intact rotor, in the inertial frame of reference, is defined as follows. EOMs of such a rotor system with gyroscopic effects, however, *without crack* are given as (Ishida, 2012),

$$\mathbf{M}'\ddot{\mathbf{q}}+\left(\mathbf{C}'-\omega\mathbf{G}'\right)\dot{\mathbf{q}}+\mathbf{K}'\mathbf{q}=\mathbf{f}'_{st}+\mathbf{f}'_{unb} \tag{5.1}$$

For a 4-DOFs model, the following system matrices and force vectors are defined in the inertial frame of reference as in Eqn. (5.2).In Eqn. (5.2), $\mathbf{M}'$, $\mathbf{C}'$, $\mathbf{G}'$ and $\mathbf{K}'$ are the mass, damping, gyroscopic and stiffness matrices of the rotor system, respectively; $\mathbf{f}'_{unb}$ and $\mathbf{f}'_{st}$ are force vectors due to the unbalance and the static deflection, respectively; $\mathbf{q}$ is the displacement vector, $\mathbf{q}_0=\left\{u_{x0} \quad u_{y0} \quad \varphi_{y_0} \quad \varphi_{x_0}\right\}^T$ corresponds to static transverse displacements, $m$ is the disc mass, $I_d$ is the diametral mass moment of inertia of the disc, $I_p$ is the polar mass moment of inertia of the disc, $c_{ij}$ are the viscous damping in the rotor system, $k_{ij}$ are the shaft stiffness, $e$ is the disc eccentricity, $\beta$ is the phase of the unbalance force, and $\omega$ is the spin speed of rotor.

$$\mathbf{M}'=\begin{bmatrix} m & 0 & 0 & 0 \\ & m & 0 & 0 \\ & & I_d & 0 \\ \text{sym} & & & I_d \end{bmatrix};\quad \mathbf{C}'=\begin{bmatrix} c_{11} & 0 & c_{12} & 0 \\ & c_{11} & 0 & c_{12} \\ & & c_{22} & 0 \\ \text{sym} & & & c_{22} \end{bmatrix};\quad \mathbf{K}'=\begin{bmatrix} k_{11} & 0 & k_{12} & 0 \\ & k_{11} & 0 & k_{12} \\ & & k_{22} & 0 \\ \text{sym} & & & k_{22} \end{bmatrix}$$

$$\mathbf{G}'=\begin{bmatrix} 0 & 0 & 0 & 0 \\ 0 & 0 & 0 & 0 \\ 0 & 0 & 0 & I_p \\ 0 & 0 & -I_p & 0 \end{bmatrix};\quad \mathbf{f}'_{unb}=\begin{Bmatrix} me\omega^2\cos(\omega t+\beta) \\ me\omega^2\sin(\omega t+\beta) \\ 0 \\ 0 \end{Bmatrix};\quad \mathbf{q}=\begin{Bmatrix} u_x \\ u_y \\ \varphi_y \\ \varphi_x \end{Bmatrix};\quad \mathbf{f}'_{st}=\begin{Bmatrix} k_{11}u_{x0} \\ k_{11}u_{y0} \\ k_{22}\varphi_{y_0} \\ k_{22}\varphi_{x_0} \end{Bmatrix} \tag{5.2}$$

The crack introduces a local flexibility matrix $\Delta\mathbf{K}'(u,t)$, which is non-linear in general. The corresponding non-linear system EOMs can be written as,

$$\mathbf{M}'\ddot{\mathbf{q}}+\left(\mathbf{C}'-\omega\mathbf{G}'\right)\dot{\mathbf{q}}+\left(\mathbf{K}'+\Delta\mathbf{K}'(u,t)\right)\mathbf{q}=\mathbf{f}'_{st}+\mathbf{f}'_{unb} \tag{5.3}$$

By the assumption of weight dominance (Refer Section **2.2.2**), the general system EOM (Eqn.(5.3)) is linearised as follows.

$$\mathbf{M}'\ddot{\mathbf{q}}+\left(\mathbf{C}'-\omega\mathbf{G}'\right)\dot{\mathbf{q}}+\mathbf{K}'\mathbf{q}=-\Delta\mathbf{K}'(t)\mathbf{q}_0+\mathbf{f}'_{unb} \tag{5.4}$$

where $\Delta\mathbf{K}'(t)$ is the additional flexibility matrix due to occurrence of crack and $-\Delta\mathbf{K}'(t)\mathbf{q}_0$ is the crack force. The modelling of crack by means of a crack flexibility matrix is elaborated in following sections.

### 5.2.2 Modelling of Crack

During the whirling, an elastic shaft at the disc location deflects (both in transverse translational and rotational displacements). Linear reaction forces and moments onto the shaft are expressed in terms of the shaft translational and rotational displacements at the disc location, with the help of influence coefficients. For an axi-symmetric shaft, the coupling of motions due to elastic forces in the vertical and horizontal planes will not be there. Hence, from elementary strength of materials the forces and moments relate to the transverse translational and rotational displacements. The following relationships hold (Timoshenko and Young, 1968) in the rotating coordinate system $\xi$-O-$\eta$ (refer Figure 5.1), for the case of an *intact shaft*.

$$\begin{Bmatrix} u_{\xi}^{\text{int}} \\ u_{\eta}^{\text{int}} \\ \varphi_{\eta}^{\text{int}} \\ \varphi_{\xi}^{\text{int}} \end{Bmatrix} = \begin{bmatrix} h_{22} & 0 & h_{23} & 0 \\ 0 & h_{22} & 0 & h_{23} \\ h_{32} & 0 & h_{33} & 0 \\ 0 & h_{32} & 0 & h_{33} \end{bmatrix} \begin{Bmatrix} f_{\xi}^{\text{int}} \\ f_{\eta}^{\text{int}} \\ M_{\xi z}^{\text{int}} \\ M_{\eta z}^{\text{int}} \end{Bmatrix} \tag{5.5}$$

with

$$h_{22} = \frac{a^2 b^2}{3EIl}; \quad h_{23} = -\frac{3a^2 l - 2a^3 - al^2}{3EIl}; \quad h_{32} = \frac{ab(b-a)}{3EIl}; \quad h_{33} = -\frac{3al - 3a^2 - l^2}{3EIl}.$$

where $l = a + b$ is the span of the simply supported shaft, $a$ being the distance of disc from the left support; $E$ is the Young's modulus of elasticity, and $I$ is the area moment of inertia. $\left(u_{\xi}^{\text{int}}, u_{\eta}^{\text{int}}\right)$ are transverse translational displacements and $\left(\varphi_{\eta}^{\text{int}}, \varphi_{\xi}^{\text{int}}\right)$ are transverse rotational displacements. Similarly, $\left(f_{\xi}^{\text{int}}, f_{\eta}^{\text{int}}\right)$ are forces and $\left(M_{\xi z}^{\text{int}}, M_{\eta z}^{\text{int}}\right)$ are moments for the case of an intact shaft. $h_{ij}$ is the influence coefficient, which is defined as the displacement in $i^{\text{th}}$ direction due to the force in $j^{\text{th}}$ direction. These influence coefficients are also called flexibility coefficients and the matrix in Eqn. (5.5) is termed as the *flexibility matrix*. With the introduction of a crack on the shaft,

additional flexibility terms add to the flexibility matrix in Eqn. (5.5). The crack flexibility matrix for a general cracked beam element with 4-DOFs has been widely discussed in literature (Papodopoulos and Dimarogonas, 1988; Dharmaraju *et al*., 2004). The *crack flexibility matrix* for a 6-DOF model is also discussed in Eqn. (2.6). In case of a 4-DOF model, the crack flexibility matrix is expressed as,

$$\begin{Bmatrix} u_{\xi}^{cr} \\ u_{\eta}^{cr} \\ \varphi_{\eta}^{cr} \\ \varphi_{\xi}^{cr} \end{Bmatrix} = \begin{bmatrix} \Delta h_{22} & 0 & 0 & 0 \\ 0 & \Delta h_{33} & 0 & 0 \\ 0 & 0 & \Delta h_{44} & \Delta h_{45} \\ 0 & 0 & \Delta h_{54} & \Delta h_{55} \end{bmatrix} \begin{Bmatrix} f_{\xi}^{cr} \\ f_{\eta}^{cr} \\ M_{\xi z}^{cr} \\ M_{\eta z}^{cr} \end{Bmatrix} \tag{5.6}$$

Here, $\left(u_{\xi}^{cr}, u_{\eta}^{cr}\right)$ are transverse translational displacements and $\left(\varphi_{\eta}^{cr}, \varphi_{\xi}^{cr}\right)$ are transverse rotational displacements due to a crack on to the shaft. Similarly, $\left(f_{\xi}^{cr}, f_{\eta}^{cr}\right)$ are forces and $\left(M_{\xi z}^{cr}, M_{\eta z}^{cr}\right)$ are moments due to the crack. The matrix in Eqn. (5.6) is termed as the *crack flexibility matrix*. In this, subscripts 2 and 3 correspond to shearing forces, 4 and 5 correspond to bending moments about two transverse directions. Combination of subscripts corresponds to cross-coupled terms. In the present work, we simplify this flexibility matrix and consider flexibilities only in the direction of crack front.

*Assumptions on crack flexibility matrix*: In the present model only 4-DOFs are considered. Flexibilities, which do not lie in the main direction of crack (i.e., direction perpendicular to the crack front), are negligible; hence, $\Delta h_{33}$ and$\Delta h_{55}$ are assumed to be zero (Gasch, 1993). In addition, neglecting cross coupling terms $\Delta h_{45}$ and $\Delta h_{54}$ (i.e., the coupling of transverse rotational displacements in two orthogonal planes due to the crack is negligibly small). The flexibility matrix due to the crack with the main flexibility terms only in the plane of crack is given as follows

$$\begin{Bmatrix} u_{\xi}^{cr} \\ u_{\eta}^{cr} \\ \varphi_{\eta}^{cr} \\ \varphi_{\xi}^{cr} \end{Bmatrix} = \begin{bmatrix} \Delta h_{22} & 0 & 0 & 0 \\ 0 & 0 & 0 & 0 \\ 0 & 0 & \Delta h_{44} & 0 \\ 0 & 0 & 0 & 0 \end{bmatrix} \begin{Bmatrix} f_{\xi}^{cr} \\ f_{\eta}^{cr} \\ M_{\xi z}^{cr} \\ M_{\eta z}^{cr} \end{Bmatrix} \tag{5.7}$$

These flexibility terms are *time independent*, which represents a fully open state of the crack. In order to define the flexibility matrix of a cracked rotor shaft, matrices in Eqn. (5.5) and Eqn. (5.7) are combined as,

$$\begin{Bmatrix} u_{\xi} \\ u_{\eta} \\ \varphi_{\eta} \\ \varphi_{\xi} \end{Bmatrix} = \left( \begin{bmatrix} h_{22} & 0 & h_{23} & 0 \\ 0 & h_{22} & 0 & h_{23} \\ h_{32} & 0 & h_{33} & 0 \\ 0 & h_{32} & 0 & h_{33} \end{bmatrix} + \begin{bmatrix} \Delta h_{22} & 0 & 0 & 0 \\ 0 & 0 & 0 & 0 \\ 0 & 0 & \Delta h_{44} & 0 \\ 0 & 0 & 0 & 0 \end{bmatrix} \right) \begin{Bmatrix} f_{\xi} \\ f_{\eta} \\ M_{\xi z} \\ M_{\eta z} \end{Bmatrix} \tag{5.8}$$

Here, $\{u_{\xi}\, u_{\eta}\, \varphi_{\eta}\, \varphi_{\xi}\}^{T}$ represents the displacement vector and $\{f_{\xi}\, f_{\eta}\, M_{\xi z}\, M_{\eta z}\}^{T}$ is the force vector corresponding to the combined flexibility matrix (i.e., of the intact shaft as well as of the crack section) in the rotating frame of reference. From Eqn. (5.8), the *matrix inversion* gives the intact shaft stiffness and crack stiffness matrices in the rotating co-ordinate system, $\xi$-O-$\eta$. For convenience of the matrix inversion, displacements are re-arranged into form of $\{u_{\xi}\varphi_{y}u_{\eta}\varphi_{x}\}^{T}$ which splits the 4×4 matrix into two 2×2 square matrix sub-blocks and two 2×2 null matrices. The matrix inversion is shown as follows,

$$\begin{Bmatrix} u_{\xi} \\ \varphi_{\eta} \\ u_{\eta} \\ \varphi_{\xi} \end{Bmatrix} = \left( \begin{bmatrix} \dfrac{1}{\left(h_{22}+\Delta h_{22}\right)\left(h_{33}+\Delta h_{44}\right)-h_{12}^{2}} \begin{bmatrix} h_{33}+\Delta h_{44} & -h_{23} \\ -h_{23} & h_{22}+\Delta h_{22} \end{bmatrix} & \begin{bmatrix} 0 & 0 \\ 0 & 0 \end{bmatrix} \\ \begin{bmatrix} 0 & 0 \\ 0 & 0 \end{bmatrix} & \dfrac{1}{h_{22}h_{33}-h_{23}^{2}} \begin{bmatrix} h_{33} & -h_{23} \\ -h_{23} & h_{22} \end{bmatrix} \end{bmatrix} \right) \begin{Bmatrix} f_{\xi} \\ M_{\xi z} \\ f_{\eta} \\ M_{\eta z} \end{Bmatrix} \tag{5.9}$$

Now, considering $\Delta h_{22}$ and $\Delta h_{44}$ to be small as compared to the intact shaft stiffness (say, of the range of 5% of intact shaft stiffness), $(h_{22}+\Delta h_{22}) \approx h_{22}$ and $(h_{33}+\Delta h_{44}) \approx h_{33}$, thus $1/\left\{\left(h_{22}+\Delta h_{22}\right)\left(h_{33}+\Delta h_{44}\right)-h_{12}^2\right\} \approx 1/\left(h_{22}h_{33}-h_{23}^2\right)$. On simplification of Eqn. (5.9) and on reordering of displacements, we get

$$\begin{Bmatrix} f_\xi \\ f_\eta \\ M_{\xi z} \\ M_{\eta z} \end{Bmatrix} = \frac{1}{h_{22}h_{33}-h_{23}^2} \begin{bmatrix} h_{33}+\Delta h_{44} & 0 & -h_{23} & 0 \\ 0 & h_{33} & 0 & -h_{23} \\ -h_{32} & 0 & h_{22}+\Delta h_{22} & -h_{23} \\ 0 & -h_{23} & 0 & h_{22} \end{bmatrix} \begin{Bmatrix} u_\xi \\ u_\eta \\ \varphi_\eta \\ \varphi_\xi \end{Bmatrix} \tag{5.10}$$

The inverted matrix in Eqn.(5.10) is split as sum of two stiffness matrices; one corresponds to the stiffness matrix of the intact shaft and the other to the additive stiffness matrix due to the crack. Also, the additive stiffness matrix due to the crack is negative. Hence,

$$\begin{Bmatrix} f_\xi \\ f_\eta \\ M_{\xi z} \\ M_{\eta z} \end{Bmatrix} = \left(\mathbf{K}'_{rot} + \mathbf{\Delta K}'_{rot}\right) \begin{Bmatrix} u_\xi \\ u_\eta \\ \varphi_\eta \\ \varphi_\xi \end{Bmatrix} \tag{5.11}$$

with

$$\mathbf{K}'_{rot} = \begin{bmatrix} k_{22} & 0 & k_{23} & 0 \\ 0 & k_{22} & 0 & k_{23} \\ k_{32} & 0 & k_{33} & 0 \\ 0 & k_{32} & 0 & k_{33} \end{bmatrix}; \qquad \mathbf{\Delta K}'_{rot} = -\begin{bmatrix} \Delta k_{22} & 0 & 0 & 0 \\ 0 & 0 & 0 & 0 \\ 0 & 0 & \Delta k_{44} & 0 \\ 0 & 0 & 0 & 0 \end{bmatrix}$$

The matrix corresponding to the intact shaft stiffness is denoted as $\mathbf{K}'_{rot}$ and the additive crack stiffness is denoted as $-\Delta\mathbf{K}'_{rot}$. The intact shaft and additive crack stiffness matrices in rotating frame of reference are time-independent, and are related to flexibility terms as follows.

$$k_{22}=\frac{h_{33}}{H},\quad k_{33}=\frac{h_{22}}{H},\quad k_{23}=k_{32}=-\frac{h_{23}}{H},\quad \Delta k_{22}=-\frac{\Delta h_{44}}{H},\quad \Delta k_{44}=-\frac{\Delta h_{22}}{H} \tag{5.12}$$

with

$$H=h_{22}h_{33}-h_{23}^2$$

The stiffness matrices in Eqn. (5.11) are in the rotating or *rotor fixed coordinate system*. Hence, they need to be transformed into the *inertial coordinate system*. Once transformed, they are substituted for intact shaft stiffness matrix $\mathbf{K}'$ and the crack stiffness matrix $\mathbf{\Delta K}'(t)$ in the system EOMs, Eqn. (5.4).

### 5.3 Transformation of Crack Stiffness Matrix

In Figure 5.1 (c), the co-ordinate system O*xyz* is the inertial frame of reference, with O as the origin defined on the bearing axis and *z* in the direction of the shaft rotation axis. In this frame, transverse translational displacements $u_x$, $u_y$ define the position of the shaft centre C; whereas transverse rotational displacements $\varphi_y$, $\varphi_x$ define the orientation of the disc. C$\xi\eta Z'$ is the rotating frame of reference of the disc in this orientation (Figure 5.1 (f)), with $\xi$ axis perpendicular to the crack front and $Z$ being the rotational axis of disc. The translational displacements $u_\xi$, $u_\eta$ and rotational displacements $\varphi_\xi$, $\varphi_\eta$ are defined in this frame of reference. In order to obtain the displacements $u_x, u_y, \varphi_x, \varphi_y$ from the displacements $u_\xi, u_\eta, \varphi_\xi, \varphi_\eta$. C*xyz* is an inertial frame of reference defined at C (Figure 5.1 (d)), parallel to O*xyz* and obtained by its translation.

Let $CX'Y'Z'$ be the inertial frame defining the disc in its offset position (Figure 5.1 (e)), with $Z'$ being the spin axis of the disc and $X'$, $Y'$ are obtained by rotational transformations due to $\varphi_y$ and $\varphi_x$. $C\xi\eta'Z'$ is its corresponding rotational frame of reference due to rotation $\varphi_z = \omega t$.

Since the displacement co-ordinates of rotating frame of reference is in $C\xi\eta'Z'$ and displacement co-ordinates of inertial frame of reference are in $Oxyz$ frame, a transformation matrix is required between the two frames of reference. The transformation matrix $\mathbf{T}$ is defined between two frames of reference.

*Transformation for translational displacements:*

*Rotation about x axis* ($\varphi_x$): Let the rotation about $x$ axis transforms coordinates of $Cxyz$ frame $(u_X, u_Y, u_Z)$ to coordinates of $CxY'Z^*$ frame $\left(u_x, u_{Y'}, u_{Z^*}\right)$ as shown in Figure 5.1 (d). The rotation matrix $\mathbf{R_x}$ is defined as follows,

$$\begin{Bmatrix} u_x \\ u_{Y'} \\ u_{Z^*} \end{Bmatrix} = \mathbf{R_x} \begin{Bmatrix} u_X \\ u_Y \\ u_Z \end{Bmatrix} \quad \text{with} \quad \mathbf{R_x} = \begin{bmatrix} 1 & 0 & 0 \\ 0 & \cos\varphi_x & \sin\varphi_x \\ 0 & -\sin\varphi_x & \cos\varphi_x \end{bmatrix} \tag{5.13}$$

*Rotation about y axis* ($\varphi_y$): Let the subsequent rotation about $Y'$ axis transforms coordinates of $CxY'Z^*$ frame $\left(u_x, u_{Y'}, u_{Z^*}\right)$ to coordinates of $CX'Y'Z'$ frame $\left(u_{X'}, u_{Y'}, u_{Z'}\right)$ as shown in Figure 5.1 (e). The frame obtained can be termed as whirling frame, but does not rotate with spin speed, $\omega$. The rotation matrix is given as $\mathbf{R_{Y'}}$.

$$\begin{Bmatrix} u_{X'} \\ u_{Y'} \\ u_{Z'} \end{Bmatrix} = \mathbf{R}_{\mathbf{Y}'} \begin{Bmatrix} u_x \\ u_{Y'} \\ u_{Z^*} \end{Bmatrix} \quad \text{with} \quad \mathbf{R}_{\mathbf{Y}'} = \begin{bmatrix} \cos\varphi_y & 0 & -\sin\varphi_y \\ 0 & 1 & 0 \\ -\sin\varphi_y & 0 & \cos\varphi_y \end{bmatrix} \tag{5.14}$$

*Rotation about z axis* ($\varphi_z$): The rotation about $Z'$ axis transforms coordinates of $CX'Y'Z'$ frame $\left(u_{X'}, u_{Y'}, u_{Z'}\right)$ to coordinates of $C\xi\eta Z'$ frame $\left(u_{\xi}, u_{\eta}, u_{Z'}\right)$. The frame obtained can be termed as the *rotating and whirling frame*. The rotation matrix, $\mathbf{R}_{\mathbf{Z}'}$, is defined as follows

$$\begin{Bmatrix} u_{\xi} \\ u_{\eta'} \\ u_{Z'} \end{Bmatrix} = \mathbf{R}_{\mathbf{Z}'} \begin{Bmatrix} u_{X'} \\ u_{Y'} \\ u_{Z'} \end{Bmatrix} \quad \text{with} \quad \mathbf{R}_{\mathbf{Z}'} = \begin{bmatrix} \cos\varphi_z & \sin\varphi_z & 0 \\ -\sin\varphi_z & \cos\varphi_z & 0 \\ 0 & 0 & 0 \end{bmatrix} \tag{5.15}$$

The transformation matrix is obtained a sequence of body fixed spatial rotations. The transformation matrix is then obtained by pre-multiplying the sequence of individual rotation matrices. The *overall transformation* from rotating frame $P\xi\eta Z$ to inertial frame $Oxyz$ is given as follows

$$\begin{Bmatrix} u_{\xi} \\ u_{\eta} \\ u_{Z} \end{Bmatrix} = \begin{Bmatrix} u_x \\ u_y \\ u_z \end{Bmatrix} + \left( \mathbf{R} \begin{Bmatrix} u_X \\ u_Y \\ u_Z \end{Bmatrix} \right) \tag{5.16}$$

with $\mathbf{R} = \mathbf{R}_{\xi}\mathbf{R}_{\mathbf{Z}'}\mathbf{R}_{\mathbf{Y}'}\mathbf{R}_{\mathbf{x}} = \begin{bmatrix} \cos\varphi_z & -\sin\varphi_z & \varphi_y \\ \sin\varphi_z & \cos\varphi_z & -\varphi_x \\ \left(\varphi_x \sin\varphi_z - \varphi_y \cos\varphi_z\right) & \left(\varphi_x \cos\varphi_z - \varphi_y \sin\varphi_z\right) & 1 \end{bmatrix}$

Where $\lfloor x_d \quad y_d \quad z_d \rfloor^T$ define the position of inertial frame *Cxyz* from the origin of reference frame *Oxyz* .Making small angle assumption for all coordinates except $\varphi_z$, where $\varphi_z = \omega t$ , the *overall rotational transformation matrix*, $\mathbf{R}$ , is obtained as given in Eqn.(5.16).

*Transformation of angular velocities*: The transformation of angular velocities in rotating coordinates to angular velocities in inertial coordinates is obtained as the sum of angular velocity vectors acting in three different directions (Genta, 2005), namely, $\dot{\varphi}_x$ about the *x* axis, $\dot{\varphi}_y$ about the *y* axis, and $\dot{\varphi}_z$ about the *z* axis. If corresponding angular velocities in rotational coordinates are $\omega_\xi$, $\omega_\eta$ and $\omega_z$, the transformation is defined as,

$$\begin{Bmatrix} \omega_\xi \\ \omega_\eta \\ \omega_z \end{Bmatrix} = \mathbf{R}_\xi \left( \mathrm{R}_{Z'} \left( \mathrm{R}_{Y'} \left\{ \begin{matrix} \dot{\varphi}_x \\ 0 \\ 0 \end{matrix} \right\} + \left\{ \begin{matrix} 0 \\ \dot{\varphi}_y \\ \end{matrix} \right\} \right) + \left\{ \begin{matrix} 0 \\ 0 \\ \dot{\varphi}_z \end{matrix} \right\} \right) \tag{5.17}$$

Substituting for matrices $\mathbf{R}_{Y'}$, $\mathbf{R}_{Z'}$, and $\mathbf{R}_\xi$, and as the same transformation holds for angular displacements, the following transformation matrix is defined

$$\begin{Bmatrix} \varphi_\xi \\ \varphi_\eta \\ \varphi_z \end{Bmatrix} = \begin{bmatrix} \cos\varphi_z & \sin\varphi_z & 0 \\ -\sin\varphi_z & \cos\varphi_z & 0 \\ 0 & 0 & 1 \end{bmatrix} \begin{Bmatrix} \varphi_x \\ \varphi_y \\ \varphi_z \end{Bmatrix} \tag{5.18}$$

*Overall transformation matrix:* Hence, the overall transformation matrix $\mathbf{T}$ corresponding to generalised coordinates (i.e., *x*, *y*, $\varphi_y$ and $\varphi_x$) is defined as,

$$\begin{Bmatrix} u_x \\ u_y \\ \varphi_y \\ \varphi_x \end{Bmatrix} = \mathbf{T} \begin{Bmatrix} u_\xi \\ u_\eta \\ \varphi_\eta \\ \varphi_\xi \end{Bmatrix} \quad \text{with} \quad \mathbf{T} = \begin{bmatrix} \cos\varphi_z & \sin\varphi_z & 0 & 0 \\ -\sin\varphi_z & \cos\varphi_z & 0 & 0 \\ 0 & 0 & \cos\varphi_z & \sin\varphi_z \\ 0 & 0 & -\sin\varphi_z & \cos\varphi_z \end{bmatrix} \tag{5.19}$$

Now, the intact shaft and additive crack stiffness matrices defined in the rotating co-ordinate system (Eqn. (5.11)) can be transformed to corresponding inertial co-ordinate system using Eqn. (5.19). This is described now in the following section.

## 5.4 Final System Equations of Motion

Using Eqn. (5.11) and Eqn. (5.19), the transformation of additive crack stiffness matrix $\Delta\mathbf{K}'_{rot}$ is obtained as follows with $\varphi_z = \omega t$,

$$\Delta\mathbf{K}'(t) = \mathbf{T}^T \Delta\mathbf{K}'_{rot} \mathbf{T} = -\begin{bmatrix} \Delta k_{22}\cos^2\omega t & \Delta k_{22}\cos\omega t\sin\omega t & 0 & 0 \\ \Delta k_{22}\sin\omega t\cos\omega t & \Delta k_{22}\sin^2\omega t & 0 & 0 \\ 0 & 0 & \Delta k_{44}\cos^2\omega t & \Delta k_{44}\cos\omega t\sin\omega t \\ 0 & 0 & \Delta k_{44}\sin\omega t\cos\omega t & \Delta k_{44}\sin^2\omega t \end{bmatrix} \tag{5.20}$$

The transformation of the intact shaft stiffness matrix gives the same matrix as,

$$\mathbf{K}' = \mathbf{T}^T \mathbf{K}'_{rot} \mathbf{T} = \begin{bmatrix} k_{22} & 0 & k_{23} & 0 \\ 0 & k_{22} & 0 & k_{23} \\ k_{32} & 0 & k_{33} & 0 \\ 0 & k_{32} & 0 & k_{33} \end{bmatrix} \tag{5.21}$$

In contrast to the additive crack stiffness matrix $-\Delta\mathbf{K}'_{rot}$, the stiffness matrix $\Delta\mathbf{K}'$ is time-dependent. Here, the time dependency represents the time variation of stiffness of an open crack

along the inertial co-ordinates $x$ and $\varphi_y$. Whereas, the periodic opening/closing of the crack due to *switching* is introduced into the model by means of a function, $s(t)$. Introducing $s(t)$ thereby,

$$\mathbf{\Delta K}(t) = s(t)\mathbf{\Delta K}'(t) \tag{5.22}$$

On using the crack stiffness matrix $\mathbf{\Delta K}(t)$, with the static deflections ($u_{y0} = 0$ and $\varphi_{x0} = 0$), we get the crack force in Eqn. (5.4) as follows

$$-\mathbf{\Delta K}(t)\mathbf{q}_0 = s(t)\begin{Bmatrix} \left(\Delta k_{22}\cos^2\omega t\right)u_{x_0} \\ \left(\Delta k_{22}\sin\omega t\cos\omega t\right)u_{x_0} \\ \left(\Delta k_{44}\cos^2\omega t\right)\varphi_{y_0} \\ \left(\Delta k_{44}\sin\omega t\cos\omega t\right)\varphi_{y_0} \end{Bmatrix} \tag{5.23}$$

On substituting Eqn. (5.21) and Eqn. (5.23) in Eqn. (5.4), the final system EOM is obtained as,

$$\begin{bmatrix} m & 0 & 0 & 0 \\ & m & 0 & 0 \\ & & I_d & 0 \\ \text{sym} & & & I_d \end{bmatrix}\begin{Bmatrix} \ddot{u}_x \\ \ddot{u}_y \\ \ddot{\varphi}_y \\ \ddot{\varphi}_x \end{Bmatrix} + \left(\begin{bmatrix} c_{11} & 0 & c_{12} & 0 \\ & c_{11} & 0 & c_{12} \\ & & c_{22} & 0 \\ \text{sym} & & & c_{22} \end{bmatrix} - \omega\begin{bmatrix} 0 & 0 & 0 & 0 \\ 0 & 0 & 0 & 0 \\ 0 & 0 & 0 & I_p \\ 0 & 0 & -I_p & 0 \end{bmatrix}\right)\begin{Bmatrix} \dot{u}_x \\ \dot{u}_y \\ \dot{\varphi}_y \\ \dot{\varphi}_x \end{Bmatrix}$$

$$+\begin{bmatrix} k_{22} & 0 & k_{23} & 0 \\ & k_{22} & 0 & k_{23} \\ & & k_{33} & 0 \\ \text{sym} & & & k_{33} \end{bmatrix}\begin{Bmatrix} u_x \\ u_y \\ \varphi_y \\ \varphi_x \end{Bmatrix} = s(t)\begin{Bmatrix} \left(\Delta k_{22}\cos^2\omega t\right)u_{x_0} \\ \left(\Delta k_{22}\sin\omega t\cos\omega t\right)u_{x_0} \\ \left(\Delta k_{44}\cos^2\omega t\right)\varphi_{y_0} \\ \left(\Delta k_{44}\sin\omega t\cos\omega t\right)\varphi_{y_0} \end{Bmatrix} + \begin{Bmatrix} me\omega^2\cos(\omega t+\beta) \\ me\omega^2\sin(\omega t+\beta) \\ 0 \\ 0 \end{Bmatrix} \tag{5.24}$$

The above system EOMs of a 4-DOF cracked rotor system will be used for development of identification algorithm for crack parameters. Before that we shall now obtain time and frequency domain responses for the above model.

### 5.5 Time and Frequency Responses

Now, solutions in time domain for a 4-DOF model of the cracked rotor system given by Eqn. (5.24) are discussed. In the case of a 4-DOF rotor system describing transverse translational ($u_x$ and $u_y$) as well as rotational motion ($\varphi_y$ and $\varphi_x$), its system EOMs were obtained as Eqn. (5.24). Now, a set of complex coordinates can be defined that allows writing (Eq.(5.24)) in a complex form. Complex displacement variables $r$ and $\phi$ are defined as, $r = u_x + \mathrm{j}\, u_y$ and $\phi = \varphi_y + \mathrm{j}\, \varphi_x$. While combining equations in Eqn. (5.24) in the complex form, gyroscopic terms combine as, $\left(-I_p \omega \dot{\varphi}_x\right) + \mathrm{j}\, \left(I_p \omega \dot{\varphi}_y\right) = \mathrm{j}\, I_p \omega \dot{\phi}$. Hence, the final system EOM of a cracked rotor with gyroscopic effects in the inertial co-ordinates is given as follows,

$$\bar{\mathbf{M}}\ddot{\mathbf{v}} + \left(\bar{\mathbf{C}} - \mathrm{j}\omega\bar{\mathbf{G}}\right)\dot{\mathbf{v}} + \bar{\mathbf{K}}\mathbf{v} = \Delta\bar{\mathbf{k}} \sum_{i=-\infty}^{+\infty} p_i e^{\mathrm{j}i\omega t} + \bar{\mathbf{f}}_{unb} \tag{5.25}$$

Here, $\bar{\mathbf{M}} = \begin{bmatrix} m & 0 \\ 0 & I_d \end{bmatrix}$; $\bar{\mathbf{C}} = \begin{bmatrix} c_{11} & c_{12} \\ c_{21} & c_{22} \end{bmatrix}$; $\bar{\mathbf{G}} = \begin{bmatrix} 0 & 0 \\ 0 & -I_p \end{bmatrix}$; $\bar{\mathbf{K}} = \begin{bmatrix} k_{22} & k_{23} \\ k_{32} & k_{33} \end{bmatrix}$;

$\mathbf{v} = \begin{Bmatrix} r \\ \phi \end{Bmatrix}$; $\Delta\bar{\mathbf{k}} = \begin{Bmatrix} \Delta k_{22} u_{x_0} \\ \Delta k_{44} \varphi_{y_0} \end{Bmatrix}$; $\sum_{i=-\infty}^{+\infty} p_i e^{\mathrm{j}i\omega t} = \frac{1}{2} s(t)\left(1 + e^{2\mathrm{j}\omega t}\right)$; $\bar{\mathbf{f}}_{unb} = \begin{Bmatrix} m\omega^2 e e^{\mathrm{j}\beta} \\ 0 \end{Bmatrix}$;

The first and second terms on the RHS are forces due to the crack and the unbalance, respectively. Forces are in the complex form. Crack forces are further generalised as $u_{x_0} \Delta k_{22} \sum_{i=-\infty}^{+\infty} p_i e^{\mathrm{j}i\omega t}$ or

$\varphi_{y_0}\Delta k_{44}\sum_{i=-\infty}^{+\infty} p_i e^{\mathrm{j}i\omega t}$ , where $p_i$ is defined as in Eqn. (2.18). These harmonics can be forward or reverse in the direction (*i.e.*, the sign).

The forced vibration response of the cracked Laval rotor can be studied using the time and frequency response plots. The system EOM (Eqn. (5.25)) are linear and coupled in stiffness and damping matrices, and also due to gyroscopic couples. Complex displacements $r$ and $\phi$ as a function of time can be obtained from particular integrals of the second order differential equation. From Eqn. (5.25), the particular integral due to the crack forcing and the unbalance is given in closed-form as,

$$\mathbf{v}(t)=\sum_{i=-\infty}^{\infty}\mathbf{D}_i p_i \Delta\bar{\mathbf{k}}\, e^{\mathrm{j}i\omega t}+\mathbf{D}_i\bar{\mathbf{f}}_{unb}\, e^{\mathrm{j}\omega t} \tag{5.26}$$

with

$$\mathbf{D}_i=\left[\left(\bar{\mathbf{K}}-(i\omega)^2\bar{\mathbf{M}}\right)+\mathrm{j}(i\omega)\left(\bar{\mathbf{C}}-\mathrm{j}\omega\bar{\mathbf{G}}\right)\right]^{-1}.$$

The displacement with time can be obtained using the above equation. The system EOMs can also be used for framing the EOM in frequency domain, from which the full-spectrum response can be obtained.

Closed-form solutions (Eqns. (2.19) and (5.26)) of 4-DOF and cracked rotor system would be used to compare numerically generated responses and especially during the crack identification. Now, frequency responses are discussed.

The assumed solution for the system EOMs (Eqn.(5.25)) can be written as,

$$\mathbf{v}(t) = \sum_i \bar{\mathbf{v}}_i \; e^{j\lambda_i t} \tag{5.27}$$

where $\lambda_i = i\omega$, and $i$ is defined as explained in the above paragraph. In general $i$ varies from -∞ to ∞ and $\bar{\mathbf{v}}_i$ is a function of frequency. On substituting the assumed solution into the EOM, for a particular harmonic $i$, the frequency domain equation is written as,.

$$\left[\left(-(i\omega)^2 \bar{\mathbf{M}}\right) + \mathrm{j}(i\omega)\left(\bar{\mathbf{C}} - \mathrm{j}\omega\bar{\mathbf{G}}\right) + \bar{\mathbf{K}}\right]\bar{\mathbf{v}}_i = p_i \Delta\bar{\mathbf{k}} + \bar{\mathbf{f}}_{unb} \tag{5.28}$$

The crack force coefficient $p_i$ and the response coefficient $\bar{\mathbf{v}}_i$, are obtained from discrete frequency domain using the *full-spectrum* equations (Eqn. (4.1) and Eqn. (4.2)). Now, the numerical illustrations of the cracked rotor system using time and frequency responses are performed.

### 5.6 Numerical Responses for a 4-DOF Cracked Rotor System

In this section, numerical illustrations are performed for a 4-DOF cracked rotor model. The closed-form time-domain responses and frequency-domain full-spectrum responses are obtained. Time-integrated responses also can be use and demonstrated in previous chapters. The effect of gyroscopic couple on cracked rotor critical speed is observed. The system EOM of the cracked rotor (Eqn.(5.24)) is considered for the numerical simulation. For the case of gyroscopic effects in a rotor with *thin disc*, $I_p = 2I_d$. The data given in Table 5-1 are considered for the numerical simulation.

Stiffness matrices of the intact rotor shaft are obtained by the inversion of influence coefficient matrix obtained for a simply supported rotor with an offset load (Timoshenko and Young, 1968). The static translational and rotational deflections are also obtained accordingly. Additive stiffness

terms due to the crack are considered as 5% of the magnitude of the intact shaft stiffness. Damping terms are considered for an under-damped case of 0.015 damping ratio. Following matrices are obtained for simulation.

$$[M]=\begin{bmatrix} 1.5\text{ kg} & 0 \\ 0 & 0.0024\text{ kg-m}^2 \end{bmatrix};\quad [K]=\begin{bmatrix} 1.0432\times10^6\text{ N/m} & 0.0890\times10^6\text{ N-m/rad} \\ 0.0890\times10^6\text{ N/m} & 0.0235\times10^6\text{ N-m/rad} \end{bmatrix};$$

$$[C]=\begin{bmatrix} 38\text{ N-s/m} & 11\text{ Nm-s/rad} \\ 11\text{ N-s/m} & 6\text{ Nm-s/rad} \end{bmatrix};\quad [G]=\begin{bmatrix} 0 & 0 \\ 0 & 0.0045 \end{bmatrix}\text{kg-m}^2$$

Table 5-1 Data for the numerical simulation

| **Parameters** | **Values** |
|---|---|
| Disk mass, $m$ | 1.5 kg |
| Disk radius, $r$ | $7.75\times10^{-2}$ m |
| Disk thickness, $t$ | $3.2\times10^{-2}$ m |
| Shaft diameter, $d$ | $1.6\times10^{-2}$ m |
| Shaft length, $l$ | 0.386 m |
| Disk position from left support, $a$ | 0.2560 m |
| Young's modulus, $E$ | $2.1\times10^{11}$ N/m$^2$ |
| Crack stiffness terms: $\Delta k_{22}$ | 52165 N/m |
| $\Delta k_{44}$ | 1175 N-m/rad |
| Static deflections: $u_{x0}$ | $2.2593\times10^{-5}$ m |
| $\varphi_{y0}$ | $7.8874\times10^{-5}$ rad |
| Disk eccentricity, $e$ | $0.1\times10^{-6}$ m |
| Static unbalance phase angle, $\beta$ | $10^0$ |

Eqn. (5.26) and Eqn. (5.28) are used to obtain time and frequency responses, respectively. The crack has the opening/closing profile, $s(t)$, as shown in Figure 2.3, is considered. The function $s(t)$ can also take any other periodic time varying function and hence only square wave is not a limitation on the present model.

Displacements versus time responses of the cracked rotor with the excitation due to crack and unbalance forces, are shown in Figure 5.2 and Figure 5.3. Responses correspond to a spin speed of 100 rad/s. Displacement responses in the $x$ and $y$ directions appear different as the crack force is different in $x$ and $y$ directions as given in Eqn. (5.24). Full-spectrum plots of the translational and rotational displacements are also shown in these figures. The full-spectrum plot shows harmonics of 1×, 2×, 3×, 5× and 7× of the spin speed. These response harmonics are present both in the same and reverse direction of the rotor spin; however, these are not symmetric about zero frequency line. These are shown in the positive and negative halves of the full-spectrum plot. Figure 5.4 and Figure 5.5 shows the response without crack showing 1× harmonic due to unbalance force. The effect of gyroscopic couple on the cracked rotor critical speed is shown in Figure 5.6. For the case of resonance in responses of 1× harmonic component, the critical speed of cracked rotor system for the translational and rotational displacements is observed. The critical speed is 664 rad/s whereas with the gyroscopic couple, the critical speed increases to 680 rad/s. Similarly, the resonance in the crack response of 2× harmonic component is observed. The critical speed for it is 336 rad/s, whereas with the gyroscopic couple the critical speed increases to 340 rad/s. The viscous damping in rotor system ($c$) used for numerical simulation is 38 N-s/m and the disc mass is 1.5 kg. As the first critical of the rotor response is observed at 680 rad/s, the corresponding damping ratio of the system is $\zeta = 0.019$.

In Figure 5.2 (b), the positive half of the frequency axis corresponds to forward whirling response frequencies. While, the negative half of the frequency axis correspond to the reverse whirling response frequencies. The peaks of the forward whirl frequency components correspond to the following harmonics: 1×, 2×, 3× and 5×.Whereas the reverse whirl frequency components correspond to: -1×, -3× and -5×. The peak at zero frequency corresponds to the constant term in the Fourier series expansion (DC component, which in rotor corresponds to displacement due to a constant load which is the disc mass). These peaks are termed as response coefficients ($r_i$).

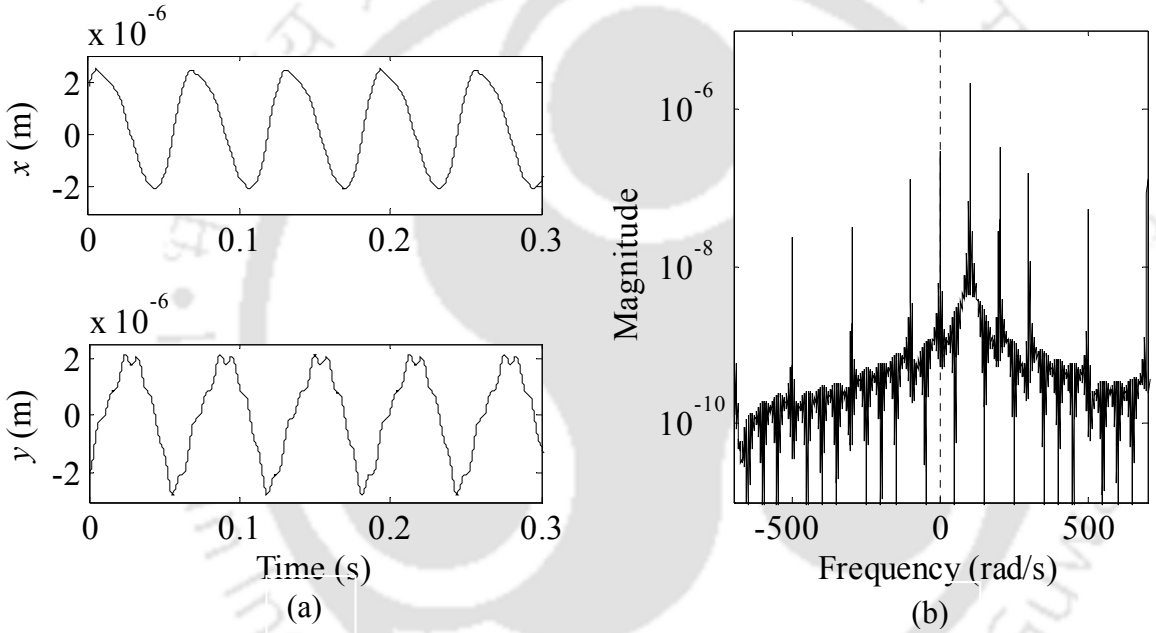


Figure 5.2 (a) Cracked rotor response plots of $x$ displacement (above) and $y$ displacement (below) (b) Full-spectrum plot of ($x$ + j $y$) showing harmonics of the crack excitation

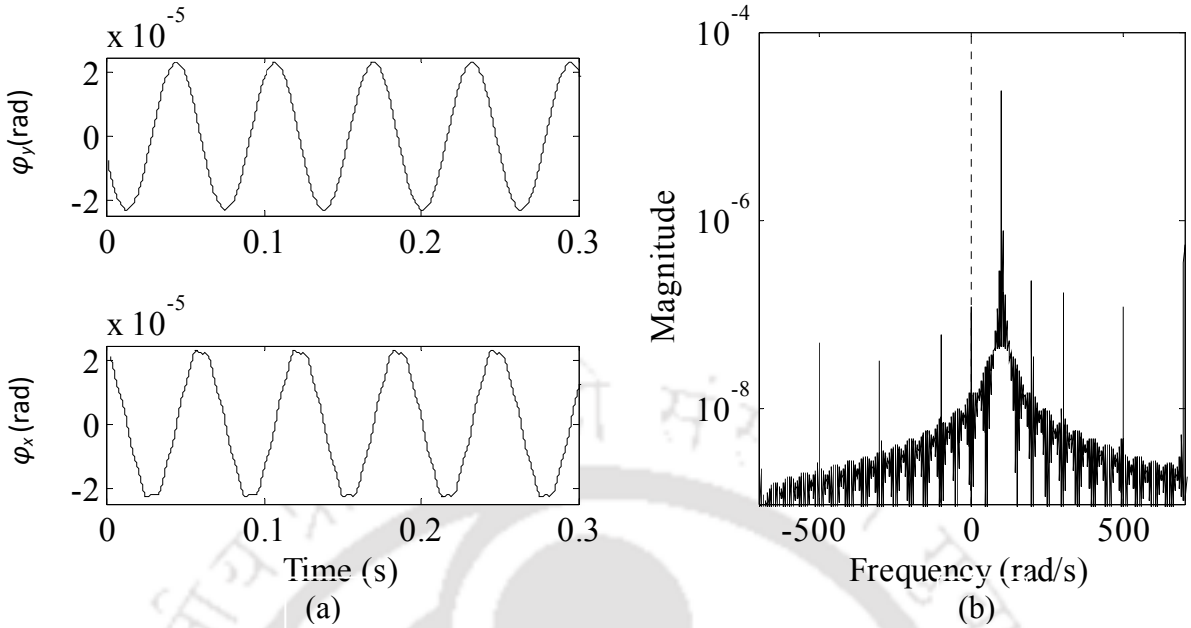


Figure 5.3 (a) Cracked rotor response plots of $\varphi_y$ displacement (above) and $\varphi_x$ displacement (below) (b) full-spectrum plot of ($\varphi_y$ + j $\varphi_x$) showing harmonics of crack excitation

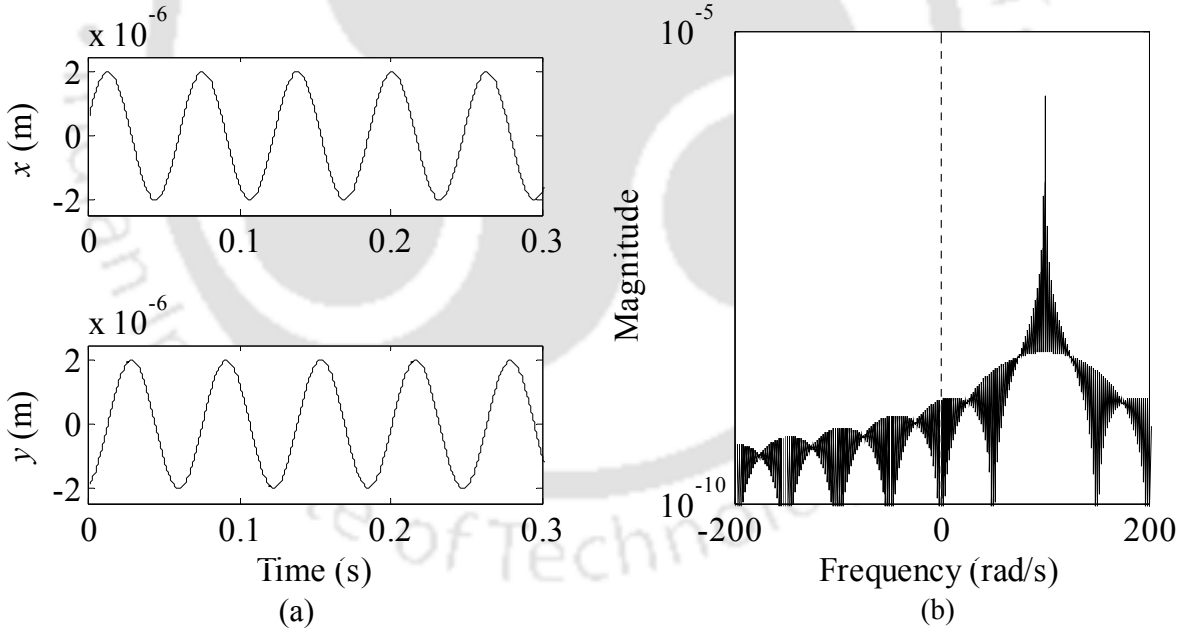


Figure 5.4 (a) Unbalanced intact rotor response plots of $x$ displacement (above) and $y$ displacement (below) (b) full-spectrum plot of ($x$ + j $y$) showing frequency component due to the unbalance excitation

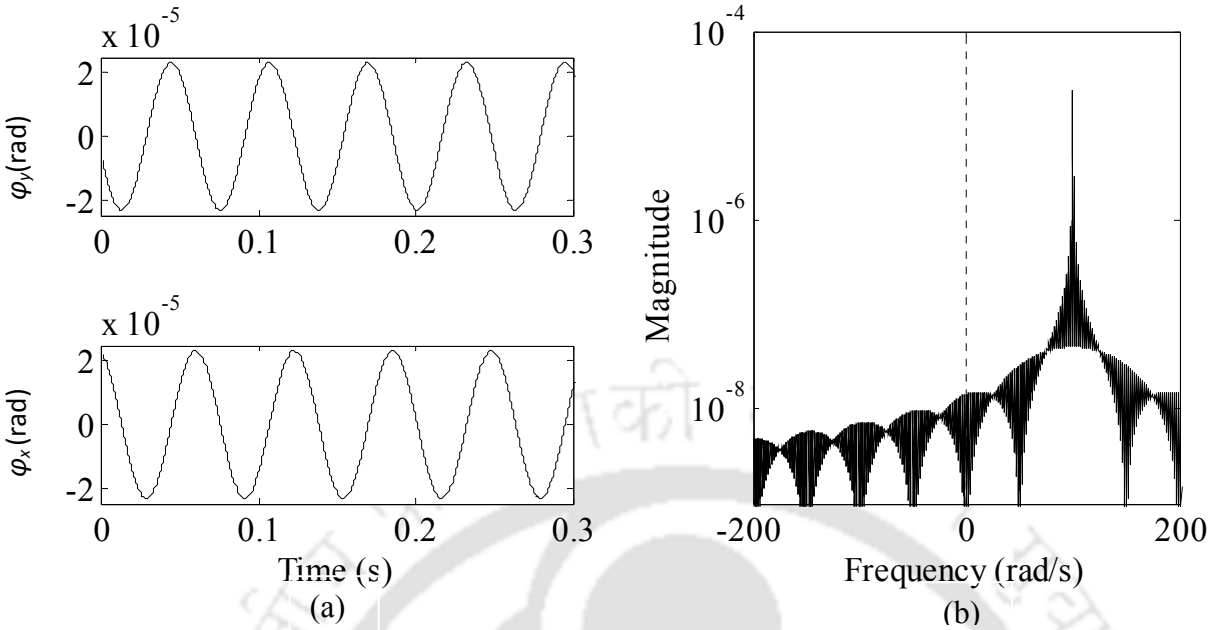


Figure 5.5 (a) Unbalance intact rotor response plots of $\varphi_y$ displacement (above) and $\varphi_x$ displacement (below) (b) Full-spectrum plot of ($\varphi_y$ + j $\varphi_x$) showing frequency component due to the unbalance excitation

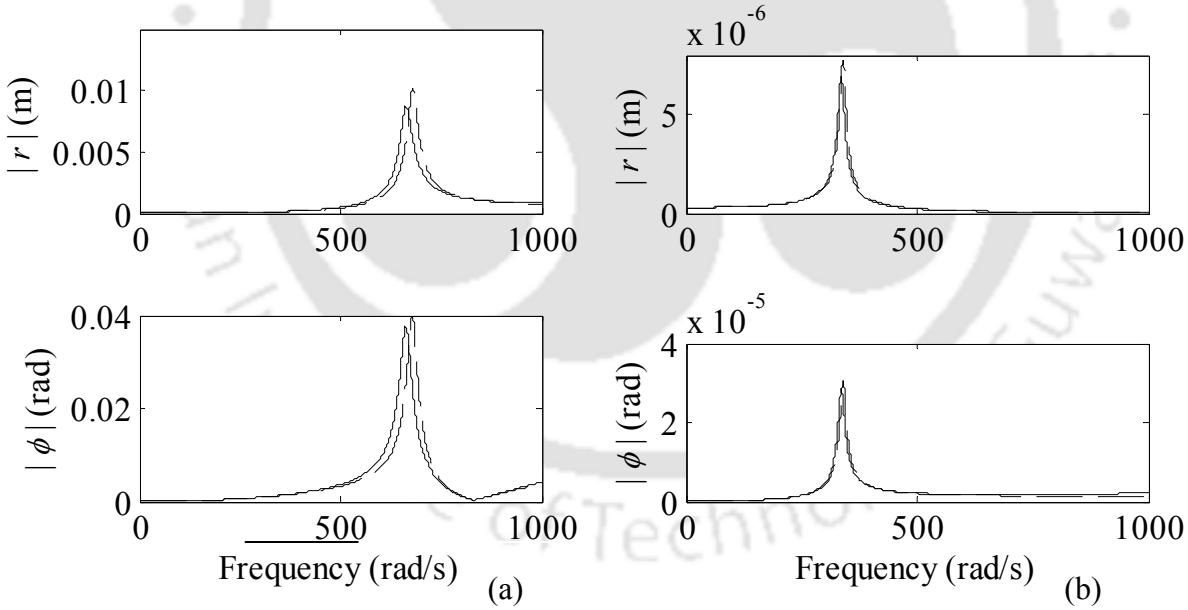


Figure 5.6 (a) The response plot of 1× component of crack and unbalance force for translational displacement (above) and rotational displacement (below) (b)The response plot of 2× component of crack force for translational displacement (above) and rotational displacement (below) (without gyroscopic, - - - - with gyroscopic)

The numerical simulations have been performed for the cracked rotor in the time and frequency domains. The effect of gyroscopic couple on the rotor critical speed is also observed. Now, identification algorithms are derived to estimate crack and unknown system parameters, which is the main focus of the present chapter.

## 5.7 Identification Using Full-Spectrum Responses

In this section, an identification algorithm is developed to identify the crack parameter, namely, additive crack stiffness; along with unknown system parameters, unbalance eccentricity and viscous damping. The system EOMs in time domain (Eqn. (5.25)) and in frequency domain (Eqn. (5.26)) are used for this purpose. The identification algorithm is developed for using multiple spin speeds as input to the algorithm. Also, the identification algorithms are further extended to estimate the switching crack forces, which can give an actual idea of the crack opening/closing function. As EOMs contain the rotational DOFs, it causes a practical limitation to measure accurately. Hence, a Dynamic reduction scheme is used to first obtain the reduced EOMs in time and frequency domains. The reduced EOMs which need only the input of translational displacements are then used for parameter identification.

*Reduction of system EOMs*: The system EOMs with 4-DOFs are shown in Eqn. (5.24). The time domain equations are re-written as,

$$\begin{bmatrix} m & 0 & 0 & 0 \\ & m & 0 & 0 \\ & & I_d & 0 \\ \text{sym} & & & I_d \end{bmatrix} \begin{Bmatrix} \ddot{u}_x \\ \ddot{u}_y \\ \ddot{\varphi}_y \\ \ddot{\varphi}_x \end{Bmatrix} + \left( \begin{bmatrix} c_{11} & 0 & c_{12} & 0 \\ & c_{11} & 0 & c_{12} \\ & & c_{22} & 0 \\ \text{sym} & & & c_{22} \end{bmatrix} - \omega \begin{bmatrix} 0 & 0 & 0 & 0 \\ 0 & 0 & 0 & 0 \\ 0 & 0 & 0 & I_p \\ 0 & 0 & -I_p & 0 \end{bmatrix} \right) \begin{Bmatrix} \dot{u}_x \\ \dot{u}_y \\ \dot{\varphi}_y \\ \dot{\varphi}_x \end{Bmatrix}$$

$$+ \begin{bmatrix} k_{22} & 0 & k_{23} & 0 \\ & k_{22} & 0 & k_{23} \\ & & k_{33} & 0 \\ \text{sym} & & & k_{33} \end{bmatrix} \begin{Bmatrix} u_x \\ u_y \\ \varphi_y \\ \varphi_x \end{Bmatrix} = \begin{Bmatrix} \text{Re}\left(\Delta k_{22} u_{x_0} p_i e^{\text{j}i\omega t}\right) \\ \text{Im}\left(\Delta k_{22} u_{x_0} p_i e^{\text{j}i\omega t}\right) \\ \text{Re}\left(\Delta k_{44} u_{x_0} p_i e^{\text{j}i\omega t}\right) \\ \text{Im}\left(\Delta k_{22} u_{x_0} p_i e^{\text{j}i\omega t}\right) \end{Bmatrix} + \begin{Bmatrix} \text{Re}\left(me\omega^2 e^{j(\omega t+\beta)}\right) \\ \text{Im}\left(me\omega^2 e^{j(\omega t+\beta)}\right) \\ 0 \\ 0 \end{Bmatrix} \tag{5.29}$$

Similarly, the corresponding system EOMs in frequency domain are considered. For a particular harmonic $i$ of the crack force,

$$\left( -(i\omega)^2 \begin{bmatrix} m & 0 & 0 & 0 \\ & m & 0 & 0 \\ & & I_d & 0 \\ \text{sym} & & & I_d \end{bmatrix} + \text{j}(i\omega) \left( \begin{bmatrix} c_{11} & 0 & c_{12} & 0 \\ & c_{11} & 0 & c_{12} \\ & & c_{22} & 0 \\ \text{sym} & & & c_{22} \end{bmatrix} - \omega \begin{bmatrix} 0 & 0 & 0 & 0 \\ 0 & 0 & 0 & 0 \\ 0 & 0 & 0 & I_p \\ 0 & 0 & -I_p & 0 \end{bmatrix} \right) + \begin{bmatrix} k_{22} & 0 & k_{23} & 0 \\ & k_{22} & 0 & k_{23} \\ & & k_{33} & 0 \\ \text{sym} & & & k_{33} \end{bmatrix} \right) \begin{Bmatrix} U_i^x \\ U_i^y \\ \Phi_i^y \\ \Phi_i^x \end{Bmatrix}$$

$$= \begin{Bmatrix} \Delta k_{22} u_{x_0} \\ \Delta k_{22} u_{x_0} \\ \Delta k_{44} u_{x_0} \\ \Delta k_{44} u_{x_0} \end{Bmatrix} + \begin{Bmatrix} me\omega^2 e^{j\beta} \\ me\omega^2 e^{j\beta} \\ \left(I_p - I_d\right)\alpha\omega^2 e^{j\gamma} \\ \left(I_p - I_d\right)\alpha\omega^2 e^{j\gamma} \end{Bmatrix} \tag{5.30}$$

Here, $U_i^x$ and $U_i^y$ are the translational complex displacements, whereas $\Phi_i^y$ and $\Phi_i^x$ are the rotational complex displacements in frequency domain. Now, dynamic condensation method is introduced to eliminate use of rotational displacements in system EOMs.

*Dynamic condensation* essentially consists of elimination of certain unwanted DOFs. The DOFs eliminated in the process are called as *slaves* while the DOFs retained for the analysis are called as *masters*. Discarded coordinates (slaves) would correspond to points in the model, which are non-critical, or of secondary interest such as rotational DOFs, intermediate location on the shaft, etc. Here, rotational DOFs are eliminated. Since, in identification procedure it is not possible to measure responses at all DOFs in the practical scenario, condensation is carried out. The state vector (displacement vector), the force vectors, the mass matrix, and stiffness matrix are partitioned into sub-vectors and sub-matrices relating to the masters DOFs, and slave DOFs, which are to be eliminated. When no forces or moments are applied at the slave DOFs (here it is assumed that initial tilt of the disc is negligibly small to procedure appreciable moments), the frequency domain equations (Eqn. (5.30)) can be partitioned as follows, where subscript *m* and *s* represent masters and slaves, respectively.

$$\left(-(i\omega)^2\begin{bmatrix}\mathbf{M}_{mm} & 0\\ 0 & \mathbf{M}_{ss}\end{bmatrix}+\mathrm{j}(i\omega)\left(\begin{bmatrix}\mathbf{C}_{mm} & \mathbf{C}_{ms}\\ \mathbf{C}_{sm} & \mathbf{C}_{ss}\end{bmatrix}-\omega\begin{bmatrix}0 & 0\\ 0 & \mathbf{G}_{ss}\end{bmatrix}\right)+\begin{bmatrix}\mathbf{K}_{mm} & \mathbf{K}_{ms}\\ \mathbf{K}_{sm} & \mathbf{K}_{ss}\end{bmatrix}\right)\begin{Bmatrix}\mathbf{Q}_m\\ \mathbf{Q}_s\end{Bmatrix}=\begin{Bmatrix}\mathbf{f}\\ 0\end{Bmatrix} \tag{5.31}$$

With the sub-matrices and sub-vectors defined as,

$$\mathbf{M}_{mm}=\begin{bmatrix}m & 0\\ 0 & m\end{bmatrix} \qquad \mathbf{M}_{ss}=\begin{bmatrix}I_d & 0\\ 0 & I_d\end{bmatrix}$$

$$\mathbf{C}_{mm}=\begin{bmatrix} c_{11} & 0 \\ 0 & c_{11} \end{bmatrix} \qquad \mathbf{C}_{ms}=\mathbf{C}_{sm}=\begin{bmatrix} c_{12} & 0 \\ 0 & c_{12} \end{bmatrix} \qquad \mathbf{C}_{ss}=\begin{bmatrix} c_{22} & 0 \\ 0 & c_{22} \end{bmatrix}$$

$$\mathbf{G}_{ss}=\begin{bmatrix} 0 & I_p \\ -I_p & 0 \end{bmatrix}$$

$$\mathbf{K}_{mm}=\begin{bmatrix} k_{22} & 0 \\ 0 & k_{22} \end{bmatrix} \qquad \mathbf{K}_{ms}=\mathbf{K}_{sm}=\begin{bmatrix} k_{23} & 0 \\ 0 & k_{23} \end{bmatrix} \qquad \mathbf{K}_{ss}=\begin{bmatrix} k_{33} & 0 \\ 0 & k_{33} \end{bmatrix}$$

$$\mathbf{f}=\begin{Bmatrix} \Delta k_{22} u_{x_0} p_i \\ \Delta k_{22} u_{x_0} p_i \end{Bmatrix}+\begin{Bmatrix} me\omega^2 e^{\mathrm{i}\beta} \\ me\omega^2 e^{\mathrm{i}\beta} \end{Bmatrix}$$

$$\mathbf{Q}_m=\begin{Bmatrix} U_i^x \\ U_i^y \end{Bmatrix} \qquad \mathbf{Q}_s=\begin{Bmatrix} \Phi_i^x \\ \Phi_i^y \end{Bmatrix}$$

The Eqn. (5.31) can be expanded into two equations as,

$$-(i\omega)^2[\mathbf{M}_{mm}]\{\mathbf{Q}_m\}+[\mathbf{K}_{mm}]\{\mathbf{Q}_m\}+[\mathbf{K}_{ms}]\{\mathbf{Q}_s\}=\mathbf{f} \tag{5.32}$$

and

$$-(i\omega)^2[\mathbf{M}_{ss}]\{\mathbf{Q}_s\}+[\mathbf{K}_{sm}]\{\mathbf{Q}_m\}+[\mathbf{K}_{ss}]\{\mathbf{Q}_s\}=\mathbf{0} \tag{5.33}$$

Here, $\omega$ is the spin speed of the cracked rotor, $\mathbf{Q}_m$ and $\mathbf{Q}_s$ are the displacement vectors corresponding to master and slave DOFs, and $\mathbf{f}$ is the force vector due to crack and unbalance. The Eqn. (5.33) can be re-arranged as,

$$\mathbf{Q}_s=-\left(\mathbf{K}_{ss}-(i\omega)^2\mathbf{M}_{ss}\right)\mathbf{K}_{sm}\mathbf{Q}_m \tag{5.34}$$

Considering an identity equation,

$$\mathbf{Q}_m=\mathbf{I}\mathbf{Q}_m \tag{5.35}$$

Where $\mathbf{I} = \begin{bmatrix} 1 & 0 \\ 0 & 1 \end{bmatrix}$ is an identity matrix. The Eqn. (5.34) and Eqn. (5.35) can be combined as,

$$\begin{Bmatrix} \mathbf{Q}_m \\ \mathbf{Q}_s \end{Bmatrix} = \mathbf{T}^d \mathbf{Q}_m \tag{5.36}$$

With $\mathbf{T}^d = \begin{bmatrix} 1 & 0 \\ 0 & 1 \\ \dfrac{-k_{23}}{k_{33} - (i\omega)^2 I_d} & 0 \\ 0 & \dfrac{-k_{23}}{k_{33} - (i\omega)^2 I_d} \end{bmatrix}$

Here, $\mathbf{T}^d$ is the transformation matrix for the dynamic condensation which eliminates the rotational co-ordinates $\varphi_y$ and $\varphi_x$. Let $T_{31}^d = \dfrac{-k_{23}}{k_{33} - (i\omega)^2 I_d}$. In the above transformation, apart from mass and stiffness matrices, frequency $i\omega$ also appears. For the transformation matrix it is chosen as $i\omega = \omega_{central}$. Here, $\omega_{central}$ is called as the central frequency, and it is chosen as the geometrical mean of the measurement spin speed range of interest. When a constant $\omega_{central}$ is chosen, the transformation is fixed and hence can be substituted in the time domain EOMs. Hence, on substituting the transformation Eqn. (5.36) in to the time domain EOMs,

$$\left(\mathbf{T}^d\right)^T \left( \begin{bmatrix} \mathbf{M}_{mm} & 0 \\ 0 & \mathbf{M}_{ss} \end{bmatrix} \mathbf{T}^d \begin{Bmatrix} \ddot{\mathbf{q}}_m \\ \ddot{\mathbf{q}}_s \end{Bmatrix} + \begin{bmatrix} \mathbf{K}_{mm} & \mathbf{K}_{ms} \\ \mathbf{K}_{sm} & \mathbf{K}_{ss} \end{bmatrix} \mathbf{T}^d \begin{Bmatrix} \mathbf{q}_m \\ \mathbf{q}_s \end{Bmatrix} + \left( \begin{bmatrix} \mathbf{C}_{mm} & \mathbf{C}_{ms} \\ \mathbf{C}_{sm} & \mathbf{C}_{ss} \end{bmatrix} - \omega \begin{bmatrix} 0 & 0 \\ 0 & \mathbf{G}_{ss} \end{bmatrix} \right) \mathbf{T}^d \begin{Bmatrix} \dot{\mathbf{q}}_m \\ \dot{\mathbf{q}}_s \end{Bmatrix} \right)$$

$$= \left(\mathbf{T}^d\right)^T \mathbf{f}_c + \left(\mathbf{T}^d\right)^T \mathbf{f}_{unb} \tag{5.37}$$

Here, $\mathbf{q}_m = \begin{Bmatrix} u_x \\ u_y \end{Bmatrix}$

$$\mathbf{M}^d = \left(\mathbf{T}^d\right)^T \begin{bmatrix} \mathbf{M}_{mm} & 0 \\ 0 & \mathbf{M}_{ss} \end{bmatrix} \mathbf{T}^d = \begin{bmatrix} m + \left(T_{31}^d\right)^2 & \\ & m + \left(T_{31}^d\right)^2 \end{bmatrix}$$

$$\mathbf{K}^d = \left(\mathbf{T}^d\right)^T \begin{bmatrix} \mathbf{K}_{mm} & \mathbf{K}_{ms} \\ \mathbf{K}_{sm} & \mathbf{K}_{ss} \end{bmatrix} \mathbf{T}^d = \begin{bmatrix} k_{22} + 2T_{31}^d k_{23} + \left(T_{31}^d\right)^2 k_{33} & \\ & k_{22} + 2T_{31}^d k_{23} + \left(T_{31}^d\right)^2 k_{33} \end{bmatrix}$$

$$\mathbf{C}^d = \left(\mathbf{T}^d\right)^T \begin{bmatrix} \mathbf{C}_{mm} & \mathbf{C}_{ms} \\ \mathbf{C}_{sm} & \mathbf{C}_{ss} \end{bmatrix} \mathbf{T}^d = \begin{bmatrix} c_{11} + 2T_{31}^d c_{12} + \left(T_{31}^d\right)^2 c_{22} & \\ & c_{11} + 2T_{31}^d c_{12} + \left(T_{31}^d\right)^2 c_{22} \end{bmatrix}$$

$$\mathbf{G}^d = \left(\mathbf{T}_{31}^d\right)^T \omega \begin{bmatrix} 0 & 0 \\ 0 & \mathbf{G}_{ss} \end{bmatrix} \mathbf{T}_{31}^d = \begin{bmatrix} 0 & \left(T_{31}^d\right)^2 I_p \\ -\left(T_{31}^d\right)^2 I_p & 0 \end{bmatrix}$$

$$\mathbf{f}_c^d = T_{31}^d \mathbf{f}_c \qquad \mathbf{f}_{unb}^d = T_{31}^d \mathbf{f}_{unb}$$

The reduced EOMs are written as,

$$\mathbf{M}^d \ddot{\mathbf{q}}_m + \left(\mathbf{C}^d - \omega \mathbf{G}^d\right) \dot{\mathbf{q}}_m + \mathbf{K}^d \mathbf{q}_m = \mathbf{f}_c + \mathbf{f}_{unb} \tag{5.38}$$

Here,

$$\mathbf{f}_c = \begin{Bmatrix} \Delta k_{22} \cos^2 \omega t \; x_0 \\ \Delta k_{22} \sin \omega t \cos \omega t \; x_0 \end{Bmatrix} \quad \mathbf{f}_{unb} = \begin{Bmatrix} me\omega^2 \cos\left(\omega t + \beta\right) \\ me\omega^2 \sin\left(\omega t + \beta\right) \end{Bmatrix}$$

The EOMs in Eqn. (5.37) are combined together as a single equation in a complex form as,

$$\left(m+\left(T_{31}^{d}\right)^{2} I_{d}\right)\ddot{r}+\left(c_{11}+2T_{31}^{d}c_{12}+\left(T_{31}^{d}\right)^{2} c_{22}+j\, I_{p}\omega\left(T_{31}^{d}\right)^{2}\right)\dot{r}+\left(k_{22}+2T_{31}^{d}k_{23}+\left(T_{31}^{d}\right)^{2} k_{33}\right)r$$
$$=\Delta k_{22}x_{0}\sum_{i=-n}^{n}p_{i}e^{ji\omega t}+me\omega^{2}e^{j(\omega t+\beta)} \tag{5.39}$$

Here, $r=u_x+\mathrm{j}\,u_y$. The corresponding EOM in frequency domain is written as,

$$\left(-(i\omega)^{2}\left(m+\left(T_{31}^{d}\right)^{2} I_{d}\right)\right)+j(i\omega)\left(c_{11}+2T_{31}^{d}c_{12}+\left(T_{31}^{d}\right)^{2} c_{22}+j\, I_{p}\omega\left(T_{31}^{d}\right)^{2}\right)+\left(k_{22}+2T_{31}^{d}k_{23}+\left(T_{31}^{d}\right)^{2} k_{33}\right)r_{i}$$
$$=\Delta k_{22}x_{0}p_{i}+me\omega^{2}e^{j\beta} \tag{5.40}$$

Now, for parameter identification, the frequency equation is split into known and unknown parts, and re-arranged such that the unknown crack and system parameters are grouped in a vector, as follows. Here, the phase angle due to unbalance is also estimated.

$$\begin{bmatrix} j\,(i\omega)r_{i} & -x_{0}p_{i} & -m\omega^{2} \end{bmatrix}\begin{Bmatrix} c_{11} \\ \Delta k_{22} \\ ee^{j\beta} \end{Bmatrix}=(i\omega)^{2}\left(m+\left(T_{31}^{d}\right)^{2} I_{d}\right)+\left(i\omega^{2}\right)\left(T_{31}^{d}\right)^{2} I_{p}-\left(k_{22}+2T_{31}^{d}k_{23}+\left(T_{31}^{d}\right)^{2} k_{33}\right)r_{i} \tag{5.41}$$

From Eqn. (5.41) it is seen that the number of equations is one, where as the number of unknown coefficients are three. Hence, it is an underdetermined system. It can be converted in to an overdetermined system if the number of equations is increased. For this, similar equations in frequency domain are written for various harmonics *i* of the crack force. For e.g., equations can be written similarly for harmonic components $i=-7,-5-,3,-1,0,1,2,3,5,7$. In general, $i=-n,...,0,...,n$. The generalized identification algorithm for *n* harmonic components is as follows.

$$\mathbf{A}_{4((2n+1)\times 3)} = \begin{bmatrix} \mathrm{j}(-n\omega)r_{-n} & 0 & -x_0 p_{-n} \\ . & . & . \\ . & . & . \\ . & . & . \\ \mathrm{j}(-\omega)r_{-1} & 0 & -x_0 p_{-1} \\ 0 & 0 & -x_0 p_0 \\ \mathrm{j}(\omega)r_1 & -m\omega^2 & -x_0 p_1 \\ \mathrm{j}(2\omega)r_2 & 0 & -x_0 p_2 \\ . & . & . \\ . & . & . \\ . & . & . \\ \mathrm{j}(n\omega)r_n & 0 & -x_0 p_n \end{bmatrix}$$

$$\mathbf{x}_{4(3\times 1)} = \begin{Bmatrix} c \\ ee^{\mathrm{j}\beta} \\ \Delta k_{22} \end{Bmatrix}$$

$$\mathbf{b}_{4((2n+1)\times 1)} = \begin{Bmatrix} (n\omega)^2\left(m+\left(T_{31}^d\right)^2 I_d\right)+\left(-n\omega^2\right)\left(T_{31}^d\right)^2 I_p-\left(k_{22}+2T_{31}^d k_{23}+\left(T_{31}^d\right)^2 k_{33}\right)r_{-n} \\ . \\ . \\ . \\ (\omega)^2\left(m+\left(T_{31}^d\right)^2 I_d\right)+\left(-\omega^2\right)\left(T_{31}^d\right)^2 I_p-\left(k_{22}+2T_{31}^d k_{23}+\left(T_{31}^d\right)^2 k_{33}\right)r_{-n} \\ -\left(k_{22}+2T_{31}^d k_{23}+\left(T_{31}^d\right)^2 k_{33}\right)r_0 \\ (\omega)^2\left(m+\left(T_{31}^d\right)^2 I_d\right)+\left(\omega^2\right)\left(T_{31}^d\right)^2 I_p-\left(k_{22}+2T_{31}^d k_{23}+\left(T_{31}^d\right)^2 k_{33}\right)r_1 \\ (4\omega)^2\left(m+\left(T_{31}^d\right)^2 I_d\right)+\left(2\omega^2\right)\left(T_{31}^d\right)^2 I_p-\left(k_{22}+2T_{31}^d k_{23}+\left(T_{31}^d\right)^2 k_{33}\right)r_2 \\ . \\ . \\ . \\ (n\omega)^2\left(m+\left(T_{31}^d\right)^2 I_d\right)+\left(n\omega^2\right)\left(T_{31}^d\right)^2 I_p-\left(k_{22}+2T_{31}^d k_{23}+\left(T_{31}^d\right)^2 k_{33}\right)r_n \end{Bmatrix} \quad (5.42)$$

Separating the real and imaginary parts of equation Eqn. (5.42) yields the following equations

$$\mathbf{A}_4^r\mathbf{x}_4^r-\mathbf{A}_4^i\mathbf{x}_4^i=\mathbf{b}_4^r \tag{5.43}$$

and

$$\mathbf{A}_4^i\mathbf{x}_4^r+\mathbf{A}_4^r\mathbf{x}_4^i=\mathbf{b}_4^r \tag{5.44}$$

where superscripts *r* and *i* represent the real and imaginary parts, respectively. Eqns. (5.43) and (5.44) can be combined in the matrix form as

$$\begin{bmatrix}\mathbf{A}_4^r & -\mathbf{A}_4^i\\ \mathbf{A}_4^i & \mathbf{A}_4^r\end{bmatrix}_{(4n+2)\times 6}\begin{Bmatrix}\mathbf{x}_4^r\\ \mathbf{x}_4^i\end{Bmatrix}_{(6\times 1)}=\begin{Bmatrix}\mathbf{b}_4^r\\ \mathbf{b}_4^i\end{Bmatrix}_{(4n+2)\times 1} \tag{5.45}$$

Here, $\mathbf{x}_4^r=\lfloor c \quad e\cos\beta \quad \Delta k_{22}\rfloor^T$ and $\mathbf{x}_4^i=\lfloor 0 \quad e\sin\beta \quad 0\rfloor^T$. The zero row element $\mathbf{x}_4^i(1,1)=0$ and their corresponding columns in the regression matrix (i.e., $-\mathbf{A}_4^i(1,1)\ldots-\mathbf{A}_4^i((2n+1),1)$, $\mathbf{A}_4^r(1,1)\ldots\mathbf{A}_4^r((2n+1),1)$ are eliminated. Similarly eliminating $\mathbf{x}_4^i(3,1)=0$ and its corresponding columns in the regression matrix $-\mathbf{A}_4^i(1,3)\ldots-\mathbf{A}_4^i((2n+1),3)$ and $\mathbf{A}_4^r(1,3)\ldots\mathbf{A}_4^r((2n+1),3)$, yields a reduced matrix equation in the following form

$$\mathbf{A}'_{4((4n+2)\times 4)}\mathbf{x}'_{(4\times 1)}=\mathbf{b}'_{4((4n+2)\times 1)} \tag{5.46}$$

In Eqn. (A.5), vector $\mathbf{x}'_4=\lfloor c \quad e\cos\beta \quad \Delta k_{22} \quad e\sin\beta\rfloor^T$ contains unknown parameters to be estimated. The estimated parameters are tabulated as follows in Table 5-3 to Table 5-7.

*Identification of crack force*: The identification of crack force terms is carried out using Eqn. (4.19) , it uses only force coefficients $p_{\pm i}$, which are now directly obtained using full-spectrum. The full-spectrum equation Eqn. (4.1) is used for obtaining these coefficients for the input to the identification algorithm. The generalized form of identification algorithm is as follows.

$$\mathbf{A}_{5((2n+1)\times(2n+3))} = \left[\mathbf{D}_1 \ \mathbf{D}_2\right] \tag{5.47}$$

Here,

$$\mathbf{D}_1 = \begin{bmatrix} \mathrm{j}(-n\omega)r_{-n} & 0 & -x_0 & 0 & 0 & 0 & 0 \\ . & . & . & . & . & . & . \\ . & . & . & . & . & . & . \\ . & . & . & . & . & . & . \\ \mathrm{j}(-\omega)r_{-1} & 0 & 0 & 0 & 0 & 0 & -x_0 \\ 0 & 0 & 0 & 0 & 0 & 0 & 0 \\ \mathrm{j}(\omega)r_1 & -m\omega^2 e^{\mathrm{j}\beta} & 0 & 0 & 0 & 0 & 0 \\ \mathrm{j}(2\omega)r_2 & 0 & 0 & 0 & 0 & 0 & 0 \\ . & . & . & . & . & . & . \\ . & . & . & . & . & . & . \\ . & . & . & . & . & . & . \\ \mathrm{j}(n\omega)r_n & 0 & 0 & 0 & 0 & 0 & 0 \end{bmatrix}$$

$$\mathbf{D}_2 = \begin{bmatrix} 0 & 0 & 0 & 0 & 0 & 0 & 0 \\ . & . & . & . & . & . & . \\ . & . & . & . & . & . & . \\ . & . & . & . & . & . & . \\ 0 & 0 & 0 & 0 & 0 & 0 & 0 \\ -x_0 & 0 & 0 & 0 & 0 & 0 & 0 \\ 0 & -x_0 & 0 & 0 & 0 & 0 & 0 \\ 0 & 0 & -x_0 & 0 & 0 & 0 & 0 \\ . & . & . & . & . & . & . \\ . & . & . & . & . & . & . \\ . & . & . & . & . & . & . \\ 0 & 0 & 0 & 0 & 0 & 0 & -x_0 \end{bmatrix} \qquad \mathbf{x}_{5((2n+3)\times 1)} = \begin{Bmatrix} c \\ ee^{\mathrm{j}\beta} \\ \Delta k_{22} p_{-n} \\ . \\ . \\ . \\ \Delta k_{22} p_{-1} \\ \Delta k_{22} p_0 \\ \Delta k_{22} p_1 \\ \Delta k_{22} p_2 \\ . \\ . \\ . \\ \Delta k_{22} p_n \end{Bmatrix}$$

$$\mathbf{b}_{5((2n+1)\times 1)} = \left\{ \begin{array}{c} (n\omega)^2\left(m+\left(T_{31}^d\right)^2 I_d\right)+\left(-n\omega^2\right)\left(T_{31}^d\right)^2 I_p-\left(k_{22}+2T_{31}^d k_{23}+\left(T_{31}^d\right)^2 k_{33}\right)r_{-n} \\ . \\ . \\ . \\ (\omega)^2\left(m+\left(T_{31}^d\right)^2 I_d\right)+\left(-\omega^2\right)\left(T_{31}^d\right)^2 I_p-\left(k_{22}+2T_{31}^d k_{23}+\left(T_{31}^d\right)^2 k_{33}\right)r_{-n} \\ -\left(k_{22}+2T_{31}^d k_{23}+\left(T_{31}^d\right)^2 k_{33}\right)r_0 \\ (\omega)^2\left(m+\left(T_{31}^d\right)^2 I_d\right)+\left(\omega^2\right)\left(T_{31}^d\right)^2 I_p-\left(k_{22}+2T_{31}^d k_{23}+\left(T_{31}^d\right)^2 k_{33}\right)r_1 \\ (4\omega)^2\left(m+\left(T_{31}^d\right)^2 I_d\right)+\left(2\omega^2\right)\left(T_{31}^d\right)^2 I_p-\left(k_{22}+2T_{31}^d k_{23}+\left(T_{31}^d\right)^2 k_{33}\right)r_2 \\ . \\ . \\ . \\ (n\omega)^2\left(m+\left(T_{31}^d\right)^2 I_d\right)+\left(n\omega^2\right)\left(T_{31}^d\right)^2 I_p-\left(k_{22}+2T_{31}^d k_{23}+\left(T_{31}^d\right)^2 k_{33}\right)r_n \end{array} \right\} \quad (5.48)$$

Separating Eqn. (5.48) into the real and imaginary parts, and reassembling yields,

$$\mathbf{A}'_{5((4n+2)\times(2n+4))}\mathbf{x}'_{5((2n+4)\times 1)} = \mathbf{b}'_{5((2n+4)\times 1)} \quad (5.49)$$

with

$$\mathbf{x}'_4 = \lfloor c \quad e\cos\beta \quad e\sin\beta \quad \Delta k_{22}p_{-n} \quad \ldots \quad \Delta k_{22}p_{-1} \quad \Delta k_{22}p_0 \quad \Delta k_{22}p_1 \quad \ldots \quad \Delta k_{22}p_n \rfloor^T$$

Where the vector $\mathbf{x}'_4$ contains the unknown crack force terms to be estimated. The condition of the regression matrix to be inverted has a role in obtaining better estimates of unknown parameters. This is obtained by considering regression equations at multiple measurement speed.

*Identification at multiple measurement speeds*: Identification algorithms presented above correspond to a single measurement speed. For accommodating estimation with a set of multiple measurement speeds, the regression equation Eqn. (5.42) is modified as,

$$\begin{bmatrix} \mathbf{A}_4(\omega_1) \\ \mathbf{A}_4(\omega_2) \\ \vdots \\ \mathbf{A}_4(\omega_q) \end{bmatrix}_{(2n+1)q\times 3} \mathbf{x}_{4(3\times 1)} = \begin{Bmatrix} \mathbf{b}_4(\omega_1) \\ \mathbf{b}_4(\omega_2) \\ \vdots \\ \mathbf{b}_4(\omega_q) \end{Bmatrix}_{(2n+1)q\times 1} \tag{5.50}$$

Similarly, the regression equation, Eqn. (5.48) is modified as,

$$\begin{bmatrix} \mathbf{A}_5(\omega_1) \\ \mathbf{A}_5(\omega_2) \\ \vdots \\ \mathbf{A}_5(\omega_q) \end{bmatrix}_{(2n+1)q\times 3} \mathbf{x}_{2(3\times 1)} = \begin{Bmatrix} \mathbf{b}_5(\omega_1) \\ \mathbf{b}_5(\omega_2) \\ \vdots \\ \mathbf{b}_5(\omega_q) \end{Bmatrix}_{(2n+1)q\times 1} \tag{5.51}$$

The identification algorithms are presented for identification of crack, unbalance, and damping using data from full-spectrum responses. The force and response coefficients can be chosen directly from the full-spectrum plots, which also generalize identification algorithms. Now, the illustrations for the frequency domain based identification are presented.

## 5.8 Numerical Illustrations for Identification Algorithms using Full-Spectrum

In the present section, identification algorithms (Eqn. (5.50) and Eqn. (5.51)) are used to estimate the fault parameters. The estimation is performed completely in frequency domain. The force coefficients $p_i$ and response coefficients $r_i$ , which are obtained using the full-spectrum, are used as an input to identification algorithms. The estimation of parameters is discussed in following subsection.

### 5.8.1 Simultaneous estimation of Damping, Eccentricity, and Additive Crack Stiffness in Frequency Domain

Different ranges of frequencies are chosen from which responses are taken for the identification algorithm. Figure 5.6 shows the critical speed (with gyroscopic effect) of once per revolution frequency component of force at 680 rad/s. Similarly, the critical speeds due to twice per revolution component of crack force occurs at 340 rad/s, while the critical speed due to thrice per revolution frequency component of crack force occurs at 226 rad/s. Based on the critical speeds and their half-power points, the following ranges of measurement spin-speeds are chosen as shown in Table 5-2in steps of 1 rad/s. The estimates are obtained using different sets of measurement spin-speeds.

Table 5-2 Different speed range and harmonics considered for estimation

| Cases | Spin-speed range (rad/s) | Harmonics ($i$) considered |
|---|---|---|
| Case A | 30 to 224 | -7, -5, -3, -1, 0,1, 2, 3, 5, 7 |
| Case B | 228 to 336 | -7,-5, -3, -1, 0, 1, 3, 5,7 |
| Case C | 343 to 650 | -5,-3, -1, 0, 1, 3,5 |

The central frequency $\omega_{central}$ in the transformation matrix $\mathbf{T}^d$ is chosen as the mean of the measurement spin-speed range. For e.g., for case A, it is chosen as 112 rad/s. The estimates are obtained for various ranges of measurement spin-speeds (Table 5-2). The estimates of additive crack stiffness, unbalance eccentricity, and viscous damping are shown in Table 5-3. The estimates are found to conform well to the assumed parameters.

Table 5-3 Parameters estimates for measurement cases A, B, and C using full-spectrum responses

| Parameters | Assumed values | 1 to 224 rad/s | 228 to 336 rad/s | 343 to 640 rad/s |
|---|---|---|---|---|
| Damping, $c$ (N-s/m) | 38 | 37.99 | 37.99 | 37.48 |
| Eccentricity, $e$ (m) $\times 10^6$ | 0.1 | 0.099 | 0.101 | 0.101 |
| $e = \sqrt{(e\cos\beta)^2 + (e\sin\beta)^2}$ | | | | |
| Unbalance phase angle, $\beta$ (rad) | 0.175 | 0.1745 | 0.1744 | 0.1751 |
| $\beta = \tan^{-1}\left(e\sin\beta \big/ e\cos\beta\right)$ | | | | |
| Crack stiffness, $\Delta k_{22}$ (N/m) | 52165 | 52165.09 | 52165.89 | 52161.18 |

The parameters are also estimated for various noise levels as in Table 5-4 to Table 5-7.

Table 5-4 Parameters estimates for measurement cases A, B, and C with various noise levels

| Parameters | % Noise | Assumed values | 1 to 224 rad/s | 228 to 336 rad/s | 343 to 640 rad/s |
|---|---|---|---|---|---|
| Damping, | 1 | | 38.16 | 38.10 | 37.96 |
| $c$ (N-s/m) | 2 | 38 | 38.32 | 38.11 | 38.05 |
| | 5 | | 38.54 | 38.13 | 38.36 |
| Eccentricity, | 1 | | 0.099 | 0.093 | 0.100 |
| $e$ (m) × $10^6$ | 2 | 0.1 | 0.099 | 0.090 | 0.099 |
| | 5 | | 0.098 | 0.114 | 0.098 |
| Unbalance | 1 | | 0.204 | 0.171 | 0.174 |
| phase angle, | 2 | 0.175 | 0.234 | 0.174 | 0.178 |
| $\beta$ (rad) | 5 | | 0.325 | 0.179 | 0.184 |
| Crack stiffness, | 1 | | 51862.79 | 51954.58 | 51836.57 |
| $\Delta k_{22}$ (N/m) | 2 | 52165 | 51560.79 | 51674.49 | 51562.71 |
| | 5 | | 50653.95 | 50843.94 | 50874.06 |

### 5.8.2 Simultaneous Estimation of Damping, Eccentricity, and Crack Forces in Frequency Domain

Table 5-5 Estimates of crack force parameters for measurement cases A with various noise levels

| Parameters | Assumed values | Estimates in measurement spin-speed ranges 1 to 224 rad/s | | | |
|---|---|---|---|---|---|
| | | 0% Noise | 1% Noise | 2% Noise | 5% Noise |
| $\Delta k_{22}p_1$ (N/m) | 16604 | 16604.38 | 16504.40 | 16406.78 | 16113.85 |
| $\Delta k_{22}p_2$ (N/m) | 13041 | 13041.23 | 12964.52 | 12887.80 | 12657.47 |
| $\Delta k_{22}p_3$ (N/m) | 5535 | 5535.22 | 5504.31 | 5473.61 | 5380.68 |
| $\Delta k_{22}p_5$ (N/m) | 1106 | 1107.20 | 1098.43 | 1089.69 | 1063.64 |
| $\Delta k_{22}p_7$ (N/m) | 475 | 474.63 | 462.85 | 451.62 | 421.62 |
| $\Delta k_{22}p_0$ (N/m) | 13041 | 13041.32 | 12967.33 | 12893.35 | 12671.84 |
| $\Delta k_{22}p_{-7}$ (N/m) | 266 | 263.77 | 258.33 | 259.94 | 283.52 |
| $\Delta k_{22}p_{-5}$ (N/m) | 475 | 474.63 | 470.19 | 465.73 | 428.51 |
| $\Delta k_{22}p_{-3}$ (N/m) | 1106 | 1107.20 | 1096.57 | 1086.03 | 1055.05 |
| $\Delta k_{22}p_{-1}$ (N/m) | 5535 | 5535.23 | 5505.98 | 5476.79 | 5389.68 |

The identification algorithm for the estimation of crack force terms is presented in the regression equation Eqn. (5.48). The estimates for the different ranges of spin-speeds (Table 5-2) are tabulated as in Table 5-7 to Table 5.7. These estimates conform well to the assumed values.

Table 5-6 Estimates of crack force parameters for measurement case B with various noise levels

| Parameters | Assumed values | Estimates in measurement spin-speed ranges 228 to 336 rad/s | | | |
|---|---|---|---|---|---|
| | | 0% Noise | 1% Noise | 2% Noise | 5% Noise |
| $\Delta k_{22}p_1$ (N/m) | 16604 | 16573.17 | 16470.11 | 16415.29 | 16250.40 |
| $\Delta k_{22}p_2$ (N/m) | 13041 | 13041.17 | 12959.66 | 12884.45 | 12646.05 |
| $\Delta k_{22}p_3$ (N/m) | 5535 | 5535.24 | 5609.09 | 5580.31 | 5487.04 |
| $\Delta k_{22}p_5$ (N/m) | 1106 | 1107.20 | 1009.69 | 1015.04 | 1218.36 |
| $\Delta k_{22}p_7$ (N/m) | 475 | 474.63 | 337.49 | 289.71 | 720.83 |
| $\Delta k_{22}p_0$ (N/m) | 13041 | 13041.35 | 12971.65 | 12902.05 | 12693.89 |
| $\Delta k_{22}p_{-7}$ (N/m) | 266 | 263.77 | 192.59 | 131.88 | 229.19 |
| $\Delta k_{22}p_{-5}$ (N/m) | 475 | 474.63 | 346.82 | 237.85 | 408.80 |
| $\Delta k_{22}p_{-3}$ (N/m) | 1106 | 1107.19 | 1121.12 | 1135.49 | 1177.73 |
| $\Delta k_{22}p_{-1}$ (N/m) | 5535 | 5535.23 | 5526.75 | 5518.24 | 5494.36 |

Table 5-7 Estimates of crack forces parameters for case C with various noise levels

| Parameters | Assumed values | Estimates in measurement speed range 343 to 650 rad/s | | | |
|---|---|---|---|---|---|
| | | 0% Noise | 1% Noise | 2% Noise | 5% Noise |
| $\Delta k_{22}p_1$ (N/m) | 16604 | 16172.92 | 15153.90 | 15073.73 | 14876.18 |
| $\Delta k_{22}p_2$ (N/m) | 13041 | 13042.39 | 12848.60 | 12790.35 | 12662.35 |
| $\Delta k_{22}p_3$ (N/m) | 5535 | 5535.57 | 5462.96 | 5432.17 | 5351.48 |
| $\Delta k_{22}p_5$ (N/m) | 1106 | 1107.21 | 1108.71 | 1113.50 | 1139.42 |
| $\Delta k_{22}p_0$ (N/m) | 13041 | 13041.32 | 12967.87 | 12894.51 | 12674.49 |
| $\Delta k_{22}p_{-5}$ (N/m) | 475 | 474.62 | 395.98 | 429.69 | 326.01 |
| $\Delta k_{22}p_{-3}$ (N/m) | 1106 | 1107.17 | 915.11 | 913.51 | 927.08 |
| $\Delta k_{22}p_{-1}$ (N/m) | 5535 | 5535.41 | 4501.02 | 4477.31 | 4412.55 |

The figures Figure 5.7 and Figure 5.8 show the percentage error of estimates for various cases of measurement spin speed ranges. Here, the number in the abscissa of Figure 5.7 respresents the estimated parameter corresponding to the same row number in vector $\{X\}$ of Eqn. (5.52). Similarly, the number in the abscissa of Figure 5.8 represents the estimated parameter corresponding to the same row number in vector $\{X\}$ of Eqn. (5.53).

$$X = \{c \quad e \quad \beta \quad \Delta k_{22}\}^T \tag{5.52}$$

$$X = \{c \quad e \quad \Delta k_{22} \quad \Delta k_{22}p_1 \quad \Delta k_{22}p_2 \quad \Delta k_{22}p_3 \quad \Delta k_{22}p_5 \quad \Delta k_{22}p_7 \quad \Delta k_{22}p_0 \quad \Delta k_{22}p_{-7} \quad \Delta k_{22}p_{-5} \quad \Delta k_{22}p_{-3} \; \Delta k_{22}p_{-1}\}^T \tag{5.53}$$

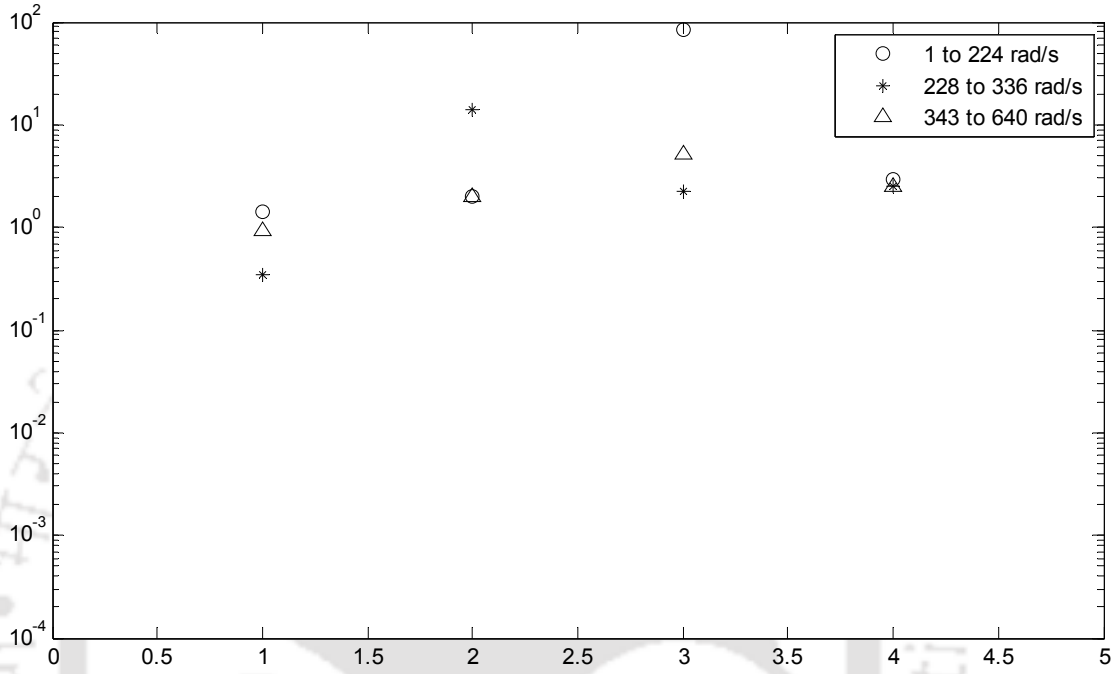


Figure 5.7 Percentage error of estimates of crack force for different spin-speed ranges with 5% response noise

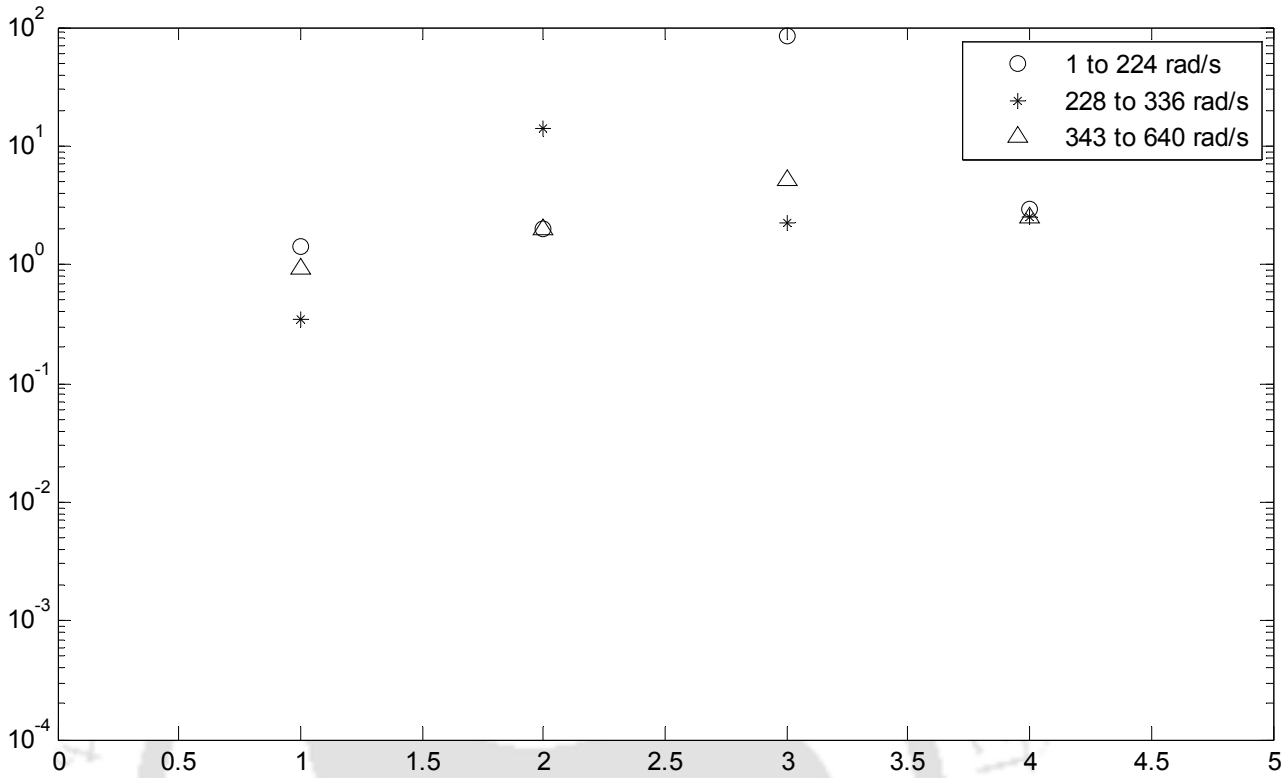


Figure 5.8 Percentage error of estimates of crack force for different spin-speed ranges with 5% response noise

### 5.8.3 Concluding Remarks

- The aim of the present chapter is to demonstrate identification algorithms for the estimation of the crack and unknown system parameters, for a general 4-DOF cracked rotor system.
- In this chapter, a 4-DOF cracked rotor model is presented. Two transverse translational displacements and two transverse rotational displacements are defined. The effect of gyroscopic couple is considered due an offset disc.
- The crack model is considered as a switching crack model. The crack parameter considers two additive crack stiffness terms; one in the direction of translational displacement and the

other in the direction of the rotational displacement. The crack axial location parameter is not considered. The crack flexibility matrices are defined in rotating co-ordinate system.

- A general 6-DOF transformation matrix is presented for the translation and rotational co-ordinates, of a rotor system with an offset disc. Flexibility matrices of the crack section are transformed to inertial co-ordinates and inverted to obtain the intact shaft stiffness matrix and the additive crack stiffness matrix.
- The system EOMs are obtained and defined in a complex form, which facilitates the use of the full-spectrum tool. Complex responses are obtained in the time and frequency domains.
- The system EOMs are reduced using the dynamic condensation for eliminating rotational displacements, which is otherwise difficult to measure accurately in practice. The reduced system EOMs are used to frame the identification algorithms.
- Identification algorithms are written in a regression form to estimate the crack and other unknown system parameters. The estimates are obtained using least squares method and are found to match with assumed parameters.

•

# CHAPTER 6

# Experimental Study of a Fatigue Crack in a Rotor

## 6.1 Overview of the Present Work

The primary characteristic of a rotor fatigue crack is its opening/closing mechanism termed as the *breathing*. The literature on rotor fatigue cracks has relatively few experimental studies. However, most of experimental studies involve study of hacksaw or wire-cut EDM crack or welded shaft crack. These kinds of induced cracks do not mimic the breathing behavior of a rotor fatigue crack. Although, several mathematical models exist, an experimentally determined breathing model is hardly available in literatures. Considering these aspects, an experimental set up of a rotor has been planned with a *fatigue crack* artificially initiated in its shaft. The following section discusses the fabrication and assembly of such a rotor set up along with its vibration measurement instrumentation. In later sections, processing of the acquired signals followed by estimation of unknown crack and system parameters has been carried out. Experimental crack forces have also been estimated.

## 6.2 Experimental Setup of Fatigue Cracked Rotor

A mild steel shaft containing a transverse v-notch (which acts as stress raiser) was fabricated using lathe operations. A fatigue crack was initiated in the shaft at the tip of v-notch using a *servo hydraulic machine* with a standard *three point bending fixture* for a cyclic fatigue loading. The rotor setup consists of a motor, a shaft with a fatigue crack supported by two bearings at ends, an offset disc, and a flexible coupling interconnecting the motor and rotor shafts. The shaft vibration displacements in two transverse directions are measured using *Eddy current displacement probes*. The *displacement magnitude* and *phase angle* are acquired at

individual *measurement speeds* below the system's first critical speed. A standard data acquisition system is used for the purpose. The experimental setup in detail is now presented.

### 6.2.1 Experimental Design and Layout

An experimental setup was planned for studying a fatigue crack in a rotor system. The experimental setup used a mild steel shaft in which a fatigue crack was generated. The shaft with disc mass was supported on bearings and connected to the motor shaft using a coupling. Primary objectives of the experimentation included determining the breathing behaviour of a fatigue crack, and identifying a crack using model-based identification algorithms. Vibration measurements were taken using displacement sensors and the photo-sensitive sensor for measuring a reference signal for the phase calculation. A line diagram for the experimental layout is shown in Figure 6.1.Part numbers are mentioned in Figure 6.1 and the corresponding lists of parts are tabulated in Table 6-1. A top view of the experimental setup is shown in Figure 6.2.

Table 6-1 List of parts of the experimental rotor setup

| Part No. | Part Name | Part No. | Part Name |
|---|---|---|---|
| (1) | Bed | (7) | Shaft with crack |
| (2) | Rotor bed | (8) | Bearing holder × 2 |
| (3) | Motor base | (9) | Bearing holder base ×2 |
| (4) | Additional motor base | (10) | Shims × 4 |
| (5) | Motor | (11) | Disk |
| (6) | Coupling | (12) | Sensor holder at crack location |

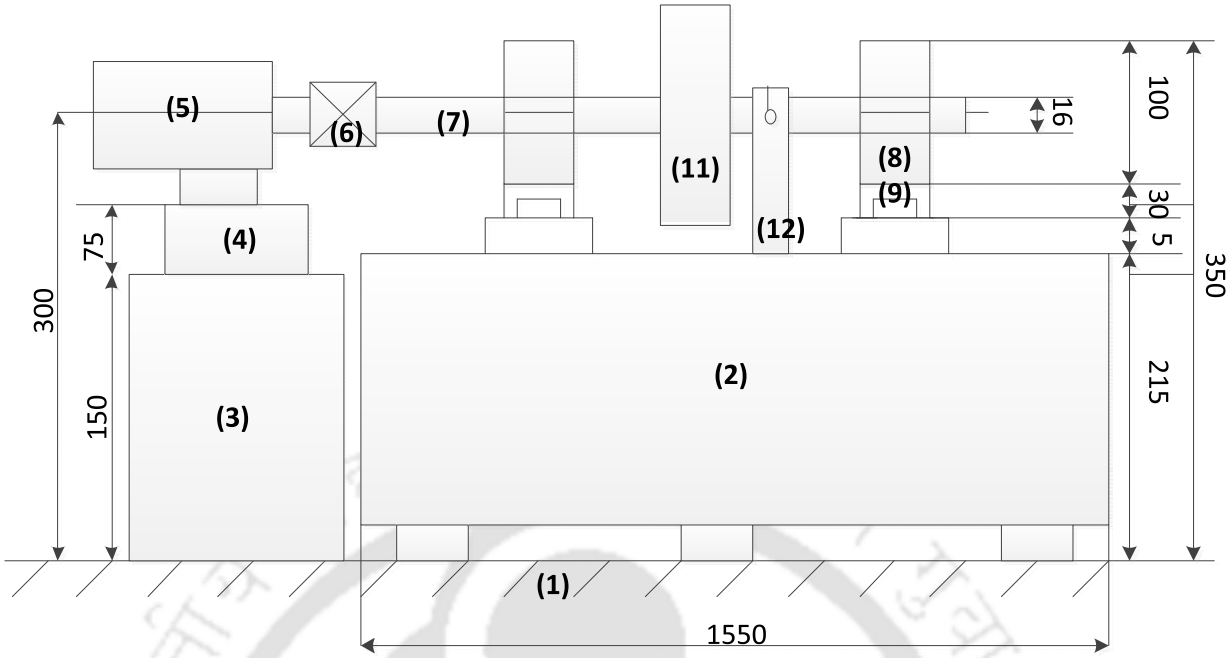


Figure 6.1 Plan for experimental setup of a cracked rotor

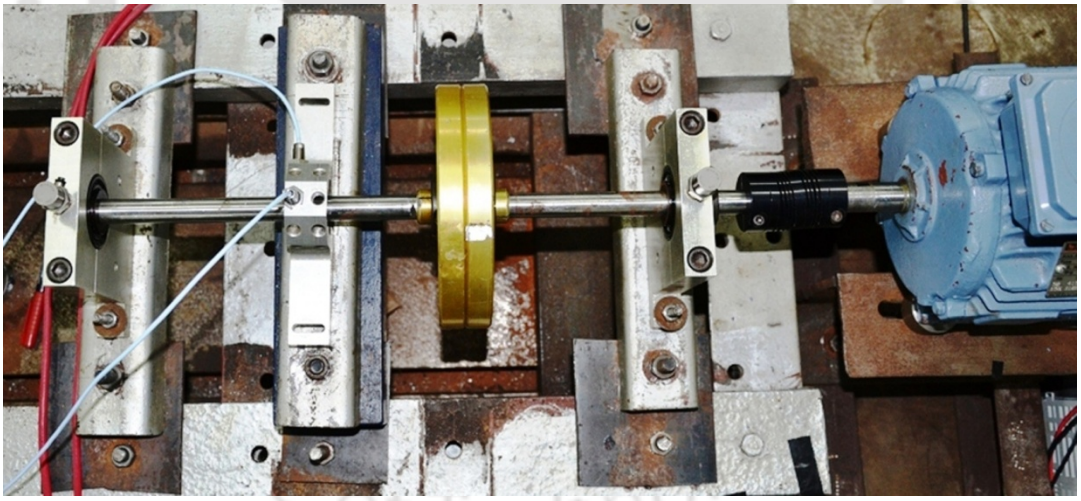

Figure 6.2 Top view of the experimental cracked rotor set up

Now, various components of experimental setup are elaborated in following sections.

### 6.2.2 Electric Motor

An *electric motor* drives the rotor setup through a flexible coupling. The electric motor was a low voltage three-phase TEFC (Totally Enclosed Fan Cooled) squirrel cage induction motor, supplied by BCH Electric Limited, India. A rigid base with C-Channels supported the electric motor as shown in Figure 6.3. Some of motor specifications are shown in Table 6-2.

Table 6-2 Motor specifications

| | |
|---|---|
| Ref. Standards | IS: 325-1996 |
| No. of Poles | 6 Pole |
| Ambient temperature | $50^0$ C |
| Supply Voltage/ ± variation | 415 V A.C. ± 10% |
| Frequency/ ± variation | 50 Hz ± 5% |
| RPM | 2845 |
| KW/ HP | 0.75/ 1.0 |
| Direction of rotation | Bi-directional |
| Vibration level | As per normal class of IS: 12075-1986 |
| Noise level | As per IS: 12065-1987 |
| Motor shaft | Threaded center hole- As per DIN 332, Part-2<br>Key and Keyway- As per IS: 2048-1983 |

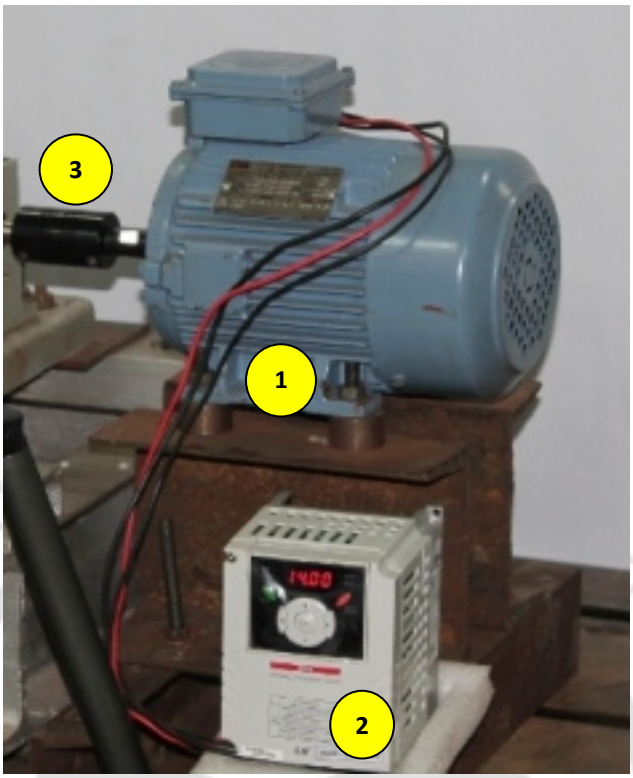


Figure 6.3 A drive unit: (1) An electric motor (2) A variable frequency drive for the motor speed control and (3) A flexible coupling connecting the motor and rotor shafts

### 6.2.3 Variable Frequency Drive

A variable frequency drive (VFD) regulated the three-phase AC motor. The VFID used was of LS Starvert make (Part no. (2) in Figure 6.3). The VFID or controller is programmable to accelerate the motor to a maximum set speed with a given angular acceleration or decelerate it from maximum speed to the rest. The controller used in the present work required a single phase input power (terminal wiring as per specification) and catered to a motor rating of up to 0.75kW. It had an operator interface and a digital tachometer display. The control method employed was sensor-less vector control. It is a variable frequency drive (VFD) control strategy that improves motor performance by regulating the VFD output based on a mathematical determination of motor characteristics and operating conditions. Operating conditions are estimated from measurements of electrical parameters. Sensor-less vector control is called “sensor-less” to distinguish it from vector

control with an encoder feedback, which optimizes the motor performance by regulating the VFD output based on the motor shaft speed and the position feedback from an encoder. Specifications of the controller are given in Table 6-3.

Table 6-3 Specifications of VFID controller

| | |
|---|---|
| Inverter Type | SV008iG5A-1 |
| Max capacity | [HP] 1 [kW] 0.75 |
| Max frequency | 400 Hz |
| Rated input frequency | 50 Hz |
| Control method | Sensor-less vector control |
| Frequency setting resolution | Digital: 0.01Hz<br>Analog: 0.06Hz |

### 6.2.4 Flexible Coupling

A flexible beam coupling of aluminum (Make: Ruland) connects the extended motor-shaft to the rotor-shaft (Figure 6.3 (3)). Also known as *helical coupling*, it transmitted torque between two shafts while allowed for the angular misalignment, the parallel offset and even the axial motion, of one shaft relative to the other. A single piece of a material became flexible by removal of the material along a spiral path resulting in a helical shape. A beam coupling did not exhibit the backlash found in some multi-piece couplings. The coupling had screws on both the motor and the rotor assembly sides for assembly and loosening. Some of coupling specifications are provided in Table 6-4.

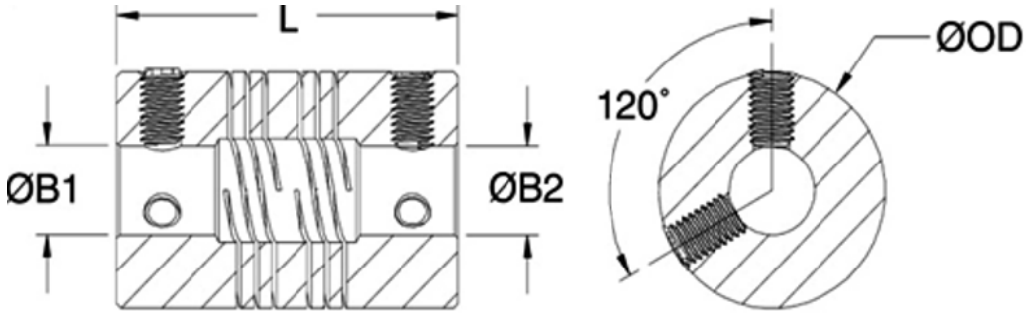


Figure 6.4 A flexible beam coupling

Table 6-4 Specifications of the flexible coupling

| Specification | FSR24-10-6-A | |
|---|---|---|
| Bore, *B*1 | 0.625” | (15.875 mm) |
| Bore, *B*2 | 0.375” | (9.525 mm) |
| OD | 1.5” | (38.1 mm) |
| Length, *L* | 2.25” | (57.15 mm) |
| Shaft Penetration | 1.042” | (26.467 mm) |
| Set screw | M6 | |
| Static Torque | 95 lb-in | (1094 kg-mm) |
| Torsional stiffness | 0.043 Deg/lb-in (0.381 x $10^{-4}$ Deg/N-mm) | |
| Moment of inertia | 0.1023 lb-in$^2$ | (29.964 kg-mm$^2$) |
| Angular misalignment | $3^0$ | |
| Parallel misalignment | 0.008” | (0.203 mm) |
| Axial motion | 0.005” | (0.127 mm) |

(Conversion factors: 1 inch = 25.4 mm; 1 lb-in = 11.521 kg-mm)

### 6.2.5 Bearings and Bearing Housings

Two self-aligning ball bearings supported the rotor shaft. Bearings were sealed and had a snap ring for the axial location. The tapping on the bearing housing facilitated transducer mounting. The bearing had a bore of 15.8 mm and an outer diameter of 47 mm. The shaft and the bearing had an interference fit. Bearings had inserts designed for set-screw locking to the shaft.

### 6.2.6 Rotor Disc

The rotor disc consisted of standard aluminum disc of 15.24 cm diameter and of mass 1 kg, placed at an offset location of the shaft span. The disc had 10-degree interval threaded holes for means of balancing or introducing the unbalance.

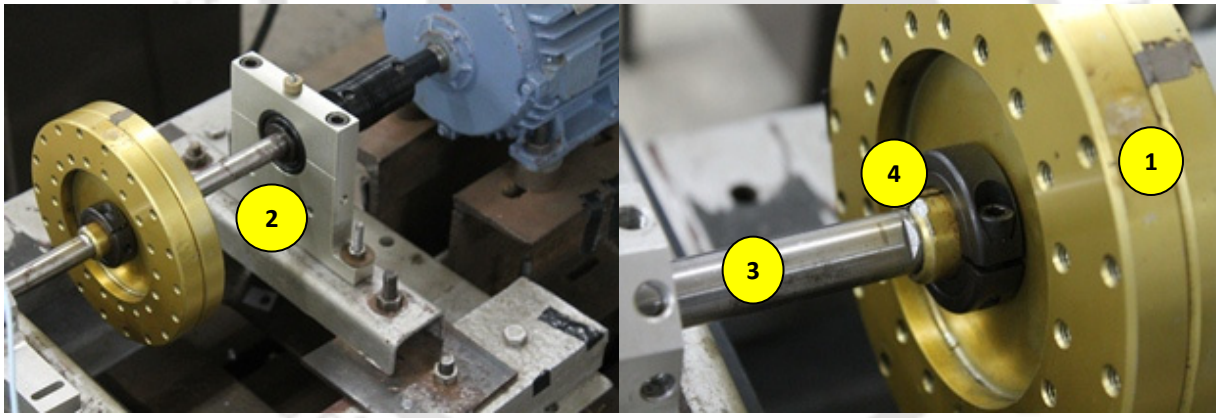


Figure 6.5 Close view of (left) bearing block (right) disc: (1) The disc (2) Bearings in horizontal split-type housing, mount for the accelerometer on the top (3) The shaft
(4) The notch with fatigue crack

### 6.2.7 Rotor Shaft

A mild steel rotor shaft of 15.8 mm diameter and 545 mm length was prepared as follows. Turning of a 25 mm diameter AISI 1018 low carbon steel shaft was performed to the required dimension followed by grinding of the outer diameter (OD) in an external cylindrical grinding machine by

holding the shaft in between lathe centers. The surface finishing of the outer surface was 0.2 μm Ra. The material composition of AISI 1018 is given in Table 6-5 and material properties are given in Table 6-6.

Table 6-5 Material composition of the rotor shaft

| Element | C | Fe | Mn | P | S |
|---|---|---|---|---|---|
| % Wt. | 0.14-0.2 | 98.81-99.26 | 0.6-0.9 | 0.04 | 0.05 |

Table 6-6 Material properties of the rotor shaft

| Property | At 25°c |
|---|---|
| Density | 7.87 g/cc |
| Hardness, Brinell | 131 |
| Tensile strength, ultimate | 450 MPa |
| Tensile strength, yield | 380 MPa |
| Elongation at break | 16% in 50 mm |
| Reduction of area | 40 % |
| Modulus of elasticity | 200 GPa |
| Bulk modulus | 140 GPa |
| Poisson's ratio | 0.29 |
| Shear modulus | 80 GPa |

A notch was machined using a horizontal-type milling machine with a $45^0$ angle-milling cutter. The notch was located axially offset at a distance of 225 mm from one end. The generation of fatigue crack is now discussed.

### 6.2.8 Generation of Fatigue Crack

The fatigue crack is the progressive and localised structural damage that occurs when the material is subjected to a cyclic loading. The objective of the work is to initiate a crack (fatigue pre-crack) in a notched shaft, for experimental purpose of the crack identification. Most of earlier experimental studies involved the study of hacksaw or wire-cut EDM crack or welded shaft crack. These kinds of induced cracks do not mimic the breathing behavior of a rotor crack. Also, no standards are available for fatigue testing of plain round shafts. Hence, the generation of fatigue crack was a difficult process.

*Initiation of fatigue crack*: The fatigue crack is expected to initiate at the notch position of the shaft specimen, which has maximum local stress (stress concentration). A sharp 900 V-notch was machined. A $90^0$ V-notch is generated on the shaft. The depth of the V-notch is around 1mm. The specimen shaft with V-notch was subjected to cyclic stress using a 100 kN servo hydraulic machine with a standard three-point bending fixture. The specimen could also be cyclically loaded in its axial direction. In both cases, the fatigue failure at notch is in mode I. Mode I is the opening mode and the dominant displacement is normal to the crack surface (Prashantkumar, 1999).

*Principle of operation*: Notched shaft specimens were supported on two precision machine fixed anvils of a defined radius (10 mm). The force was applied centrally (three-point bending). The support beam was graduated lengthwise in metric units for accurate positioning of anvils equally spaced relative to the central line. Adjustable specimen stops were provided so that the specimen could be loaded quickly and accurately positioned on the lower anvils.

Figure 6.6 Instron machine and its display console


Figure 6.7 Test shaft in the three-point bending fixture

Figure 6.8 Shaft with notch under fatigue loading

Table 6-7 Fatigue loading three point bending test configuration

| | |
|---|---|
| Machine type and capacity | Instron Servo Hydraulic 100 kN |
| Machine model | Instron 1342 |
| Test Method | Three point bending test |
| Operating Frequency | 10 Hz |
| Stress Ratio, R | 0.3 at $25^0$ c |
| Compression | 6 kN to 1.8 kN |
| Support span | 140 mm |

*Test Methodology*: In the fatigue loading, nominal maximum stress values are less than the ultimate tensile stress and yield strength limit of the material. Thus, the shaft specimen should be subjected to fatigue testing with a cyclic loading whose maximum value is well below the yield strength limit of the specimen material. The fatigue cycling could be high-cycle fatigue which requires more than $10^4$ cycles to fail where stresses are low and deformation is primarily elastic. In the low-cycle fatigue testing, stresses are high enough for plastic deformation to occur.

Once the maximum ($P_{max}$), mean ($P_{mean}$) and minimum values ($P_{min}$) for the cyclic fatigue loading are determined; the shaft specimen is subjected to this loading and the crack initiation is expected

after a certain number of cycles. In order to monitor for the crack initiation, the following methods are adopted. Experimentally determined calibration curves relate the displacement per unit load to the crack length for each specimen. The calibration relationship is given as,

$$\frac{EB\bar{v}}{P} = F\left(\frac{\bar{a}}{\bar{w}}\right) \tag{6.1}$$

where $E$ is the Young's modulus, $B$ is the specimen thickness, $\bar{w}$ is the specimen width, $\bar{v}$ is the displacement, $P$ is the load, $F\left(\frac{\bar{a}}{\bar{w}}\right)$ is the function of $\frac{\bar{a}}{\bar{w}}$ for single-edge-cracked specimens and depend on the specimen geometry, where $\bar{a}$ is the initiated crack length and $w^c$ is the specimen width. Thus, it can be seen that with constant $E$ and $B$, the load versus displacement curve is dependent on the function $F\left(\frac{\bar{a}}{\bar{w}}\right)$. With increase in the crack length $a^c$ for a given loading $P$, the displacement (positional amplitude) $v$ is expected to increase. Also, as the slope of the load versus displacement curve gives stiffness of the crack section, the stiffness or the slope of the curve is expected to decrease with the increase in the displacement. Thus, a change (increase) of 2% of the initial value of the positional amplitude can be considered as a suitable indicator of the fatigue crack initiation.

*Static loading three-point bending test*: A static 3-point bending test was conducted to determine the yield strength and modulus (stiffness) of the material. The shaft specimen was mounted with point contacts on two machine fixed anvils of defined radius. The load was applied centrally at the third point contact. The notch location was central to the support span. The deflection of the specimen was controlled at a defined strain rate of 0.5 mm/min and the corresponding loads were obtained. A load versus deflection curve is plotted from the corresponding data. It is observed from

Figure 6.9 that when the load reaches a value of 8 kN, the specimen begins noticeable plastic deformation.

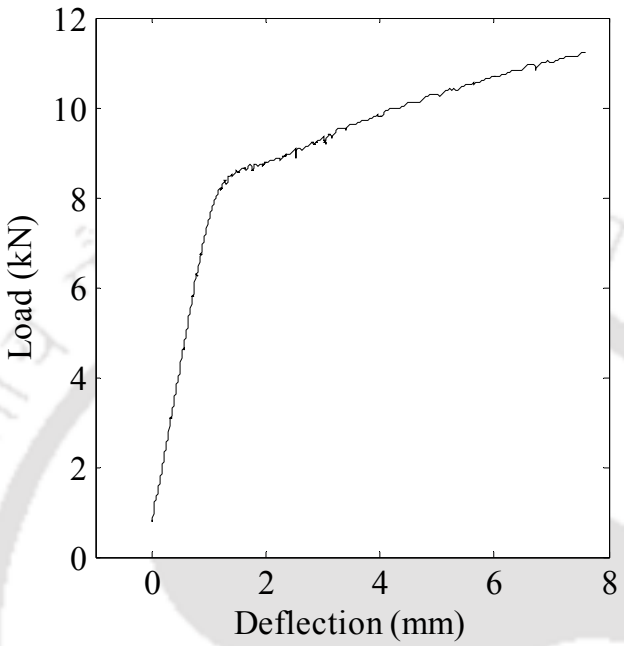


Figure 6.9 Load versus deflection variation for the test shaft with a notch

The slope of elastic portion of the curve in Figure 6.9 gives Young's modulus of the material as 2.6 GPa.

*Cyclic loading 3-point bending test*: The specimen was mounted; as described earlier in the standard 3-point bending fixture. Based on yield stress, a cyclic loading with $P_{max}$ = 6 kN and $P_{min}$ = 1.8 kN for a stress ratio of $R$ = 0.3 was provided using the servo hydraulic machine. The ratio of minimum stress to maximum stress is one cycle of loading in a fatigue test. Tensile stresses are considered positive and compressive stresses as negative. Thus, the shaft specimen was subjected to fatigue cyclic loading. The number of cycles and the corresponding displacement

values (positional amplitude) were noted. For shaft specimen the observation is tabulated in Table 6-8.

Table 6-8 Number of cycles versus positional amplitude at notch during fatigue loading

| No. of cycle | Positional amplitude (mm) | No. of cycle | Positional Amplitude (mm) |
|---|---|---|---|
| 500 | 0.2491 | 14000 | 0.2549 |
| 1000 | 0.2488 | 14500 | 0.2554 |
| 1500 | 0.2489 | 15000 | 0.2558 |
| 2000 | 0.2491 | 15500 | 0.2559 |
| 2500 | 0.2490 | 16000 | 0.2566 |
| 3000 | 0.2494 | 16500 | 0.2571 |
| 3500 | 0.2492 | 17000 | 0.2579 |
| 4000 | 0.2499 | 17500 | 0.2580 |
| 4500 | 0.2497 | 18000 | 0.2591 |
| 5000 | 0.2500 | 18500 | 0.2594 |
| 5500 | 0.2500 | 19000 | 0.2601 |
| 6000 | 0.2501 | 19500 | 0.2610 |
| 6500 | 0.2507 | 20000 | 0.2616 |
| 7000 | 0.2505 | 20500 | 0.2625 |
| 7500 | 0.2507 | 21000 | 0.2632 |
| 8000 | 0.2514 | 21500 | 0.2642 |
| 8500 | 0.2517 | 22000 | 0.2652 |
| 9000 | 0.2518 | 22500 | 0.2667 |
| 9500 | 0.2522 | 23000 | 0.2681 |
| 10000 | 0.2525 | 23500 | 0.2697 |
| 10500 | 0.2524 | 24000 | 0.2713 |
| 11000 | 0.2527 | 24500 | 0.2725 |
| 11500 | 0.2531 | 25000 | 0.2740 |
| 12000 | 0.2536 | 25500 | 0.2761 |
| 12500 | 0.2537 | 26000 | 0.2778 |
| 13000 | 0.2540 | 26400 | 0.2779 |
| 13500 | 0.2543 | | |

It is observed that the initial value of the positional amplitude at the notch section during the start of a cyclic loading was 0.2491 mm. The final value after 26400 cycles was observed as 0.2779 mm. This corresponded to 12% increase in the positional amplitude (or the stiffness) at the notch section, which indicated a fatigue crack initiation. A liquid dye penetrant was used in Dye Penetrant Inspection (DPI) to conform the presence of the initiated fatigue crack. It is based on

capillary action where the liquid dye penetrates into discontinuities of the fatigue crack. The excess dye on the surface was then wiped out. During the successive cyclic loading, the dye oozed from corners of the notch indicating the presence of fatigue crack. Thus, a fatigue crack was initiated. The shaft with the fatigue crack initiated from the V-Notch is shown for different orientation of the V-Notch in Figure 6.10 (a)–(d). During the fatigue crack generation, a permanent bow measured around 0.4 mm was set in the shaft. The need for removing the effect of bow from the measurement data of cracked rotor is important, and is considered during post-processing of measured signals.

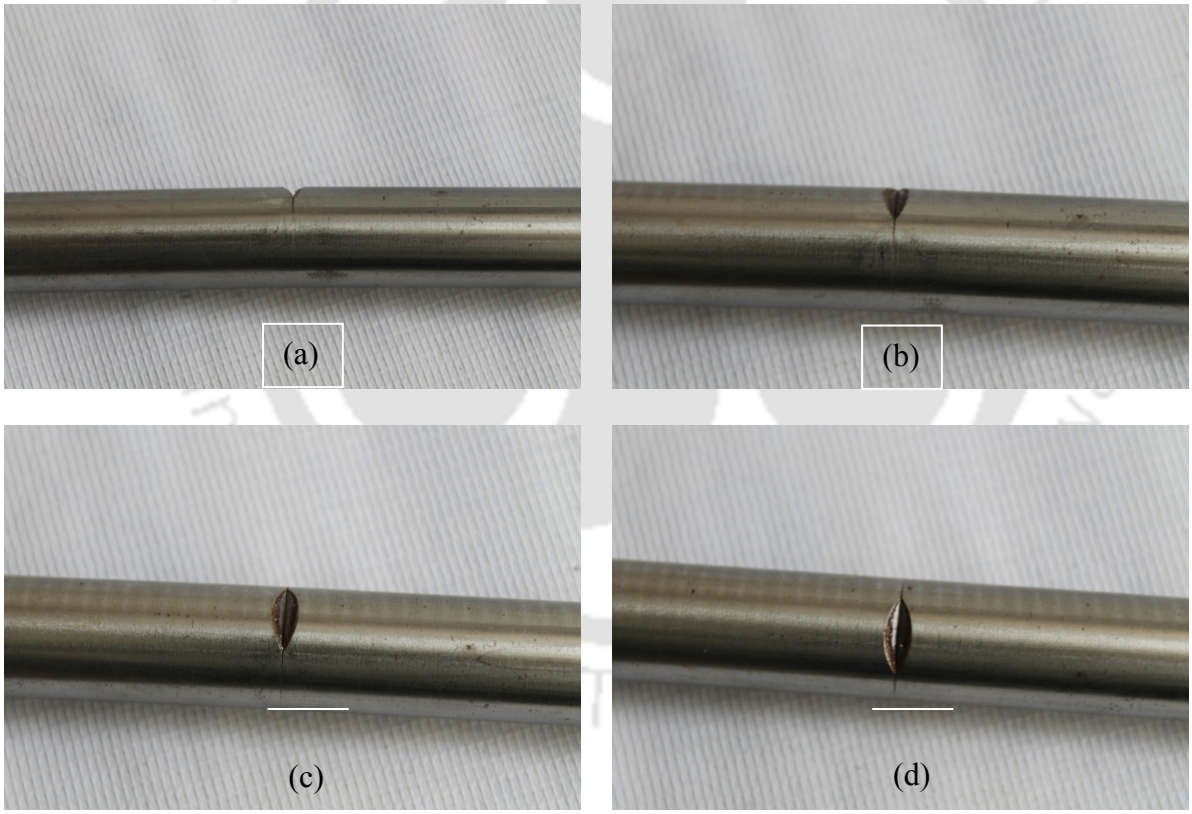


Figure 6.10 Fatigue crack generated in the notched shaft by fatigue loading (a)-(d) different orientation of the shaft

*Crack observation under optical microscope*: An optical microscope of Zeiss make was used to observe the fatigue crack. A progressive width fatigue crack of micron range was observed at 10X and 20X magnifications. Figure 6.11 (a) shows the fatigue crack initiated from the V-notch with a width of 34.71 µm. Figure 6.11 (b) shows the fatigue crack progressively decreasing in width to 26.93 µm. Figure 6.11 (c) shows the root of the fatigue crack and Figure 6.11 (d) shows the V-notch at a magnification of 20X. The actual crack depth will be obtained by breaking the shaft at the crack section. The depth of crack can be identified from the beach marks and striations, which are characteristic of a fatigue crack.

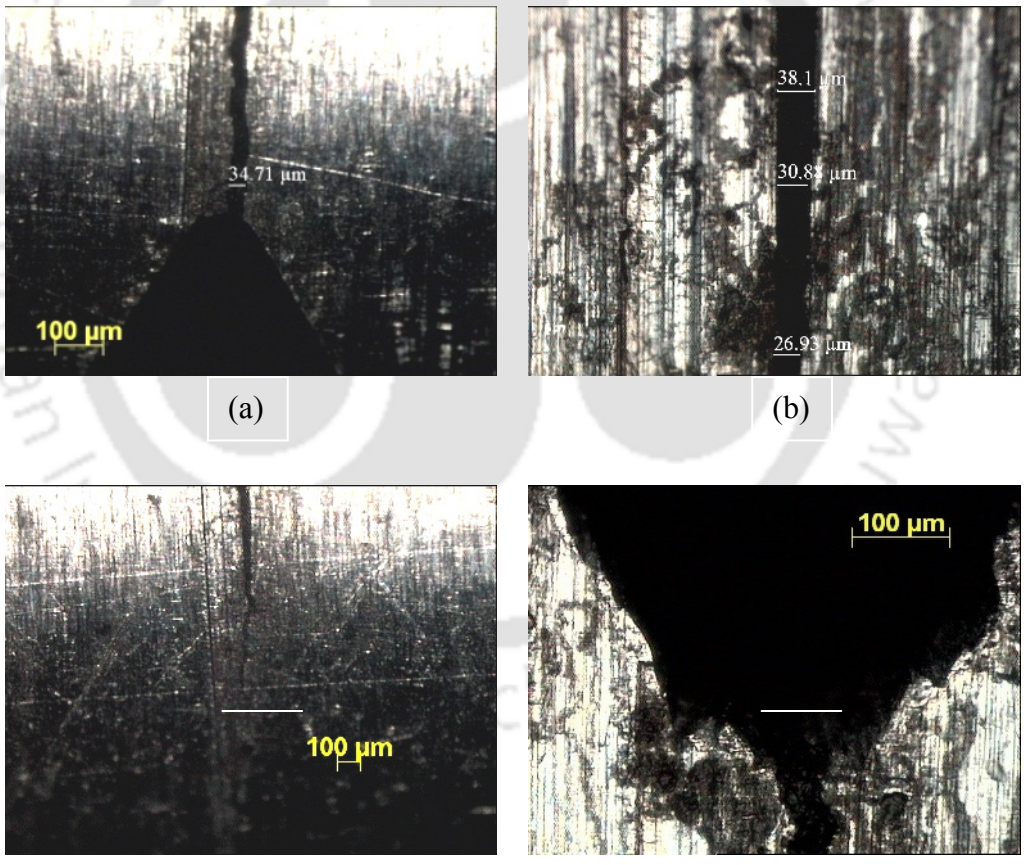


Figure 6.11 Optical microscope pictures showing a progressive fatigue crack and the notch (a) the crack growth from V-notch (b) a progressively decreasing of the crack width (c) the crack tip and (d) the V-notch

### 6.2.9 Sensors

Eddy current probes of Bently-Nevada make were used for measuring shaft displacements. They are non-contact type sensors and provide a voltage signal proportional to the gap between the probe tip and the shaft. It comprises of a probe, a length of extension cable and an oscillator/demodulator with 16V external DC supply. The proximity probe sensitivity was 7874 V/m. Probes were mounted on a stand with threaded holes as shown in Figure 6.12.

Figure 6.12 Eddy Current proximity probes for displacement measurement in two orthogonal transverse directions

Model no. 3300NSv proximity transducer system of Bently Nevada provides measuring setup for the vibration displacement. This system consists of a probe, extension cable and panel mount proximitor sensor. The transducer system has average scale factor of 7.87 V/mm, a linear range of 1.5 mm and requires -20 Vdc supply.

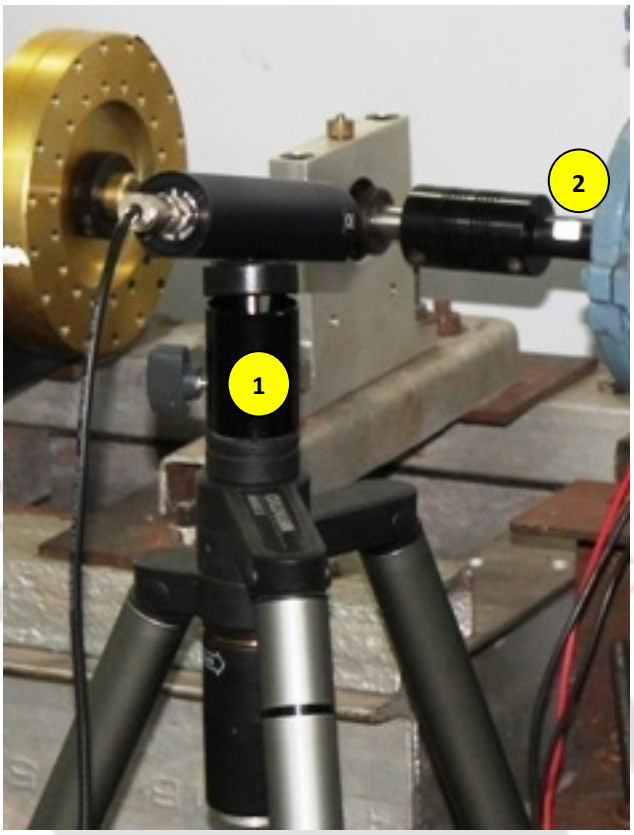


Figure 6.13 The measurement of the speed and the reference signal: (1) B&K optical tachometer probe (2) photo reflective tape for measuring the reference signal

A photoelectric tachometer probe (Model no. MM-0024 and B&K make) along with a reflective tape as a reference on the motor shaft measures speed as well as generates a reference signal for the phase angle measurement. The probe can be positioned between 50 mm and 800 mm from the object to be investigated, thus safely separating the probe from the possible contact with moving parts. The probe contains both a receiver and a transmitter of the infrared radiation. The probe mounts on a static camera tripod. The probe is directed such that its infra-red window faces the motor shaft on which a reflective tape is attached.

### 6.2.10 Data Acquisition Hardware

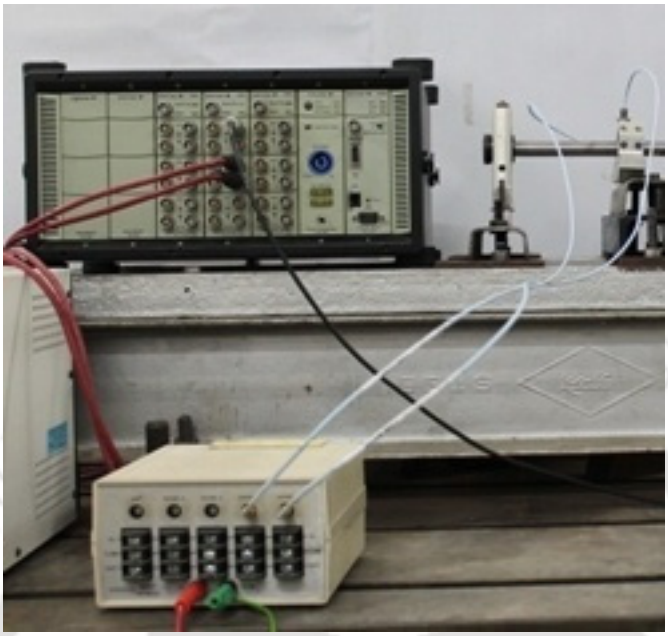

Figure 6.14 (1) A PULSE analyzer setup for the data acquisition

Pulse analyzer® 3560C is a sound and vibration analysis system. It provides the platform for the PC-based measurement from Brüel & Kjaer. A PULSE system consists of a PC with LAN interface, PULSE software, Microsoft® Windows® operating system, and data acquisition front-end hardware. Up to 10 front-ends can be combined into one measurement system with more than 200 input channels. The system has both time capture and FFT analyzers for recording the real-time data. The input/output conditioning modules perform signal conditioning and digitize transducer signals.

The PULSE software provides powerful analysis capabilities like real-time measurements, enough real-time DSP resources to perform FFT analysis on 16 channels to 25.6 kHz bandwidth (0%

overlap, 6400 lines) and 1/3-octave analysis on 6 channels to 25.6 kHz bandwidth. This performance requires a Pentium III 1GHz computer or faster.

### 6.2.11 Assembly of the Rotor Setup

The motor mounts on a base bolted to the machine bed. Integration of the motor with the VFD provides measurement speed control. The VFD terminal diagram is given in Figure 6.15, using which the motor is assembled with the VFD.

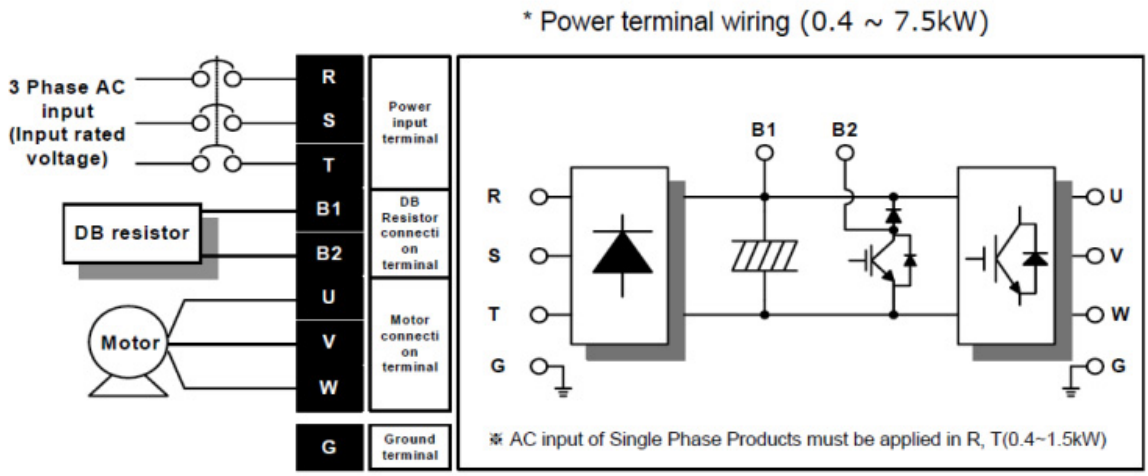


Figure 6.15 Terminal diagram of the VFD controller (Source: SV-iG5A user manual)

The shaft was fitted inside two self-aligning roller bearings, one at each end. The disc was assembled onto the shaft near by the fatigue crack. The schematic diagram of the shaft with the disc mounted on bearings is shown in Figure 6.16. Bearing housings were mounted on a cast iron test bed bolted on the machine bed.

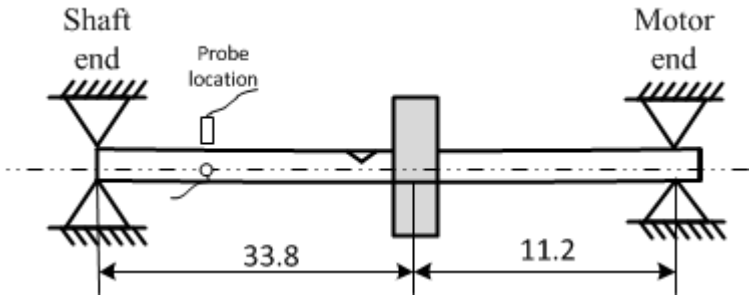


Figure 6.16 A schematic diagram of the rotor with a cracked shaft

For assembling the rotor shaft with that of the motor, heights of the motor shaft and the rotor shaft were measured from the machine bed using a height gauge. This ensured vertical alignment between two shafts by using the motor bed of customized height and shims. The motor bed was tightly bolted to the machine bed. The horizontal alignment between two shafts was ensured by means of shifting the motor position with respect to the rotor shaft centre and by means of a flexible coupling, which could accommodate a parallel misalignment of 0.008" (i.e., 0.203 mm).

Figure 6.16 depicts sensor positions. Two eddy current proximity probes were used for measuring the vibration displacement, one in the horizontal direction and another in the vertical direction, which were mounted on a rigid sensor mount as shown in Figure 6.9. The final assembly of the cracked rotor system with the measurement set up is shown in Figure 6.17.

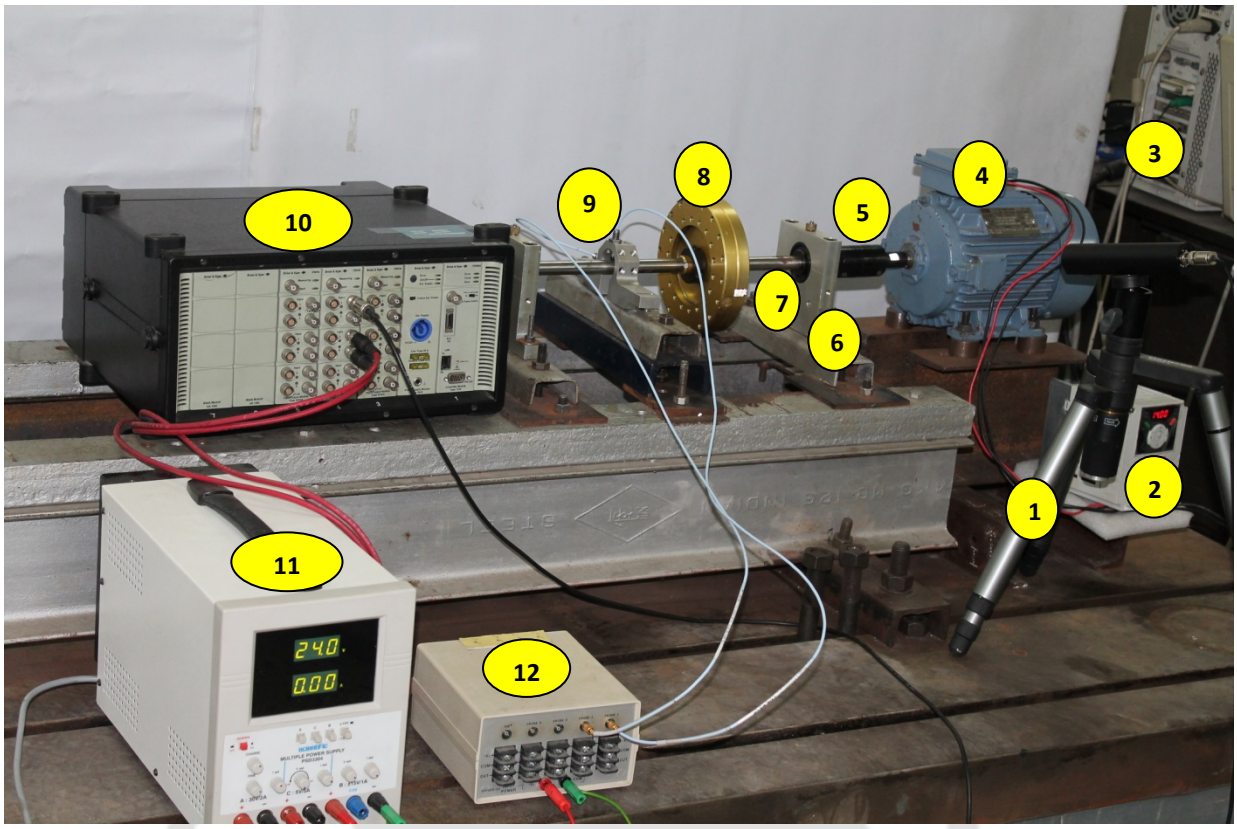


Figure 6.17 Assembly of the cracked rotor experimental setup (1) Optical tacho probe for phase measurement (2) Variable frequency drive (3) Computer for data analysis (4) Motor (5) coupling with motor shaft showing white reflective tape for phase reference (6) Sealed ball bearings with accelerometer mounting (7) Mild steel shaft with fatigue crack (8) Disc mass (9) 2 Mounted Eddy current proximity displacement probes (10) Brüel & Kjaer Data Acquisition system (11) DC power source and (12) Signal conditioner

## 6.3 Experimentation and Processing Procedure

The experimental setup of a cracked rotor was subject mainly to excitation forces due to the unbalance and the crack. The forcing due to the unbalance consists of one per revolution frequency component of the rotor spin speed (i.e., 1× harmonic). On the other hand, the forcing due to crack consists of multiple frequency components of the rotor spin speed (i.e., -5×, -3×, 1×, 7× etc.). In the present work, vibration displacements were measured for a set of *measurement spin speeds*, which were then processed and further used to test the developed identification algorithms.

Initially, free vibration tests were carried out from which natural frequencies were obtained. These correspond to critical speeds also, for the present symmetrical rotor case. Based on free vibration tests, measurement spin speed range was selected. The measurement data were acquired and further processed as follows.

### 6.3.1 Acquiring Vibration Displacement Measurements

*Eddy-current proximity probes* were used to sense vibration displacement measurements. These displacements were measured in two orthogonal directions in shaft transverse planes. An *optical tacho probe* was also used, in combination with a physical reference mark created on the motor shaft using a *photo-reflective tape*. The tacho-probe records a spike every time it crosses the reflective tape. This signal was used as a *reference signal* for measuring phase. The displacement and phase signal snow constitute the *raw measurement data*.

### 6.3.2 Removing the Effect of Shaft Bend

It has been earlier noted that the main challenge of measurement signal processing is the removal of effect of shaft bow before it could be used in the identification algorithm. A shaft bow behaves like a very large unbalance (frequency is same as rotor speed) with its magnitude independent of rotational speed. The force due to shaft bow is given as $ke_0e^{j(\omega t+\phi)}$, where the magnitude of bow effect is given by the product of shaft stiffness $k$ and the static deflection from the bearing center line $e_0$. In this case, shaft stiffness $k$ is not speed dependent. Hence, the shaft bow force, as it is generally modeled in the literature (Rao, 2001), is independent on the rotational speed. The following section discusses the compensation for the shaft bow in measurement signals, based on the slow roll data (i.e., measured displacement at very slow speed).

As a thumb rule, slow-roll speeds are typically 5% or less of the critical speed of the machine. The slow-roll data are captured at very low frequencies; typically they are 300 RPM or lower (Maalouf, 2007). This data has significant information, as faults such as misalignments and bows manifest themselves at slow-roll speeds. These problems cannot be distinguished at higher speeds, where other faults yield nearly identical signal. The compensation of slow-roll signal from the high-speed signal is performed using two different methods. One is the 1× *compensation*. This is in frequency domain where the magnitude and phase of 1× frequency component of the slow-roll vibration signal is subtracted from corresponding component of the high-speed vibration signal. Phase was referenced with respect to the reference signal measured using optical probe. The other method is *waveform compensation*, where the entire slow-roll vibration signal is subtracted from the high-speed vibration signal in time domain by stretching the slow roll data same as the high-speed data over a cycle. This is a preferred method of compensation as it uses the entire run-up signature data. However, the 1× frequency component is dominant in most cases of the shaft bend, and is used in the present work. In the present work, 1× compensation is used as follows:

The slow roll signal and measurement signal are phase compensated. Both signals are made to start from the same physical reference on the rotor shaft. Then, the full spectrum plots of two signals are obtained. Subsequently, the magnitude and phase of the 1× component of slow-roll signal is subtracted with magnitude and phase of the 1× component of measurement signal.

### 6.3.3 Phase Compensation

The slow roll signal and the measurement signal, before subtracting should start from the same physical reference on the rotor. The vibration displacement measurements from the test set up contains both magnitude and phase information. The slow-roll signal and the measurement signal both have different magnitude and phase information with respect to each other. Hence, they are to

be subtracted in the vector form. In this work, the vibration signals are processed such that they have the same phase with respect to the reference signal, i.e., their relative phase is zero. *Phase compensation* is done prior to obtaining the full-spectrum responses and 1× compensation.

## 6.4 Experimental Measurements

First, the free vibration tests are carried out to determine the critical speeds of the cracked rotor system. A measurement spin speed range is selected, in which the raw data of vibration displacements and reference phase signals are obtained.

### 6.4.1 Free Vibration Tests

The cracked rotor setup was subject to free vibration by an impact loading on its various components. Accelerometers were placed on bearing and disc locations, and vibration responses due to impact at different locations were measured. Frequency spectrum plots (i.e., FFT plots) were obtained showing natural frequencies. The bandwidth of the FFT was chosen to accommodate initial natural frequencies, by trial and error. The test was repeated and natural frequencies corresponding to the rotor system were obtained. Figure 6.18 to Figure 6.21 show free vibration response plots. During free vibration tests, the fatigue crack position remains closed and only the effect of notch as an open crack contributes to the measured natural frequency.

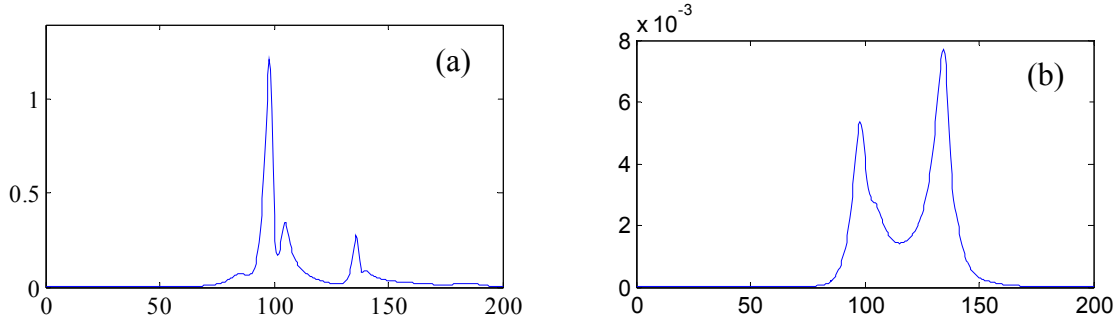


Figure 6.18 Free vibration natural frequencies while the impact position on the rotor disc from(a) accelerometer on bearing (b) accelerometer on disc

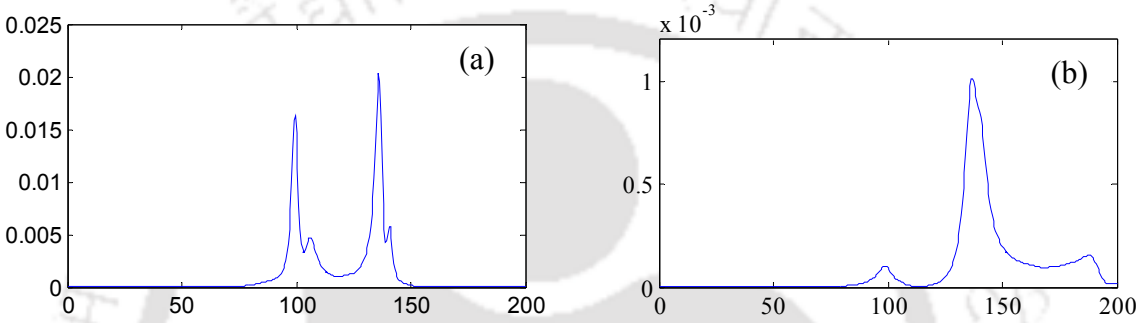


Figure 6.19 Free vibration natural frequencies while the impact position on the bearing from(a) accelerometer on bearing (b) accelerometer on disc

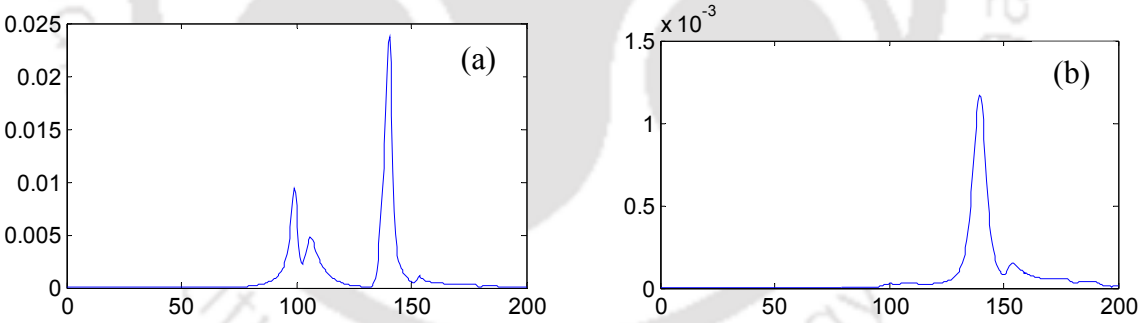


Figure 6.20 Free vibration natural frequencies while the impact position on the coupling from(a) accelerometer on bearing (b) accelerometer on disc

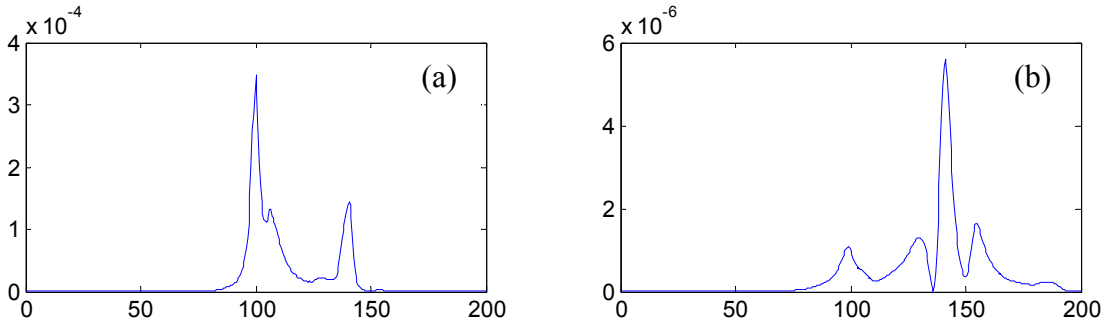


Figure 6.21 Free vibration natural frequencies while the impact position on the foundation from(a) accelerometer on bearing (b) accelerometer on disc

*Inferences from the free vibration test*: The natural frequency of the simply supported cracked rotor shaft with disc mass was 98 Hz. This corresponds to nearly the first forward critical speed of the set up. Natural frequencies corresponding to other impact locations were 136 Hz for bearing, 141 Hz for the coupling and 100 Hz for the rotor base and foundation. Based on these free vibration results, the measurement spin-speed range was chosen well below these natural frequencies to avoid critical speeds and/or resonance conditions so that crack forcing could be captured precisely.

### 6.4.2 Selection of Measurement Spin Speed Range

For acquiring vibration displacements, the measurement spin-speed range is chosen from 4 Hz to 14 Hz in steps of 1 Hz each. From the results of the free vibration test, the first critical speed of the cracked rotor system is observed at 98 Hz. Hence, for the cracked rotor set up under study, 14 Hz corresponds to the critical speed of six per revolution frequency component of the crack force.

*Slow-roll* is defined as the data collected from proximity probes observing a rotating shaft when the rotational speeds are too slow to contribute any meaningful rotor dynamic effects in the signal (Maalouf, 2007). Based on the definition of slow-roll, measurements at 4 Hz are chosen as the

slow-roll data, while measurements from 7 Hz to 14 Hz are chosen as the measurement data set for the crack identification.

### 6.4.3 Acquiring Vibration Displacement Measurements

The responses from Eddy current probes in vertical location (left) and horizontal location (right) are observed in Figure 6.22 to Figure 6.26, respectively, for various speeds.

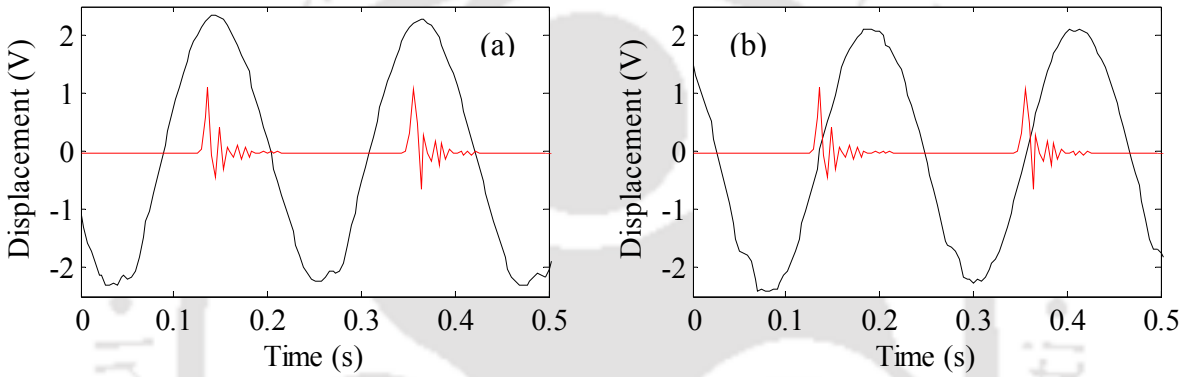


Figure 6.22 Displacement time history at 5 Hz rotor speed with the phase signal in (a) horizontal and (b) vertical sensor positions

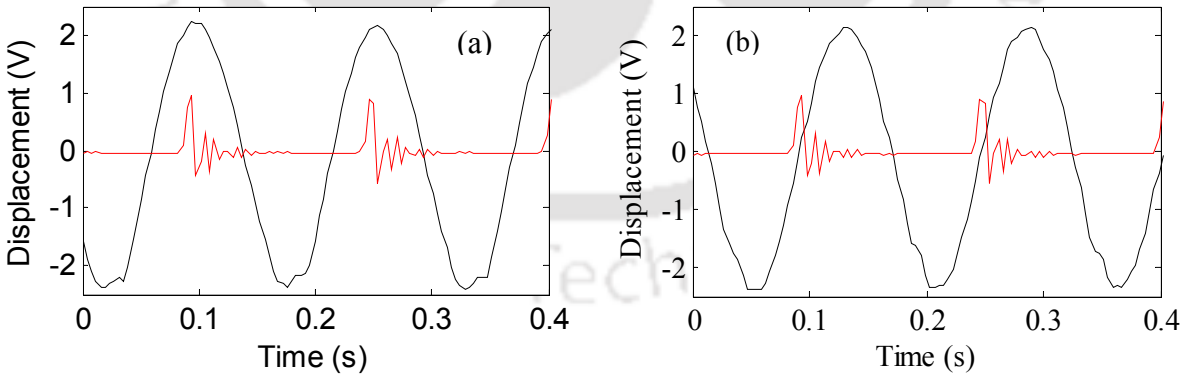


Figure 6.23 Displacement time history at 7 Hz rotor speed with the phase signal in (a) horizontal and (b) vertical sensor positions

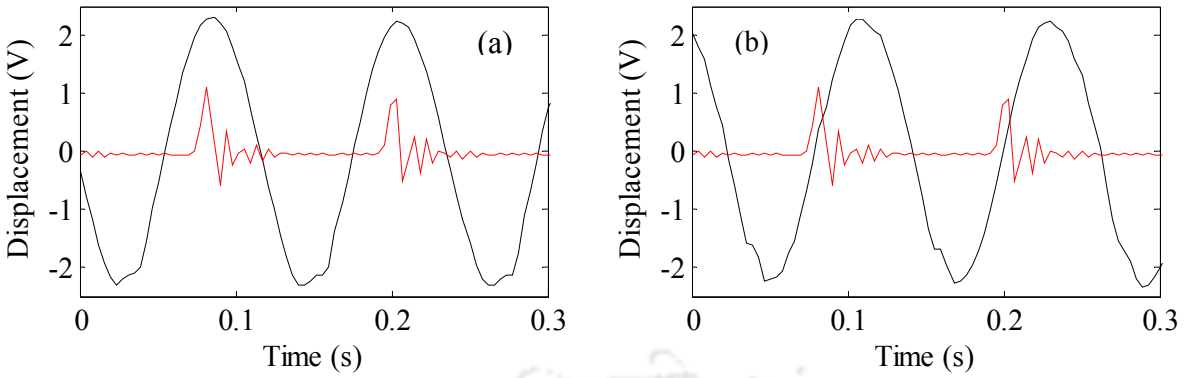


Figure 6.24 Displacement time history at 9 Hz rotor speed with the phase signal in (a) horizontal and (b) vertical sensor positions

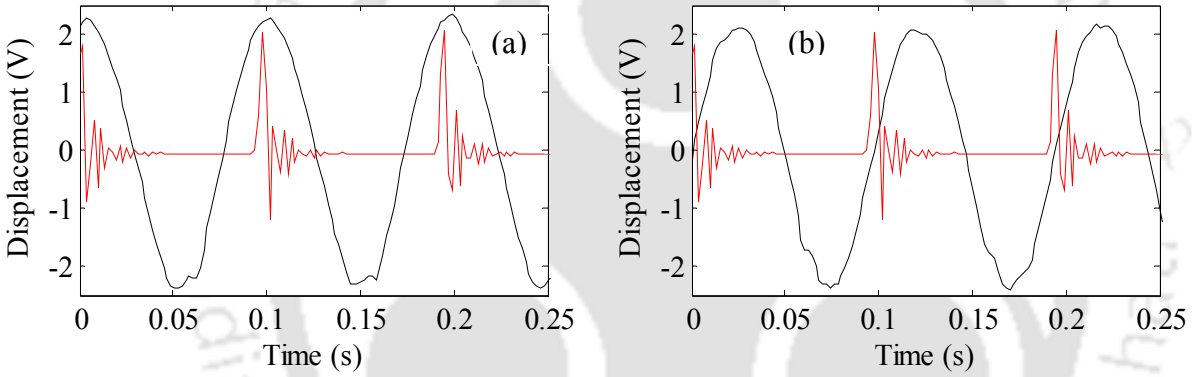


Figure 6.25 Displacement time history at 11 Hz rotor speed with the phase signal in (a) horizontal and (b) vertical sensor positions

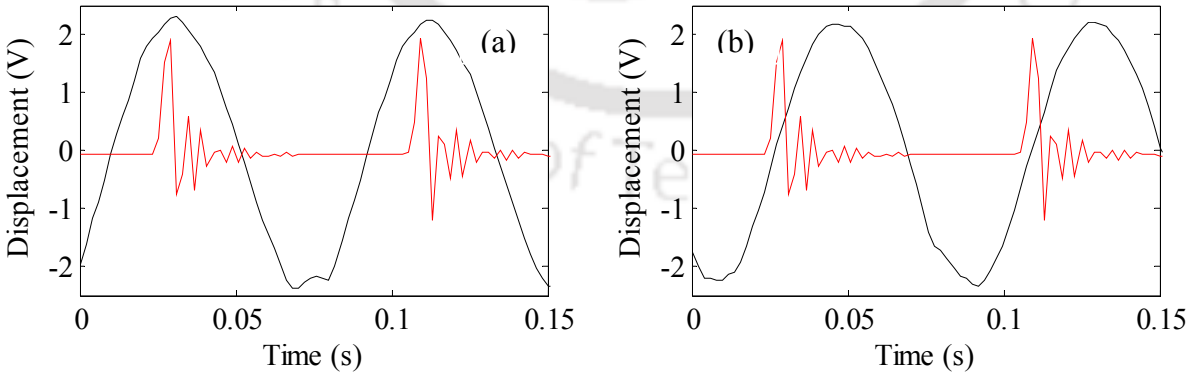


Figure 6.26 Displacement time history at 13 Hz rotor speed with the phase signal in (a) horizontal and (b) vertical sensor position

It was observed from the raw measurement data that the phase difference between the reference phase signal and the displacement signal remains nearly constant for each of the individual measurement speeds. This also confirmed the non passage of critical speed in the range of measurement speeds.

## 6.5 Signal Processing of Acquired Measurements

Here, phase compensation of the acquired signals and 1× compensation for removal of bend are carried out. For sample illustration of signal processing, the slow-roll measurement is chosen at 4 Hz and high-speed measurements are chosen at 13 Hz.

### 6.5.1 Phase Compensation

The slow roll signal and the measurement signal both have different magnitude and phase information with respect to each other. Hence, they are to be subtracted in the vector form. For a sample illustration, the slow-roll is chosen at 4 Hz and a high-speed measurement signal is chosen at 13 Hz measurement speed. For one of the Eddy current probe measurement, the plots for *displacement versus time* is shown in Figure 6.27. It can be observed that at any instant (say, $t = 0$), signal vectors are different in their magnitude and phase. (Note that the phase of the signals is measured with reference to a *physical reference mark* on the rotor. This reference mark is considered as $0^0$ phase angle and appears as a *spike* in the time domain plot).

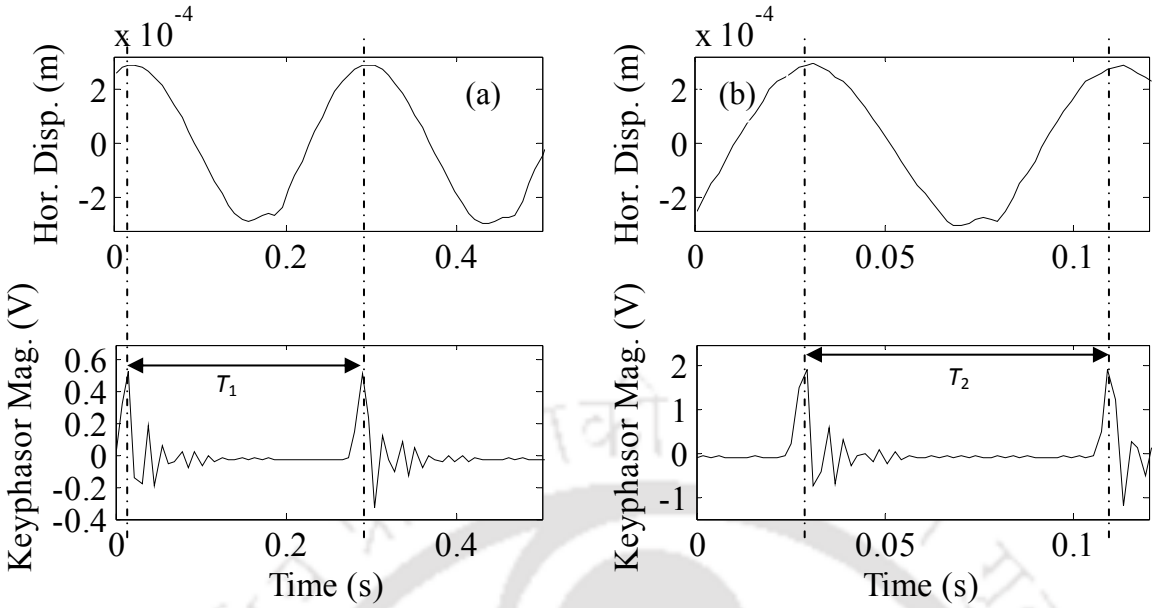


Figure 6.27 (a) Slow-roll displacement and phase signal at4 Hz
(b) Displacement and phase signal at 13 Hz

In order to subtract the signal vectors, magnitudes of signals can be subtracted one to one given that their corresponding phase angles are same. Hence, signals are *phase shifted* such that, the initial phase angle for both the signals is $0^0$, i.e., both signals are processed to start from the same phase, which is corresponding to the physical reference mark on the motor shaft. Measured signals and their corresponding phase signals for one cyclic period is shown in Figure 6.28.

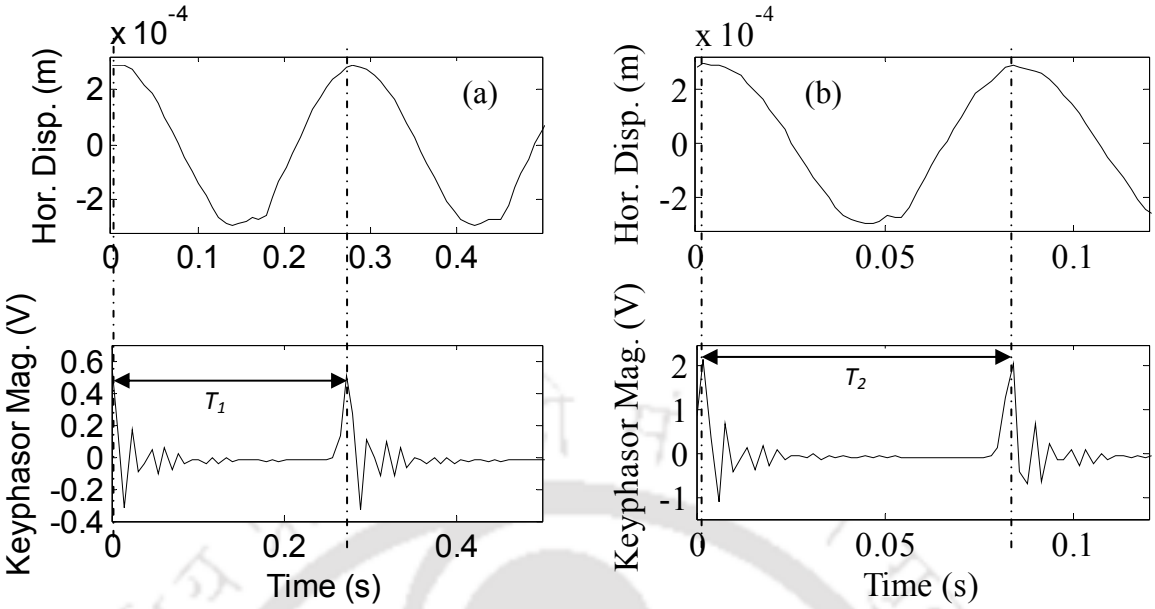


Figure 6.28 (a) Phase-shifted displacement signal at slow-roll
(b) Phase-shifted displacement signal at 13 Hz

The polar plot gives a better representation of the similar phase in two signals after phase shifting. The initial phase is zero and the phase at any other instant is same for both the signals as shown in Figure 6.29.In the polar plot representation, the start of the signals is set at $0^0$ phase angle marked as O and the end of the signals is at $360^0$ phase angle marked as □. This is for $2\pi$ phase angle length of the signals. Since, signals are periodic their subsequent phase angles will remain same. Similarly, phase compensation is carried out between the slow-roll and all other measurement signals.

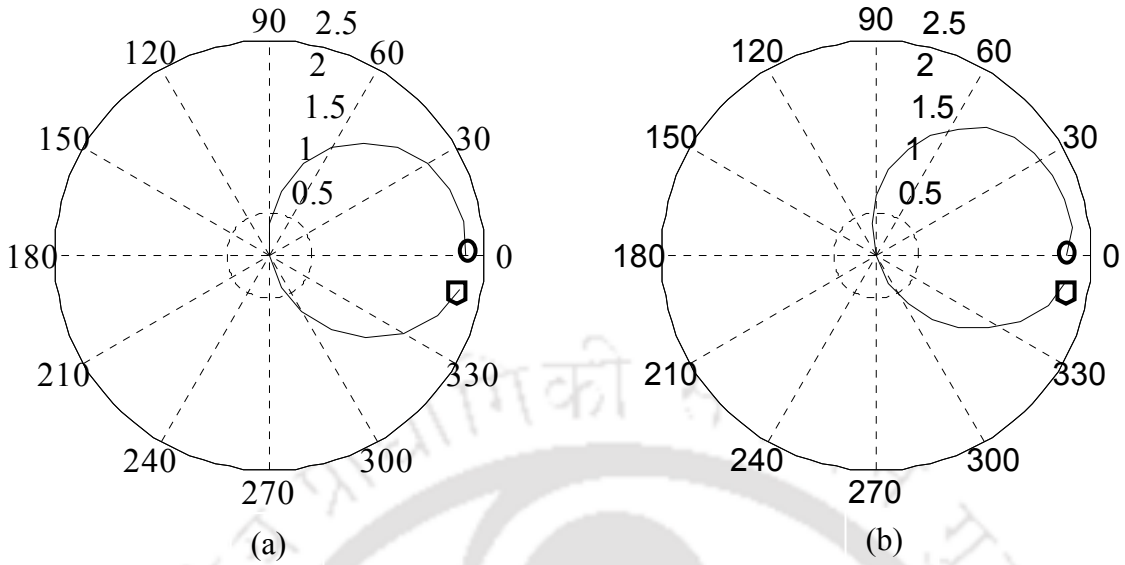


Figure 6.29 Polar plots for the first period of (a) slow-roll displacement signal (b) 13 Hz displacement signal (showing the same starting phase angle of $0^0$ for both signals) (radial direction: the shaft displacement in μm, angular direction: the shaft phase angle in deg)

### 6.5.2 1× Compensation for Bend Removal

The full-spectrum plots of the measurement signal at 13 Hz and other speeds are obtained. Their complex magnitudes, i.e., magnitude and phase of 1× frequency components are subtracted with corresponding 1× component of the full-spectrum plot of slow-roll signal. This is known as the 1× *compensation*. Then, the compensated Full-spectrum plots of displacement signals give *displacement coefficients* (Eqn. (4.2)). Displacement coefficients of measurement signals at slow-roll (4 Hz), 7 Hz, 10 Hz, and 13 Hz are shown in Figure 6.30 to Figure 6.33.

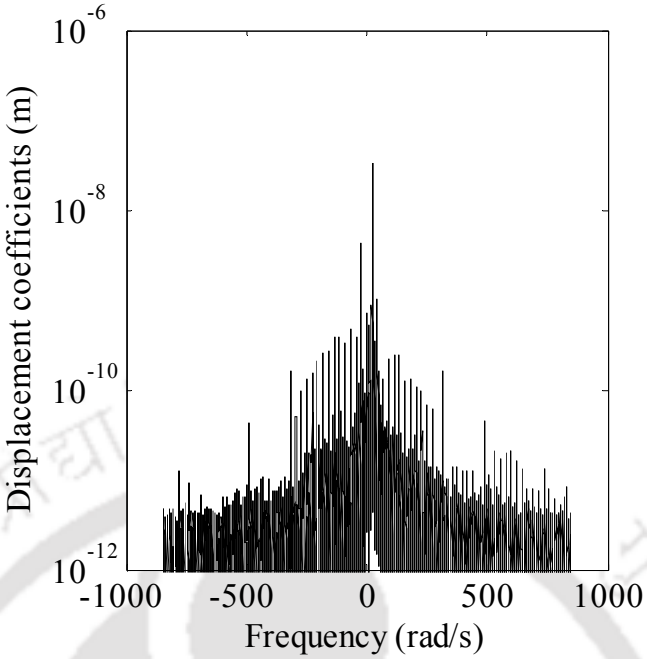


Figure 6.30 Full-spectrum plot showing displacement coefficients at the slow-roll

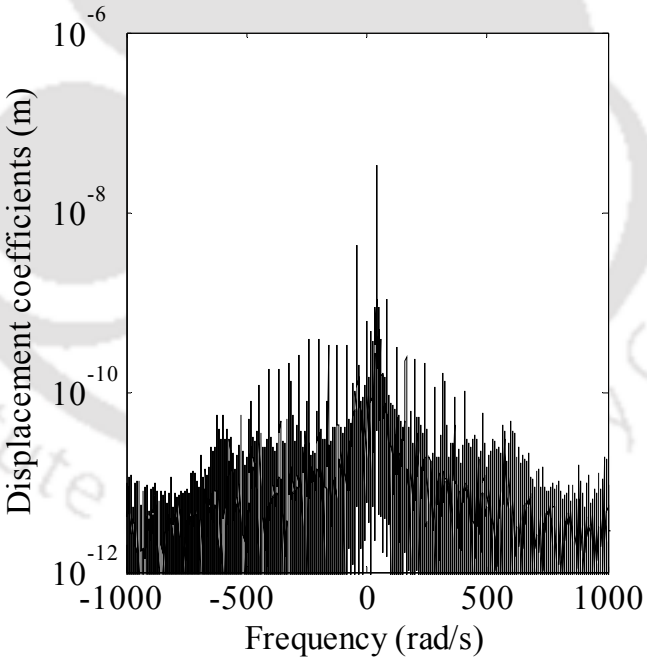


Figure 6.31 Full-spectrum plot showing displacement coefficients at 7 Hz speed after 1× compensation

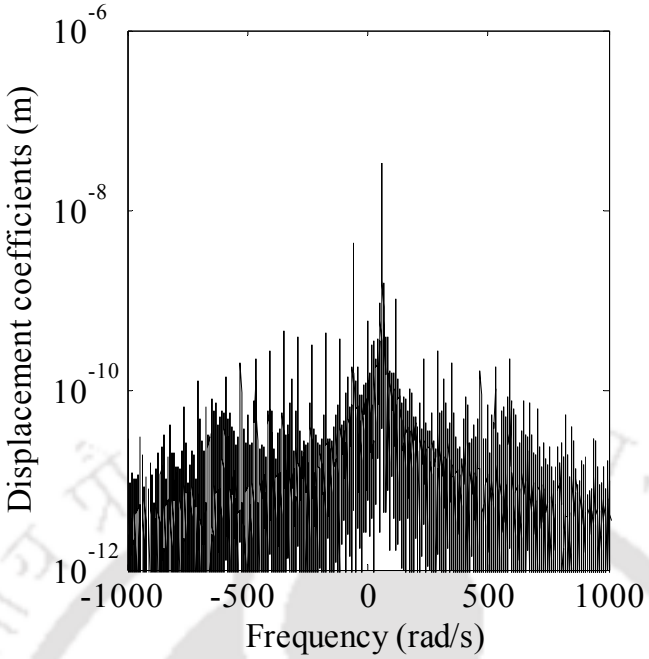


Figure 6.32 Full-spectrum plot showing displacement coefficients at 10 Hz speed after 1× compensation

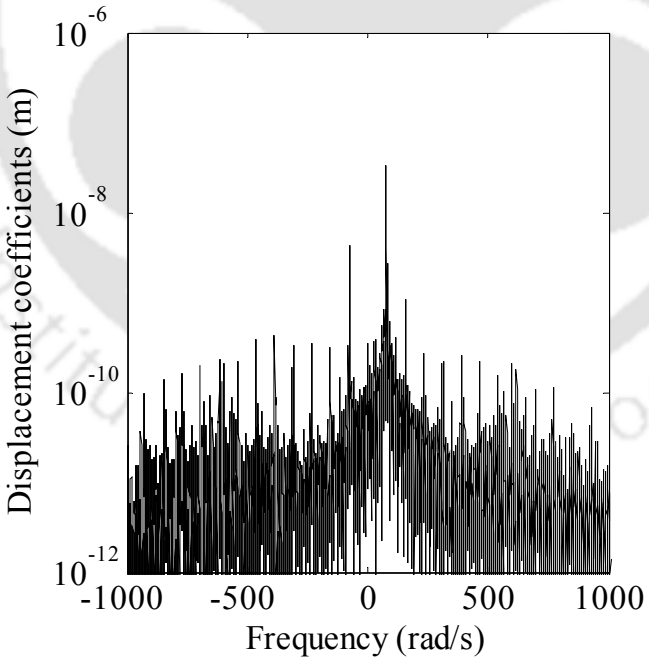


Figure 6.33 Full-spectrum plot showing displacement coefficients at 13 Hz speed after 1× compensation

### 6.6 Experimental Crack Identification

These processed displacement responses will now be used for the crack identification. The input data for identification algorithms are shown in Table 6-9.

Table 6-9 Input rotor system parameters to the identification algorithm

| | |
|---|---|
| Mass of the rotor system | $m$ = 2 kg |
| Natural frequency of the rotor system (from free-vibration tests) | $\omega_{nf}$ = 98 Hz |
| Intact shaft stiffness (With Notch) | $k = \left(\omega_{nf}^2 m\right)$ = 7.6 x $10^5$ N-m |
| Static deflection of the system | $w_x = \frac{g}{\omega_{nf}^2}$ = 2.6 x $10^{-5}$ N-m |
| Slow-roll speed | 4 Hz |
| Measurement Speeds | 7 Hz to 14 Hz in steps of 1 Hz |

The algorithms will be tested for three different sets of measurement spin speed ranges.

Table 6-10 Measurement Spin Speed Ranges

| Case | Measurement Spin Speed Range |
|---|---|
| A | 7 Hz to 10 Hz in steps of 1 Hz |
| B | 11 Hz to 13 Hz in steps of 1 Hz |
| C | 7 Hz to 13 Hz in steps of 1 Hz |

Now, the testing of identification algorithms with experimental responses is illustrated. Identification procedure is carried out according to the flow chart provided in Figure 6.34.

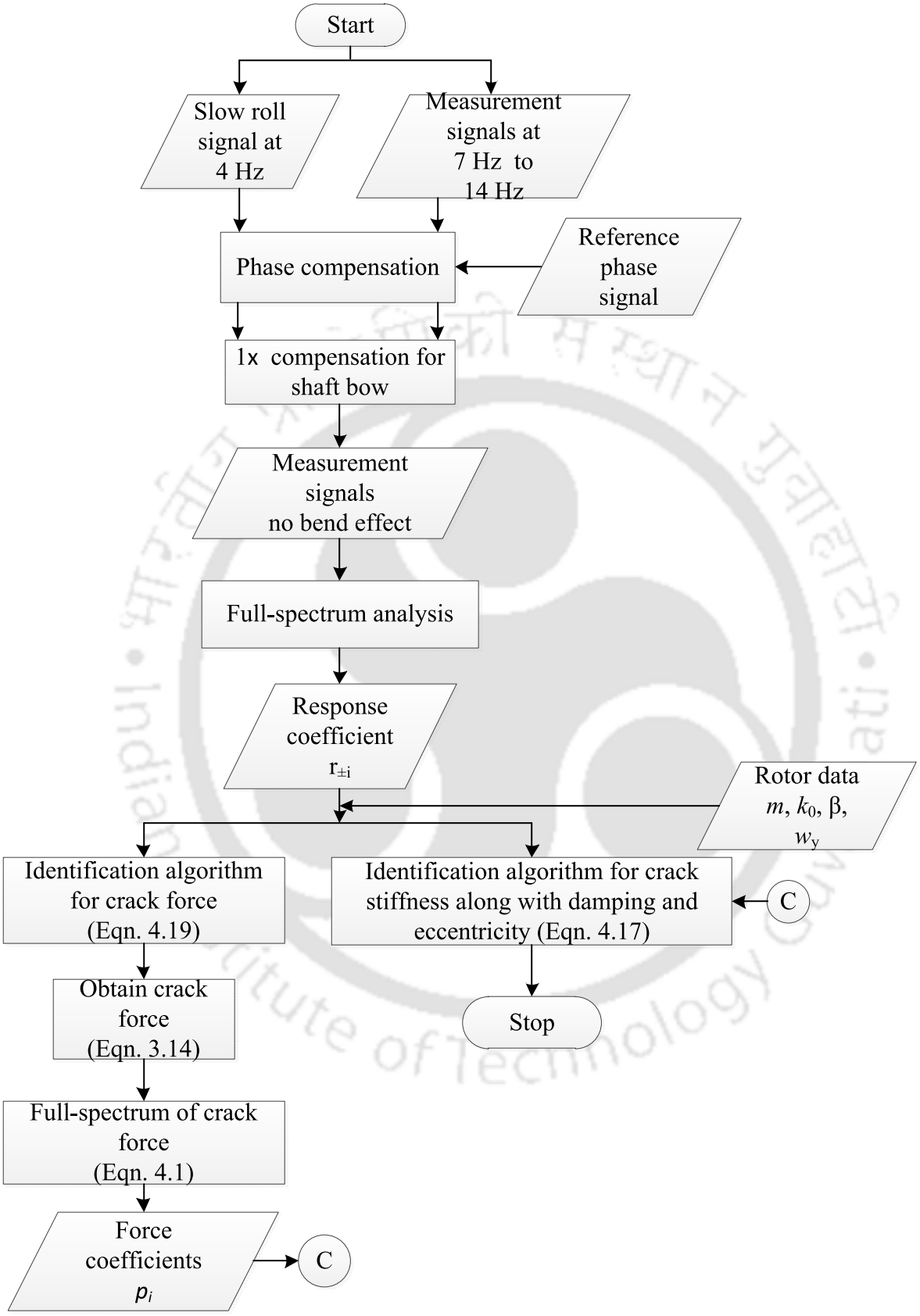


Figure 6.34 Flowchart showing experimental procedure for identification

### 6.7 Identification of Crack Force

D*isplacement coefficients* of the slow-roll compensated displacement signals are obtained for all the signals in the measurement spin-speed range of 7 Hz to 14 Hz. These coefficients are input to an *identification algorithm* which estimates the crack force (Eqn. (4.19)). The identification algorithm was described in detail in Section 4.3. Rotor system parameters used as an input to the identification of crack force are given in Table 6-9. The estimation of crack forces is performed using Eqn. 4.19. A switching crack model (containing the harmonics 1×, 2×, 3×, 5×, 7×, -1×, -3×, -5×, -7×) has been considered in developing the identification algorithm as in Eqn. 3.15. But, a generalized crack force $w_x \Delta k_{22} \sum_{i=-\infty}^{+\infty} p_i e^{\mathrm{j}i\omega t}$, with $i\omega$ indicating the forward and reverse harmonics of crack force has also been considered. Thus, the identification algorithm in Eqn. 4.19 is generalized to consider effects both switching as well as breathing crack, as the number of harmonic components considered in the algorithm are generalized.

The estimates of $\Delta k_{22} p_i$ are obtained which provide the crack force in which, $p_i$ are the force coefficients for various harmonics of crack force (which are harmonics of the rotational speed). In the estimation equation Eqn. (4.19), $i$ has been considered for the *forward* as well as *reverse* harmonics; -11×, -10×, …. , 1×, 2×, … 11×. For Case A the experimentally estimated forces in vertical and horizontal directions are shown in Figure 6.35. Similarly, plots for Case B are provided in Figure 6.36, and plots for Case C are provided in Figure 6.37.

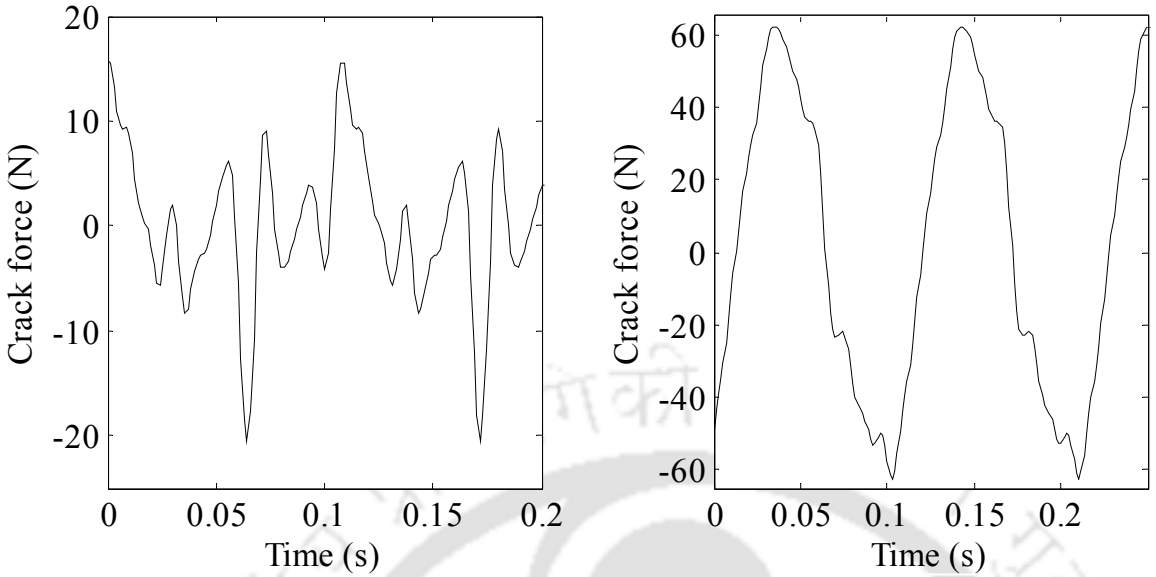


Figure 6.35 Estimates of Switching Crack forces from measurement Case A (a) along the direction of crack and (b) in the direction perpendicular to crack, at a spin speed of 7 Hz

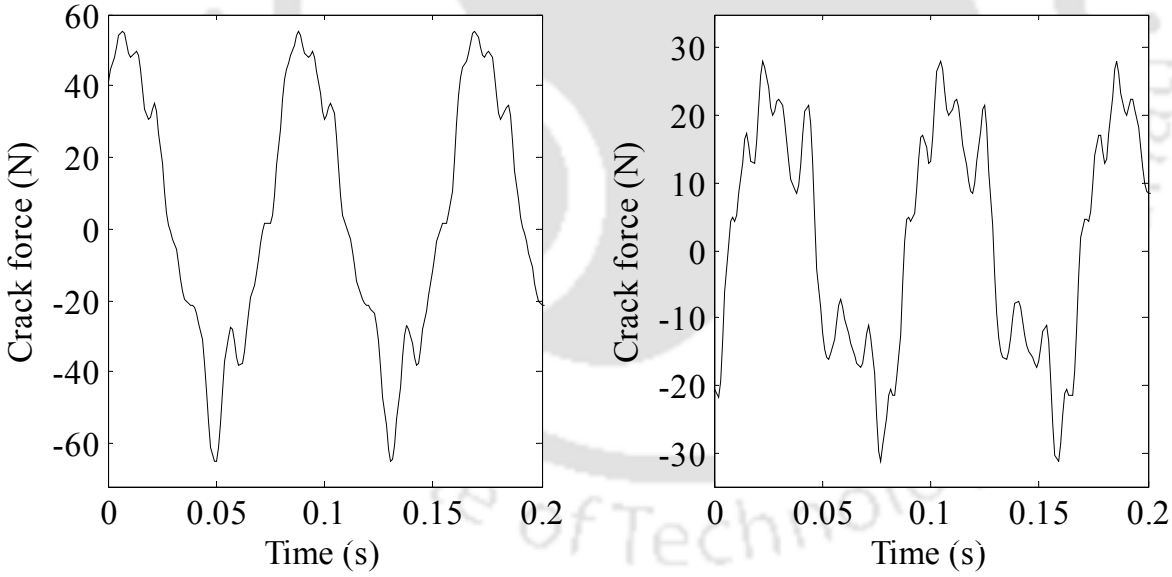


Figure 6.36 Estimates of Switching Crack forces from measurement Case B (a) along the direction of crack and (b) in the direction perpendicular to crack, at a spin speed of 11 Hz

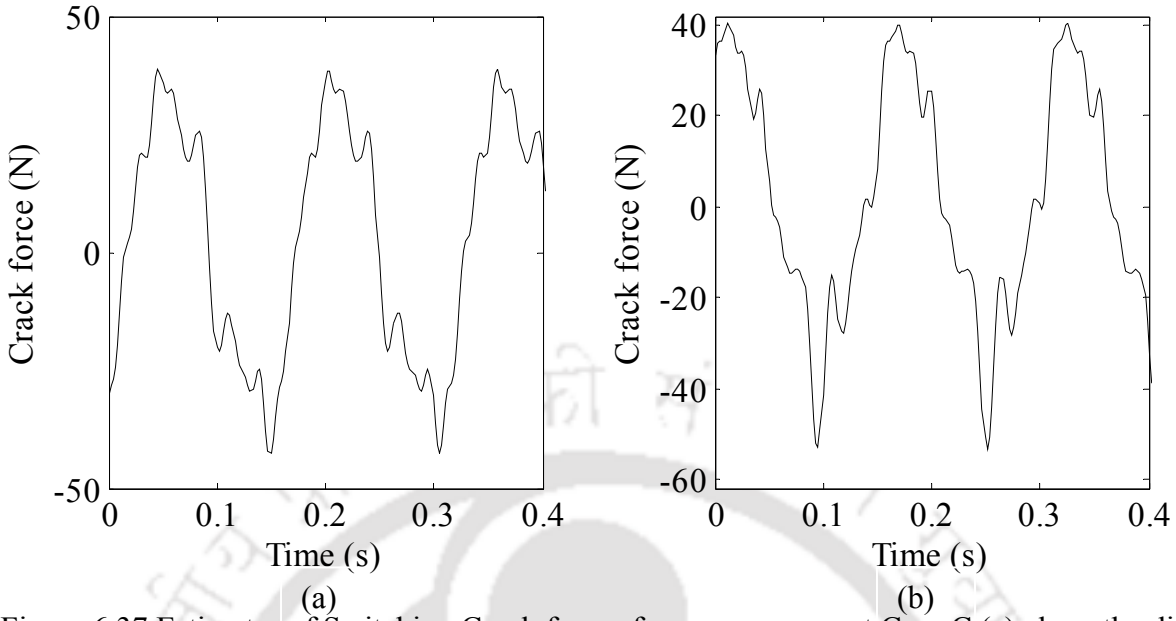


Figure 6.37 Estimates of Switching Crack forces from measurement Case C (a) along the direction of crack and (b) in the direction perpendicular to crack, at a spin speed of 14 Hz

It is observed from the estimates of crack force that, in the direction of crack, the crack force response is unsymmetrical about the mean axis, For example, for Case C the range is between -60 N to 40 N. Whereas, the crack force response in the perpendicular direction is symmetric about the mean and the range is between -40 N to 40 N. When the crack front is in the downward direction, due to the static load it is fully open, when it is upward direction then it is fully closed, and in other positions it is partially open. This causes an unsymmetrical crack force response in the direction of the fully open crack. On the other hand, a symmetrical crack force response in the direction perpendicular to the crack. The estimates of $\Delta k_{22} p_i$ for measurement Case C are obtained and tabulated inTable 6-11.

Table 6-11 Estimates of crack force terms (N/m)

| Parameter | Estimates ($\times 10^{-6}$) | Parameter | Estimates ($\times 10^{-6}$) |
|---|---|---|---|
| $\Delta k_{22}p_1$ | 0.038 | $\Delta k_{22}p_{-1}$ | 0.035 |
| $\Delta k_{22}p_2$ | 0.066 | $\Delta k_{22}p_{-2}$ | 0.066 |
| $\Delta k_{22}p_3$ | 0.007 | $\Delta k_{22}p_{-3}$ | 0.005 |
| $\Delta k_{22}p_4$ | 0.015 | $\Delta k_{22}p_{-4}$ | 0.052 |
| $\Delta k_{22}p_5$ | 0.034 | $\Delta k_{22}p_{-5}$ | 0.094 |
| $\Delta k_{22}p_6$ | 0.041 | $\Delta k_{22}p_{-6}$ | 0.147 |
| $\Delta k_{22}p_7$ | 0.048 | $\Delta k_{22}p_{-7}$ | 0.167 |
| $\Delta k_{22}p_8$ | 0.043 | $\Delta k_{22}p_{-8}$ | 0.132 |
| $\Delta k_{22}p_9$ | 0.016 | $\Delta k_{22}p_{-9}$ | 0.154 |
| $\Delta k_{22}p_{10}$ | 0.035 | $\Delta k_{22}p_{-10}$ | 0.123 |
| $\Delta k_{22}p_{11}$ | 0.034 | $\Delta k_{22}p_{-11}$ | 1.271 |
| $\Delta k_{22}p_0$ | 0.014 | | |

Full-spectrum plots of crack force Figure 6.35 to Figure 6.37 (shown in Figure 6.35 to Figure 6.37) are obtained, which give *force coefficients* (Eqn. (4.1)). Force coefficients at a measurement speed of 13 Hz are shown in Figure 6.38.These force coefficients are obtained similarly for all the measurement speeds from 7 Hz to 14 Hz.

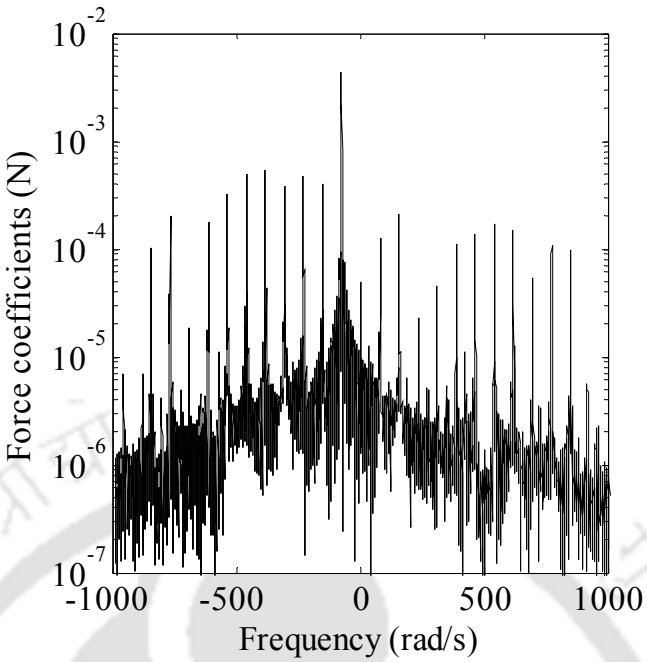


Figure 6.38 Full-spectrum plot showing force coefficients at a speed of 13 Hz

### 6.7.1 Identification of Crack, Unbalance, and Viscous Damping

From crack forces estimated at individual measurement speeds, their corresponding *force coefficients* are obtained using full-spectrum plots (Figure 6.38). Now, force coefficients and displacement coefficients are together used as an input to an identification algorithm that estimates the crack additive stiffness parameter, eccentricity due to unbalance, and shaft viscous damping. The additive stiffness parameter is an indicator of the crack. This algorithm has been described in Section 4.3. Displacement coefficients (Figure 6.30toFigure 6.33) and system parameters (Table 6-9) along with force coefficients (Figure 6.38) are used as an input to the identification algorithm (Eqn.(4.17)) to estimate the unknown fault and system parameters. Experimentally estimated parameters for the cracked rotor system are tabulated in Table 6-12.

Table 6-12 Parameter estimates from the identification algorithm

| Parameter | Estimates from Case A | Estimates from Case B | Estimates from Case C |
|---|---|---|---|
| Viscous damping, $c$ | 109.63 N-s/m | 76.802 N-s/m | 106.49 N-s/m |
| Disc eccentricity, $e$ | 0.046 m | 0.024 m | $1.8\times10^{-4}$ m |
| Additive crack stiffness, $\Delta k_{22}$ | $2.89\times10^{5}$ N/m | $3.03\times10^{5}$ N/m | $2.74\times10^{5}$ N/m |

The estimates corresponding to measurement Case C are better estimates, which includes measurements from Case A and Case B.

On comparing the estimated additive crack stiffness (i.e., $2.7\times10^{5}$ N/m) with that of intact shaft stiffness (i.e., $7.6\times10^{5}$ N/m), it can be observed that because of the induced fatigue crack, a 60% reduction in intact shaft stiffness is estimated. The ratio of intact shaft stiffness to shaft stiffness with crack can be related to the related to the ratio of diameter of intact shaft to the equivalent diameter of shaft with crack. It is givens as $\left(\frac{k_{\text{intact}}}{k_{crack}}\right)=\left(\frac{d^4_{\text{intact}}}{d^4_{crack}}\right)$. The equivalent diameter of shaft with crack is obtained as 14.2 mm. This corresponds to 10% reduction in the intact shaft diameter due to the crack growth. The effect of the notch machined to the shaft has already been considered in the shaft stiffness, obtained based on free vibration test results. A notch represents an open crack and cannot have any contribution in the variation of stiffness. Hence, the percentage reduction in stiffness corresponds to fatigue crack alone.

### 6.8 Inferences from the Experimental Results

A fatigue crack was experimentally introduced by three-point bending in a mild steel shaft. Since standards were not available for the fatigue testing of plain round shafts, a trial and error method was used along with the dye penetrant inspection to observe the initiation of crack. The shaft was assembled in a rotor-bearing-coupling set up, for the identification of crack along with unknown system parameters. The system natural frequency of the cracked rotor was observed as 98 Hz from the impact test. For measurements in the dynamic condition, spin-speeds were chosen well below critical speed (1 Hz to 13 Hz), and independent measurements were obtained at constant spin speed. Two displacement signals in orthogonal directions and one keyphasor signal for the phase were measured. The constant phase of the displacement responses was ensured as the measurement speeds did not cross any critical speed.

The processing of the acquired displacement signals is performed prior to use in identification algorithms. The slow-roll speed is chosen as 4 Hz and measurement speeds are chosen between 7 Hz to 14 Hz. The *phase compensation*, together with *1× waveform compensation* of the slow-roll measurement is done to eliminate the effect of bend in the shaft. Crack breathing forces are experimentally estimated with respect to time. The estimates of the switching crack forces in the direction of crack are plotted in. Force coefficients and displacement coefficients are obtained using the full-spectrum tool, and then fed as an input in the identification algorithm to estimate the crack parameter together with other unknown system parameters. From the obtained estimates, it is observed that the system has a damping ratio of 0.04. Also, the correction mass for estimated unbalance is obtained as 3 gm at 10 cm radius at an angle of $103^0$ with respect to the phase reference.

## 6.9 Concluding Remarks

- The aim of the present chapter is to develop an experimental set up for studying rotor crack dynamics with a fatigue crack. This was required as most of the cracks used in experimental study included hack-saw, wire-cut EDM, or welded shaft crack which do not mimic the breathing mechanism characteristic of a fatigue crack.
- A fatigue crack was artificially induced in a mild steel shaft by means of three-point bending with cyclic fatigue loading. A $90^0$ v-notch was developed by milling which acts as a stress-raiser. A 100 kN servo-hydraulic machine with standard three-point bending fixture was used for provide fatigue loading under compression with a stress ratio of 0.3. The crack initiation was observed by means of liquid dye penetration, where the dye oozes from the crack edges on its initiation.
- The developed shaft with fatigue crack was assembled in a laboratory rotor setup with bearings, couplings, motor, and disc mass components. Vibration pickups using eddy probe displacement sensors and optical tachometer for phase and speed measurements were used. The acquired signals are processed using a standard data acquisition system.
- Free-vibration tests are conducted to observe the first critical speed of the system at 98 Hz. The measurement speed range for acquiring vibration displacement in this study is form 7 Hz to 14 Hz, which is roughly below the critical speed of the six times per revolution component of the crack forcing.
- During generation of fatigue crack, a permanent bow of around 0.4 mm was set in the shaft. Hence, it was required to remove the effect of bow from the rotor crack dynamics. The method of 1× compensation in frequency domain is used.

- For 1× compensation, generally a signal with 300 RPM or less is considered. In this study, a slow-roll signal is obtained at 4 Hz (240 RPM). The slow-roll signal contains mainly the effect of shaft bow. Measurement of signals from 7 Hz to 14 Hz is considered for identification algorithm. The slow-roll signal and the high-speed measurement signal were processed to have the same phase reference. This is called as phase compensation. The phase-compensated signals were then used to obtain the full-spectrum displacement coefficients. The 1× displacement coefficients of the slow-roll and measurement signal are subtracted to remove the effect of the shaft bend.
- The 1× compensated signals are then used as an input for the developed identification algorithms. The estimates of additive crack stiffness, viscous damping, and disc eccentricity are obtained.
- The estimated viscous damping corresponds to an under-damped case with a damping ratio of 0.04.The estimated crack stiffness corresponds to a 10% reduction in shaft diameter due to crack growth. The estimates are obtained for different sets of measurements for testing the repeatability of the estimates.
- If the starting point of the selected response data is different, the phase at a frequency will be different. In the numerically simulated responses, the starting point is at time $t = 0$. In experiment also, the acquired signals can be ensured to start from same starting point, by using an external reference mark (i.e., $0^0$ phase angle).

# CHAPTER 7

# Conclusions and Scopes for Future Work

## 7.1 Conclusions

Anew model-based identification algorithm is developed for detecting a transverse fatigue crack in a rotor system. The parameters estimated from the identification algorithm are viscous damping, disc eccentricity due to unbalance, and additive stiffness due to the crack. The identification algorithm is developed based on time and frequency domain EOMs of the cracked rotor system subjected to crack and unbalance forcing. The reduction in flexibility of the shaft cross-section due to the crack is used as the hypothesis for identification algorithm. This forcing has multiple frequency components which are harmonics of the rotor spin speed. While some of the frequency components excite the rotor in a forward whirl, the others excite the rotor in a reverse whirl. Both time and frequency responses are used as an input for the developed algorithm. The advantages and defects of time and frequency based identifications are discussed. Switching crack forces are also identified. These estimates give an idea on the actual switching profile of the rotor crack.

Initially, the identification algorithm is developed in *time domain*, which uses displacement versus time responses alone as the input for identification algorithms. *Displacement coefficients* are first estimated based on the assumed solution for the closed-form response. The displacement as well as *force coefficients* corresponding to frequency responses of ±1×, +2×, ±3×, ±5×, and +7× harmonic components of spin speed are used in identification algorithms. These coefficients are in turn fed as an input to another identification algorithm to *simultaneously estimate* the crack and other unknown system parameters. The identification algorithm is extended to identify switching crack

forces. The estimates of crack force give an idea on the actual opening/closing profile of a rotor crack.

The identification algorithms are based on *inverse problem* approach and use least-squares method for obtaining estimates. For well-conditioned algorithms, the identification is carried at multiple measurement spin-speeds. The ranges of spin-speeds for testing the algorithm are based on critical speeds of various forcing frequency components considered. The estimates are compared with assumed parameters of the *direct problem*. Assumed parameters and estimates match well, indicating the robustness of the developed identification algorithm. This is true even for the case of moderate noise levels in responses. Due to type of crack model used in the present work, developed identification algorithms are applicable for small or medium sized cracks, which mean that they can be effectively used for early crack detection.

Next, identification algorithms are developed in *frequency domain*. Responses from a novel signal-processing tool, i.e., *full-spectrum* are used, which accommodates both the forward and reverse whirling frequency components of crack force and responses. The *displacement coefficients* and *force coefficients* are now directly obtained from full-spectrum plots, instead of estimating from time responses or using closed-form expressions. The need for full-spectrum in crack problem and different means of obtaining full-spectrum plots are elaborately discussed. A sample illustration of a complex time response, and its full-spectrum obtained by different means of complex DFT, and half-spectrum of orthogonal signals, are studied. The magnitude and phase values of the frequency components obtained from each of the methods are compared and observed to be same.

Full-spectrum based identification algorithms have more flexibility in terms of considering more number of harmonic components of crack force, considering any general crack opening/closing

function and its frequency spectrum, directly obtaining the force coefficients and displacement coefficients, and the reduction of data handling. The force coefficients till ±30× harmonic components of crack force are presented. The displacement as well as force coefficients corresponding to frequency responses of ±1×,+2×,±3×,±5×, and ±7× harmonic components of spin-speed have been used in the identification algorithm. The estimates of damping, disc eccentricity, and crack stiffness are obtained. The identification algorithms are extended and estimates of switching crack forces are similarly obtained. The estimates conform very well with assumed values, indicating the robustness of algorithms developed.

Next, the cracked rotor model is improved upon by considering a 4-DOF rotor model. This model has two transverse translational displacements and two transverse rotational displacements. Hence, this is a more general crack model. Two crack stiffness parameters are considered for identification: one in the direction of transverse translation, and other in the direction of transverse rotation. A general 4-DOF *transformation matrix* is developed for transformation of the crack stiffness matrix from the rotating to inertial frame of reference. Complex time responses and full-spectrum frequency responses are obtained using numerical simulations. *Dynamic condensation* is used to eliminate rotational displacements from identification, which are otherwise difficult to measure. The *reduced EOMs* in frequency domain are developed into different crack identification algorithms. Parameters of viscous damping, disc eccentricity, crack stiffness, and crack forces are estimated. The comparison of estimates with assumed values shows robustness of the developed identification algorithms in the presence of noise.

Finally, an experimental setup is developed to study the behaviour of a fatigue crack in a rotor assembly. A fatigue crack is artificially induced in a shaft with a V-notch using cyclic fatigue loading. The rotor assembly with cracked shaft is used for data acquisition and processing of vibration displacements.

### 7.2 Major Conclusions and Recommendations from the Present Work

A model-based identification algorithm is developed in time domain to estimate viscous damping, disc eccentricity due to unbalance, and additive crack stiffness. Displacement responses in two orthogonal directions in time domain are used as inputs to estimate displacement coefficients as well as the unknown fault and system parameters. The developed identification algorithms provided estimates which compare well with the assumed values of the parameters. The estimates of switching crack forces are also obtained similarly.

Similar model-based identification is developed in frequency domain, as it has advantages over identification in time domain. A novel signal-processing tool, i.e., full-spectrum obtains the displacement coefficients and force coefficients corresponding to various frequency components of crack force. Need for full-spectrum in crack problem and various methods of obtaining it are elaborately discussed. These full-spectrum coefficients are input to the developed algorithm to identify crack and unknown system parameters. The estimates of switching crack forces are also obtained. The identification algorithms are found to be robust.

Identification algorithms are developed for a cracked rotor model with gyroscopic couple. This model includes effects of disc inertia and cross-coupled flexibility and damping coefficients. The crack model has two stiffness parameters: one in the direction of transverse translation and other in

the direction of transverse rotation. Dynamic condensation eliminates the immeasurable (or at least difficult to measure accurately) rotating co-ordinates and reduced system EOMs are used to obtain identification algorithm. The identification algorithms are demonstrated for estimating crack stiffness, unknown system parameters, and crack forces.

A fatigue crack is induced experimentally in a rotor shaft. The crack was generated by means of three-point bending with cyclic fatigue loading. The crack initiation was observed and propagated to desired depth by means of liquid dye penetration method.

The experimental study of a rotor assembly with a fatigue crack in the shaft indicates vibration displacement signature, whose frequency spectrum has multiple harmonics of rotor spin speed. These frequency components of multiple harmonics result from the crack switching behaviour.

Experimental identification procedures are developed for estimating crack stiffness, unknown system parameters, and crack forces. The slow-roll 1× compensation is implemented for removing the effect of shaft bend from displacement responses. They are then used as input in identification algorithms and the estimates are obtained. The repeatability of the estimates is checked by testing the identification algorithms with different sets of measurement spin-speed ranges.

### 7.3 Limitations and Applicability

The identification algorithms are developed for simple cracked rotor models with two translational and two rotational co-ordinates. However, effects of disc moment of inertia, gyroscopic couple, and cross-coupling in flexibility and damping coefficients are considered. The dynamic condensation scheme for eliminating the rotational co-ordinates from the system EOMs is

also developed. Hence, the developed identification algorithms can be easily extended for complex finite element models using the developed mathematical models and methods.

The developed identification algorithms consider a switching crack. Since, this model of crack is applicable for initial stages of a rotor fatigue crack, the developed identification algorithms can be effectively used for early crack detection in rotor systems. Also, the crack location need not be known *apriori*.

The identification algorithms are model-based and the mathematical models developed use a single crack parameter for the identification of crack. Only the additive stiffness due to crack is considered. The crack axial location and size parameters are not considered. So, these parameters cannot be directly obtained from identification algorithms.

The identification algorithms are developed for detecting crack, but unbalance is also taken into account by considering disc eccentricity. Also, the experimental identification considers shaft bow. Hence, the developed identification algorithms can be effectively used for rotor responses with forcing due to the crack, the unbalance, and the shaft bow.

A crack near the middle of the shaft will affect the stiffness more than a crack near the bearings. Similarly, if the measurement location is changed to towards the end of shaft, the effect of crack on the shaft stiffness will be less, and subsequently the estimates of additive stiffness due to crack will also be less. Both the effects of measurement location and foundation flexibility can be included in the model before estimation by using finite element modeling and its effects could be studied.

The present cracked rotor model can be extended, to include flexibility due to foundation by FE modelling. The foundation flexibility at the supports can be modeled using a spring mass system. The dynamic stiffness terms due to foundation flexibility can be considered along with the crack stiffness term for simultaneous estimation.

Full-spectrum signal processing is developed to obtain forward and reverse whirl frequency components from complex time responses. Complex DFT, half-spectrums or orbit plots can be used to obtain magnitude and phase of full-spectrum frequency components.

Since the full-spectrum based identification algorithms are developed, and as the mathematical model includes gyroscopic couple, these identification algorithms can also be effectively used for rotor responses with both forward whirl and backward whirl frequency components.

Though the identification algorithms use a switching crack model, they have the flexibility to consider any general opening/closing crack function. Also, the full-spectrum gives flexibility to consider any number of harmonics of the frequency components of crack force, when the switching/breathing function is not known.

All the identification algorithms require measurements in two orthogonal directions. In reality the measurement locations on the shaft may not be accessible because of mountings over the shaft. However, identification algorithms do not require measurement locations near the crack.

**7.4 Scope for Future Work**

- The identification algorithms are illustrated for simple cracked rotor models. They can be extended to consider complex finite element modelling of the rotor system.
- The crack model can be extended to consider crack cross-coupled flexibility coefficients, and the same can be estimated.
- The mathematical model does not include parameters for crack quantification or location. The algorithms can be extended for estimation of size and location parameters. Also, the algorithms can be adapted for considering multiple cracks in the shaft.
- he mathematical model can be extended to consider misalignment or bearing faults along with the existing faults of crack, unbalance, and shaft bow.
- In experimental study, no filters have been used on the raw measurement data. The measurement data can be analysed for level of measurement noise and the sensitivity of the algorithms to the same. Also, procedures for pre-conditioning and removal of measurement noise at the time of signal acquisition can be studied.
- The identification algorithm could be tested for more characteristics such as: performance of the algorithms for cracks near end supports and minimum size of a crack that the algorithm can detect.
- The algorithms can be implemented to more complex rotor models, with the use of finite element methods. Lees and Friswell, 1997 and Sinha et al., 2002 study multi plane rotor balancing using modal balancing with a finite element model. The distributed unbalance is considered equivalent to a discrete distribution of unbalance, provided there are as many balance planes as active modes. The unbalance and foundation parameters are estimated from bearing pedestal vibration responses during a single run-down. The cracked element

stiffness matrix can be used along with this approach in order to model cracked rotor and implement algorithm to estimate crack and unbalance parameters.

**References**


- Adams, R. D., Cawley, P., Pye, C. J., and Stone, B. J., A vibration technique for non-destructively assessing the integrity of structures, *Journal of Mechanical Engineering Science* 1978; 20, 93-100.
- Al-Shudeifat, M. A., and Butcher, E. A., New breathing functions for the transverse breathing crack of the cracked rotor system: Approach for critical and subcritical harmonic analysis, *Journal of Sound and Vibration* 2011; 330,526-544.
- Bachschmid, N., Pennacchi, P., and Vania, A., Diagnostic significance of orbit shape analysis and its application to improve machine fault detection, *Journal of the Brazilian Society of Mechanical Sciences and Engineering* 2004; 26 (2), 200-208.
- Bachschmid, N., Pennacchi, P., Tanzi, E., and Audebert, S.,Transverse crack modeling and validation in rotor systems including thermal effects, *International Journal of Rotating Machinery* 2004;10 (4), 253-263.
- Behzad, M., Ebrahimi, A., and Meghdari, A., A new continuous model for flexural vibration analysis of a cracked beam,*Polish Maritime Research* 2008; 2 (56), 32-39.
- Cai, *Vibration Diagnostics of Elastic Shafts with a Transverse Crack*, Thesis, Faculty of computing, health and science, Edith Cowan University 2011.
- Chasalevris, A. C., Papadopoulos, C. A., Experimental detection of an early developed crack in rotor-bearing system using an AMB, *3rd International Conference of Engineering against Failure*2013;26-28 June, Kos, Greece.
- Childs, D. W., and Jordan, L. T., Clearance effects on spiral vibrations due to rubbing, *Proceedings of the ASME- Design Engineering Technical Conference* 1997; DETC97/VIB-4058.

- Christidies, S., and Barr, A. D. S., One-dimensional theory of cracked Bernoulli-Euler beams, *International Journal of Mechanical Science* 1984; 26 (11-12), 639-648.
- Cooley, J. W., and Tukey, J. W., An algorithm for the machine calculation of complex Fourier series, *Mathematics of Computation* 1965; 19, 297-301.
- Darpe, A. K., Coupled vibrations of a rotor with slant crack, *Journal of Sound and Vibration* 2007; 305 (1-2), 172-193.
- Darpe, A. K., Gupta, K., and Chawla, A., Coupled bending, longitudinal and torsional vibrations of a cracked rotor, *Journal of Sound and Vibration* 2004; 269, 33-60.
- Darpe, A. K., Gupta, K., and Chawla, A., Experimental investigations of the response of a cracked rotor to periodic axial excitation, *Journal of Sound and Vibration* 2003; 260, 265-286.
- Davies, W. G. R., and Mayes, I. W., The vibrational behavior of a multi-shaft, multi-bearing system in the presence of a propagating transverse crack, *Journal of Vibration Acoustics Stress and Reliability in Design- Transactions of ASME* 1984; 106, 146-153.
- Dharmaraju, N., Tiwari, R., and Talukdar, S., Identification of an open crack model in a beam based on force-response measurements, *Computers & Structures* 2004; 82 (2-3), 167-179.
- Dimarogonas, A. D. and Papodopoulos, C. A., Vibration of cracked shafts in bending, *Journal of Sound and Vibration* 1983; 91, 583-593.
- Dimarogonas, A. D., Vibration of cracked structures: A state of the art review, *Engineering Fracture Mechanics* 1996; 55 (5), 831-857.
- Dimentberg, F. M., *Flexural Vibrations of Rotating Shafts*, Butterworths, London, England 1961.

- Doebling, S. W., Farrar, C. R., Prime, M. B., and Shevitz, D. W., Damage identification and health monitoring of structural and mechanical systems from changes in their vibration characteristics: a literature review, Report, Los Alamos National Laboratory,*LA-13070-MS* 1996; 1-121.
- Downham, E., Vibration in rotating machinery: malfunction diagnosis- art and science, *Proceedings of the Institution of Mechanical Engineers- Vibrations in Rotating Machinery* 1976; 1-6.
- Ebrahimi, A., Heydari, M., and Behzad, M., A continuous vibration theory for rotors with an open edge crack, *Journal of Sound and Vibration* 2014; 3522-3535.
- Edwards, S., Lees, A. W., and Friswell, M. I., Fault diagnosis of rotating machinery, *Shock and Vibration Digest* 1998; 30 (1), 4-13.
- El Arem, S., and Maitournam, H., A cracked beam finite element for rotating shaft dynamics and stability analysis, *Journal of Mechanics of Materials and Structures* 2008; 3 (5), 893-910.
- Friswell, M. I., and Penny, J. E. T., Crack modeling for structural health monitoring, *Structural Health Monitoring* 2002; 1(2), 139-148.
- Friswell, M. I., Damage identification using inverse methods, *Philosophical Transactions of the Royal Society* 2007; 365 (1851), 393-410.
- Gasch, R., A survey of the dynamic behaviour of a simple rotating shaft with a transverse crack, *Journal of Sound and Vibration* 1993; 160, 313-332.
- Gauss, C. F., Demonstratio nova theorematis omnem functionem algebraicam rationalem integram unius variabilis in factores reales primi vel secundi gradus resolvi posse, *PhD thesis, Universit¨at Helmstedt* 1799; In Werke III, 1–30.

- Goldman, P., and Muszynska, A., Application of full spectrum to rotating machinery diagnostics, *Orbit* 1999; 17-21.
- Gounaris, G., and Dimarogonas, A., A finite element of a cracked prismatic beam for structural analysis, *Computers & Structures* 1988; 28 (3), 309-313.
- Grabowski, B., The vibrational behavior of a turbine rotor containing a transverse crack, *Journal of Mechanical Design* 1980; 102 (1), 140-146.
- Gudmundson, P., The dynamic behaviour of slender structures with cross-sectional cracks, *Journal of the Mechanics and Physics of Solids* 1983; 31 (4), 329-345.
- He, Z. J., Sheng, Y. D., and Qu, L. S., Rub failure signature analysis for large rotating machinery, *Mechanical Systems and Signal Processing* 1990; 4 (5), 417-424.
- Hill, J. W., and Baines, N. C., Applications of an expert system to rotating health monitoring, *Proceedings of the Institution of Mechanical Engineers- Vibrations in Rotating Machinery* 1988; 449-454.
- Irwin, W. J., Analysis of stress and strains near the end of a crack traversing a plate, *Journal of Applied Mechanics* 1957; 24, 361-364.
- Isermann, R. and Balle, P., Trends in the applications of model-based fault detection and diagnosis of technical processes, *Control Engineering Practice*1997; 5, 709-719.
- Isermann, R., Model-based fault-detection and diagnosis – status and applications, *Annual Reviews in Control* 2005; 29, 71-85.
- Iwatsubo, T., Error analysis of vibration of rotor/bearing system, *Proceedings of the Institution of Mechanical Engineers- Vibrations in Rotating Machinery* 1976; 87-92.
- Jun, O. S., Eun, H. J., Earmme, Y. Y., and Lee, C. W., Modelling and vibration analysis of a simple rotor with a breathing crack, *Journal of Sound and Vibration* 1992; 155, 273-290.

- Karthikeyan, M., and Tiwari, R., Detection, localization, and sizing of a structural flaw in a beam based on forced response measurements – An experimental investigation, *Mechanism and Machine Theory* 2010; 45, 584-600.
- Kirmsher, P. G., The effect of discontinuities on the natural frequency of beams, *Proceedings of American Society of testing and Materials* 1944; 44, 897-904.
- Lees, A. W., and Friswell, M. I., The evaluation of rotor unbalance in flexibly mounted machines, *Journal of Sound and Vibration*, 1997, 208, 671-683.
- Lee, C. W., and Han, Y. S., Use of directional Wigner distributions for identification of the instantaneous whirling orbit in rotating machinery,*7th International Symposium on Transport Phenomena and Dynamics of Rotating Machinery*1998; 22-26.
- Lee, C. W., and Joh, C. Y., Development of the use of directional frequency-response functions for the diagnosis of anisotropy and asymmetry in rotating machinery- Theory, *Mechanical Systems and Signal Processing* 1994; 8 (6), 665-678.
- Lee, Y. S., and Chung, M. J., A study on crack detection using eigenfrequency test data, *Computers and Structures* 2001; 77, 327-342.
- Liu, C., and Xiang, D., Experimental study on lateral and torsional vibration of cracked rotor with torsional excitation, *ASME Turbo Expo 2013: Turbine Technical Conference and Exposition*2013,V07AT29A011,June 3-7, San Antonio, USA.
- Lyons, R. G., *Understanding Digital Signal Processing* 2011, Third Edition, Pearson Education.
- Maalouf, M. G., Slow-speed: vibration signal analysis, *Orbit* 2007; 27 (2), 4-16.
- Mayes, I. W., and Davies, W. G. R., The vibrational behaviour of a multi-shaft, multi-bearing system in the presence of a propagating transverse crack, *Journal of Vibration Acoustics Stress and Reliability in Design- Transactions of ASME* 1976; 106, 146-153.

- Mayes, I. W., and Davies, W. G. R., Analysis of the response of a multi-rotor-bearing system containing a transverse crack in a rotor, *ASME Journal of Vibration, Acoustics, Stress and Reliability in Design* 1984; 106, 139-145.
- McFadden, P. D., and Smith, J. D., Model for the vibration produced by a single defect in a rolling element bearing, *Journal of Sound and Vibration* 1984; 96, 69-92.
- Meng, J., *Some Advanced Techniques in Fault Feature Extraction for Large Rotating Machinery*, Ph. D. dissertation, Xian Jiao Tong University 1996.
- Neale, M. J., and Woodley, B. J., A guide to the condition monitoring of machinery, *Report TRD 223for British Department of Industry* 1978.
- Nelson, H. D., and Nataraj, C., The dynamics of a rotor system with a cracked shaft, *ASME Journal of Vibration, Acoustics, Stress and Reliability in Design* 1986; 108, 189-196.
- Pandey, A. K., Biswas, M., and Samman, M. M., Damage detection from changes in curvature mode shapes, *Journal of Sound and Vibration* 1991; 145 (2), 321-332.
- Papadopoulos, C. A., and Dimarogonas, A. D., Stability of the cracked rotors in the coupled vibration mode, *ASME Journal of Vibration, Acoustics, Stress, and Reliability in Design* 1988; 110 (3), 356-359.
- Papadopoulos, C. A., The strain energy release approach for modeling cracks in rotors: A state of the art review, Mechanical *Systems and Signal Processing* 2008; 22 (4), 763-789.
- Patel, T. H., and Darpe, A. K., Application of full spectrum analysis for rotor fault diagnosis, *IUTAM Symposium on Emerging Trends in Rotor Dynamics* 2011; 1011, 535-545.
- Patton, R. J., Robustness in model-based fault diagnosis: The 1997 situation, *Annual reviews in Control* 1997; 21, 103-123.

- Pennacchi, P., Bachschmid, N., and Vania, A., A model-based identification method of transverse cracks in rotating shafts suitable for industrial machines, *Mechanical systems and signal processing* 2006; 20, 2112-2147.
- Prashant Kumar, (1999), *Elements of Fracture Mechanics*, Wheeler Publishing, New Delhi.
- Qu, L., Liu, X., and Chen, Y., (1989) Discovering the holospectrum, *Journal of Noise and Vibration Worldwide* 1989; 58-62.
- Qu, L., Xie, A. X., and Li, X., Study and performance evaluation of some nonlinear diagnostic methods for large rotating machinery, *Mechanical Mathematical Theory* 1993; 28(5), 699-713.
- Randall, R. B., *Vibration-Based Condition Monitoring*, John Wiley and Sons 2011.
- Rao, J. S., A note on Jeffcott warped rotor, *Mechanism and Machine Theory*; 2001, 37(5), 563-575.
- Rice, J. R., A path independent integral and the approximate analysis of strainconcentration by notches and cracks, *Journal of Applied Mechanics* 1968; 35, 379-386.
- Rizos, P. F., Aspragothas, N., and Dimarogonas, A. D., Identification of crack location and magnitude in a cantilever beam from the vibration modes, *Journal of Sound and Vibration* 1990; 138 (3), 381-388.
- Rytter, A., *Vibration based inspection of civil engineering structures*, Ph.D. Dissertation, Department of Building Technology and Structural Engineering 1993; Aalborg university, Denmark.
- Sabnavis, G., Kirk, R. G., Kasarda, M., and Quinn, D., Cracked shaft detection and diagnostics: a literature review, *The Shock and Vibration Digest* 2004; 36 (4), 287-296.
- Sekhar, A. S., Model-based identification of two cracks in a rotor system, *Mechanical Systems and Signal Processing* 2004; 18 (4), 977-983.

- Sekhar, A. S., Crack identification in a rotor system: a model-based approach, *Journal of Sound and Vibration* 2004; 270, 887-902.
- Shi, D., Qu, L., and Bao, M., Instantaneous purified orbit: a new tool for analysis of nonstationary vibration of a rotor system, *International Journal of Rotating Machinery* 1999; 7, 105-111.
- Singh, S. K., and Tiwari, R., Detection, localization of multiple cracks in a shaft system An experimental investigation, *Measurement* 2014;http://dx.doi.org/10.1016/j.measurement.2014.03.028 (available online).
- Singh, S. K., and Tiwari, R., Identification of a multi-crack in a shaft system using transverse frequency response functions, *Mechanism and Machine Theory* 2010; 45 (12), 1813-1827.
- Sinha, J. K., Friswell, M. I., and Edwards, S., Simplified models for the location of cracks in beam structures using measured vibration data, *Journal of Sound and Vibration* 2002; 251 (1), 13-38.
- Sinha, J. K., Friswell, M. I., Lees, A. W., and Sinha, R. K., Robust method for the rotor unbalance estimation, Proceedings of VETOMAC-2, 16-18 December 2002.
- Sinha, J. K., Higher order spectra for crack and misalignment identification in the shaft of a rotating machine, *Structural Health Monitoring* 2007; 6(4), 325-334.
- Smtih, D. M., Recognition of the causes of rotor vibration in turbomachinery, *Proceedings of the Institution of Mechanical Engineers- Vibrations in Rotating Machinery* 1976; 1-4.
- Smith, S. W., *The Scientist and Engineer's Guide to Digital Signal Processing* 1997, California Technical Publishing, San Diego.
- Southwick, D., Using Full spectrum plots, *Orbit* 1993; 14(4), 12-16.
- Southwick, D., Using Full spectrum plots Part 2, *Orbit* 1994; 15(2), 10-16.

- Stewart, R. M., Vibration analysis as an aid to the detection and diagnosis of faults in rotating machinery, *Proceedings of the Institution of Mechanical Engineers- Vibrations in Rotating Machinery* 1976; 223-229.
- Tada, H., Paris, P. C., and Irwin, G. R., *The stress Analysis of Cracks Handbook*, 3rd ed., New York: ASME 2000.
- Taylor, J. I., Back to the basics of rotating machinery vibration analysis, *Sound and Vibration* 1995; 29 (2), 12-16.
- Tiwari, R., Conditioning of regression matrices for simultaneous estimation of the residual unbalance and bearing dynamic parameters, *Mechanical Systems and Signal Processing* 2005; 19, 1082-1095.
- Thomas, D. L., Vibration monitoring strategy for large turbogenerators, *Proceedings of the Institution of Mechanical Engineers- Vibrations in Rotating Machinery* 1984; 91-99.
- Timoshenko, S., and Young, D. H., *Elements of strength of materials* 1968, Van Nostrand.
- Thomson, W. J., Vibration of slender bars with discontinuities in stiffness, *Journal of Applied Mechanics* 1943; 17, 203-207.
- Tuma, J., and Bilos, J., Fluid induced instability of rotor systems with Journal bearings, Engineering Mechanics 2007; 14, 69-80.
- Wauer, J., Modelling and formulation of equations of motion for cracked rotating shafts, *International Journal of Solids and Structures* 1990; 26, 901-914.
- Wells, A. A., Fracture control: past, present and future, *Experimental Mechanics* 1973; 13 (10), 401-410.
- Zhou, T., Sun, Z., Xu, J., and Han, W., Experimental analysis of cracked rotor, *Journal of Dynamic systems, Measurement, and Control* 2005; 127, 313-320.

## Publications from the Present Work

**Journals:**

1. C. Shravankumar and R. Tiwari, Identification of stiffness and periodic excitation forces of a transverse switching crack in a Laval rotor, *Fatigue & Fracture of Engineering Materials & Structures* 2012, 36 (3), 254-269.
2. C. Shravankumar and R. Tiwari, Detection of a fatigue crack in a rotor system using full-spectrum based estimation, *Fatigue & Fracture of Engineering Materials & Structures*, (communicated).
3. C. Shravankumar and R. Tiwari, Identification of stiffness and forces of a switching crack in an offset Laval rotor. *Mechanism and Machine Theory*, (under preparation).
4. C. Shravankumar and R. Tiwari, Experimental crack identification in a rotor system, *Measurement*. (under preparation).

**Conferences:**

1. Shravankumar C., and R. Tiwari, 2013, Model-based crack identification using full-spectrum, *ASME 2013 Gas Turbine India Conference*(*GT India 2013*), December 5-6, 2013, National Aerospace Laboratory Bangalore, Karnataka, India (GTINDIA 2013-3756).
2. Shravankumar C., and R. Tiwari, 2014, Full-spectrum response analyses of a Laval rotor with a fatigue crack, *Third National Symposium on Rotor Dynamics* (*NSRD-2014*), February 12-14, 2014, Dr. Ambedkar Institute of Technology, Bangalore, Karnataka, India.
3. Shravankumar C., and R. Tiwari, 2014, Experimental identification rotor fatigue crack forces, *9th IFToMM International Conference on Rotor Dynamics*, September 22-25, 2014, Milan, Italy (Abstract accepted).